

Brno University of Technology  
Faculty of Mechanical Engineering  
Institute of Physical Engineering

Dr. Ing. Petr Neugebauer

**High Frequency Electron Spin Resonance Spectrometry:  
Today and Tomorrow**

Habilitation thesis  
Field of habilitation: Applied physics

Brno 2017

**Keywords**

Magnetic Resonance, Electron Spin Resonance (ESR/EPR), Single Molecule Magnets (SMMs), Dynamic Nuclear Polarization (DNP), High Magnetic Fields, THz frequencies

**Klíčová slova**

Magnetická resonance, elctron spinová resonance, jedno molekulární magnety, dynamická nukleová polarizace, silné magnetické pole, Terahertzové frekvence

Habilitační práce je uložena v Areálové knihovně FSI VUT v Brně.

# TABLE OF CONTENTS

TABLE OF CONTENTS .....	3
AUTHOR.....	4
1 INTRODUCTION.....	6
2 HIGH FIELD / HIGH FREQUENCY ELECTRON SPIN RESONANCE (HFESR) .....	6
2.1 Historical Overview .....	6
2.2 Principle of magnetic resonance .....	8
2.3 ESR Spectrometer.....	9
2.3.1 <i>Cw- ESR</i> .....	10
2.3.2 <i>Frequency Domain Magnetic Resonance</i> .....	10
2.3.3 <i>Pulsed ESR</i> .....	11
3 SOLID STATE MATERIALS – GRAPHENE .....	12
3.1 Cyclotron Resonance .....	13
4 SINGLE MOLECULE MAGNETS.....	15
4.1 Introduction to Single Molecule Magnets.....	16
4.2 HFESR and SMMs .....	17
4.2.1 <i>Spin Hamiltonian</i> .....	17
4.2.2 <i>Powdered Samples</i> .....	18
4.2.3 <i>Single Crystal Studies</i> .....	19
5 DYNAMIC NUCLEAR POLARIZATION (DNP).....	19
5.1 Liquid State DNP .....	20
5.1.1 <i>Experimental Techniques and Challenges</i> .....	21
6 CONCLUSIONS AND OUTLOOK.....	22
7 ACNOWLEDGEMENT.....	25
Commented Paper 1 .....	26
Commented Paper 2 .....	35
Commented Paper 3 .....	41
Commented Paper 4 .....	46
Commented Paper 5 .....	52
Commented Paper 6 .....	65
Commented Paper 7 .....	72
Commented Paper 8 .....	80
Commented Paper 9 .....	89
8 REFERENCES .....	97

## AUTHOR



Dr. Ing. Petr Neugebauer was born on September the 13<sup>th</sup> 1980 in Uherské Hradiště, Czech Republic. He was very active boy with lot of time spent in surrounding nature of his home town Kunovice, where he built up his passion for engineering and natural science in general. In 1996, he entered high school dedicated to mechanical engineering at Uherské Hradiště, followed by the engineering studies at Brno University of Technology (BUT), Czech Republic, at the Institute of Physical Engineering. In 2005, he finished his university studies by a diploma work dedicated to design of facility for in situ area monitoring of thin films (UV-VIS Reflectometry) under supervision of Prof. J. Spousta. During the university studies, he also spent six-months (Erasmus program) at Université Joseph Fourier, Grenoble & Institute Néel CNRS, Grenoble, France.

Under supervision of Dr. L. Ranno, he was working on experimental research project dedicated to design and building of a high temperature - high impedance Hall effect measurement facility.

In 2005, he started his Ph.D. studies (Marie Curie fellowship through QuEMolNa FP6-CT-2003-504880 and Early stage researcher fellowship through MAGMANet FP6-NMP3-CT-2005-515767) in direction of magnetic resonance. His Ph.D. in Grenoble High Magnetic Field Laboratory under the supervision of Dr. Anne-Laure Barra dealt with the construction of high-frequency continuous wave and pulsed ESR (HFESR) spectrometers operating at 285 GHz. In the PhD project, he was fully responsible for the construction of the HFESR spectrometer. He developed a Fabry-Pérot resonator and a rotating sample holder for high magnetic field ESR applications based on piezoelectric steppers. This new concept, which led to significant improvement in sensitivity and crystal orientation precision, was adapted by other researchers in the ESR community. He successfully applied these methods to the study of the electronic properties of graphene and graphite (3x PRL) and single molecule nanomagnets, which led to 6 papers in high impact journals. He was the first who observed decoupled graphene by ESR spectroscopy, and could prove the extraordinary properties of graphene expressed by highest electron mobility ever reported in literature yet.

After finishing his PhD studies, he worked for two years as postdoctoral researcher (Stipendium: Center of Excellence Frankfurt - CEF) in the group of Prof. Thomas F. Prisner at the Goethe University and Biomolecular Magnetic Resonance Center (BMRZ) in Frankfurt, where his research was focused on combining HFESR and NMR spectroscopy, specifically concerning hyperpolarization of nuclei (Dynamic Nuclear Polarization, DNP) through the polarization transfer from electron to nucleus in order to enhance NMR signals. In this domain his work contributed to the development of the hardware as well as to the experimental method. He developed a unique method to determine saturation factor for the first time. His experiments led to the achievement of extremely large enhancements of the NMR signal of solvent molecules, leading to the reduction of the experimental time by three orders of magnitude, from hours to seconds.

Subsequently, he joined the group of Prof. Joris van Slageren in Stuttgart in 2012, where he is working on development and application of HFESR and Frequency Domain Magnetic Resonance (FDMR) at frequencies from 80 GHz to 1100 GHz and magnetic fields up to 17 T. His experience led to building of the worldwide state of the art and first modern HFESR/FDMR spectrometer at the University of Stuttgart in a very short time after arriving. It is the first spectrometer which can be operated either in the field domain (HFESR) by sweeping the magnetic field at fixed irradiation frequency, or in the frequency domain (FDMR), by sweeping the frequency at fixed magnetic

field. This very versatile and very sensitive spectrometer ( $10^7$  spins/(Gauss.Hz<sup>1/2</sup>)) and sets current worldwide state of the art. He used the spectrometer to solve many scientific questions which led, among the others, to more than 15 high impact papers, including papers in Nature Commun., Nature Phys. and J. Am. Chem. Soc. It attracts already attention of many scientists across the world, namely: Manchester (*UK*), Washington (*USA*), Bordeaux, Grenoble (*France*), Lisbon (*Portugal*), Valencia, Barcelona (*Spain*), Berlin, Leipzig, Stuttgart (*Germany*), Buenos Aires (*Argentina*), Brno, Olomouc (*Czech*), Vienna (*Austria*), Beijing, Xi'an (*China*), Dublin (*Ireland*), Copenhagen (*Denmark*).

In 2014, he received a DFG grant (NE1900/2-1, 240 kEUR) to study a THz and sub-THz excitations in graphene based materials by applying magneto-optical spectroscopy, through which he established his own research group. Later on, he was awarded by a DFG grant (SPP1601, NE1900/3-2, 250 kEUR) and Baden-Württemberg Elite Program stipend to further explore THz and subTHz spectroscopy at the University of Stuttgart.

In 2016, he received the ERC Starting grant “THz Frequency Rapid Scan – Electron Spin Resonance spectroscopy for spin dynamics investigations of bulk and surface materials (THz-FRaScan-ESR)”, starting date 1.1.2018. The aim of the project is to set up and develop a revolutionary broadband THz Rapid Frequency Scan Electron Spin Resonance (THz-FRaScan-ESR) spectrometer, which will substantially increase the sensitivity of current magnetic resonance methods and, more importantly, it will allow multi-frequency relaxation studies even at zero field. This completely novel concept based on rapid frequency sweeps will stimulate development of novel materials and will improve MRI applications in hospitals.

In 2017, together with colleagues from institutions in Brno University of Technology, University of Stuttgart, Centro de Investigacion Cooperativa en Nanociencias CIC NANOGUNE and Thomas Keating Ltd. obtained European grant FET-Open supported by Horizon 2020 named “Plasmon Enhanced Terahertz Electron Paramagnetic Resonance (PETER)”, starting date 1.1.2018.

He is author or co-author of 36 original scientific papers in ISI-indexed journals with over 1000 citations and h-index = 15 according to Web of Science, ResID I-7844-2013. He is a member of International EPR (ESR) society, German Priority Program (SPP1601) dealing with magnetic resonance spectroscopy and Elite program of Baden-Württemberg.

Since his Ph.D. studies Petr Neugebauer took a part in education of new students at different level of their carrier, including pupils. He is strongly determined to pursue a career in academia. He enjoys working with students. He was/is involved in teaching at the Institute of Physical and Theoretical Chemistry, Goethe University in Frankfurt am Main as well as at the Institute of Physical Chemistry, University of Stuttgart supervising Bachelor, Master and Ph.D. Students. Among the home universities, he is regularly lecturing at BUT, Czech Republic. He is regularly taking care of ERASMUS students from the BUT, supervising and mentoring their 6 month research stay at the Institute of Physical Chemistry, University of Stuttgart. Furthermore, in 2016, he was giving invited lectures (16 hours) at Beijing University and Xi'an University in China dealing with magnetic resonance spectroscopy. He supervised 2 PhD, 5 master and 6 ERASMUS students. Today, his research group is composed by 1 senior scientist, 3 postdoctoral researchers, 5 PhD and 2 MSc students.

From 1.1.2018, he became a group leader of magnetic resonance group at Central European Institute of Technology (CEITEC) in Brno University of Technology.

# 1 INTRODUCTION

High Frequency Electron Spin Resonance (HFESR) is a magneto-optical method where microwaves (MW) typically at frequencies of 100s of GHz (meV range), are used for exciting molecules with unpaired electrons. HFESR is a powerful tool to investigate samples ranging from biomolecules to heterogeneous catalysts. It delivers the high  $g$ -value resolution that is needed to characterize the electronic structure and permits study of molecules in which magnetic anisotropy (zero-field splitting, ZFS) prevents investigations at lower frequencies. In materials science, it is also applied for measurements of modern solid state materials such as graphene (Chapter 3). In studies of coupled metallic centers with large ZFS (called molecular nanomagnets (MNMs) or single-molecule magnets (SMMs)), HFESR is an essential tool providing detailed information about their magnetic properties (Chapter 4). Furthermore, in the recent boom of Nuclear Magnetic Resonance (NMR) hyperpolarization, HFESR has had an indisputable role in improving NMR signal enhancement (Chapter 5). Historically, even small progresses in magnetic resonance have dramatically changed the landscape of what is possible in NMR, including MRI in hospitals. This has already led to 10 Nobel prizes in magnetic resonance.<sup>1</sup>

This work serves as a short introduction to the HFESR methodology and its applications described in attached papers.

## 2 HIGH FIELD / HIGH FREQUENCY ELECTRON SPIN RESONANCE (HFESR)

This chapter will introduce Electron Paramagnetic Resonance (EPR), also called Electron Spin Resonance (ESR) or Electron Magnetic Resonance (EMR), which has become a major tool in diverse fields ranging from biology and chemistry to solid state physics and materials science. We start from the first realization of this experimental technique by E. K. Zavoisky and continue towards to more sophisticated techniques used nowadays. The basic principles of magnetic resonance as well as the advantages of going to higher magnetic fields and higher excitation frequencies (HFESR) will be discussed.

### 2.1 HISTORICAL OVERVIEW

The EPR technique was first invented by E. K. Zavoisky at the end of the Second World War in

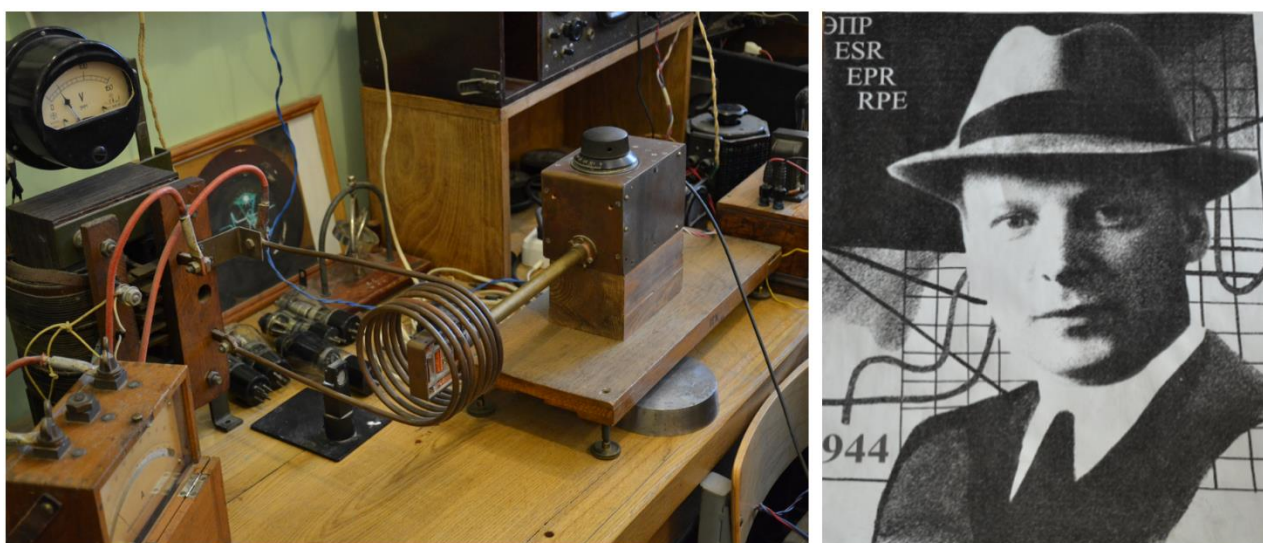


**Figure 1.** First ESR spectrometer operating at 10 MHz and 7.5 Oe designed by E. K. Zavoisky (1907-1976) in 1944 in Kazan. Pictures kindly provided by S. Zvyagin.

Kazan (USSR, today Russia) as a consequence of the availability of microwave (MW) components developed for RADAR. He employed the newly developed MW techniques in the construction of the first ESR spectrometer (Figure 1).<sup>2</sup> Soon after him, two years later (in 1946) in United States, and independently of E. K. Zavoisky, the Nuclear Magnetic Resonance (NMR) technique was developed by E. M. Purcell together with his colleagues R. Pound and H. Torrey at Radiation Laboratory at Massachusetts Institute of Technology.<sup>3</sup> E. M. Purcell together with F. Bloch (Stanford University) were honored in 1952 by the Nobel prize: “for their development of new methods for nuclear magnetic precision measurements and discoveries in connection therewith”.<sup>1</sup> The work of E. K. Zavoisky was recognized much later on and he was honored posthumously by the prestigious ISMAR Award of the International Society of Magnetic Resonance in 1977.

First experiments, NMR and ESR, were performed in the continuous wave (cw) regime. In 1950, E. L. Hahn conducted an experiment at University of Illinois with radio frequency (rf) pulses and observed a nuclear spin echo, which was the starting point not only for pulsed NMR techniques.<sup>4</sup> However, in ESR it took a decade until first coherent manipulations of electronic spin were done in sodium-ammonia solutions<sup>5</sup>, on electron donors in silicon<sup>6</sup> and the first pulsed ESR spectrometers were developed and described.<sup>7</sup> At the same time the pulsed NMR experiment already start to fully explore the possibilities of pulsed techniques. This was the point when NMR and ESR techniques continued in different ways. Whereas for NMR it was much easier to create coherent MHz pulses and thus fully explore the pulsed technique, creating new pulse sequences, multi-dimensional experiments etc., the situation for EPR was completely different. Today NMR almost completely moved from cw to pulsed operation, except for rare solid state physics applications. The problem in creating sufficiently short pulses and detecting fast transitions, often more than one order of magnitude faster than in NMR, limited ESR mainly to cw-ESR applications for a long time.

In 1957, G. Feher (*born in Bratislava, Czechoslovakia in 1924*) published his work in Bell labs where he pointed out the importance of the increase of the irradiation frequency for the sensitivity and the resolution of ESR spectrometers,<sup>8</sup> see Figure 2. However, it took a few decades until this prediction could be experimentally realized. The first to overcome the initial problems was the group of Ya. S. Lebedev from Moscow in the 1970s with the implementation of the first 148 GHz (D-band)/5.3 T ESR spectrometer.<sup>9</sup> The work of Lebedev was followed by several groups across the world in the 1980s. The group of W. R. Potter (Roswell Park Memorial Institute, Buffalo, New York) used 70 GHz (V-band)/ 2.5 T spectrometer to investigate trapped electrons in irradiated single crystals of polyhydroxy compounds.<sup>10</sup> The group of K. Möbius (Freie Universität Berlin) reported in 1984 an ESR spectrometer operating at 94 GHz (W-band)/3.4 T.<sup>11</sup> In 1988, the group of J. H. Freed (Cornell University) pushed the limit to 250 GHz/8.9 T by applying time quasi-optics (QO) made of Teflon lenses in ESR for the first time.<sup>12</sup> The first pulsed HFESR spectrometer operating at 95 GHz was reported in 1989 by the group of J. Schmidt (Huygens Laboratory, Leiden).<sup>13</sup> Simultaneously, a multi-frequency high field ESR spectrometer was developed by L.-C. Brunel (Grenoble High Magnetic Field Laboratory, GHMFL) going to fields as high as 20 T using resistive magnets.<sup>14, 15</sup> In 1992, group of R. G. Griffin (Francis Bitter National Magnet Laboratory, Massachusetts Institute of Technology) reported pulsed spectrometer operating at 140 GHz.<sup>16</sup> At the same time in the Griffin group, the first pioneering work on high frequency Dynamic Nuclear Polarization (DNP) is conducted.<sup>17, 18</sup> Few years later, in 1995 a pulsed HFESR spectrometer operating even at 604 GHz using a pulsed far-infrared laser was reported in GHMFL. This renaissance was further boosted by reporting in 1998 an ESR spectrometer relying on QO techniques based on reflection (mirrors) and corrugated waveguides by the group of P. C. Riedi (St. Andrews University), with respect to transmission (lenses) used previously, this way low loss broadband HFESR spectrometers are used nowadays in most HFESR laboratories.

ESR methods are progressing now as fast as the NMR technique in the second half of the last century. X-band (10 GHz), Q-band (35 GHz), W-band (95 GHz) and even 263 GHz pulsed ESR spectrometers are commercially available (mainly from Bruker or Jeol) and many pulsed experiments have become routine (ESEEM, HYSCORE, etc.). Double resonance techniques such as PELDOR<sup>19</sup> (DEER)<sup>20</sup> enable determination of the structure and kinetic properties of large molecules, which for different reasons were impossible before<sup>21</sup> and have become a useful complementary method to NMR and X-ray diffraction techniques in structure determination. Moreover, both techniques NMR and ESR are combined in DNP experiments, where ESR transitions are used to polarize nuclei via electron polarization transfer. The HFESR development is also strongly driven by the DNP experiments pioneered by Griffin at high fields and high frequencies.<sup>17, 18</sup> DNP experiments at ESR frequencies of 263 GHz, 329 GHz and 394 GHz corresponding to proton NMR frequencies of 400 MHz, 500 MHz and 600 MHz, respectively, are becoming routine equipment of NMR labs. Today many laboratories are still developing their own HFESR equipment<sup>22-27</sup>, pushing the work on new methodology and application of ESR further.<sup>28-32</sup>

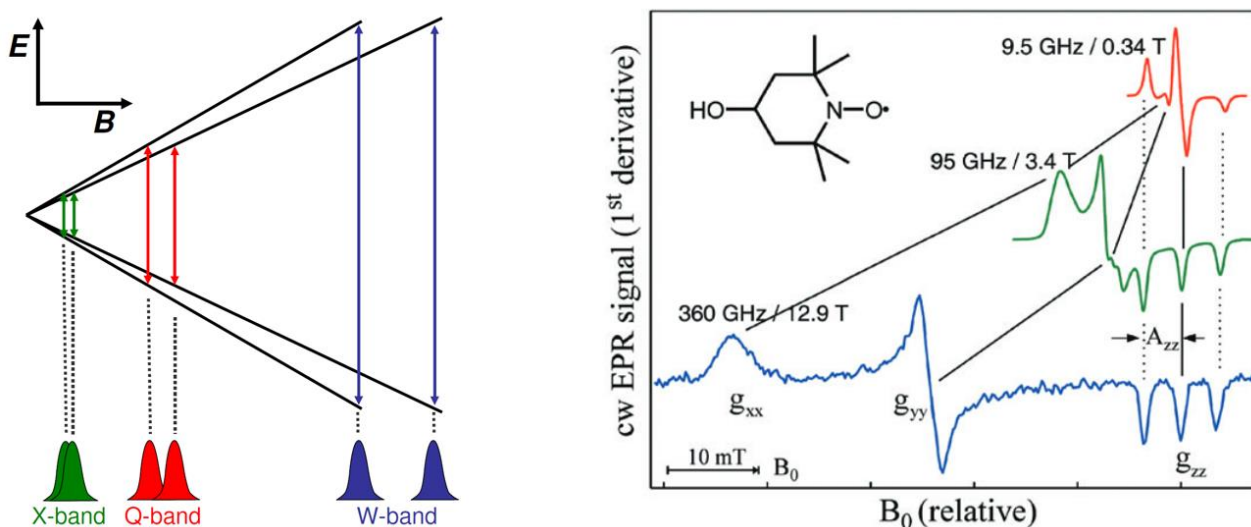


**Figure 2.** *Left:* Schematic expression of the effect of increasing magnetic field on the spectral resolution of two species with a close  $g$ -value. Whereas at X-band (10 GHz) frequencies the species are overlapping at W-band (95 GHz) frequencies they are fully resolved. *Right:* First-derivative cw EPR spectra of a nitroxide radical (OH-TEMPO) in frozen water solution at different microwave frequency/B settings. The spectra are plotted relative to the fixed  $g_{zz}$  value. Note the increased resolution of the anisotropic  $g$ -factor, picture reprinted from reference.<sup>33</sup>

## 2.2 PRINCIPLE OF MAGNETIC RESONANCE

Particles such as, for instance, electrons or nuclei possess an intrinsic magnetic moment called spin, marked  $S$  or  $I$ , respectively. In case of electron, the total magnetic moment  $J$  of a particle is composed of its spin  $S$  and its orbital moment  $L$  ( $J = L + S$ ). In presence of an external magnetic field  $\mathbf{B}$ , the total magnetic moment starts to precess around the direction of the applied field  $\mathbf{B}$  with an angular (Larmor) frequency  $\omega_L = \gamma \mathbf{B}$ , where  $\gamma$  is gyromagnetic ratio. The main difference between ESR and NMR techniques is in the magnitude of the Larmor frequency, which is connected to the gyromagnetic ratio  $\gamma = qg/(2m)$ , where  $q$  is charge,  $g$  is  $g$ -factor and  $m$  is the mass either of the electron or the nucleus which is about three orders of magnitude higher. The difference in mass of the electron with respect to the nucleus leads to resonances at different frequencies. When in ESR the resonance is observed in the GHz range, in NMR occurs at MHz frequencies. The lower frequency makes the experiment technically easier, thus the NMR technique progressed much faster than ESR.

ESR can be easily explained on the hydrogen atom which has one electron ( $S = 1/2$ ,  $L = 0$ ). In zero external magnetic field, the electron has two degenerate eigenstates, called spin UP ( $M_S = +1/2$ ) or spin DOWN ( $M_S = -1/2$ ). The presence of an external magnetic field  $\mathbf{B}$  lifts the degeneracy of the  $\pm 1/2$  spin states (Zeeman effect). The energy difference  $\Delta E$  (Zeeman splitting) between the upper and lower state is

$$\Delta E = hf_{\text{ex}} = g_e \mu_B \mathbf{B},$$

where  $g_e$  is the  $g$ -factor (Lande factor) of the electron and  $\mu_B$  is the Bohr magneton. The above equation implies that the splitting is directly proportional to the external magnetic field  $\mathbf{B}$ . Resonance absorption can occur if we apply an appropriate oscillating magnetic field  $\mathbf{B}_1$ , perpendicular to the external field  $\mathbf{B}$ , oscillating at frequency  $f_{\text{ex}}$ . Similar resonance expression can be written to NMR. However in the real experiment, we do not manipulate/excite only one spin, but ensemble of many spins, which are in a sample. We introduce magnetization  $\mathbf{M}$ , a macroscopic value describing sum of all spins in the sample, which is manipulated during the experiment. To describe the time evolution of  $\mathbf{M}$  during the experiment semi-classically, Bloch equations are commonly used. More details about the description of the magnetic resonance experiment can be found in one of the recommended text books of J. A. Weil & J. R. Bolton<sup>34</sup> and J. Keeler.<sup>35</sup>

Furthermore, from the above expression can be deduced that if there is a  $g$ -anisotropy, at higher fields and thus at higher frequencies it can be better resolved. This is schematically demonstrated on two species of slightly different  $g$ -values (Figure 2). Whereas at X-band frequencies and even at Q-band frequencies, it could be very difficult to resolve the two components correctly, at W-band frequencies they could be already completely separated and the  $g$ -values resolved correctly (Figure 2). The resolution of a W-band spectrometer can be considered as one order of magnitude higher than that of an X-band spectrometer; at 300 GHz the factor is about 30, if no broadening of the absorption lines is induced at higher frequencies. For the same reasons, HFESR leads to enhanced spectral resolution for powder patterns, originating from orientation distribution. For instance, this is the case of a sample containing only the radical TEMPO in a non-oriented form (powder or frozen solution, Figure 2*Right*). The  $g_e$  principal values as well as the hyperfine interaction associated with the  $z$ -axis ( $A_{zz}$ ) are in HFESR clearly observed. The spectrum of the same sample at X-band (9.5 GHz) frequency collapses in a single line signal with hyperfine structure. To obtain the  $g$ -anisotropy or to associate the field independent hyperfine interaction to the  $z$ -axis is much more complicated. Beside the increased resolution the HFESR allows access to paramagnetic species which possess large Zero Field Splittings (ZFSs) as it is in case of Single Molecule Magnets (Chapter 4). SMMs are difficult to study without HFESR. Furthermore, HFESR also provides higher sensitivity thanks to enhanced Boltzmann factor.

### 2.3 ESR SPECTROMETER

EPR spectroscopy has been the object of many technical changes and improvements within the last decades as was already mentioned. The improvements went hand in hand with developments in different fields of physics, e.g. physics of semiconductors (detectors and sources of MWs), physics of superconducting materials (magnets), astronomy (QO propagation) etc. Thanks to these developments, ESR spectrometers could move to higher frequencies and pulsed operation could also be implemented. The development of high frequency and HFESR spectrometers allowed resolving many phenomena difficult or even impossible to observe before. Especially, it allowed determining small  $g$  differences and accessing integer spin systems with large ZFSs (which were called "ESR silent" before). In this section, a general overview of the HFESR spectrometer operating in continuous wave (CW), pulsed mode or in frequency domain will be given.

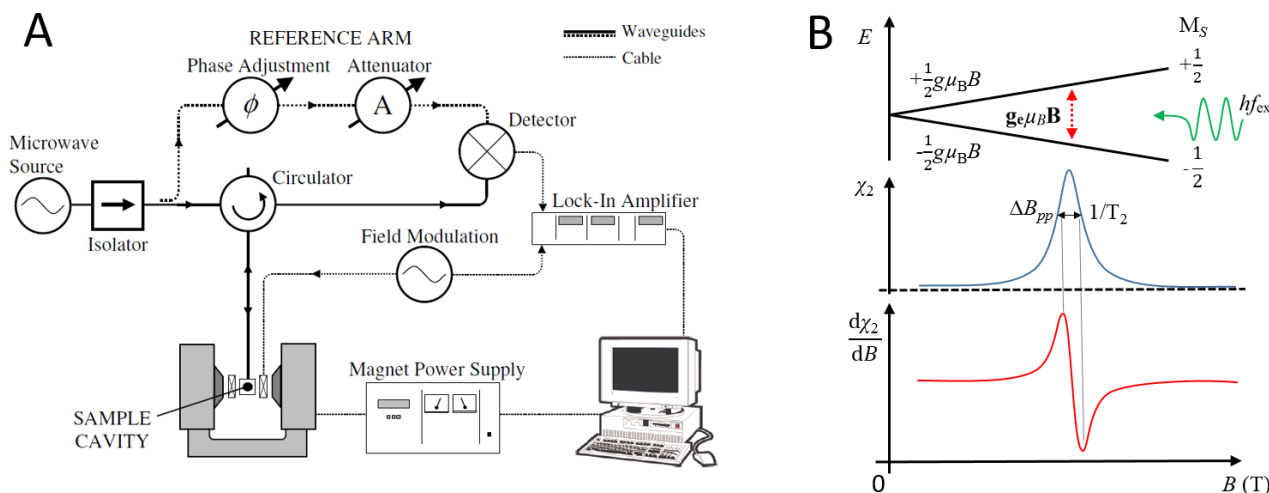


**Figure 3.** A) Schema of typical cw-ESR spectrometer operating in homodyne configuration with all its components indicated in the figure. B) An illustration of ESR experiment.

### 2.3.1 Cw- ESR

With respect to NMR, the ESR spectrometers operated in cw mode are still dominant in ESR community. This is due to that cw-ESR is simple and offer very valuable contain of information especially when is performed at several frequencies - multi frequency ESR (Figure 2Right).

The cw-ESR spectrometer (Figure 3A) is composed of a stable MW source (typically Klystrons, Traveling Wave Tubes, Gunn diodes, High Frequency Amplifiers, IMPATT diodes etc.).<sup>36</sup> The MW is then directed from the source either by rectangular waveguides up to W-band frequency or through QO in HFESR spectrometers. MW goes through an isolator which protects the source from unwanted backward reflected MW. MW is directed to a sample, which is located in a MW resonator to enhance weak  $B_1$  field on the sample, which is either single mode resonator at low frequencies or typically Fabry-Pérot resonator at high frequencies. The resonator is located in the center of magnetic field which is slowly changing and the ESR spectrum is recorded as a function of it at constant irradiation frequency (field domain). The magnetic field is either generated by resistive magnets (up to 3 T) or by superconducting coils. On top of the main magnetic field  $B$ , a small modulation magnetic field is added oscillating at frequencies of several kHz in order to increase sensitivity by phase sensitive detection. At magnetic resonance, MW is absorbed (changed) and it is backward reflected towards a circulator which directs the ESR signal into a detector (mixer, zero biased detector, bolometer etc.). The signal is decoded at modulation frequency and the resulting ESR spectrum is then derivative of an absorption spectrum (Figure 3B).

### 2.3.2 Frequency Domain Magnetic Resonance

ESR has traditionally been performed at a fixed MW frequency (GHz range), while sweeping the external field (field domain). This was done for reasons of limited sweepability of MW sources used. In addition, working at a fixed frequency allows using a cavity or other type of resonator to enhance the sensitivity of the inherently insensitive ESR technique. In the 1960 and 70s, a number of Frequency Domain Magnetic Resoance (FDMR) studies had appeared mainly by Sievers and Richards.<sup>37, 38</sup> This work was essentially discontinued after 1980. From the late 1990s, the technique was revived by Mukhin, Dressel and Van Slageren,<sup>39-42</sup> and later also by Schnegg.<sup>43</sup> Only limited studies could be conducted due to available broadband sources. Nowadays, especially in the terahertz range, broadband sources are available. Working instead at fixed magnetic field and sweeping MW frequency (frequency domain) has distinct advantages. First of all, for many samples the energy splittings of interest are caused by field independent interactions, such as zero-

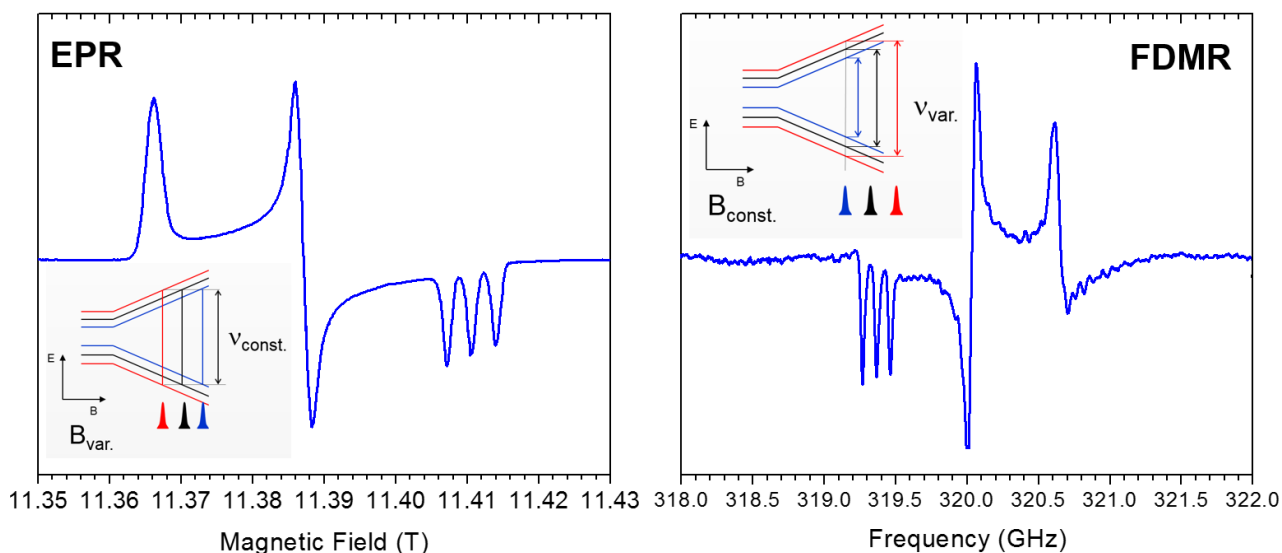


**Figure 4.:** Schematic explanation of ESR (EPR) and FDMR spectra. While in EPR, the MW frequency is kept constant and the spectrum is recorded as a function of magnetic field, in FDMR it is the opposite. This results in an “inverted” spectrum. In EPR, the first observed transition is that which corresponds to the highest  $g$ -value whereas in FDMR it is the last, as shown in the bottom part of the figure.

field splitting or crystal field splitting (single molecule magnets). In a FDMR spectrum recorded even at zero field, the energy spectrum of the material under study is then directly read off. In contrast, in the field domain, the HFESR spectrum must be recorded at many different frequencies, where subsequent extrapolation to zero field gives the energy spectrum. Thus, FDMR is inherently faster than HFESR. Secondly, if the energy spectrum spans a very broad energy range up to several THz, the magnetic fields required for HFESR cannot be achieved with dc magnets any longer. Thirdly, FDMR spectra can be recorded while the superconducting magnet is in persistent mode, thus saving on the nonrenewable resource of liquid helium. Finally, applying a sizable magnetic field can change the properties of the sample itself, and can also lead to higher-order field dependent interactions becoming non-negligible. All these reasons favor performing experiments in the frequency domain.

The appearance of ESR and FDMR spectra can be seen on Figure 5., where ESR and FDMR spectrum of  $^{14}\text{N}$ -TEMPOL is shown. While in ESR, the MW frequency is kept constant and the spectrum is recorded as a function of magnetic field, in FDMR it is the opposite. This results in an “inverted” spectrum. In ESR, the first observed transition is that which corresponds to the highest  $g$ -value whereas in FDMR it is the last, as shown in the insets of the figure. The drawback of the FDMR method is that it is very sensitive to any standing waves in the system, which can be seen in the FDMR spectrum.

### 2.3.3 Pulsed ESR

Since 1950, when first coherent pulsed manipulation of spins was observed by E. L. Hahn many scientists dreamt about their own pulsed ESR spectrometer. Pulsed ESR experiments<sup>44</sup> were primarily used to determine spin relaxation times,  $T_1$  – spin-lattice and  $T_2$  – spin-spin relaxation (Figure 5.). Nowadays, since discovery of site-directed spin labeling<sup>45, 46</sup> by W. L. Hubble in 1989 at University of California one of the key application of pulsed ESR spectrometers is Pulsed Electron-Electron Double Resonance<sup>19</sup> (PELDOR or DEER<sup>20</sup>) spectroscopy, a method used to measure distance between typically two individual spins.<sup>32, 47</sup>

In the basic experiments shown on Figure 5. are used two pulses:  $\pi/2$  ( $90^\circ$ ) and  $\pi$  ( $180^\circ$ ). The nomenclature comes from the angular change of the direction of magnetization  $\mathbf{M}$  (ensemble of spins) which is manipulated during the experiment on a Bloch sphere and the time dependence of

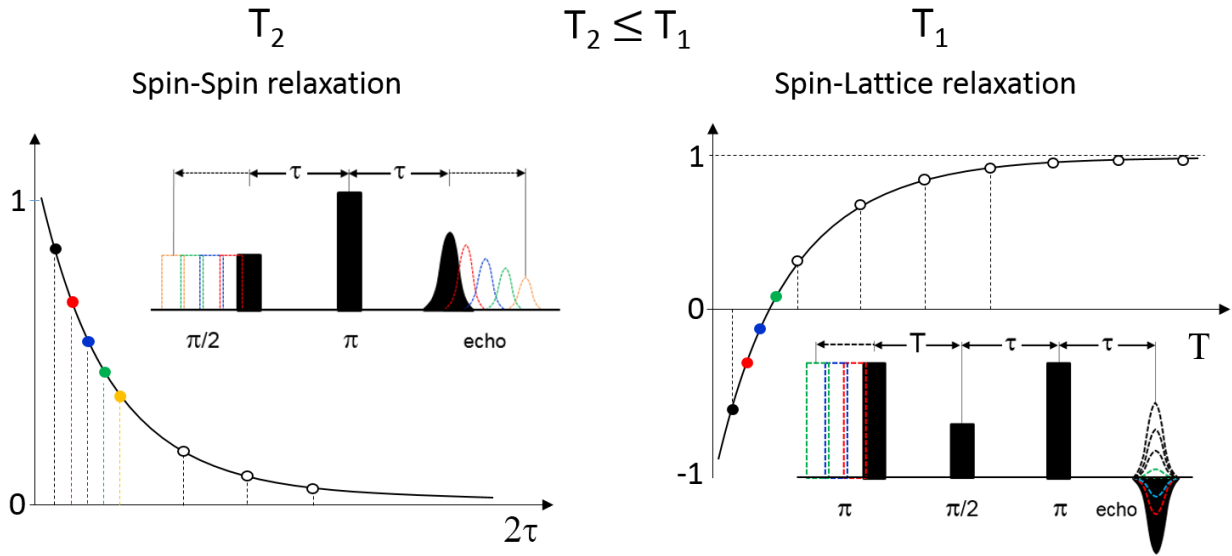


**Figure 5.** Two types of pulse experiments (sequences) used to determine  $T_1$  (spin-lattice) and  $T_2$  (spin-spin) relaxation times by pulsed ESR.

the magnetization is described by Bloch equations.<sup>44</sup> In the first experiment on Figure 5. is the  $T_2$ -time determined by the *Hahn sequence* ( $\pi/2 - \tau - \pi - \tau - \text{echo}$ ). The spacing  $\tau$  between the pulses is changing and the echo intensity  $I$  (proportional to  $M$ ) is monitored. As the  $\tau$  is rising the echo intensity decrease:

$$M(2\tau) = M(0) \cdot \exp(-2\tau/T_2)$$

The second type of experiment on the Figure 5. is called *inversion recovery* and it is used to determine spin-lattice relaxation time –  $T_1$ . In this experiment in front of the Hahn echo sequence is placed additional  $\pi$  pulse ( $\pi - T - \pi/2 - \tau - \pi - \tau - \text{echo}$ ) separated by time  $T$ . During the experiment the Hahn echo sequence remain constant and the spacing  $T$  of the first pulse ( $\pi$ ) is changing. The exponential curve is then recorded as a function of spacing  $T$  with respect to intensity of echo.

$$M_z(T) = M_z(0) \cdot (1 - \exp(-T/T_1))$$

The inversion recovery experiment can be understood as  $180^\circ$  rotation of a magnetized sample in the applied magnetic field and observing how the magnetization tends to align with magnetic field. The equilibrium magnetization  $M_z(0)$  is inverted opposite to the magnetic field by  $\pi$  pulse and its recovery is monitored by the Hahn echo sequence.

Pulsed ESR instruments with respect to cw-ESR experiment are demanding on a MW source. In order to access fast relaxation times the pulses should be short, meaning that has to provide very high  $B_1$ -field on the sample. Typically  $\pi/2$  pulses of length of few nanoseconds and MW sources of several hundreds of Watts are used.

### 3 SOLID STATE MATERIALS – GRAPHENE

Graphene is a relatively young material, observed for the first time in 2004 by K. S. Novoselov and A. K. Geim.<sup>48</sup> Since its discovery, graphene has fascinated thousands of scientists as well as engineers around the world. Today there is more than 120 000 publications dealing with graphene according to web of science. Graphene, which is the basic unit for the construction of bulk

graphite,<sup>49</sup> consists of a one-atom thick two-dimensional (2D) lattice of carbon atoms with a honeycomb structure and has extraordinary electronic properties. The electronic properties are the consequence of its linear band structure (dispersion) in the vicinity of the K and K' points, often called Dirac points (Figure 6). At the Dirac points, the conduction and valence bands are touching each other, which makes graphene a zero gap semiconductor (or a zero-overlap semimetal). The linearity of the dispersion makes graphene unique with respect to conventional materials with a classical parabolic dispersion, leading to charge carriers (electrons and holes) acting as massless particles, Dirac fermions, with a Fermi velocity  $v_F$  of about  $10^6 \text{ m}\cdot\text{s}^{-1}$  which approaches the speed of light. These unique properties of graphene do not only exist at very low temperatures and extreme conditions, as might be expected, but they are preserved up to room temperature, as we and others have shown.<sup>50</sup> Combined, this makes graphene an excellent playground for probing quantum electrodynamic properties like the Klein paradox and Zitterbewegung and makes graphene a promising material for future applications.<sup>51-55</sup>

Recently, there has been a great deal of progress in preparation of manmade graphene by methods including chemical vapor deposition and epitaxial growth. However, the quality (in terms of electron mobilities) of these manmade graphene samples does not yet reach those of graphene decoupled from bulk graphite, evidenced by our observation of mobilities of  $10^7 \text{ cm}^2/(\text{V}\cdot\text{s})$  in graphene on graphite.<sup>27, 56, 57</sup> This extremely high mobility enables the Landau level quantization to appear at magnetic fields as low as 1 mT (see attached papers).<sup>56</sup> The ability to produce graphene of exceedingly high quality on a large scale is an essential prerequisite for the development of graphene-based devices. High-quality graphene displays ballistic electron transport at large distances which, if this material is successfully incorporated into devices, will lead to a breakthrough in electronics. It can be foreseen that in near future, graphene's superior material characteristics, ranging from its crystal structure over mechanical strength to the electronic properties will be elaborated in novel devices which are nowadays impossible due to limited quality of used current materials.

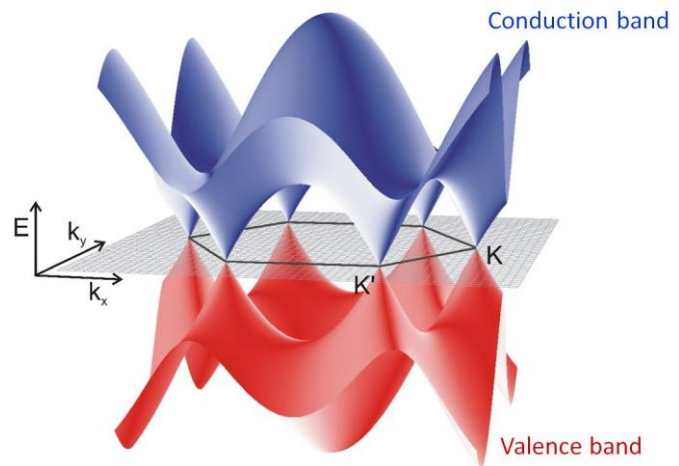


**Figure 6.:** Band structure (Brillouin zone) of graphene. The conduction (blue) and valence (red) bands touch at K and K' (Dirac) points in momentum space, around which the dispersion is linear, creating so-called Dirac cones.

### 3.1 CYCLOTRON RESONANCE

The electronic properties of graphene samples are typically investigated by transport measurements. However, these measurements only probe the Fermi level. Furthermore the transport measurement itself may cause defect formation in graphene, obscuring the properties intrinsic to the sample.<sup>57</sup> Spectroscopic measurements, on the other hand, allow noninvasive measurement of the electronic structure, not only in the vicinity of the Fermi level, but throughout the entire band structure. For the investigation of low-energy excitations, magneto-optical methods such as HFESR and far infrared (FIR) magneto-spectroscopy are relevant in particular, benefiting from their high sensitivities, as shown by a number of previous studies, including our own

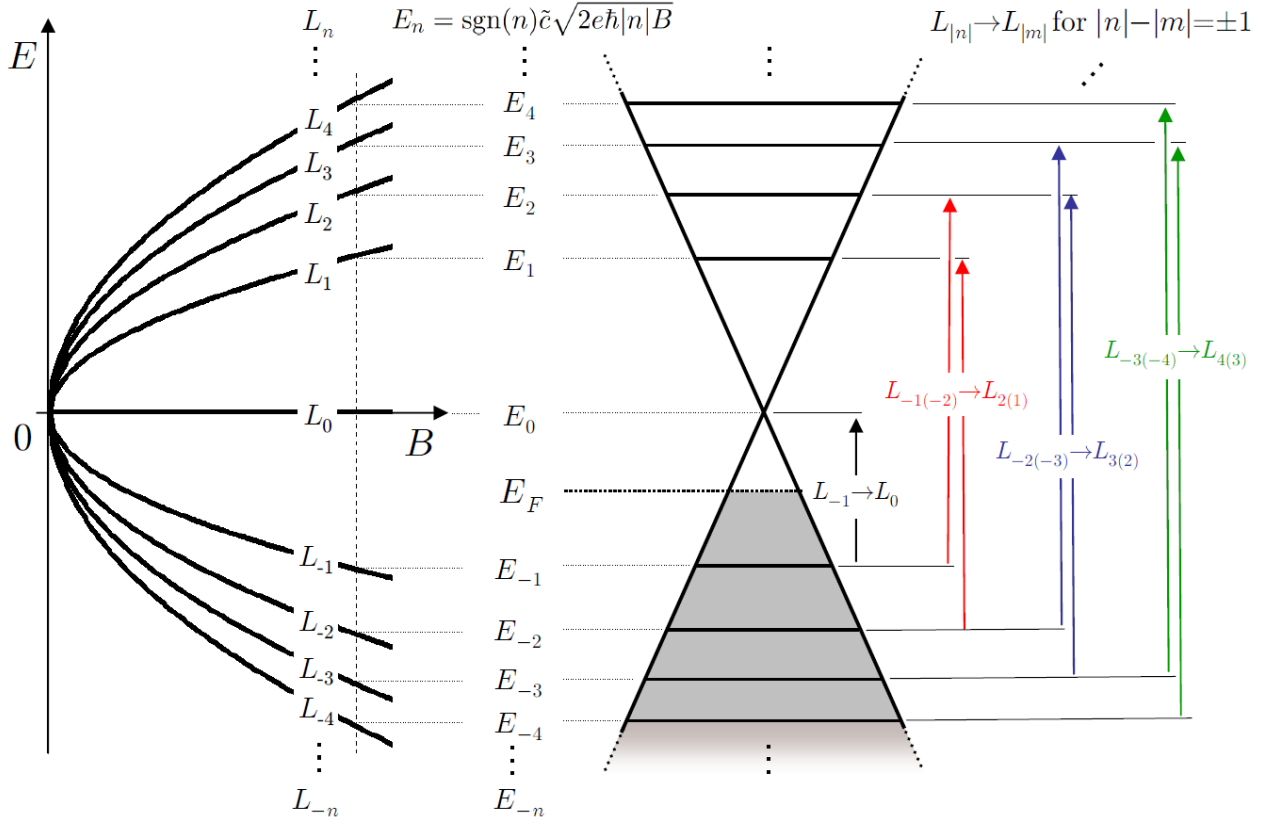


**Figure 7.:** Left: Schematic evolution of LLs  $L_n$  in graphene with applied magnetic field  $\mathbf{B}$ . Right: Optically allowed transitions in  $p$ -doped graphene for a given magnetic field  $\mathbf{B}$ .  $n$  and  $m$  denote indexes of LLs.

works.<sup>50, 56, 58</sup> Of these methods, HFEPFR probes the lowest energy range between 100-1000 GHz (0.4-4 meV), while FIR typically probes the energy range from 1 to 10 THz (4-40 meV). In magnetic field, the electronic states in graphene become quantized into Landau levels (LLs)  $E_n$ :

$$E_n = \pm v_F \sqrt{2e\hbar B |n|}, \quad n = \dots, -2, -1, 0, 1, 2, \dots$$

where  $n$  is the LL index,  $\pm$  refers to electrons (+) and holes (-) states and  $e$  is the electron charge. Due to graphene's unique linear band structure, the LLs are not equally spaced and evolve with  $\sqrt{B}$  (Figure 7). This implies rather high sensitivity of electronic states (LLs) in graphene to the applied magnetic field. Conversely, the investigation of the LLs in a magnetic field allows detailed understanding of the low-energy electronic structure of graphene.

On Figure 8, one can see how powerful HFESR is today with respect to previously used instruments. The Figure 8.A show experiments performed on single flakes of natural graphite of size 1 mm x 0.5 mm and thickness 25  $\mu\text{m}$  recorded by the author in Stuttgart at 370 GHz and 5 K, unpublished. The spectrum is very rich. In the low field region signal originating from graphene is visible.<sup>56</sup> At fields of 0.05 – 0.80 T, about 20 cyclotron resonance harmonics are observed originating from conduction electrons in bulk graphite, where the fundamental cyclotron resonance can be observed at about 0.8 T. Signals at fields above 0.8 T are not fully understood spectral features and are currently under investigation. To compare the superior quality expressed by many spectral features of the present HFESR data, on a Figure 8.B is an averaged magneto-absorption spectrum of high quality graphite of diameter 1 cm and thickness 25  $\mu\text{m}$  recorded by Galt *et al.* at 24 GHz and 1.1 K.<sup>55</sup> On Figure 8C, an averaged magneto-absorption spectrum of pyrolytic graphite of size 1 cm x 0.7 cm and thickness about 1 mm recorded by Doezema *et al.* at 890 GHz and 4.2 K.<sup>59</sup> Furthermore, the HFESR is very sensitive to impurities of investigated samples. This

is very valuable information to the industry dealing with the large scale production of graphene for future applications.

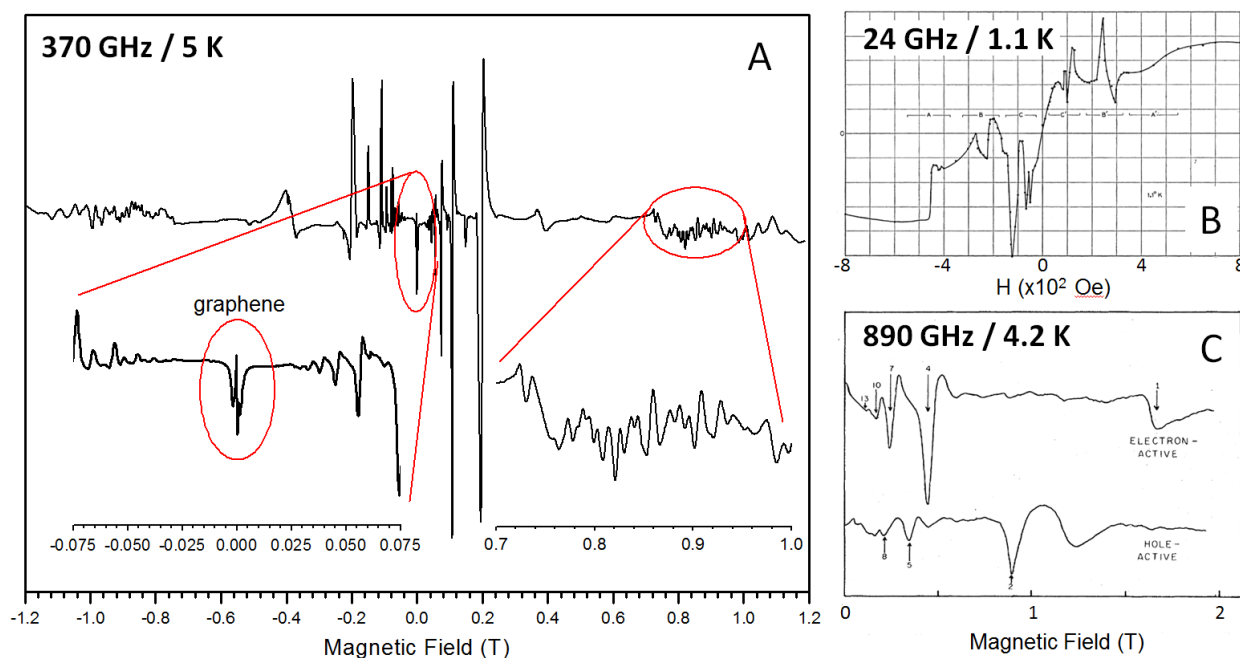


**Figure 8.:** A) A single shot magneto-absorption (HFESR) spectrum of natural graphite of size 1 mm x 0.5 mm and thickness 25  $\mu\text{m}$  recorded by the author in Stuttgart at 370 GHz and 5 K, unpublished. The spectrum is very rich, where in the low field region signal originating from graphene (see attached papers) is visible, at fields above 0.8 T not fully understood spectral features are observed. For data quality comparison: B) An averaged magneto-absorption spectrum of high quality graphite of diameter 1 cm and thickness 25  $\mu\text{m}$  recorded by Galt *et al.* at 24 GHz and 1.1 K, Ref. [54]. C) An averaged magneto-absorption spectrum of pyrolytic graphite of size 1 cm x 0.7 cm and thickness about 1 mm recorded by Doezema *et al.* at 890 GHz and 4.2 K, Ref. [58].

## 4 SINGLE MOLECULE MAGNETS

By the end of the 1980s, molecular magnetism had seen the emergence of a new research area: the study of high nuclearity spin clusters, which are complex molecules containing a large number of spins most often carried by transition metal ions.<sup>60</sup> Among these molecules, the ones possessing a large spin ground state associated with an Ising type anisotropy (Figure 9.A) have been under particular focus.<sup>61</sup> The macroscopic large spin of these molecular systems (Figure 9.B) together with a negative Zero-Field Splitting (ZFS) results in the presence of a barrier for the reversal of their magnetization at low temperatures. The main consequence is a slow relaxation which, below a blocking temperature, leads to a behaviour quite similar to the one of superparamagnets.<sup>62</sup> Due to these properties, they have been named Single Molecule Magnets (SMMs). At the low temperatures, they exhibit a hysteresis in their magnetization curve with a step-like shape (Figure 9.C), a signature of the presence of Quantum Tunneling of the Magnetisation (QTM).<sup>63, 64</sup>

HFESR proved to be one of the most powerful methods to precisely determine the magnetic anisotropy of SMMs. This chapter will introduce the power of HFESR spectroscopy in molecular magnetism on an example of a  $\text{Fe}_4$ -complex.<sup>65</sup>

## 4.1 INTRODUCTION TO SINGLE MOLECULE MAGNETS

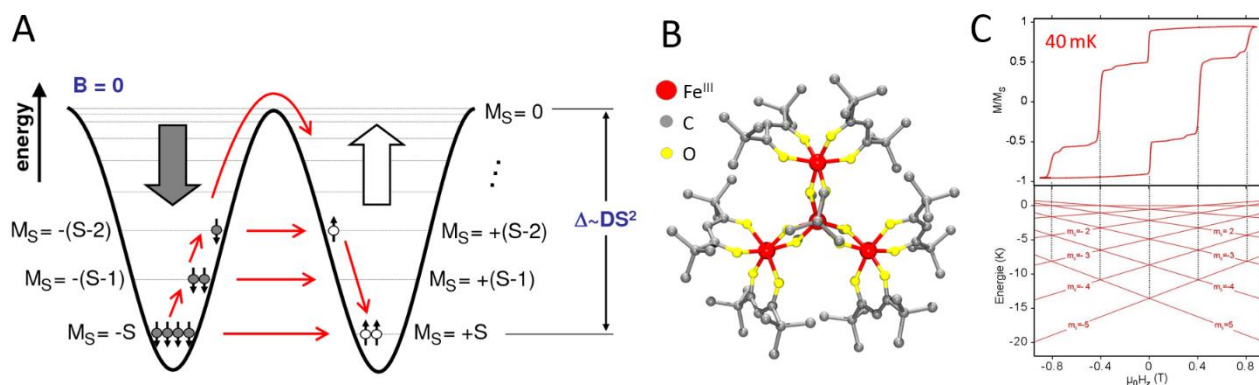


**Figure 9.:** A) Schematic description of energy levels in SMMs using double well potential (Ising type anisotropy) at zero magnetic field. The high of the barrier  $\Delta$  between the two ground  $M_S$  states is proportional to the size of  $D$  (axial ZFS parameter) and  $S^2$ . Thanks to the energy barrier  $\Delta$  the system can be blocked in one of the  $M_S$  state. The system relax into equilibrium either overcoming the energy barrier or via Quantum Tunneling of Magnetization (QTM). B)  $\text{Fe}_4$  complex is an example of SMM which is composed by four antiferromagnetically coupled  $\text{Fe}^{\text{III}}$  ions with spin of  $5/2$  leading to a total giant spin of molecule 5. C) A hysteresis loop recorded for the  $\text{Fe}_4$  complex at 40 mK. Typical steps in magnetization are observed due to QTM presented in SMMs between the opposite  $M_S$  states on the other side of an energy barrier.

SMMs possess a large spin ground state  $S$ , resulting in exchange interactions between their magnetic centers. Often, it is possible to stabilize a large spin ground state even when only antiferromagnetic interactions are present, due to the competition between all the interaction pathways resulting from the structure of the molecule. As SMMs have an easy-axis magnetisation, their spin ground state  $S$  is split by a negative axial ZFS term,  $D$ . Thus, inside the ground multiplet, the levels  $M_S = \pm S$  are the lowest in energy and the level  $M_S = 0$  is the highest, the energy difference being  $\Delta \approx DS^2$ , where  $\Delta$  is an energy barrier for the reversal of the magnetization (Figure 9A). At low temperature, when only the ground spin state is thermally populated, the relaxation time of the magnetisation increases when the temperature decreases due to the presence of the barrier. In a first temperature regime, this relaxation will involve phonons (multiple Orbach process), whereas at the lowest temperatures relaxation will take place through quantum tunnelling of the lowest  $M_S$  states and will be temperature independent. The step-like shape of the magnetic hysteresis curve is the signature of a relaxation involving QTM. The steps in the magnetisation curve (Figure 9C) appear when tunnelling is made possible by energy levels degeneracy. If  $\Delta$  is sufficiently high the magnetisation can be preserved for a long time. Therefore, it is in principle possible to store information in such a molecule. The first complex identified to behave as a SMM was the  $\text{Mn}_{12}\text{Ac}$  complex.<sup>61, 66</sup> Despite being the first SMM discovered, it took two decades until it lost the record of the highest temperature for which magnetic hysteresis was observed. Despite the enormous synthetic effort made during twenty years to increase the magnetic energy barrier  $\Delta$ , it has only been possible to do it for a unique complex  $\text{Mn}_6$ .<sup>67, 68</sup> Today, due to difficulties of obtaining large energy barrier using transition metal complexes the interest moved to Single Ion Magnets based on rare earth ions, lanthanides and actinides. The great interest is due to their large angular momenta and their huge anisotropies.<sup>69</sup> The origin of the huge magnetic anisotropy is a consequence of the crystal field (CF) splitting of the ground multiplet of the lanthanide ion.<sup>70</sup> These properties engender slow relaxation of the magnetic moment to give single molecule magnet (SMM) behavior, making them potentially suitable for use in novel ultrahigh-density magnetic data storage devices in future.

Besides the interest in increase of the magnetic anisotropy barrier  $\Delta$ , another important trend in SMM research nowadays is dealing with examining SMM behavior when the complexes are organized on solid surfaces or anchored to them.<sup>71-73</sup> For applications such as information storage, quantum computing<sup>74-76</sup> or molecular spintronics<sup>77, 78</sup> it is necessary to find a way how to deposit molecules on suitable substrates and maintaining their properties when deposited on the surface. In the following text, we describe the power of HFESR on one of Fe<sub>4</sub> derivatives (Figure 9.B) on which have been shown maintaining its SMM properties upon grafting on a surface.<sup>72</sup>

## 4.2 HFESR AND SMMS

HFESR proved to be one of the most powerful methods to precisely determine the magnetic anisotropy of SMMs.<sup>65, 79-101</sup> In this section, we highlight some of the most important features of HFESR for the study of SMMs on a particular case of tetrairon(III) molecule. Due to the large anisotropy of SMMs, these complexes are inaccessible to classical ESR spectrometers operating at low frequencies (X-band, 0.3 cm<sup>-1</sup>), either being ESR silent or giving rise to very incomplete spectra. Going to higher frequencies to overcome the energy gaps of the ground spin multiplet is necessary, also because SMMs have integer spin values. To give an (extreme) example, the splitting between the lowest occupied states  $M_S = \pm 10$  and  $M_S = \pm 9$  in the Mn<sub>12</sub>Ac is about 10 cm<sup>-1</sup> (300 GHz); hence ESR spectrometers operating at low frequencies cannot probe this transition.

### 4.2.1 Spin Hamiltonian

To interpret the ESR spectra of SMMs the Giant Spin Hamiltonian formalism is used:

$$H = H_Z + H_{CF} = \mu_B \mathbf{S} \cdot \mathbf{g}_e \cdot \mathbf{B} + D[\mathbf{S}_z^2 - \frac{1}{3}S(S+1)] + E(\mathbf{S}_x^2 - \mathbf{S}_y^2) + \sum_{k,q} B_k^q O_k^q$$

where  $\mu_B \mathbf{S} \cdot \mathbf{g}_e \cdot \mathbf{B}$  is the Zeeman Hamiltonian  $H_Z$  associated with the external magnetic field  $\mathbf{B}$ , and  $D[\mathbf{S}_z^2 - \frac{1}{3}S(S+1)] + E(\mathbf{S}_x^2 - \mathbf{S}_y^2)$  is the crystal (ligand) field Hamiltonian which describes the magnetic anisotropy (ZFS) of the system at second order.  $S_x$ ,  $S_y$ ,  $S_z$  are the three components of the

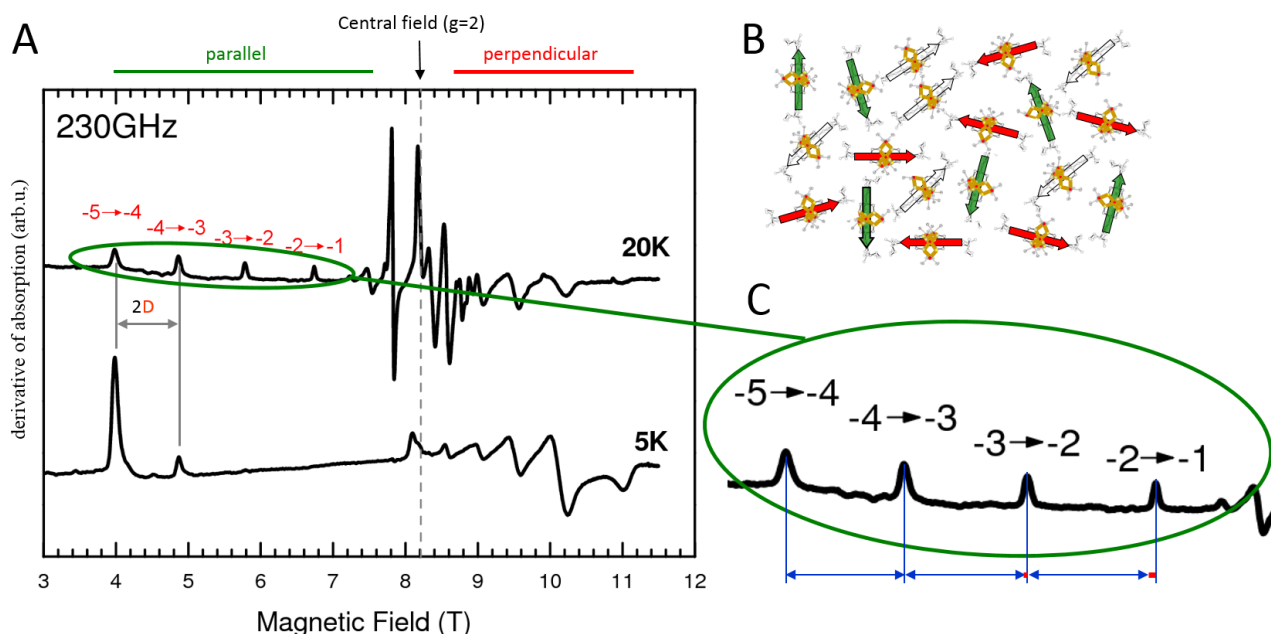


**Figure 10.:** A) HFESR spectrum of compressed powder of Fe<sub>4</sub> complex 2 from Ref. [64] recorded at 230 GHz, 5 and 20 K. B) schematic representation of a powdered sample with highlighted magnetic orientation of the molecules with respect to external magnetic field. C) Detailed view on  $M_S \pm M_{S\pm 1}$  transitions in parallel region indicating presence of higher order terms by increasing spacing between the consecutive transitions.

spin operator  $\mathbf{S}$ . The  $D$  and  $E$  terms are the axial and rhombic anisotropy parameters of the system. They are related by  $-1/3 \leq E/D \leq +1/3$ . When the ratio  $E/D = 1/3$  the system is totally rhombic, whereas in the case of  $E = 0$  the system is axially symmetric.  $D$  can be either negative or positive, corresponding to an easy-axis or an easy-plane anisotropy respectively. The last term in the spin Hamiltonian  $\sum_{k,q} B_k^q O_k^q$  describes higher order terms associated with a large spin values  $S$ , where  $O_k^q$  are Stevens operators and the  $B_k^q$  are the corresponding parameters, which are defined by the symmetry of the complex.<sup>102</sup>

#### 4.2.2 Powdered Samples

HFESR spectra of SMMs are usually easy to analyze. The ZFS parameters can be obtained from HFESR either on polycrystalline (powdered) or single crystal samples. The powdered samples are pressed into pellets (in our case typically 20-30 mg of a sample is used for 5 mm pellet) in order to avoid orientation effects caused by strong magnetic field. Very often powder spectrum is only recorded as a large amount of information can be extracted from it.

On the Figure 10, experimental powder spectra obtained for a  $\text{Fe}_4$  sample (complex 2 in Ref.<sup>65</sup>) at 230 GHz, 5 K and 20 K are shown. Powder spectrum contain information about all possible orientations of the investigated sample. When we look on the HFESR spectrum, we can divide the spectrum into two parts, perpendicular and parallel around the central  $g$ -value (8.2 T). From the size of these two regions, we can distinguish the sign of  $D$  parameter of ZFS. In this particular case the sign is negative. The parallel region corresponds to signal coming from molecules with easy-axis aligned with the applied field. Conversely, the signal in the high field part of the spectrum corresponds to the magnetic field in the hard-plane. The negative sign of the  $D$ -parameter is further confirmed by the measurements at elevated temperature, where we see rise and decrease of the peak amplitudes in the parallel region, note the peak at 4 T. Furthermore, the  $M_S \pm M_{S \pm 1}$  transitions can be easily assigned and the spacing between the consecutive peaks is proportional to  $2D$ ,  $D = -0.449 \text{ cm}^{-1}$ . The careful inspection of the spacing of the parallel transitions (Figure 10C) reveals that the line-to-line separation slightly increases when moving to high magnetic field, thus pointing to presence of higher order terms of Giant Spin Hamiltonian, which are better distinguished from a single crystal measurements.

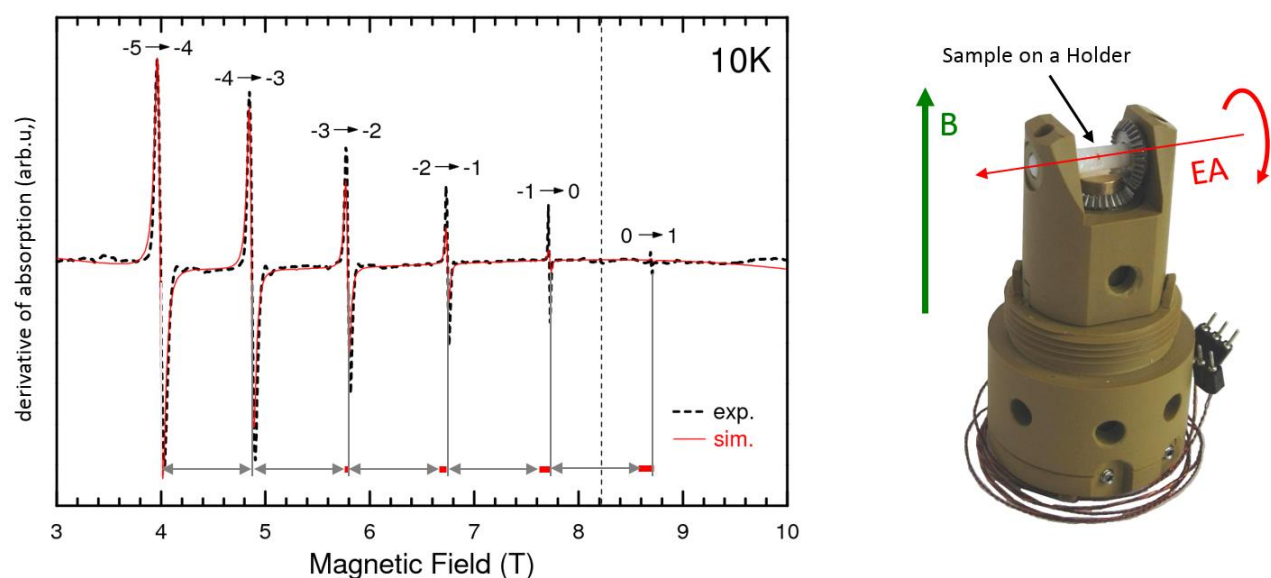


**Figure 11.:** Single crystal HFESR spectrum of the same  $\text{Fe}_4$  complex as in Figure 10 recorded at 230 GHz and 10 K in orientation of magnetic field applied along easy axis of the  $\text{Fe}_4$  complex. Right: Photograph of developed a single crystal rotator used in our single crystal studies with the rotation around easy-axis (EA) perpendicular to applied magnetic field, rotation in hard plane, see Ref. [81].



polarization is enhanced by transferring the relatively larger electron polarization either from native paramagnetic center or by adding polarizing agents<sup>103, 104</sup> to NMR active nuclei by microwave irradiation of ESR transitions.<sup>17, 18, 105-107</sup>

A. W. Overhauser proposed the idea to polarize nuclei in metals by applying MW excitation to the electron resonance transition already in 1953 at University of Illinois.<sup>108</sup> The experimental proof of this concept was shown by T.R. Carver, C.P. Slichter (from the same institute as A. W. Overhauser) on Li metal at low magnetic fields even before the theoretical paper was published.<sup>109</sup> The DNP work was mainly concentrated on a work at low frequencies and fields. The DNP renaissance started with the work mainly associated with Griffin group at MIT in early 1990, performing experiments at 5 T.<sup>17, 18</sup> The Griffin group was mainly focused on solid state DNP and have demonstrated polarization transfer mechanisms that scale more efficiently with applied field than previously expected.<sup>110</sup> DNP enhancements of  $-10$  for  $^1\text{H}$  and  $-40$  for  $^{13}\text{C}$  were observed on the solid sample using magic angle spinning (MAS) DNP on polystyrene doped by BDPA ( $\alpha$ ,  $\gamma$ -bisdiphenylene- $\beta$ -phenylallyl) radical at room temperature and were considerably larger than expected.<sup>17</sup> MAS-DNP experiments on real life samples of arginine and the protein T4 lysozyme came soon after with observed enhancement over 100.<sup>18</sup> The liquid state DNP took another decade until J. H. Ardenkjær-Larsen perform his experiment in Malmö, Sweden in 2003.<sup>111</sup> The obtained enhancement over 10 000 in  $^{13}\text{C}$  spectrum of urea (natural abundance  $^{13}\text{C}$ ) using a trityl radical and dissolution DNP triggered the rush in DNP spectroscopy. Today, MAS-DNP is routine experiment in many NMR laboratories and liquid state DNP is still undergoes certain development.<sup>112</sup>

## 5.1 LIQUID STATE DNP

Improving sensitivity is a key issue in NMR spectroscopy. Even a small signal enhancement by a factor of 2 shortens the acquisition time by a factor of 4. Now imagine, what will be possible to track in NMR experiments if the experimental times on MRI machines in hospitals will be shortened by several order of magnitude. There is strong belief that this enormous increase in sensitivity and time will be possible by implementation of liquid DNP into hospital applications. In the liquid state, the active DNP mechanism is the Overhauser effect. The theoretical description of Overhauser DNP in liquids is based on the Solomon equation<sup>113</sup> with steady state solution for Overhauser enhancement  $\varepsilon_{OE}$ :

$$\varepsilon_{OE} = \frac{\langle I_z \rangle - I_0}{I_0} = -\frac{\gamma_e}{\gamma_n} \cdot f \cdot s \cdot \xi$$

where  $\langle I_z \rangle$  is nuclear magnetization and  $I_0$  is the nuclear polarization in thermal equilibrium.  $\gamma_e$  and  $\gamma_n$  are the gyromagnetic ratios of the electron and the nucleus, respectively, *i.e.*  $\gamma_e/\gamma_n \approx -660$  for protons,<sup>114</sup>  $f=1- T_{1R}/T_{1W}$  is the leakage factor, which can be determined from the nuclear  $T_1$  in the presence ( $T_{1R}$ ) and in the absence of radicals in the solution ( $T_{1W}$ ), and reflects the influence of radicals on nuclear relaxation rate of the used solvent. The factor  $s$  denotes the saturation factor, which describes how well the electron transition is saturated by the MW irradiation. It ranges from 0 for no saturation, *i.e.* thermal population, to 1 for a fully saturated electron spin transition with equalized populations. The saturation factor  $s$  depends on:

$$s = \frac{1}{n} \frac{\gamma_s^2 B_{MW}^2 T_{1e} T_{2e}}{(1 + \gamma_s^2 B_{MW}^2 T_{1e} T_{2e})}$$

where  $n$  is number of ESR lines,  $B_{MW}$  is MW field on the sample,  $T_{1e}$  and  $T_{2e}$  are relaxation times of electron. The last parameter is called the coupling factor  $\xi$ . While the optimization of  $f$  and  $s$  is

rather a technical issue, the coupling factor  $\xi$  reflects the nature of the polarization transfer between the electron and nuclear spins and cannot be easily controlled. The coupling factor  $\xi$  describes the efficiency of the cross-relaxation processes and is given by:

$$\xi = \frac{w_2 - w_0}{w_0 + 2w_1 + w_2}$$

where  $w_2$  is double quantum relaxation rate,  $w_0$  is zero quantum relaxation rate,  $w_1$  is nuclear spin relaxation rate and  $w_2$  is double quantum relaxation rate (Figure 13). The coupling factor depends on the dynamics and the energetics of the electron–nuclear spin system. For pure dipolar coupling it is a positive quantity, which can take the maximum value of 0.5 at low magnetic field values and decreases with increasing magnetic field.

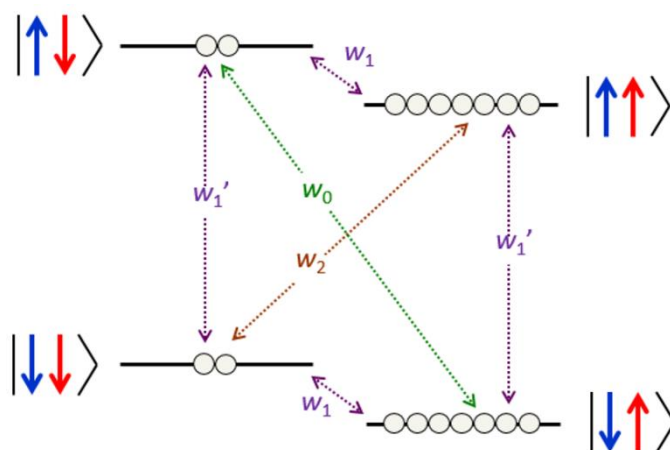


**Figure 13.:** Energy level diagram for an electron spin  $S = 1/2$  (in blue) coupled to a nuclear spin  $I = 1/2$  (in red).  $w_1$ : nuclear spin relaxation rate,  $w_1'$ : electron spin relaxation rate,  $w_2$ : double quantum relaxation rate,  $w_0$ : zero quantum relaxation rate.

### 5.1.1 Experimental Techniques and Challenges

There are three types of approaches how to perform liquid state DNP spectroscopy at high magnetic fields. First is the original dissolution DNP, where sample is polarized at cryogenic temperature (below 5 K) and then hot liquid is injected in order to quickly warm up the sample.<sup>111, 115</sup> Second one is a shuttle-DNP, where the electron spins are excited at low magnetic fields and low frequencies, afterwards the sample or even the whole probe is shuttled rapidly into a high magnetic field for NMR detection.<sup>116, 117</sup> The third one is in-situ DNP, where MW excitation and detection is done at the same magnetic field.<sup>105, 106, 118</sup>

From the above is clear that the liquid state DNP is technically challenging and each approach has its advantages and disadvantages. In the first two approaches complicated mechanism have to be built in order to move or to dissolve the DNP sample, on the other side large samples can be used. In the last case, the MW heating associated with high power MW irradiation has to be taken into account.

The in-situ-DNP was used by the author in investigation of DNP enhancement of water (paper 8) and organic solvents (paper 9). The schematic description of the experimental DNP double resonance cavity is shown on Figure 14.<sup>118</sup> The cavity was designed for 400 MHz  $^1\text{H}$ -NMR and 263 GHz ESR. The walls of the cavity are made out of thin copper stripe and serves as a radio frequency (RF) coil with inner diameter of 1.48 mm as well as an outer walls for a  $\text{TE}_{011}$  MW cavity. The MW cavity is tuned using plungers with silver coating at the fronts. The sample is

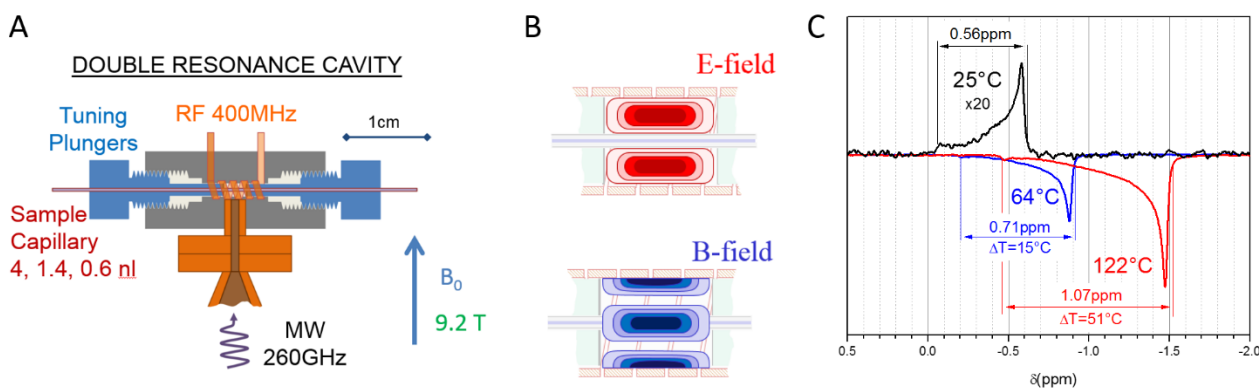


**Figure 14.:** A) Schema of a double resonance cavity for in-situ-DNP. The walls of cavity are made out of thin copper stripe and serves as a radio frequency (RF) coil as well as an outer walls for a TE<sub>011</sub> MW cavity. The sample in a small capillary with outer diameter max. 150 μm is inserted through the plungers into the cavity, with sample volumes inside the active area indicated in the figure. The MW is coupled to the cavity from the bottom via small coupling hole in the copper stripe. B) Distribution of MW electrical and magnetic field inside the TE<sub>011</sub> cavity. The sample heating is associated with the oscillating electrical field. C) <sup>1</sup>H-NMR signal obtained on water with 40 mM <sup>14</sup>N-TEMPOL radical in the double resonance cavity without applied MW (in black) and with MW (in color). Note, that the origin of the distorted <sup>1</sup>H-NMR peak is due to this particular experimental configuration. When the MW is applied the signal is inverted and the broadening of the original peak is visible, pointing out the temperature distribution over the sample.

loaded in a capillary with outer diameter of 150 μm and with the inner diameters in the range from 10 μm to 100 μm. The capillary is then inserted through the plungers into the cavity. The sample volumes inside the active area of the cavity are indicated in the Figure 14A. The MW is coupled to the cavity from the bottom via small coupling hole in the copper stripe. As already mentioned, the key problem in in-situ-DNP is associated with MW heating, which is associated with the oscillating electrical field. The distribution of MW electrical field and magnetic field inside TE<sub>011</sub> cavity is shown on Figure 14B. Even though, the electrical component of MW is well separated from the sample the MW heating can be enormous as can be seen from Figure 14C. The figure shows the <sup>1</sup>H-NMR signal obtained on water with 40 mM <sup>14</sup>N-TEMPOL radical without applied MW (in black) and with applied MW (in color). Note, the shape of the peak, which is in typical high resolution NMR about 1 Hz broad. The origin of the distorted peak is due to the fact that the tiny cylindrical sample is aligned perpendicular to applied field and the field is heavily distorted by the metallic structure of the cavity itself.<sup>119</sup> When the MW is applied the peak is inverted due to a negative enhancement. When we look closer on the broadening of the peaks one can estimate a large temperature gradients over the tiny sample. The peak temperature can even well above boiling point (MW overheating).<sup>105</sup>

Up to now, DNP spectrometers were mainly based on high power continuous MW irradiation (tens of Watts) and the research was mainly focused rather on simple molecules than large biologically relevant molecules. Today, first experiments on larger molecules are performed and pulsed MW schemes become implemented, which may reduce MW heating.<sup>120</sup> Another challenges lie in optimization of polarizing agents (radicals) for liquid DNP experiments. Furthermore, there is still lot to do on the hardware side as well as on the DNP theory, as the observed experimental enhancements are still not fully understood.

## 6 CONCLUSIONS AND OUTLOOK

In this thesis we have introduced ESR technique as a powerful method in many directions of science. We started with historical development of the method to recent days. We introduce the principles of the conventional continuous wave (cw) ESR (field domain) with respect to Frequency Domain Magnetic Resonance (FDMR). The principles of pulsed ESR where shown on

two basic experiments used to determine  $T_1$  (longitudinal, spin-lattice) and  $T_2$  (transversal, spin-spin) relaxations times. We then moved to the application of high frequency / high field ESR (HFESR) starting with applications in solid state physics, demonstrating the high sensitivity of recent instruments on graphene and graphite. Single Molecule Magnets (SMMs), where HFESR proved to be one of the most powerful methods to precisely determine the magnetic anisotropy of these systems, were introduced. The power of the technique was explained on an example of a  $\text{Fe}_4$ -complex. The last example in HFESR spectroscopy was its application in signal enhancement of NMR spectroscopy, Dynamic Nuclear Polarization (DNP). All that gave an overview of the application of HFESR up today.

However much is still unknown about spin interactions with surfaces and spin dynamics at frequencies above 95 GHz. The standard method, pulsed HFESR, is not suitable for many crucial samples. Currently, the highest frequency commercially available pulsed HFESR spectrometer operates at a frequency of 263 GHz (at a cost of >1.5 M€). The spectrometer is restricted to that particular frequency and due to the use of cavities with mm dimensions only to either powdered or liquid samples. It means that almost nothing is known about electron spin relaxation at higher frequencies, especially of thin films and bulk materials. This is particularly a problem in quantum computation at THz frequencies and the rapidly growing hyperpolarization methods in Nuclear Magnetic Resonance, where in both cases optimization of the spin relaxation of the system is essential. The pulsed 263 GHz ESR spectrometer uses very tiny single mode cavity of size 0.5 mm ( $\lambda/2$ ) and the sample is placed into 100  $\mu\text{m}$  capillary which limits all studies. Furthermore, the combination of high MW power and the single mode cavity requires a delay (deadtime) between the end of the last excitation MW pulse and the start of data acquisition to allow the cavity response to ring down and to protect sensitive detectors from burn out. This means that pulsed ESR spectroscopy concept is inherently limited to relaxation times longer than several hundreds of

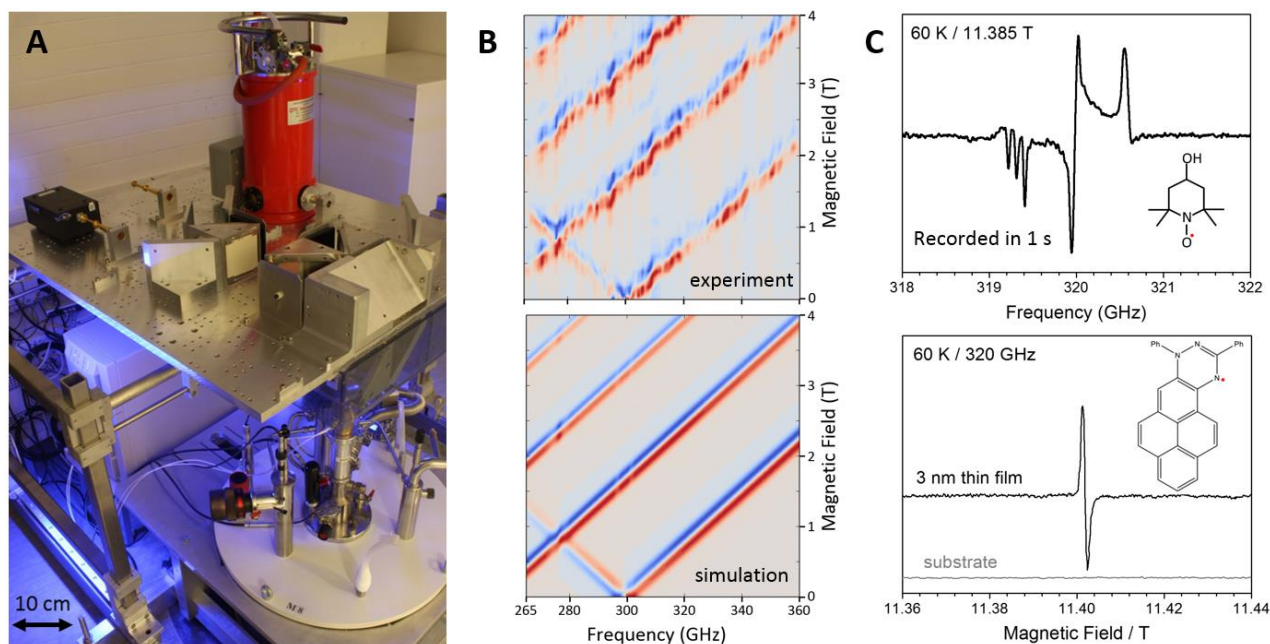


**Figure 15.:** A: The combined HFESR/FDMR spectrometer recently developed by me at the University of Stuttgart. B: First full field-frequency diagram of an oriented tiny crystal (0.1 mg) of the Mn12Ac single molecule magnet recorded only in 30 minutes with corresponding simulation below. C: Top: Single scan FDMR spectrum recorded in the non-resonant cavity in only 1 s for 1 mg of 100  $\mu\text{M}$  of the  $^{14}\text{N}$ -TEMPOL radical (inset) at 60 K and magnetic field of 11.385 T. Bottom: Single scan HFESR of a thin layer (3 nm) of a Pyren-Blatter radical recorded at 60 K and at 320 GHz in the non-resonant cavity. The sample (inset) was prepared by Prof. Rajca, University of Nebraska–Lincoln, and the evaporation was carried out by PD Dr. Casu at the University of Tübingen. Note: All figures are unpublished results.

nanoseconds. I recently set up the first broadband CW High-Frequency ESR/Frequency Domain Magnetic Resonance (HFESR/FDMR) spectrometer at the University of Stuttgart (Figure 15A), which operates seamlessly in a very broad frequency range from 85 GHz to 1100 GHz, and sets the current worldwide state of the art for broadband ESR spectrometers. It can be tuned to any frequency in the given range, for example to frequency specific to molecular motions. It is the first spectrometer which can operate either in the field domain (HFESR) by sweeping the magnetic field at fixed irradiation frequency, or in the frequency domain (FDMR), by sweeping the frequency at fixed magnetic field. The sample can be placed in a non-resonant cavity (5 mm in diameter), on a rotating sample holder (Figure 11*Right*) or in a tunable Fabry-Pérot resonator ( $Q = 1200$  at 330 GHz). In FDMR, the spectrometer possesses a very high sensitivity, which led to the first FDMR measurement of a tiny single crystal of a SMM of mass only 0.1 mg (Figure 15B) as well as of a thin film with 100  $\mu\text{m}$   $^{14}\text{N}$ -TEMPOL radical embedded in 1 mg of polystyrene (Figure 15C Top). It is also possible to record spectra of only a 3 nm thin film of an organic radical (Figure 15C Bottom). This makes the HFESR/FDMR spectrometer an outstandingly powerful tool. However, the presented HFESR/FDMR spectrometer is approaching its technical limits and it was not primarily built for measurements of relaxation times. Furthermore, the spin coherence time can be extracted from ESR, if the magnetic field sweep rate is fast compared to the relaxation times.<sup>121</sup> For sweep rates faster than the coherence time, the directly detected spectrum will show oscillations in the signal response (transient effects, wiggles) (Figure 16), which allow the determination of the coherence time.<sup>122</sup> Transient effects were first observed by Bloembergen in 1948 during his work in NMR spectroscopy.<sup>123</sup> This observation led to the development of correlation NMR and Fourier Transform (FT)-NMR spectroscopy by J. Dadok (*born in Dětmarovice, Czechoslovakia 1926*).<sup>124, 125</sup> In ESR, such effects were observed only much later.<sup>126</sup> Nowadays rapid scan ESR, pioneered by the Denver group, is performed by few groups mainly at low frequencies (below 10 GHz) by fast magnetic sweeps at a constant microwave frequency using resonant cavities. This limits the experiments to narrow spectra (radicals), for which the spectral response fits within the bandwidth of the resonant cavity.<sup>28, 29</sup> However, the method can be reconsidered and instead of fast magnetic sweeps at constant frequency, fast frequency sweeps at a constant magnetic field can be implemented, similarly to FDMR (Figure 15B). Nowadays, it is

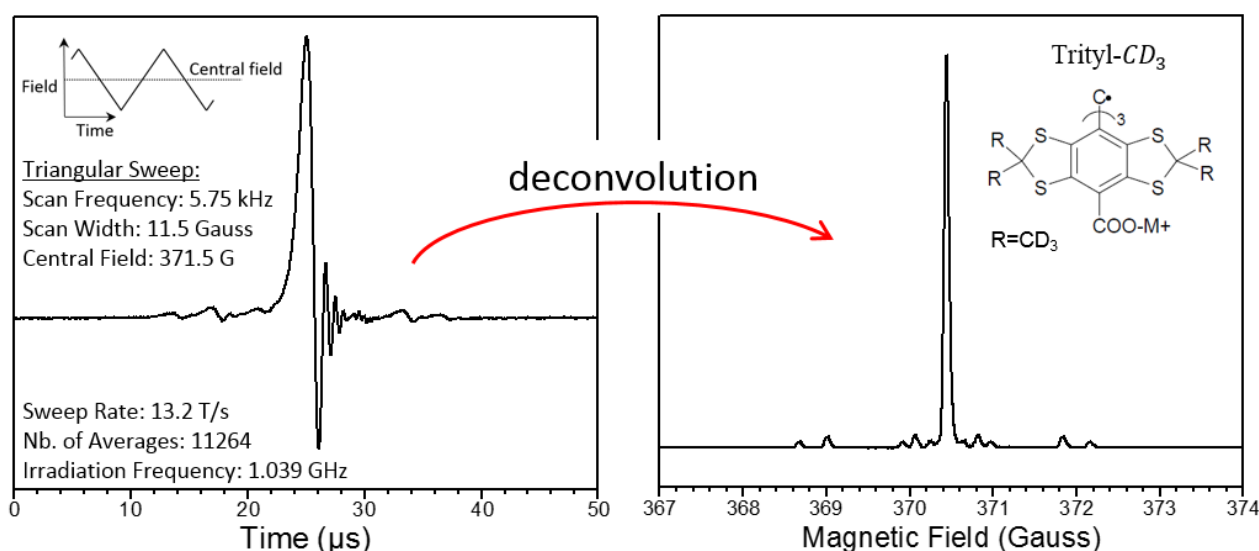


**Figure 16.:** Left: Rapid Field Scan ESR spectrum showing transient effects of 0.2 mM Nycomed triarylmethyl (trityl- $\text{CD}_3$ ) radical recorded by author in the ESR centrum in Denver. The spectrum was recorded in 2 seconds using triangular magnetic sweeps with 11.5 G width and 5.75 kHz sweep frequency, corresponding to sweep rate of 13.2 T/s ( $\sim 0.37$  THz/s), at constant 371.5 G central field and irradiation frequency 1 GHz. Right: Deconvoluted rapid field scan ESR spectrum of the trityl- $\text{CD}_3$  radical.

possible by a current technology to build THz-Frequency-Rapid-Scan-ESR (THz-FRaScan-ESR) spectrometer capable of capturing spin dynamics of various systems at the user selected frequency in broad frequency range. The above described developments are already starting to be realized at Brno University of Technology, with the international team of PhD and MSc students under supervision of experienced scientists. With the strong belief, that we can put Brno back to the center of magnetic resonance development.<sup>127</sup>

## 7 ACNOWLEDGEMENT

It is very long list of people, which guided me to this point and to whom I would like to express my: THANK YOU! I would like to start with my parents, they were always supportive and passion over all the years. Teachers and tutors, who were very enthusiastic about the science and motivate me in the early years of my carrier. I would like to thank to my colleagues from Stuttgart and Frankfurt for creating nice environment and stimulating scientific atmosphere in the past years. Then, I would like to express my gratitude to Tomáš Šikola for kicking me out of “comfortable nest”, Anne-Laure Barra and Wolfgang Wernsdorfer for the introduction to molecular magnetism and electron spin resonance spectroscopy. Milan Orlita, for nights spent by measurements of graphene. Last but not least to Thomas Prisner and Joris van Slageren for mentoring me on my way to scientific maturity, my life partner Lucie and our kids for all we are doing.

**COMMENTED PAPER 1**

**P. Neugebauer\***, D. Bloos, R. Marx, P. Lutz, M. Kern, M. Tuček, D. Aguilà, J. Vaverka, C. Dietrich, O. Ouari, R. Clérac and J. van Slageren

Ultra-broadband EPR in field and frequency domains for applications from dynamic nuclear polarisation to single-molecule magnets

Submitted to: *Phys. Chem. Chem. Phys.* 2017



## Ultra-broadband EPR in field and frequency domains for applications from dynamic nuclear polarisation to single-molecule magnets

Received 00th January 20xx,  
Accepted 00th January 20xx

DOI: 10.1039/x0xx00000x

www.rsc.org/

P. Neugebauer<sup>a,†</sup>, D. Bloos<sup>a</sup>, R. Marx<sup>a</sup>, P. Lutz<sup>a</sup>, M. Kern<sup>a</sup>, M. Tuček<sup>a,b</sup>, D. Aguilà<sup>c,d</sup>, J. Vaverka<sup>b,e</sup>, C. Dietrich<sup>a</sup>, O. Ouarif, R. Clérac<sup>c,d</sup> and J. van Slageren<sup>a‡</sup>

Electron Paramagnetic Resonance (EPR) is a powerful technique to investigate the electronic and magnetic properties of a wide range of materials. We present the first combined Terahertz (THz) Field and Frequency Domain Electron Paramagnetic Resonance (HFEPFR/FDMR) spectrometer designed to investigate the electronic structure and magnetic properties of molecular systems, thin films and solid state materials in a very broad frequency range of 85–1100 GHz. High resolution frequency-field (Zeeman) maps (170–380 GHz by 0–15 T) recorded on two single-molecule magnets,  $[\text{Mn}_2(\text{saltmen})_2(\text{ReO}_4)_2]$  and  $[\text{Mn}_2(\text{salpn})_2(\text{H}_2\text{O})_2](\text{ClO}_4)_2$ , give direct access to the field-dependence of the energy level diagram. Furthermore, we explore the frequency sweep capability of the spectrometer by performing experiments on the AMUPol polarizing agent at 263, 329 and 394 GHz, at frequencies relevant to dynamic nuclear polarisation (DNP) experiments at 400, 500 and 600 MHz, respectively.

### Introduction

Electron Paramagnetic Resonance (EPR) spectroscopy is a very powerful tool for investigation of a variety of systems that contain unpaired electrons. It is thus important in branches of physics, chemistry and biology.<sup>1–9</sup> It is sensitive to the static electronic properties of paramagnetic centres as well as to the molecular motional dynamics. EPR spectrometers are typically operated at fixed microwave (MW) frequencies of 10 GHz (X-band) and a magnetic field of ca. 0.3 T corresponding to free electron  $g$ -value of 2. However, soon after first EPR experiments by Zavoiskii (1944),<sup>10</sup> the advantage of performing EPR experiments at high frequencies and fields (HFEPFR) was realized.<sup>11</sup> High frequencies and fields lead to dramatic increases of the absolute sensitivity as a result of the larger Boltzmann factor, as well as higher filling factors, due to the decrease of cavity size ( $\approx \lambda$ ) necessary with smaller wavelengths (at 10 GHz,  $\lambda = 3$  cm, while at 300 GHz,  $\lambda = 1$  mm).

Furthermore, the advantages of HFEPFR also lie in the delivery of high  $g$ -value resolution, which allows establishing the electronic and geometric structures of active centres in enzymes,<sup>9</sup> for example. High frequencies also give access to large energy gaps, as in the case of large zero-field splittings (ZFSs), which has been shown extensively through the work on transition metal complexes and molecular nanomagnets.<sup>12, 13</sup> Today HFEPFR spectrometers are widespread and commonly operated at MW frequencies around 300 GHz<sup>13–20</sup> and now also commercially available. HFEPFR development is also strongly driven by DNP experiments<sup>21–24</sup> at high fields where the intrinsically poor NMR sensitivity, caused by the small nuclear spin polarization, can be enhanced by exciting EPR transitions, where the large electron spin polarizations can be transferred to the nuclear spins. Note that the field strengths required for proton NMR frequencies of 400, 500 and 600 MHz lead to 263, 329 and 394 GHz EPR frequencies for electron spins with a  $g$ -value close to the free-electron value of 2.00. For instrumental reasons, EPR experiments are conventionally performed at fixed MW frequencies by sweeping the magnetic field. A fixed frequency allows the use of resonant structures, which enhances the MW magnetic field at a sample position and thus the sensitivity. However, because single mode cavities decrease in size with radiation wavelength, the maximum sample size decreases at high frequencies limiting the use of such resonators. Frequency Domain Magnetic Resonance (FDMR) experiments are performed at a fixed field by sweeping the frequency, necessitating the omission of a resonator. The advantages of FDMR over field-swept HFEPFR are: (i) the frequency-swept spectrum corresponds directly to the energy spectrum, (ii) the experiments can be performed in

<sup>a</sup> Institute of Physical Chemistry, University of Stuttgart, Pfaffenwaldring 55, D-70569 Stuttgart, Germany.

<sup>b</sup> Institute of Physical Engineering, Brno University of Technology, Technická 2, 61669, Brno, Czech Republic.

<sup>c</sup> CNRS, CRPP, UPR 8641, F-33600 Pessac, France.

<sup>d</sup> Univ. Bordeaux, CRPP, UPR 8641, F-33600 Pessac, France

<sup>e</sup> Central European Institute of Technology, CEITEC BUT, Technická 3058/10, 61600, Brno, Czech Republic.

<sup>f</sup> Aix Marseille Univ, CNRS, ICR 7273, 13013 Marseille, France.

<sup>†</sup> petr.neugebauer@ipc.uni-stuttgart.de

<sup>‡</sup> slageren@ipc.uni-stuttgart.de

Electronic Supplementary Information (ESI) available: [details of any supplementary information available should be included here]. See DOI: 10.1039/x0xx00000x

the absence of a magnetic field that could influence sample properties, (iii) the frequency can be swept much faster than the field, which allows access to spin dynamics in CW measurements (rapid scan EPR).<sup>25, 26</sup> FDMR studies were mainly pioneered in the 1960 and 70s by Sievers<sup>27</sup> and Richards<sup>28</sup>, discontinued in 80's and then later on revived from the late 1990s by Mukhin, Dressel and van Slageren<sup>29</sup>, and later also by Schnegg.<sup>30, 31</sup> One drawback is that the frequency-dependent standing wave pattern in the radiation beam, can lead to artefacts in the spectrum.

In our work, we combine the advantages of both conventional HF EPR as well as of FDMR and we present a first combined HF EPR and FDMR spectrometer. We use the capability of the spectrometer to produce, high resolution frequency-field (Zeeman) maps of single-molecule magnets as well as to measure FDMR spectra of DNP polarizing agents at relevant fields.

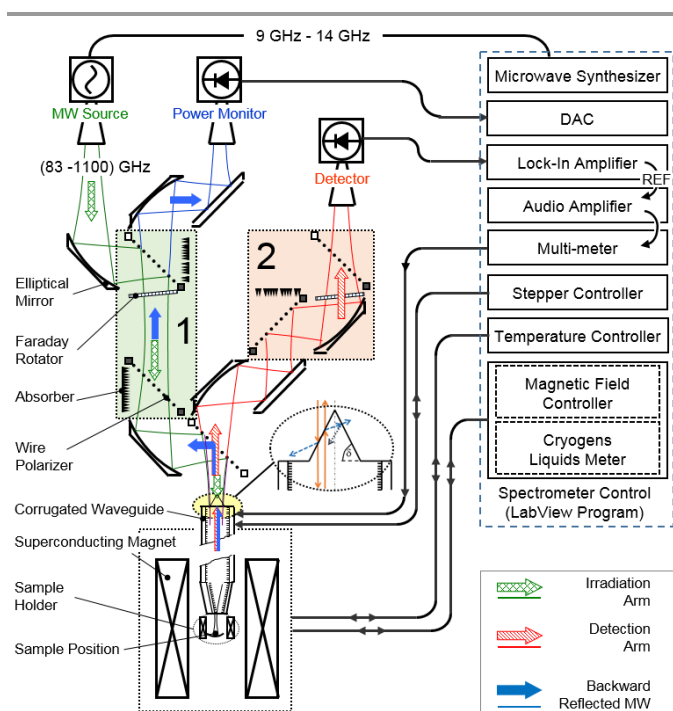


**Figure 1.** Overall layout of the combined HF EPR/FDMR spectrometer. The spectrometer is equipped with a quasi-optical (QO) bridge including dedicated corrugated waveguides optimized for the frequency bands centred around 315 and 630 GHz. The spectrometer operates in induction mode. The direction of MWs between the QO components is indicated where two QO isolators in irradiation arm (1) and in detection arm (2), respectively, are highlighted.

## Experimental

### Synthesis

<sup>14</sup>N-TEMPOL (4-Hydroxy-2,2,6,6-tetramethylpiperidine 1-oxyl), BDPA ( $\alpha,\gamma$ -Bisdiphenylene- $\beta$ -phenylallyl) and polystyrene (density 1.04 g/ml at 25°C) were obtained from Sigma Aldrich. The biradical AMUPol was synthesized according to literature.<sup>32</sup> TEMPOL, BDPA radicals were dissolved together with polystyrene in the desired ratio into toluene. Thin film

samples with a mass of ca. 1 mg were prepared by drop casting, and subsequent overnight evaporation of the toluene. The investigated single molecule magnets,  $[\text{Mn}_{12}\text{O}_{12}(\text{CH}_3\text{COO})_{16}(\text{H}_2\text{O})_4]\cdot 2(\text{CH}_3\text{COOH})\cdot 4(\text{H}_2\text{O})$ , abbreviated  $\text{Mn}_{12}\text{AC}$ ,<sup>33</sup>  $[\text{Mn}_2(\text{saltmen})_2(\text{ReO}_4)_2]$  and  $[\text{Mn}_2(\text{salpn})_2(\text{H}_2\text{O})_2](\text{ClO}_4)_2$  were synthesized according to literature.<sup>34, 35</sup>

### Combined HF EPR/FDMR spectrometer

The combined HF EPR/FDMR spectrometer (Figure 1, photograph in Figure S1) uses a solid state microwave (MW) source allowing operation in very broad frequency range from 82.5 GHz to 1100 GHz. The MW source is based on a computer controlled 8-20 GHz synthesizer providing input MW to 85-125 GHz Amplifier Multiplier Chain (AMC), followed by a combination of full-band frequency multipliers covering the frequency range from 170 up to 1100 GHz. All these MW parts are from Virginia Diodes Inc. (VDI). The power output in a given frequency band is rather flat with respect to traditional FDMR sources such as Backward Wave Oscillators (BWO). This is of great advantage in case of FDMR experiments, because it eliminates the need for normalization of experimental data with respect to irradiation power. The output power from the MW source across all frequencies can be found in the ESI (Figure S2).

To propagate the MW, we use a low loss quasi-optical (QO) bridge and waveguide<sup>36</sup> (Thomas Keating Ltd.). Outside the cryostat, the MW is propagated as free space linearly polarized Gaussian beam between broadband off-axial QO components (indicated in Figure 1) arranged on a QO table. In the cryostat, low loss oversized corrugated waveguides optimized for 315 or 630 GHz are used for propagating the MW in the  $\text{HE}_{11}$  mode. The QO table is placed on a movable stand allowing loading of the sample rod into the cryomagnet as well as horizontal, vertical and angular alignment of the QO bridge. The alignment is done by micrometric screws allowing fine tuning of the MW coupling into corrugated waveguides. The MW from the source is coupled to the QO bridge by dedicated corrugated horns for a given frequency band. Afterwards, it is propagated in free space on the QO table hitting the first off-axial mirror, which is used to refocus the divergent Gaussian beam (MW is refocused every 250 mm). The beam is then reflected by a vertical wire grid polarizer, defining a linear polarization, transmitted through an exchangeable Faraday rotator, which rotates the polarization by 45°. It passes through 45° wire grid polarizer, which in combination with previous vertical wire grid and a Faraday rotator forms a QO circulator (Figure 1. Pos. 1).<sup>37</sup> After that the beam is again refocused by an elliptical mirror, reflected by a wire grid polarizer and coupled into a 1.8 m long, 18 mm inner diameter corrugated waveguide used to propagate MWs inside the cryostat. The corrugated waveguides are tapered at the sample position either to 5 mm or 2 mm by corrugated tapers in order to focus MW on the sample. We have developed a versatile sample holder fabricated from VESPEL SP21 and SP22 which takes a variety of easy exchangeable inserts for pellets,

air-sensitive samples, a semi-confocal Fabry-Pérot resonator and a single crystal rotator (see Figure S3). For adjusting mirrors and a sample orientation in the Fabry-Pérot resonator and in the single crystal rotator, respectively, we use piezo steppers and controllers from Attocube Systems AG. The sample holder features a modulation coil made from 0.3 mm copper wire, which produces around 1 Gauss/mA modulation amplitude at the sample position. To generate and detect the modulation field, we use a Stanford Research SR830 Lock-In amplifier providing a modulation signal which is amplified by InterM L-1400 audio amplifier and the modulation current is read by a Tektronix DMM4040 multimeter. Modulation frequencies of 1 kHz (HFEPFR) to 30 kHz (FDMR) are used. The sample temperature is monitored by a calibrated Cernox temperature sensor. The sample is located in centre of magnetic field generated by a superconducting solenoid with magnetic field up to 15 T (17 T at 2.2 K) equipped with a Variable Temperature Insert (VTI) cryostat with an inner diameter of 30 mm, both from Oxford Instruments Ltd. The maximum sweep rate of the magnet is 1 T/min in the range up to 15 T and the VTI allows temperatures in the range from 1.6 to 300 K.

The spectrometer is operated in induction mode,<sup>37</sup> which works as follows. The linearly polarized MW excitation (green arrow in Figure 1) upon interaction with the sample is reflected back either by the gold coated mirror underneath of the sample (double pass transmission) or by the sample itself. The MW then returns to the QO bridge in the same corrugated waveguide. In case of resonance, the returned MW is no longer linearly polarized, because one of the circular MW radiation components interacts more strongly with the sample than the other. The polarizer above the cryostat thus splits the signal into co-polar and cross-polar signals. The former is the MW that is mainly unaffected (background signal) by the sample whereas the latter is the MW containing information about the sample. The co-polar signal is directed to a power monitor (blue arrow in Figure 1), whereas the cross-polar signal goes to a bolometer detector (red arrow in Figure 1). The cross-polar MW beam carrying the EPR signal goes through a second QO circulator (Pos. 2 in Figure 1) before reaching the detector. The isolation between the co-polar and cross-polar signals is more than 30 dB, which greatly reduces the noise level on the detector. The radiation is detected either by a helium cooled bolometer (broad band, QMC Instruments Ltd.) or by Zero Bias Detectors (ZBDs, only dedicated frequency bands, VDI). The bolometer is an InSb hot-electron Bolometer type QFI/XBI with enhanced absorption by inhomogeneously tuned permanent magnets allowing operation up to 1.5 THz. The detector signal is demodulated at the field modulation frequency, leading detection of derivative spectra. While for the detection of EPR signal we mainly use the bolometer, the ZBDs are primarily used to monitor output power from the source as well as to monitor the state of MW coupling to the Fabry-Pérot resonator by monitoring the backward reflected MW from the sample. More details about used detectors can be found in Table S1 of ESI.

To control the HFEPFR/FDMR spectrometer, we use the GPIB and LAN interfaces of the used electronic devices and home-written control program in LabVIEW (G-Code). The software offers a graphical user interface to control of the main parameters of the spectrometer, e.g., frequency, magnetic field, temperature and in the case of single crystal rotator also the orientation of the sample. We have implemented script-based automation of the measurements.

More details on the combined HFEPFR/FDMR spectrometer can be found in the ESI.

## Results and discussion

### Suppression of standing waves and sensitivity determination

As already mentioned, in FDMR spectroscopy, standing waves in the system lead to artefacts deforming the signal of interest. For these reasons, the off-axis arrangement (the lack of parallel flat surfaces) of the QO components helps to reduce the build-up of unwanted standing waves. Additionally, two QO circulators have been implemented into the system to prevent bouncing of MW between source and sample (Pos. 1 in Figure 1) and sample and detector (Pos. 2 in Figure 1). Furthermore, the use of conical instead of flat windows (inset Figure 1) from High Density Polyethylene (HDPE) on top of the corrugated waveguide greatly suppresses standing waves in the system (Figure 2). Note that the FDMR spectra and HFEPFR spectra are inverted with respect to each other (see Figure S5 in ESI). The effect of implementation the second Faraday rotator can be seen on Figure 2A, where oscillations at 57 MHz ( $\lambda/2 \approx 2.6$  m, corresponding to distance sample-detector) are largely suppressed.

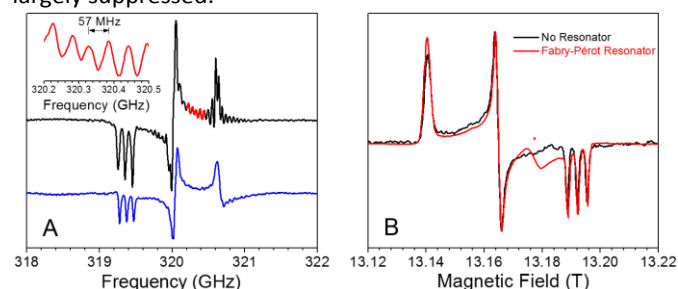


**Figure 2.** (A) FDMR measurements on a 100  $\mu\text{M}$   $^{14}\text{N}$ -TEMPOL diluted in polystyrene matrix at 60 K. The top spectrum (black) was recorded employing only the QO isolator in the transmission arm of the spectrometer. In the inset, a detail of standing wave oscillations is shown with a period about 57 MHz ( $\lambda/2 \approx 2.6$  m), which corresponds to the distance between the sample and the detector. The bottom spectrum (blue) was recorded by using QO isolators in both transmission and detection arms; (B) Comparison of measurements of 10  $\mu\text{M}$   $^{14}\text{N}$ -TEMPOL diluted in polystyrene matrix at 370 GHz and 60 K using Fabry-Pérot resonator (in red) and non-resonant sample holder (in black). The Fabry-Pérot resonator provides one order of magnitude better signal to noise ratio with respect to non-resonant cavity. The signal marked by \* originates from impurities in the Fabry-Pérot mirrors.

The absolute sensitivity (minimum number of detectable spins) of the spectrometer was determined at 60 K from a series of field-swept HFEPFR measurements BDPA and  $^{14}\text{N}$ -TEMPOL radicals at several spin concentrations (Figure S6). From these, signal-to-noise ratios were determined. Extrapolation to a signal-to-noise ratio of 1 gives at 5 K an absolute sensitivity of

$10^7$  spins/(G.Hz<sup>1/2</sup>) at 370 GHz using our Fabry-Pérot resonator. Without the use of this resonator, the sensitivity is one order of magnitude worse (Figure 2B). In FDMR, the sensitivity is estimated to be  $10^9$  spins/Gauss and it is mainly limited by the remaining standing-waves in the system. The high sensitivity is underlined by the fact that we were able to perform FDMR measurements on small single crystals (0.1 mg of Mn<sub>12</sub>Ac), Figure S7 in ESI. While so far, single crystal FDMR experiments had only been possible on single crystal mosaics.<sup>38</sup>

### [Mn<sub>2</sub>] single-molecule magnets

We have investigated dinuclear Mn(III) complexes. The first of these [Mn<sub>2</sub>(saltmen)<sub>2</sub>(ReO<sub>4</sub>)<sub>2</sub>] (abbreviated Mn<sub>2</sub>saltmen) was reported to be magnetically isolated dinuclear complex, with an  $S = 4$  spin ground state resulting from ferromagnetic interaction between  $S = 2$  Mn(III) centers.<sup>34</sup> In contrast, the second complex, [Mn<sub>2</sub>(salpn)<sub>2</sub>(H<sub>2</sub>O)<sub>2</sub>](ClO<sub>4</sub>)<sub>2</sub> (abbreviated Mn<sub>2</sub>salpn), is a supramolecular chain of such dinuclear complexes due to non-negligible exchange interactions between the [Mn<sub>2</sub>] building blocks.<sup>35</sup> These investigations also serve to assess and demonstrate the broadband capabilities of the newly developed spectrometer. Both compounds are structurally very similar (Figure S8). To investigate the interdimer exchange interactions in more detail, we performed comprehensive HFEPFR and FDMR studies of both complexes at temperatures from 5 to 30 K, and frequencies up to 720 GHz.

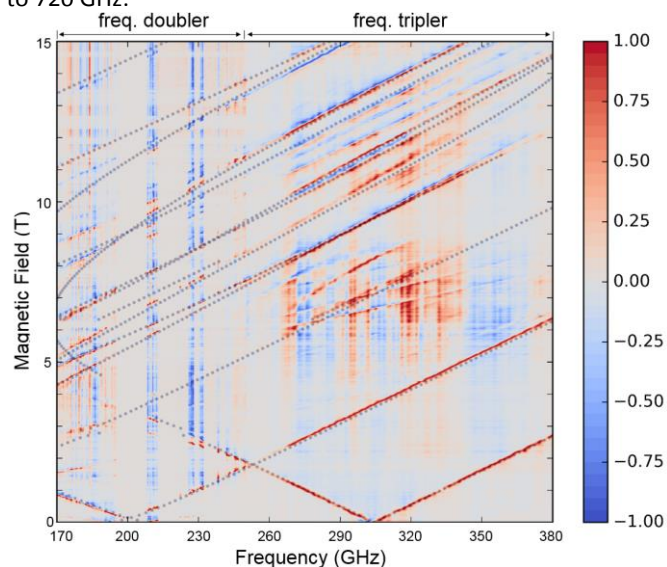


**Figure 3.** 220 GHz wide FDMR map of Mn<sub>2</sub>saltmen complex at 30 K overlaid by an EasySpin<sup>39</sup> simulation in grey dotted lines using parameters from Table 1. The high resolution map is composed by 10000 x 20000 points in magnetic field and frequency directions, respectively, and was recorded in 8 hours. Comparison between HFEPFR spectra extracted from the map and the conventionally recorded HFEPFR can be found in the ESI Figures S9 and S10.

First, we recorded 20000-points FDMR spectra on a powder sample of Mn<sub>2</sub>saltmen in the range of 170 – 250 GHz and 250 – 380 GHz, using a doubler and tripler of the AMC output frequency, respectively. FDMR spectra were recorded at 10000 different fields between 0 and 15 T, using 1 ms time-constant and 30 kHz modulation frequency, to give the field-frequency-

map depicted in Figure 3. This is a direct image of the energy level diagram of Mn<sub>2</sub>saltmen as a function of magnetic field. The total recording time is 8 hours, whereas, at a scan rate of 1 T/min, 200 days would be required to compose the same map from field-swept spectra. This corresponds to a speedup factor of 600. Such a map allows detailed tracing of the frequency dependence of magnetic resonance lines. This allows tracking transitions even through level crossings, as well as accurately determining the size of these level crossings. Cuts along the field axis demonstrate that an EPR spectrum extracted from the field-frequency map is identical to the conventional field-domain HFEPFR spectrum (Figures S9 and S10). Selected FDMR measurements at various fields are shown in Figure S11. For detailed analysis, also multifrequency field-swept HFEPFR spectra up to frequencies of 720 GHz were recorded (Figure 4A), using 300 ms time-constant and 1 kHz modulation frequency. These spectra reveal two strong resonance lines that extrapolate to zero-field values of 305 and 201 GHz, respectively. In the strong exchange approximation, these resonance lines would correspond to  $|S M_S\rangle = |4 \pm 4\rangle$  to  $|4 \pm 3\rangle$  and  $|4 \pm 3\rangle$  to  $|4 \pm 2\rangle$  transitions, respectively, from which a zero-field splitting (ZFS) value of the ground state of  $D_{S=4} \approx -2$  K can be extracted. However, simulations reveal that the many additional features in the spectra cannot be reproduced in this manner. Therefore the exchange coupling and ZFS must be considered at the same level, by means of a microscopic spin Hamiltonian.

A suitable microscopic spin Hamiltonian for a chain of interacting dimers is:

$$\hat{H} = -J \sum_{i=1}^N \hat{S}_{i,1} \hat{S}_{i,2} - J' \sum_{i=1}^N \hat{S}_{i,2} \hat{S}_{i+1,1} + D \sum_{i=1}^N (\hat{S}_{i,1,z}^2 + \hat{S}_{i,2,z}^2) + E \sum_{i=1}^N (\hat{S}_{i,1,x}^2 - \hat{S}_{i,1,y}^2 + \hat{S}_{i,2,x}^2 - \hat{S}_{i,2,y}^2) + \hat{S} \cdot \mathbf{g} \cdot \mathbf{B}, \text{ eq.1}$$

where  $J$  is the exchange interaction within each dimer, which was reported to be ferromagnetic with  $J = 5.3$  K.<sup>34</sup>  $J'$  is the interdimer exchange interaction, while  $D$  and  $E$  are the axial and rhombic zero-field splitting of the manganese(III) ions. The  $D$  value was reported to be  $D = -4.0$  K.<sup>34</sup> For Mn<sub>2</sub>saltmen,  $J'$  is taken to be zero.<sup>34</sup>

Extensive simulations resulted in the spin Hamiltonian parameters reported in Table 1, which reproduce the experimental spectra at all frequencies quite well (Figure 3 and 4). The intradimer interaction strength is found to be the same as that found from magnetic measurements. The  $D$ -value turns out to be slightly larger than that derived previously. Interestingly, the HFEPFR measurements allowed the determination of the  $g$ -value anisotropy, as well as the small rhombicity present in this system. This rhombicity can lead to quantum tunnelling of the magnetisation, which shortcuts the energy barrier toward relaxation of the magnetic moment. This leads to lower effective energy barriers found in dynamic magnetic susceptibility measurements compared to those expected from the  $D$ -value. Possible origins of remaining discrepancies between experimental and simulated spectra include anisotropic exchange couplings and non-collinearities of  $\mathbf{g}$ -,  $\mathbf{D}$ - and  $\mathbf{J}$ -tensors. Full consideration of these issues would, however, lead to severe over-parametrization.

HFEPFR spectra recorded on Mn<sub>2</sub>salpn (Figure 4B), are qualitatively similar with the notable difference that the

resonance lines are almost twice as broad. Simulations revealed that the HFEP spectra can be satisfactorily reproduced without taking into account interdimer interactions, i.e.,  $J' = 0$  in eq.1. The resulting parameters (Table 1) are comparable to both literature and those found for  $Mn_2$  saltmen. The main difference is the absence of rhombic distortion and in more accurate estimation of  $J$  and ZFS parameters ( $D$  and  $E$ ). This results in fewer transitions being allowed and, hence, fewer features in the HFEP spectra. The influence of the interdimer interaction is thus only reflected indirectly, namely by the increased linewidth. The linewidth increase is attributed to increased spin relaxation, leading to line broadening. In agreement with this attribution, the magnetic resonance lines are best described by Lorentzian rather than Gaussian functions. For both  $[Mn_2]$  compounds the spin Hamiltonian parameters derived here can be used to simulate the temperature dependence of the magnetic susceptibilities, leading to results that are virtually indistinguishable from the original fits (Figure S12).

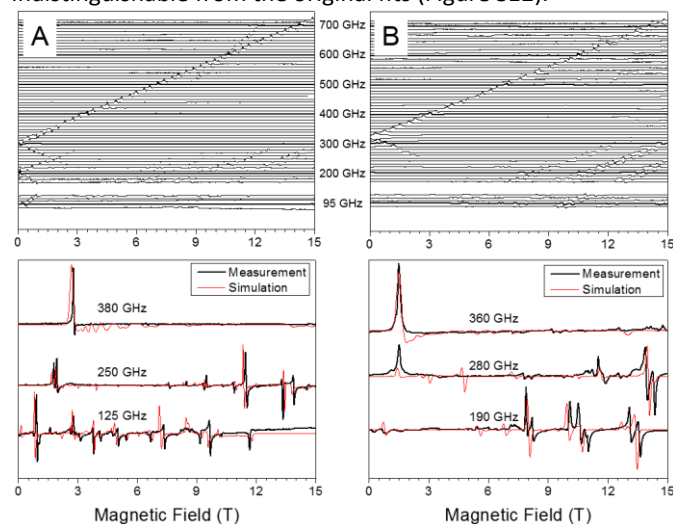


**Figure 4.** Normalized HFEP spectra for  $Mn_2$  saltmen (A) and  $Mn_2$  salpn (B) measured at 5 K and at frequencies up to 720 GHz. Below, selected HFEP spectra with corresponding simulations in EasySpin<sup>39</sup> using parameters from Table 1.

**Table 1.** Spin Hamiltonian parameters derived for  $Mn_2$  salpn and  $Mn_2$  saltmen

System	Method	$g_{  }$	$g_{\perp}$	$J/K$	$D/K$	$E/D$
$Mn_2$ saltmen	HFEP	1.95(1)	1.96(1)	5.4(5)	-4.9(1)	0.08
	SQUID <sup>34</sup>	2.00	2.00	5.3	-4.0	
$Mn_2$ salpn	HFEP	1.92(1)	1.96(1)	4.6(5)	-5.1(1)	0
	SQUID <sup>35</sup>	1.96	1.96	3.6	-4.5	0

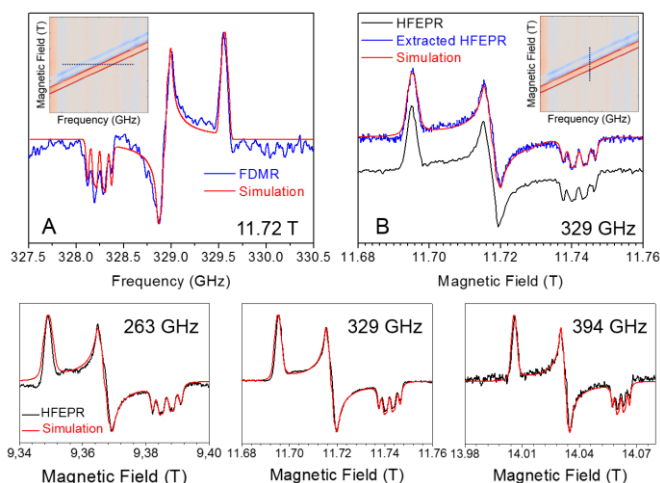


**Figure 5.** FDMR and HFEP of 10 mmol/L AMUPol in polystyrene recorded at 80 K. (A) FDMR spectrum recorded at 11.72 T and in 1 s taken from the frequency-field map as indicated by the dotted line in inset of the figure. (B) Extracted HFEP spectrum from the map (inset) at 329 GHz together with a simulation and compared to conventional HFEP spectra at the same frequency. Note that the signal to noise ratio is about the same value, in spite of the different time-constants of 1 ms and 300 ms used for FDMR map and HFEP spectrum, respectively. (Below) HFEP spectra together with simulations using EasySpin<sup>39</sup> at 263, 329 and 394 GHz.

#### AMUPol DNP polarizing agent

Dynamic Nuclear Polarization (DNP) is a fast growing experimental technique in solid state NMR spectroscopy at low temperature,<sup>21, 22</sup> where polarizing agents (paramagnetic species) are added to a solution sample. By MW excitation of the EPR transition of the polarizing agent, the much higher polarization of the electron spin at a given frequency and temperature can be transferred to the intrinsically weakly polarized nuclear spin. By this method the NMR sensitivity can be enhanced by factors of theoretically up to 658 or 2617 for  $^1H$  NMR or  $^{13}C$  NMR, respectively. The NMR enhancement that is achieved in practice is strongly determined by which polarizing agent is used. Therefore there is a great interest in optimizing these agents, and, concurrently their *in-situ* characterisation. Because NMR spectrometers employ fixed field magnets, conventional field-swept EPR measurements cannot be carried out in NMR magnets. In contrast, the spectrometer discussed here allows for measurements in the frequency domain at DNP relevant frequencies of ca. 263, ca. 329 and ca. 394 GHz which correspond to proton NMR frequencies of 400, 500 and 600 MHz, respectively.

Figure 5 displays FDMR, HFEP and field-frequency maps recorded at 80 K on samples of AMUPol (Figure S13) diluted into polystyrene at a concentration of 10 mmol/L. The resonance map (inset of Figures 5A and 5B) was created by stacking FDMR scans recorded between 11.5 and 11.9 T using a 1 ms time-constant and 30 kHz modulation frequency. Figure 5B shows the extracted 329 GHz HFEP spectrum compared to the conventionally recorded HFEP spectrum at the same frequency. Note, if we extract EPR lines out of the resonance maps (Figure 5B), the sensitivity is of the same order or slightly better than in EPR if we take into account the time constant used in the experiments (see also Figure S10 in ESI). To

simulate the experimental data, we use the spin Hamiltonian  $\hat{H}$  describing 2 nitroxide radicals by 3 separate terms:

$$\hat{H} = \hat{H}_{HFI} + \hat{H}_{EEI} + \hat{H}_{EZI},$$

$$\hat{H}_{HFI} = \sum_{i=1}^2 \hat{S}_i^T \mathbf{A}_i \hat{I}_i; \quad \hat{H}_{EEI} = \sum_{i>j}^2 \hat{S}_i^T \mathbf{D} \hat{S}_j,$$

where  $\hat{H}_{HFI}$  describes the hyperfine interaction (HFI),  $\hat{H}_{EEI}$  the electron-electron interaction (EEI) and  $\hat{H}_{EZI}$  the electron Zeeman interaction (EZI) in rotated frame.  $\mathbf{A}$  is the hyperfine interaction tensor,  $\mathbf{D}$  is the dipolar coupling tensor,  $\hat{I}$  is the nuclear spin operator and  $\hat{S}$  is the electron spin operator. The hyperfine interaction between an electron and the opposite nitrogen nucleus as well as hyperfine couplings to non-nitrogen nuclei are neglected.  $\hat{H}_{EZI}$  in rotated frame:

$$\hat{H}_{EZI} = \mu_B \sum_{i=1}^2 \mathbf{B}^T \mathbf{g} \hat{S}_i = \mu_B \sum_{i=1}^2 \mathbf{B}^T \mathbf{R} \mathbf{R}^T \mathbf{g} \mathbf{R} \mathbf{R}^T \hat{S}_i = \mu_B \sum_{i=1}^2 \mathbf{B}^T \mathbf{g}' \hat{S}'_i$$

$$\mathbf{R} = \mathbf{R}(\alpha, \beta, \gamma)$$

is defined by rotation tensor  $\mathbf{R}(\alpha, \beta, \gamma)$ , where  $\alpha, \beta, \gamma$  are the Euler angles.  $\mu_B$  is the Bohr magneton and  $\mathbf{B}^T$ ,  $\mathbf{g}'$  and  $\hat{S}'$  are the magnetic field tensor,  $\mathbf{g}$ -tensor and electron spin operator, respectively, in rotated frame. Note that the coordination frame of all these interactions is different. The best parameters obtained by simulation are listed in Table 2.

**Table 2.** Parameters obtained by simulating experimental FDMR and HFEPFR data at 263, 329 and 394 GHz, of 10 mmol/L of AMUPol in polystyrene, where  $g_i$  are the  $\mathbf{g}$ -tensor components,  $A_{ii}$  is parallel component of the tensor describing the hyperfine coupling to a  $^{14}\text{N}$  nucleus ( $i = 1$ ),  $D_i$  is the dipolar coupling between the two electrons in the AMUPol molecule. For the best fit we had to rotate the  $\mathbf{g}$ -tensor with respect to  $\mathbf{D}$ -tensor by  $25^\circ \pm 10^\circ$ .  $D_i^*$  is the value which was reported by Gast et al.<sup>40</sup> for a 7 mmol/L frozen solution of AMUPol in glycerol- $d_8$ /D<sub>2</sub>O/H<sub>2</sub>O mixture in volume ratio 60/30/10.  $D_i^{**}$  is the value of Sauvée et al.<sup>32, 41</sup> using 1 mmol/L AMUPol in water or tetrachloroethane solution.

$i$	$g_i$	$A_{ii}$ (MHz)	$D_i$ (MHz)	$D_i^*$ (MHz)	$D_i^{**}$ (MHz)
x	$2.00988 \pm 0.00001$	$27.0 \pm 1.0$	$-21 \pm 1$	-53.0	-35.0
y	$2.00604 \pm 0.00001$	$38.0 \pm 1.0$	$-21 \pm 1$	+26.5	17.5
z	$2.00188 \pm 0.00001$	$94.3 \pm 0.5$	$+42 \pm 2$	+26.5	17.5

The obtained dipolar  $D = 42$  and isotropic exchange  $J = 0$  coupling differs from values obtained in recent HFEPFR studies of AMUPol obtained at frequencies up to 275 GHz by Gast et al.,<sup>40</sup> and by an earlier X-band measurements and DFT calculations studies of Sauvée et al.,<sup>32, 41</sup> also listed in the Table 2. Our best fits were obtained by rotation of the  $\mathbf{g}$ -tensor around z-axis by  $25^\circ \pm 10^\circ$  with respect to  $\mathbf{D}$ -tensor and without need to incorporate isotropic exchange coupling  $J$  ( $J = 0$ ), whereas the Gast et al. obtained a fit with  $50^\circ$  rotation and using isotropic exchange coupling strength 43 MHz, in addition to the dipolar coupling  $D = 53$  MHz. Sauvée et al. obtained  $D = 35$  MHz and  $J = 44$  MHz with  $64^\circ$   $\mathbf{g}$ -tensor rotation. We attribute the differences (Figure S14) to the different matrix as well to the molecular environment (polarity, hydrogen bonds) used in these particular EPR and HFEPFR/FDMR experiments. In our case we use polystyrene matrix. Gast et al. used a frozen

solution of 7 mmol/L of AMUPol in glycerol- $d_8$ /D<sub>2</sub>O/H<sub>2</sub>O mixture in volume ratio 60/30/10. Sauvée et al. used water or tetrachloroethane solution of 1 mmol/L and experiments were performed in liquid solution at room temperature, where through-space spin exchange interactions can arise from dynamic conformational changes in solution. The obtained discrepancy shows how important the local environment is for the spin Hamiltonian parameters and, hence, for the functioning of the polarizing agents during the DNP experiments. Figure 6 shows the effect of variation of the isotropic  $J$ -coupling on the HFEPFR simulations compared to our experimental data. Note the peaks in region marked by arrows, which demonstrate that for different values of the  $J$ -coupling, additional spectral features appear in the simulated spectra. The importance of the multi-frequency approach can be seen for values of  $J = 43$  MHz, where the spectral features are manifested clearly only at 329 GHz. Thus multi frequency studies at high frequencies are needed for robust analysis. Additional information can be found in ESI.

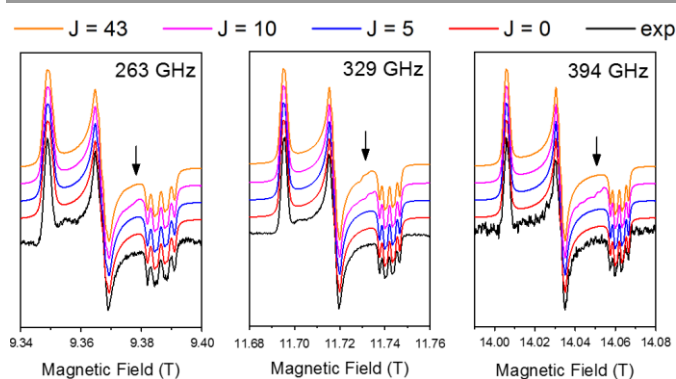


**Figure 6.** Simulation of the AMUPol experimental spectra (in black) for different magnitude of isotropic  $J$ -coupling (in colour). Note that the peaks in region marked by arrow, at different values of  $J$ -coupling appearance of additional spectral features is visible. Furthermore the importance of multi frequency approach can be seen for values of  $J = 43$  MHz, where the spectral features are manifested clearly in the simulation at 329 GHz only.

In addition to the presented experimental data, we used the described spectrometer to investigate magnetic couplings and anisotropies of molecular systems based on lanthanides<sup>5-7</sup> or transition metal complexes,<sup>8, 41-52</sup> as well as in solid state physics.<sup>53, 54</sup>

## Conclusions

The performed experiments underline the versatility of the presented ultra-broadband HFEPFR/FDMR spectrometer capable to perform experiments on wide range of sample types (solutions, crystals, powders) using a modular sample holder. We demonstrate its high sensitivity in field and frequency domains. We performed for the first-time high resolution resonance (Zeeman) maps on single-molecule magnets as well on radicals, containing a large amount of information. The resonance (Zeeman) maps were recorded in an extremely short time using fast frequency sweeps. Together with ultra-broad range of frequencies (almost 1 THz wide) this

enables us to investigate resonance transitions over a large range of fields and frequencies. This yields a large amount of information about the investigated spin system enabling a better understanding of complex systems. This makes the analysis more robust. Furthermore, the experimental data obtained on the DNP polarizing agent AMUPol, show the power of our spectrometer capable to provide *in-situ* information on DNP relevant fields and frequencies. The results obtained at these frequencies show how important is the environment for DNP polarizing agents at high frequencies. Performing *in-situ* experiments at these frequencies, especially in frequency domain, will provide important information not only in progress of magnetic resonance but also in investigation of variety of materials at THz frequencies in future.

## Acknowledgements

This work was supported by the DFG German Priority Program (SPP1601: SL104/3-1,2, NE1900/3-2; NE1900/2-1, INST41/863-1), as well as by the Baden-Württemberg Foundation. We gratefully acknowledge technical support from Virginia Diodes Inc. (Jeffrey Hesler, Cliff Rowland); Thomas Keating Ltd. (Richard Wylde, Kevin Pike). Furthermore, we thank Michael Benzinger and Matthias Kohler (Keysight Technologies Inc.) for lending us the high frequency network analyser, Jan Kubat (CRYTUR spol. s r.o.) for providing the sapphire rods used in rotating sample holder. Furthermore, we would like to express our thanks to Timo Gissibl, Harald Giessen for optical lithography at the University of Stuttgart and Dalibor Šulc from Central European Institute of Technology (CEITEC) in Brno for mirror fabrication, CEITEC – open access project, ID number LM2011020. This work was also supported in France by the CNRS, the Agence Nationale de la Recherche (ANR-12-PDOC-0038), the University of Bordeaux, the Région Nouvelle Aquitaine, the GdR MCM-2: Magnétisme et Commutation Moléculaires and the MOLSPIN COST action CA15128.

## Contribution of authors

P. Neugebauer and J. van Slageren designed the overall experiment setup and supervised the work; D. Bloos and R. Marx performed the majority of the experiments and were involved in the design of the apparatus; P. Lutz and M. Tuček performed simulations of the EPR spectra of the [Mn<sup>2+</sup>]-complexes and AMUPol, respectively; D. Aguilà and R. Clérac synthesized the [Mn<sup>2+</sup>]-complexes; C. Dietrich was involved in the sensitivity determination; M. Kern and J. Vaverka were involved in design of the hardware parts of the combined HFEPR/FDMR spectrometer and O. Ouari synthesised AMUPol sample used in our studies.

## References

1. P. Neugebauer, M. Orlita, C. Faugeras, A. L. Barra and M. Potemski, *Phys. Rev. Lett.*, 2009, **103**, 136403.

2. K. Bader, D. Dengler, S. Lenz, B. Endeward, S.-D. Jiang, P. Neugebauer and J. van Slageren, *Nat. Commun.*, 2014, **5**, 5304.
3. M. Orlita, P. Neugebauer, C. Faugeras, A. L. Barra, M. Potemski, F. M. D. Pellegrino and D. M. Basko, *Phys. Rev. Lett.*, 2012, **108**, 017602.
4. Y.-Y. Zhu, T.-T. Yin, S.-D. Jiang, A.-L. Barra, W. Wernsdorfer, P. Neugebauer, R. Marx, M. Dörfel, B.-W. Wang, Z.-Q. Wu, J. van Slageren and S. Gao, *Chem. Commun.*, 2014, **50**, 15090-15093.
5. Y. Rechkemmer, J. E. Fischer, R. Marx, M. Dörfel, P. Neugebauer, S. Horvath, M. Gysler, T. Brock-Nannestad, W. Frey, M. F. Reid and J. van Slageren, *J. Am. Chem. Soc.*, 2015, **137**, 13114-13120.
6. E. Moreno Pineda, N. F. Chilton, R. Marx, M. Dörfel, D. O. Sells, P. Neugebauer, S.-D. Jiang, D. Collison, J. van Slageren, E. J. L. McInnes and R. E. P. Winpenny, *Nat. Commun.*, 2014, **5**, 5243.
7. M. Gysler, F. El Hallak, L. Ungur, R. Marx, M. Hakl, P. Neugebauer, Y. Rechkemmer, Y. Lan, I. Sheikin, M. Orlita, C. E. Anson, A. K. Powell, R. Sessoli, L. F. Chibotaru and J. van Slageren, *Chem. Sci.*, 2016, **7**, 4347-4354.
8. P. Lutz, D. Aguilà, A. Mondal, D. Pinkowicz, R. Marx, P. Neugebauer, B. Fåk, J. Ollivier, R. Clérac and J. van Slageren, *Phys. Rev. B*, 2017, **96**, 094415.
9. K. Mobius, A. Savitsky, A. Schnegg, M. Plato and M. Fuchs, *Phys. Chem. Chem. Phys.*, 2005, **7**, 19-42.
10. E. K. Zavoisky, *Zh. Eksp. Teor. Fiz.*, 1945, **15**, 253.
11. G. Feher, *Bell Syst. Tech. J.*, 1957, **36**, 449-484.
12. A. L. Barra, A. Caneschi, D. Gatteschi and R. Sessoli, *J. Am. Chem. Soc.*, 1995, **117**, 8855-8856.
13. A. K. Hassan, L. A. Pardi, J. Krzystek, A. Sienkiewicz, P. Goy, M. Rohrer and L. C. Brunel, *J. Magn. Reson.*, 2000, **142**, 300-312.
14. B. Náfrádi, R. Gaál, T. Fehér and L. Forró, *J. Magn. Reson.*, 2008, **192**, 265-268.
15. P. Neugebauer and A.-L. Barra, *Appl. Magn. Reson.*, 2010, **37**, 833-843.
16. G. W. Morley, L.-C. Brunel and J. van Tol, *Rev. Sci. Instrum.*, 2008, **79**, 064703.
17. E. J. Reijerse, *Appl Magn Reson*, 2009, **37**, 795.
18. T. A. Siaw, A. Leavesley, A. Lund, I. Kaminker and S. Han, *J. Magn. Reson.*, 2016, **264**, 131-153.
19. H. Blok, J. A. J. M. Disselhorst, S. B. Orlinskii and J. Schmidt, *J. Magn. Reson.*, 2004, **166**, 92-99.
20. K. A. Earle, B. Dzikovski, W. Hofbauer, J. K. Moscicki and J. H. Freed, *Magn. Reson. Chem.*, 2005, **43**, S256-S266.
21. C. Griesinger, M. Bennati, H. M. Vieth, C. Luchinat, G. Parigi, P. Höfer, F. Engelke, S. J. Glaser, V. Denysenkov and T. F. Prisner, *Prog. Nucl. Magn. Reson. Spectrosc.*, 2012, **64**, 4-28.
22. Q. Z. Ni, E. Daviso, T. V. Can, E. Markhasin, S. K. Jawla, T. M. Swager, R. J. Temkin, J. Herzfeld and R. G. Griffin, *Acc. Chem. Res.*, 2013, **46**, 1933-1941.
23. P. Neugebauer, J. G. Krummenacker, V. P. Denysenkov, G. Parigi, C. Luchinat and T. F. Prisner, *Phys. Chem. Chem. Phys.*, 2012, **15**, 6049 - 6056.
24. P. Neugebauer, J. G. Krummenacker, V. P. Denysenkov, C. Helmling, C. Luchinat, G. Parigi and T. F. Prisner, *Phys. Chem. Chem. Phys.*, 2014, **16**, 18781-18787.

25. S. S. Eaton, R. W. Quine, M. Tseitlin, D. G. Mitchell, G. A. Rinard and G. R. Eaton, in *Multifrequency Electron Paramagnetic Resonance*, Wiley-VCH, 2014, pp. 3-67.
26. J. S. Hyde, R. A. Strangeway, T. G. Camenisch, J. J. Ratke and W. Froncisz, *J. Magn. Reson.*, 2010, **205**, 93-101.
27. P. M. Champion and A. J. Sievers, *J. Chem. Phys.*, 1980, **72**, 1569-1582.
28. P. L. Richards, *J. Appl. Phys.*, 1963, **34**, 1237-1238.
29. J. van Slageren, S. Vongtragool, B. Gorshunov, A. A. Mukhin, N. Karl, J. Krzystek, J. Telsler, A. Muller, C. Sangregorio, D. Gatteschi and M. Dressel, *Phys. Chem. Chem. Phys.*, 2003, **5**, 3837-3843.
30. A. Schnegg, J. Behrends, K. Lips, R. Bittl and K. Holldack, *Phys. Chem. Chem. Phys.*, 2009, **11**, 6820-6825.
31. J. Lu, I. O. Ozel, C. A. Belvin, X. Li, G. Skorupskii, L. Sun, B. K. Ofori-Okai, M. Dinca, N. Gedik and K. A. Nelson, *Chem. Sci.*, 2017.
32. C. Sauvée, M. Rosay, G. Casano, F. Aussenac, R. T. Weber, O. Ouari and P. Tordo, *Angew. Chem., Int. Ed.*, 2013, **52**, 10858-10861.
33. T. Lis, *Acta Cryst. B*, 1980, **36**, 2042-2046.
34. H. Miyasaka, R. Clérac, W. Wernsdorfer, L. Lecren, C. Bonhomme, K.-i. Sugiura and M. Yamashita, *Angew. Chem., Int. Ed.*, 2004, **116**, 2861-2865.
35. L. Lecren, W. Wernsdorfer, Y.-G. Li, A. Vindigni, H. Miyasaka and R. Clérac, *J. Am. Chem. Soc.*, 2007, **129**, 5045-5051.
36. P. F. Goldsmith, *Proceedings of the IEEE*, 1992, **80**, 1729-1747.
37. G. M. Smith, J. C. G. Lesurf, R. H. Mitchell and P. C. Riedi, *Rev. Sci. Instrum.*, 1998, **69**, 3924-3937.
38. J. van Slageren, S. Vongtragool, B. Gorshunov, A. Mukhin and M. Dressel, *Phys. Rev. B*, 2009, **79**, 224406.
39. S. Stoll and A. Schweiger, *J. Magn. Reson.*, 2006, **178**, 42-55.
40. P. Gast, D. Mance, E. Zurlo, K. L. Ivanov, M. Baldus and M. Huber, *Phys. Chem. Chem. Phys.*, 2017, **19**, 3777-3781.
41. S. H. Schlindwein, K. Bader, C. Sibold, W. Frey, P. Neugebauer, M. Orlita, J. v. Slageren and D. Gudat, *Inorg. Chem.*, 2016, **55**, 6186-6194.
42. S. Realista, A. J. Fitzpatrick, G. Santos, L. P. Ferreira, S. Barroso, L. C. J. Pereira, N. A. G. Bandeira, P. Neugebauer, J. Hruby, G. G. Morgan, J. van Slageren, M. J. Calhorda and P. N. Martinho, *Dalton Trans.*, 2016, **45**, 12301-12307.
43. M. van der Meer, Y. Rechkemmer, F. D. Breitgoff, R. Marx, P. Neugebauer, U. Frank, J. van Slageren and B. Sarkar, *Inorg. Chem.*, 2016, **55**, 11944-11953.
44. M. van der Meer, Y. Rechkemmer, F. D. Breitgoff, S. Dechert, R. Marx, M. Dorfel, P. Neugebauer, J. van Slageren and B. Sarkar, *Dalton Trans.*, 2016, **45**, 8394-8403.
45. A. Abhervé, M. Palacios-Corella, J. M. Clemente-Juan, R. Marx, P. Neugebauer, J. van Slageren, M. Clemente-León and E. Coronado, *J. Mater. Chem. C*, 2015, **3**, 7936-7945.
46. I. Nemeč, R. Marx, R. Herchel, P. Neugebauer, J. van Slageren and Z. Trávníček, *Dalton Trans.*, 2015, **44**, 15014-15021.
47. I. Nemeč, R. Herchel, M. Kern, P. Neugebauer, J. van Slageren and Z. Trávníček, *Materials*, 2017, **10**, 249.
48. M. van der Meer, Y. Rechkemmer, U. Frank, F. D. Breitgoff, S. Hohloch, C.-Y. Su, P. Neugebauer, R. Marx, M. Dorfel, J. van Slageren and B. Sarkar, *Chem. Eur. J.*, 2016, **22**, 13884-13893.
49. Y. Rechkemmer, F. D. Breitgoff, M. van der Meer, M. Atanasov, M. Hakl, M. Orlita, P. Neugebauer, F. Neese, B. Sarkar and J. van Slageren, *Nat. Commun.*, 2016, **7**, 10467.
50. D. Schweinfurth, Y. Rechkemmer, S. Hohloch, N. Deibel, I. Peremykin, J. Fiedler, R. Marx, P. Neugebauer, J. van Slageren and B. Sarkar, *Chem. Eur. J.*, 2014, **20**, 3475 – 3486.
51. M. G. Sommer, R. Marx, D. Schweinfurth, Y. Rechkemmer, P. Neugebauer, M. van der Meer, S. Hohloch, S. Demeshko, F. Meyer, J. van Slageren and B. Sarkar, *Inorg. Chem.*, 2017, **56**, 402-413.
52. J.-J. Liu, S.-D. Jiang, P. Neugebauer, J. van Slageren, Y. Lan, W. Wernsdorfer, B.-W. Wang and S. Gao, *Inorg. Chem.*, 2017, **56**, 2417-2425.
53. M. Orlita, C. Faugeras, A.-L. Barra, G. Martinez, M. Potemski, D. M. Basko, M. S. Zholudev, F. Teppe, W. Knap, V. I. Gavrilenko, N. N. Mikhailov, S. A. Dvoretiskii, P. Neugebauer, C. Berger and W. A. de Heer, *J. Appl. Phys.*, 2015, **117**, 112803.
54. M. Orlita, D. M. Basko, M. S. Zholudev, F. Teppe, W. Knap, V. I. Gavrilenko, N. N. Mikhailov, S. A. Dvoretiskii, P. Neugebauer, C. Faugeras, A. L. Barra, G. Martinez and M. Potemski, *Nat. Phys.*, 2014, **10**, 233-238.

**COMMENTED PAPER 2**

K. Bader, D. Dengler, S. Lenz, B. Endeward, S.D. Jiang, **P. Neugebauer**, J. van Slageren  
Room Temperature Quantum Coherence in a Potential Molecular Qubit

*Nat. Commun.*, 5, 5304 (2014).

ARTICLE

Received 12 May 2014 | Accepted 18 Sep 2014 | Published 20 Oct 2014

DOI: 10.1038/ncomms6304

# Room temperature quantum coherence in a potential molecular qubit

Katharina Bader<sup>1</sup>, Dominik Dengler<sup>1</sup>, Samuel Lenz<sup>1</sup>, Burkhard Endeward<sup>2</sup>, Shang-Da Jiang<sup>3</sup>, Petr Neugebauer<sup>1</sup> & Joris van Slageren<sup>1</sup>

The successful development of a quantum computer would change the world, and current internet encryption methods would cease to function. However, no working quantum computer that even begins to rival conventional computers has been developed yet, which is due to the lack of suitable quantum bits. A key characteristic of a quantum bit is the coherence time. Transition metal complexes are very promising quantum bits, owing to their facile surface deposition and their chemical tunability. However, reported quantum coherence times have been unimpressive. Here we report very long quantum coherence times for a transition metal complex of 68  $\mu\text{s}$  at low temperature (qubit figure of merit  $Q_M = 3,400$ ) and 1  $\mu\text{s}$  at room temperature, much higher than previously reported values for such systems. We show that this achievement is because of the rigidity of the lattice as well as removal of nuclear spins from the vicinity of the magnetic ion.

<sup>1</sup>Institut für Physikalische Chemie, Universität Stuttgart, Pfaffenwaldring 55, D-70569 Stuttgart, Germany. <sup>2</sup>Centre for Biomolecular Magnetic Resonance, Institute of Physical and Theoretical Chemistry, Goethe University Frankfurt, D-60438 Frankfurt am Main, Germany. <sup>3</sup>Physikalisches Institut, Universität Stuttgart, Pfaffenwaldring 57, D-70569 Stuttgart, Germany. Correspondence and requests for materials should be addressed to J.v.S. (email: slageren@ipc.uni-stuttgart.de).

The essence of a quantum bit is a system that can be put into an arbitrary coherent superposition state of two or more levels. The lifetime of such a superposition state (quantum coherence time) is the time available for the quantum computation. Many remarkable results have been obtained in this area<sup>1–4</sup>, but suitable qubits for the construction of a real quantum computer that outperforms today's classical computers have yet to be found. This is partly owing to conflicting requirements: on the one hand, quantum coherence times  $T_M$  must be orders of magnitude longer than the time for an individual quantum operation. The ratio of these is the qubit figure of merit that should be larger than 10,000 to allow for fault tolerant quantum computing. On the other hand, for some of the most useful quantum algorithms, a great many qubits need to be put into a collective superposition state (entanglement) that requires interqubit interactions. However, interactions of a qubit with its surroundings (including other qubits) are the cause for the decay of the quantum superposition states of the qubits. Electron-spin-based qubits are a good compromise between sufficiently long coherence times and ability to interact with other quantum bits. Coherence times in the millisecond range have been obtained in diamond nitrogen-vacancy (NV) centres<sup>1</sup>. In this material, a substitutional nitrogen atom combines with an adjacent vacancy to form an  $S=1$  species. However, it is challenging to develop many-qubit systems from these materials. Indeed, for example, decreasing the size of the diamond to the nanoscale (which potentially allows stronger interactions with other qubits) drastically decreases the coherence time of the NV centre<sup>5</sup>.

Molecular species, such as transition metal complexes, are very promising in this respect, because interqubit interactions can be tailored at will<sup>6</sup>. In addition, molecules can be deposited in regular arrays on surfaces, which is a prerequisite for addressing qubits. Molecular surface self-assembly techniques have reached the stage where the size of the ordered array is essentially determined by the size of the atomically flat plateaus of the substrate<sup>7</sup>. Surprisingly little has been published on quantum coherence times in mononuclear and polynuclear transition metal complexes<sup>8,9</sup>. In recent years, especially the quantum coherence in exchange coupled molecular nanomagnets (MNMs) has received much attention<sup>8,10–22</sup>. The often stated advantage of such systems is the presence of additional spin states that can theoretically allow switching of the interqubit coupling<sup>23</sup>. On the other hand, population leakage to these additional spin states is detrimental to qubit performance. Furthermore, their very presence will shorten spin–lattice ( $T_1$ ) relaxation times<sup>24</sup>, limiting the maximum achievable quantum coherence time<sup>25</sup>. Indeed, quantum coherence times of polynuclear MNMs tend to become immeasurably short above 10 K. This disadvantage has led to renewed interest in mononuclear systems, with quantum coherence being reported at temperatures as high as 80 K (ref. 26). It has been shown that in dilute conditions, the (superhyperfine) interaction with nuclear spins that are weakly coupled to the electron spin is the factor that limits the quantum coherence time in MNMs<sup>20,27</sup>. Therefore, we have aimed to remove nuclear spins as much as possible from the immediate surroundings of the metal ion that constitutes the qubit. The main magnetic nuclei in typical organic ligands are hydrogens (<sup>1</sup>H). Carbon (98.9% <sup>12</sup>C), oxygen (99.8% <sup>16</sup>O) and sulfur (99.2% <sup>32,34</sup>S) are virtually nuclear spin free. Nitrogen (<sup>14</sup>N) possesses a nuclear spin, but its magnetic moment is much weaker. Hence we have used a ligand without hydrogen atoms.

Here we report an investigation of quantum coherence in  $(\text{PPh}_4)_2[\text{Cu}(\text{mnt})_2]$  (**1Cu**,  $\text{mnt}^{2-}$  = maleonitriledithiolate or 1,2-dicyanoethylene-1,2-dithiolate) doped into the diamagnetic isostructural host  $(\text{PPh}_4)_2[\text{Ni}(\text{mnt})_2]$  (**1Ni**). In addition, we investigate the derivative with a deuterated  $\text{PPh}_4^+$  counter ion.

We find quantum coherence times of up to 68  $\mu\text{s}$  at low temperatures, which are among the highest reported for molecular coordination compounds. Importantly, quantum coherence in this system persists up to room temperature with coherence times in the (sub)microsecond range. It is noteworthy that metal dithiolates have been investigated intensively, regarding their conductivity properties, and were shown to be semiconductors or possess metallic or—under pressure—even superconducting properties<sup>28,29</sup>, as well as being processable by thin film methods<sup>30,31</sup>.

## Results

**Synthesis and sample preparation.** Compounds **1Cu** and **1Ni** (Fig. 1) were synthesized by published procedures (see Supplementary Figs 1–5 for characterization data)<sup>32</sup>. The deuterated derivatives **1CuD** and **1NiD** in which all hydrogen atoms of the  $\text{PPh}_4^+$  counter ion have been replaced by deuterium were synthesized in the same manner. The salt  $\text{PPh}_4\text{Br-d20}$  was synthesized by literature methods<sup>33</sup>. In concentrated conditions, quantum coherence times are limited by intermolecular interactions between electron spins. Hence, to investigate quantum coherence in **1Cu**, we prepared powder samples of nominally 0.001 mol percent of **1Cu** in diamagnetic **1Ni** and 0.01% of **1CuD** in **1NiD**. These samples (**1Cu**<sub>0.001%</sub> and **1Cu**<sub>0.01%D</sub>) were investigated by means of pulsed Q-band electron paramagnetic resonance (EPR) spectroscopy ( $\nu = 34\text{--}35$  GHz). Preliminary measurements showed that at this doping level, electron–electron interactions play no role in the spin dynamics.

**Electron spin echo-detected EPR spectra.** Figure 2 shows the electron spin echo (ESE)-detected EPR spectra, recorded by means of the standard Hahn echo sequence with fixed interpulse distances while sweeping the magnetic field (Supplementary Fig. 6). In the low field half of the spectra, four clear widely spaced steps, and in the high-field half four more narrowly spaced peaks can be observed. This spectral shape is common for mononuclear copper(II) complexes and is the result of anisotropic hyperfine coupling of the electron spin to the  $I=3/2$  copper nuclear spin, in combination with an axial  $g$ -tensor. Spectral fits (Fig. 2) yielded  $g_{\parallel} = 2.0925 \pm 0.0005$ ,  $g_{\perp} = 2.0227 \pm 0.0005$ ,  $A_{\parallel} = 500 \pm 5$  MHz,  $A_{\perp} = 118 \pm 5$  MHz. These parameters are quite usual for

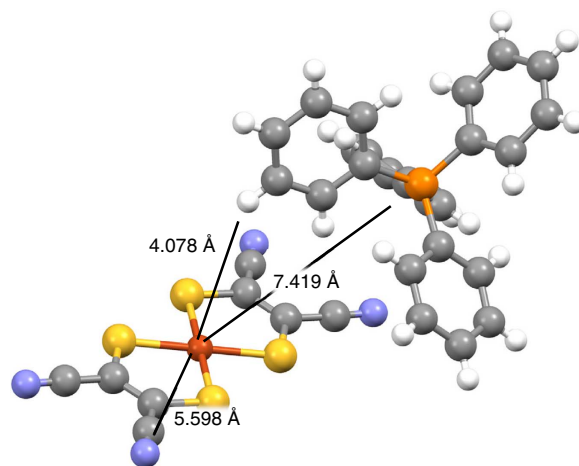


**Figure 1 | Structure of 1Cu.** Distances between the metal ion and the nearest nuclei with nonzero spins are indicated in Å. Colours: copper-brown, sulfur-yellow, carbon-grey, nitrogen-blue, phosphorus-orange and hydrogen-white.

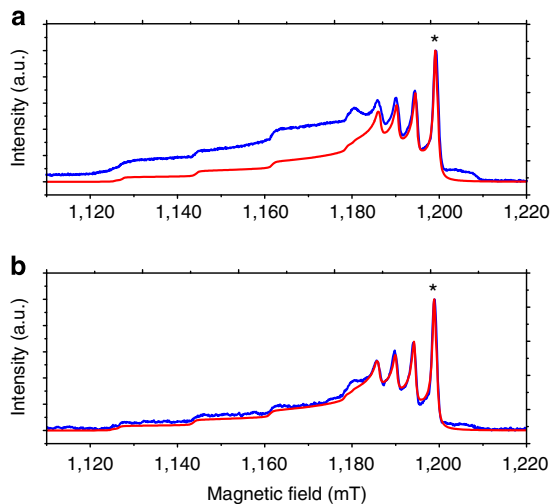


**Figure 2 | ESE-detected Q-band EPR spectra of compound  $1\text{Cu}_{0.001\%}$ .** Experimental results for EPR spectra (blue) recorded at  $T = 7\text{ K}$  (**a**) and  $T = 120\text{ K}$  (**b**), and simulation (red) using parameters given in the text.

copper(II) complexes and very comparable to those reported for  $(\text{NBu}_4)_2[\text{Cu}(\text{iso-mnt})_2]$  ( $\text{iso-mnt}^{2-} = \text{iso-maleonitriledithiolate}$  or  $1,1\text{-dicyanoethylene-2,2-dithiolate}$ )<sup>34</sup>. The discrepancy between experiment and fit for the  $7\text{ K}$  spectrum is not clear to us. It disappears at a temperature of ca.  $120\text{ K}$ .

**Investigation of quantum coherence.** The fact that a spin echo is observed at all immediately confirms that quantum coherence is observed in  $1\text{Cu}_{0.001\%}$ , even at temperatures as high as  $120\text{ K}$ . Hence, we have studied in detail the quantum coherence of  $1\text{Cu}_{0.001\%}$  in the temperature range  $7\text{--}300\text{ K}$  (Fig. 3 and Supplementary Fig. 7), where again we used the Hahn echo sequence, varying the interpulse distance  $\tau$ . The measurements were performed at the fixed field position given by the asterisk \* in Fig. 2, which corresponds to the transition  $|m_s, m_I\rangle = |-1/2, +3/2\rangle$  to  $|+1/2, +3/2\rangle$  in the  $g_{\perp}$  region. All data could be fitted to stretched exponential decay functions (equation (1)), as is quite common for transition metal systems<sup>9</sup>:

$$I(2\tau) = I(0) \exp\left[-\left(\frac{2\tau}{T_M}\right)^x\right] \quad (1)$$

where  $I$  is the integrated echo intensity,  $2\tau$  is the delay between initial pulse and echo and  $x$  is the stretch factor. The factor  $x$  ranges between 2 and 3 when the decoherence is dominated by flip-flop processes between nuclear spins (spin diffusion), and is close to 1 when decoherence is dominated by physical motion of the magnetic nuclei<sup>9</sup>. In the latter case the semi-logarithmic plot of  $I$  versus  $2\tau$  will be a straight line. Figure 3 demonstrates that this is the case for the coherence time measurements at higher temperatures ( $T > 150\text{ K}$ ). At lower temperatures,  $x$  increases and reaches values of almost 2.5 at the lowest investigated temperatures (Fig. 4 and Supplementary Table 1). The coherence time at the lowest measurement temperature ( $T = 7\text{ K}$ ) is  $9.23 \pm 0.01\ \mu\text{s}$ . This is among the very longest decoherence times ever reported for coordination complexes, and 3.5 times longer than observed for  $\text{CuPc}$ <sup>26</sup>. To our knowledge, only one paper reports on coherence times that are several times longer, namely for  $\text{Cr}^{\text{VO}}(\text{HCA})^-$  and vanadyl ion, both in deuterated  $\text{H}_2\text{O}/\text{glycerol}$  solution<sup>35</sup>. For exchange coupled, polynuclear species, again only one report of a longer coherence time can be found, namely for  $\text{Cs}[\text{Cr}_7\text{NiF}_8(\text{Piv-d}_9)_{16}]$ ,  $T_M = 15\ \mu\text{s}$ , albeit at the much lower temperature of  $1.5\text{ K}$  (ref. 10). The coherence time of  $1\text{Cu}_{0.001\%}$  is largely temperature

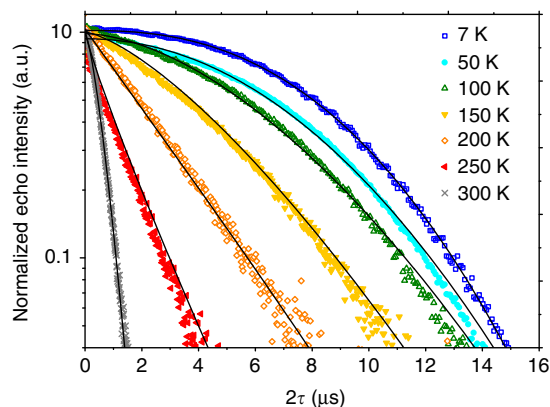


**Figure 3 | Hahn echo decay curves at different temperatures for compound  $1\text{Cu}_{0.001\%}$ .** Integrated echo intensity normalized to the echo intensity immediately after the spectrometer deadtime as a function of delay between initial pulse and echo, at various temperatures as indicated. Solid lines are fits using equation (1), see text.

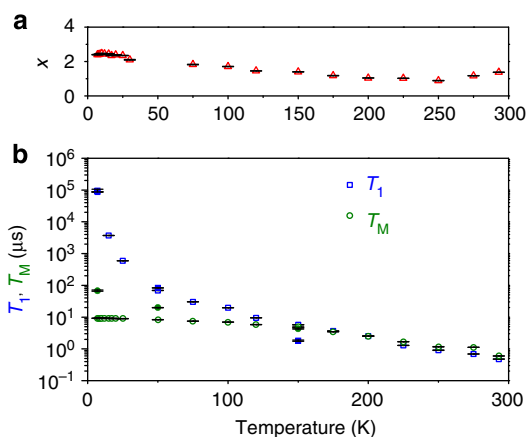


**Figure 4 | Temperature dependence of electron spin relaxation times.** (**a**) Stretch factor  $x$  as a function of temperature ( $1\text{Cu}_{0.001\%}$  only). (**b**) Spin-lattice relaxation ( $T_1$ ) and phase memory time ( $T_M$ ) as a function of temperature. Open symbols belong to  $1\text{Cu}_{0.001\%}$ , filled symbols belong to  $1\text{Cu}_{0.01\%}$ . Error bars in all panels correspond to the s.d. of the fits.

independent up to the very high temperature of  $\sim 100\text{ K}$ , beyond which it decreases slowly (Fig. 4 and Supplementary Table 1). Astonishingly, even at room temperature, a respectable coherence time of  $600 \pm 2\text{ ns}$  was found. From values reported in literature, only vanadyl tetratolylporphyrin comes close<sup>36</sup>.

Our results compare very favourably with those reported for other copper(II) dithiolates, for example,  $2\% \text{Cu}^{2+}$  in  $(\text{NBu}_4)_2[\text{Ni}(\text{i-mnt})_2]$  with  $T_M = 0.5\ \mu\text{s}$  (ref. 37) and a  $N,N'$ -dimethylformamide frozen solution of  $[\text{Cu}(\text{dmit})_2]^{2-}$  ( $\text{dmit} = 1,3\text{-dithiole-2-thione-4,5-dithiolate}$ ) with  $T_M = 0.52\ \mu\text{s}$  (ref. 38) both at low temperatures ( $T < 25\text{ K}$ ). Even in the rather concentrated sample  $1\text{Cu}1.5\%$ , a coherence time of  $3.97 \pm 0.05\ \mu\text{s}$  was found at  $7\text{ K}$  (Supplementary Fig. 8). Hence,  $1\text{Cu}$  clearly outperforms these other copper complexes also in concentrated conditions. This fact shows the importance of small structural details in the design and development of molecular qubits. Hence,  $1\text{Cu}_{0.001\%}$  could function as a quantum bit, even at room temperature. To prove that we can perform (simple) coherent spin manipulations, we have carried out nutation measurements at different microwave powers, where Rabi-like oscillations of the echo intensity are clearly observed (Supplementary Fig. 9).

**Decoherence mechanisms.** Our earlier investigations on  $[\text{Fe}_4(\text{acac})_6(\text{Br-mp})_2]$  (acacH is acetyl acetone and Br-mpH<sub>3</sub> is 2-(bromomethyl)-2-(hydroxymethyl)-1,3-propanediol) revealed a strong correlation between the spin–lattice relaxation time  $T_1$  and the coherence time  $T_M^{22}$ . Therefore, we determined  $T_1$  and its temperature dependence by means of the inversion recovery sequence. The results (Fig. 4 and Supplementary Fig. 10) demonstrate that at high temperatures ( $T > 120$  K),  $T_1$  and  $T_M$  are indeed essentially the same, suggesting that the latter is determined by the former. In addition, there may be a contribution from nuclear spin motions, for example, librational motions of the phenyl rings of the tetraphenylphosphonium counter ion or of phenyl ring flips<sup>9</sup>. Towards lower temperatures,  $T_1$  increases markedly and reaches  $T_1 = 87.4 \pm 0.2$  ms at 7 K. Such  $T_1$  times are long, but not unprecedented<sup>9</sup>. The fact that such a wide range of essential temperature independence of  $T_M$  is found for **1Cu**<sub>0.001%</sub> is owing to the fact that  $T_1$  is extremely long at low temperatures.  $T_1$  decreases slowly with increasing temperature and only reaches values comparable to  $T_M$  (10  $\mu$ s) above 100 K. We attribute the long  $T_1$  to a relatively rigid lattice, as well as the square planar coordination geometry, which is predicted to give rise to longer  $T_1$  times than a tetrahedral geometry<sup>39</sup>. This then suggests that a design criterion for high-temperature molecular qubits is the engineering of a long  $T_1$ .

In contrast, at low temperatures, decoherence is dominated by the interaction with nuclear spins. Considering the distances from the crystal structure, the strongest (dipolar) hyperfine coupling is expected to one of the phenyl protons, with  $A_{\text{dip},\parallel} = 2.5$  MHz. The <sup>14</sup>N atom of the dithiolate ligand is much more weakly coupled at  $A_{\text{dip},\parallel} = 0.10$  MHz. Accordingly, we have prepared the derivative of **1Cu** with a deuterated PPh<sub>4</sub><sup>+</sup>-d<sub>20</sub> counter ion. Pulsed Q-band measurements (on a different, less sensitive pulsed Q-band EPR spectrometer; Fig. 4, Supplementary Fig. 11 and Supplementary Table 3) on the sample **1Cu**<sub>0.01%</sub>**D** show an identical quantum coherence time at 150 K (to **1Cu**<sub>0.001%</sub>), proving that the results are robust and independent of the used spectrometer. Also, the results are independent of concentration in this range, given that the nominal concentration of the deuterated sample is 10 times higher. Finally, the quantum coherence time is indeed determined by  $T_1$  at this temperature. The  $T_1$  time is slightly shorter, which we attribute to the poor signal to noise at this relatively high temperature. Towards lower temperatures,  $T_M$  strongly increases, reaching a value of  $68 \pm 3$   $\mu$ s at 7 K. At lowest temperatures, the decay is biexponential. We attribute the shorter component  $T_M = 4.6 \pm 0.3$   $\mu$ s to those molecules that possess some electron spin–spin interaction with other molecules, which will statistically occur in a randomly diluted system. The  $T_M$  value for the slow component is comparable to the abovementioned Cr<sup>VO</sup>(HCA)<sup>−</sup> and vanadyl ion in solution. The advantage of **1Cu** over these systems are that not only does it have a long coherence time at low temperatures but it also has a quantum coherence time of 1  $\mu$ s at room temperature (on contrast to Cr<sup>VO</sup>(HCA)<sup>−</sup> and vanadyl ion in solution). Second, it is well defined (in contrast to vanadyl ion in solution) and non-toxic (in contrast to carcinogenic chromium(V))<sup>40,41</sup>, important for use in devices. Finally **1Cu** belongs to a semiconducting class of compounds (also important for addressing). Taking the ratio of  $T_M$  and the  $\pi/2$  pulse length, we arrive at a single qubit figure of merit  $Q_M \approx 3,400$ .

## Discussion

We have demonstrated extremely long coherence times both at low ( $\sim 68$   $\mu$ s) and high temperatures ( $\sim 1$   $\mu$ s) in **1Cu** and **1CuD**. This was achieved by removal of weakly coupled nuclear spins

and the rigid lattice of the compound. Hence, we have now overcome the first hurdle for the exploitation of molecular compounds as quantum bits in quantum information processing applications. Clearly, there is still scope for improvement by further removing any nuclear spins from the material. In addition, a great deal of work remains to be done on the detailed understanding of the mechanisms behind  $T_1$  and  $T_M$ , including investigating the frequency and orientation dependences of the relaxation times, as well as the study of hyperfine couplings by means of ENDOR. Finally, optimization of the dithiolate ligand as well as studies on the corresponding vanadyl complexes can be envisioned. All these investigations are now underway. Clearly, material optimization is only the first step on the road to developing a functional quantum computer. We believe that following steps will include tailoring of interqubit interactions<sup>6</sup>, incorporation of photoswitchable linkers to modulate qubit entanglement<sup>42</sup>, surface deposition<sup>26</sup> and implementation of local control, for example, by means of diamond NV centres<sup>43</sup>.

## Methods

**Synthesis and sample preparation.** The compounds **1Cu** and **1Ni** were prepared according to a literature procedure, and were characterized by infrared, ultraviolet/visible, elemental analysis, SQUID magnetometry and X-ray crystallography (Supplementary Information)<sup>32</sup>. Deuterated tetraphenylphosphoniumbromide was synthesized in a pressure cylinder with deuterated starting material according to a literature procedure<sup>33</sup>. The doped powder **1Cu**<sub>0.001%</sub> was prepared by rapid evaporation of an acetone solution of **1Cu** and **1Ni** in the correct molar ratio. Samples of **1Cu**<sub>0.001%</sub> were finely ground, placed into EPR quartz tubes and evacuated overnight. **1Cu**<sub>0.01%</sub>**D** was prepared analogously. The tubes were closed with stop cocks (X-band) or by flame-sealing (Q-band).

**EPR measurements.** CW X-Band EPR spectra were recorded on a Bruker EMX spectrometer ( $\nu = 9.47$  GHz, Stuttgart). Pulsed EPR measurements were performed with a Bruker Elexsys E580 at Q-band ( $\nu = 34$  GHz, Frankfurt, **1Cu**<sub>0.001%</sub>) and a home-built<sup>44</sup> pulsed Q-band spectrometer ( $\nu = 35$  GHz, Stuttgart, **1Cu**<sub>0.01%</sub>**D** and **1Cu**<sub>1.5%</sub>). Temperatures between 7 and 275 K were obtained with an Oxford Instruments CF935 continuous flow helium cryostat, room temperature measurements were done at  $\sim 294$  K without external temperature regulation. Typical pulse lengths were 16 ns ( $\pi/2$ ) and 32 ns ( $\pi$ ) (Frankfurt) and 20 ns ( $\pi/2$ ) and 40 ns ( $\pi$ ) (Stuttgart). For ESE-detected EPR spectra, the Hahn Echo pulse sequence ( $\pi/2 - \tau - \pi - \tau - \text{echo}$ ) with fixed delay times of  $\tau = 140$  and 160 ns at 7 and 120 K, respectively, were applied under sweeping the magnetic field. Phase memory times were measured also with Hahn echo sequence, here at a fixed magnetic field under variation of the delay time  $\tau$ . For measuring spin–lattice-relaxation times, the inversion recovery sequence ( $\pi - T - \pi/2 - \tau_{\text{fix}} - \pi - \tau_{\text{fix}} - \text{echo}$ ) with  $\tau_{\text{fix}} = 140$  ns and phase cycling was applied. Nutation measurements were performed with a nutation pulse of variable length followed by a Hahn echo sequence (nutation pulse– $\tau_{\text{nut}} - \pi/2 - \tau_{\text{fix}} - \pi - \tau_{\text{fix}} - \text{echo}$ ) with  $\tau_{\text{nut}} = 400$  ns,  $\tau_{\text{fix}} = 140$  ns and different pulse powers.

**Data analysis and simulation.** ESE-detected spectra were simulated with Easy-Spin<sup>45</sup>. Errors of fit parameters ( $g$  and hyperfine values) were estimated by eye.  $T_M$  relaxation data were normalized to the first measurement point and fitted with Origin, indicated deviations correspond to the standard errors. Phase memory times ( $T_M$ ) were extracted from fitting (stretched) exponentials, equation (1), to the Hahn echo decay curves. Experimental data of inversion recovery were fitted with a biexponential function for 7–25 K (fast and slow components) and for higher temperatures mono-exponential fits were applied.

## References

- Balasubramanian, G. *et al.* Ultralong spin coherence time in isotopically engineered diamond. *Nat. Mater.* **8**, 383–387 (2009).
- Morton, J. J. L. *et al.* Electron spin relaxation of N@C60 in CS<sub>2</sub>. *J. Chem. Phys.* **124**, 014508 (2006).
- Tyryshkin, A., Lyon, S., Astashkin, A. & Raitsimring, A. Electron spin relaxation times of phosphorus donors in silicon. *Phys. Rev. B* **68**, 193207 (2003).
- Morley, G. W. *et al.* The initialization and manipulation of quantum information stored in silicon by bismuth dopants. *Nat. Mater.* **9**, 725–729 (2010).
- Knowles, H. S., Kara, D. M. & Atatüre, M. Observing bulk diamond spin coherence in high-purity nanodiamonds. *Nat. Mater.* **13**, 21–25 (2014).
- Timco, G. A. *et al.* Engineering the coupling between molecular spin qubits by coordination chemistry. *Nat. Nanotechnol.* **4**, 173–178 (2009).

7. Barth, J. V. Molecular architectonic on metal surfaces. *Ann. Rev. Phys. Chem.* **58**, 375–407 (2007).
8. van Slageren, J. New directions in electron paramagnetic resonance spectroscopy on molecular nanomagnets. *Top. Curr. Chem.* **321**, 199–234 (2012).
9. Eaton, S. S. & Eaton, G. R. Relaxation times of organic radicals and transition metal ions. *Biol. Magn. Reson.* **19**, 29–154 (2000).
10. Wedge, C. J. et al. Chemical engineering of molecular qubits. *Phys. Rev. Lett.* **108**, 107204 (2012).
11. Choi, K. Y. et al. Coherent manipulation of electron spins in the Cu<sub>3</sub> spin triangle complex impregnated in nanoporous silicon. *Phys. Rev. Lett.* **108**, 067206 (2012).
12. Lutz, P., Marx, R., Dengler, D., Kromer, A. & van Slageren, J. Quantum coherence in a triangular Cu<sub>3</sub> complex. *Mol. Phys.* **111**, 2897–2902 (2013).
13. Yang, J. et al. Observing quantum oscillation of ground states in single molecular magnet. *Phys. Rev. Lett.* **108**, 230501 (2012).
14. Zaripov, R. et al. Boosting the electron spin coherence in binuclear Mn complexes by multiple microwave pulses. *Phys. Rev. B* **88**, 094418 (2013).
15. Moro, F. et al. Coherent electron spin manipulation in a dilute oriented ensemble of molecular nanomagnets: pulsed EPR on doped single crystals. *Chem. Commun.* **50**, 91–93 (2014).
16. Takahashi, S. et al. Coherent manipulation and decoherence of S = 10 single-molecule magnets. *Phys. Rev. Lett.* **102**, 087603 (2009).
17. Takahashi, S. et al. Decoherence in crystals of quantum molecular magnets. *Nature* **476**, 76–79 (2011).
18. Bertaina, S. et al. Quantum oscillations in a molecular magnet. *Nature* **453**, 203 (2008).
19. Shim, J. H. et al. Decoherence window and electron-nuclear cross relaxation in the molecular magnet V<sub>15</sub>. *Phys. Rev. Lett.* **109**, 050401 (2012).
20. Ardavan, A. et al. Will spin-relaxation times in molecular magnets permit quantum information processing? *Phys. Rev. Lett.* **98**, 057201 (2007).
21. Mitrikas, G., Sanakis, Y., Raptopoulou, C. P., Kordas, G. & Papavassiliou, G. Electron spin–lattice and spin–spin relaxation study of a trinuclear iron(III) complex and its relevance in quantum computing. *Phys. Chem. Chem. Phys.* **10**, 743 (2008).
22. Schlegel, C., van Slageren, J., Manoli, M., Brechin, E. K. & Dressel, M. Direct observation of quantum coherence in single-molecule magnets. *Phys. Rev. Lett.* **101**, 147203 (2008).
23. Troiani, F. & Affronte, M. Molecular spins for quantum information technologies. *Chem. Soc. Rev.* **40**, 3119–3129 (2011).
24. Bencini, A. & Gatteschi, D. *EPR of Exchange Coupled Systems* (Springer-Verlag, 1990).
25. Schweiger, A. & Jeschke, G. *Principles of Pulse Electron Paramagnetic Resonance* (Oxford Univ. Press, 2001).
26. Warner, M. et al. Potential for spin-based information processing in a thin-film molecular semiconductor. *Nature* **503**, 504–508 (2013).
27. Schlegel, C., van Slageren, J., Timco, G., Winpenny, R. E. P. & Dressel, M. Origin of superhyperfine interactions in the antiferromagnetic ring Cr<sub>7</sub>Ni. *Phys. Rev. B* **83**, 134407 (2011).
28. Cassoux, P., Valade, L., Kobayashi, H., Clark, R. A. & Underhill, A. E. Molecular metals and superconductors derived from metal complexes of 1,3-dithiol-2-thione-4,5-dithiolate(dmit). *Coord. Chem. Rev.* **110**, 115–160 (1991).
29. Coropceanu, V. et al. Charge transport in organic semiconductors. *Chem. Rev.* **107**, 926–952 (2007).
30. Dalgleish, S., Awaga, K. & Robertson, N. Formation of stable neutral copper bis-dithiolene thin films by potentiostatic electrodeposition. *Chem. Commun.* **47**, 7089–7091 (2011).
31. Dalgleish, S., Yoshikawa, H., Matsushita, M. M., Awaga, K. & Robertson, N. Electrodeposition as a superior route to a thin film molecular semiconductor. *Chem. Sci.* **2**, 316–320 (2011).
32. Lewis, G. R. & Dance, I. Crystal supramolecular motifs for [Ph<sub>4</sub>P]<sup>+</sup> salts of [M(mnt)<sub>2</sub>]<sup>2-</sup>, [M(mnt)<sub>2</sub>]<sup>-</sup>, [M(mnt)<sub>2</sub>]<sub>2</sub><sup>2-</sup>, [M(mnt)<sub>3</sub>]<sup>3-</sup> and [M(mnt)<sub>3</sub>]<sup>2-</sup> (mnt<sup>2-</sup> = maleonitriledithiolate). *J. Chem. Soc. Dalton Trans.* 3176–3185 (2000).
33. Horner, L., Mummertney, G., Moser, H. & Beck, P. Phosphororganische Verbindungen. 51. Die Einführung von Arylresten in Tertiäre Phosphine mit Hilfe von Komplexen der Übergangsmetalle (Komplexsalzmethode). *Chem. Ber.* **99**, 2782–2788 (1966).
34. Taylor, P. F. & Vaughan, R. A. Electron spin resonance and relaxation studies of some organic copper salts. *J. Phys. C Solid State Phys.* **3**, 579 (1970).
35. Eaton, G. R. & Eaton, S. S. Solvent and temperature dependence of spin echo dephasing for chromium(V) and vanadyl complexes in glassy solution. *J. Magn. Reson.* **136**, 63–68 (1999).
36. Du, J. L., Eaton, G. R. & Eaton, S. S. Effect of molecular motion on electron spin phase memory times for copper(II) complexes in doped solids. *Appl. Magn. Reson.* **6**, 373–378 (1994).
37. Kirmse, R., Solovev, B. V. & Tarasov, B. G. Elektronen-Spin-Gitter- und Spin-Spin-Relaxation von Cu(II) in Ni(II)-bis(1,1-dicyanoäthylen-2,2-dithiolat)-Einkristallen. *Ann. Phys.* **486**, 352–360 (1974).
38. Hoffmann, S. K., Goslar, J., Lijewski, S. & Zalewska, A. EPR and ESE of Cu<sub>4</sub> complex in Cu(dmit)<sub>2</sub>: g-Factor and hyperfine splitting correlation in tetrahedral Cu–sulfur complexes. *J. Magn. Reson.* **236**, 7–14 (2013).
39. Fielding, A. J. et al. Electron spin relaxation of copper(II) complexes in glassy solution between 10 and 120 K. *J. Magn. Reson.* **179**, 92–104 (2006).
40. Chiu, A. et al. Review of chromium (VI) apoptosis, cell-cycle-arrest, and carcinogenesis. *J. Environ. Sci. Health. C* **28**, 188–230 (2010).
41. Shi, X. L. et al. Cr(IV) causes activation of nuclear transcription factor-kappa B, DNA strand breaks and dG hydroxylation via free radical reactions. *J. Inorg. Biochem.* **75**, 37–44 (1999).
42. Teki, Y., Miyamoto, S., Nakatsuji, M. & Miura, Y. pi-Topology and spin alignment utilizing the excited molecular field: Observation of the excited high-spin quartet (S = 3/2) and quintet (S = 2) states on purely organic pi-conjugated spin systems. *J. Am. Chem. Soc.* **123**, 294–305 (2001).
43. Dolde, F. et al. High-fidelity spin entanglement using optimal control. *Nat. Commun.* **5**, 3371 (2014).
44. Tkach, I. et al. A homebuilt ESE spectrometer on the basis of a high-power Q-band microwave bridge. *Appl. Magn. Reson.* **35**, 95–112 (2008).
45. Stoll, S. & Schweiger, A. EasySpin, a comprehensive software package for spectral simulation and analysis in EPR. *J. Magn. Reson.* **178**, 42–55 (2006).

## Acknowledgements

We thank Dr Wolfgang Frey (Institut für Organische Chemie, Universität Stuttgart) for crystallographic measurements, Professor Martin Dressel (1. Physikalisches Institut, Universität Stuttgart) for access to the SQUID magnetometer and the Deutsche Forschungsgemeinschaft, the Fonds der chemischen Industrie, the Center for Integrated Quantum Science and Technology IQ<sup>ST</sup>, the Alexander von Humboldt-Foundation (S.-D.J.) and the Center for Biomolecular Magnetic Resonance at the Goethe University Frankfurt for funding.

## Author contributions

K.B. synthesized all compounds, prepared all samples, coordinated and participated in all pulsed EPR experiments on **1Cu<sub>0.001%</sub>**, carried out all pulsed EPR measurements on **1Cu<sub>1.5%</sub>**, **1Cu<sub>0.01%</sub>D** and analysed the data. D.D. participated in pulsed EPR experiments. S.L. participated in the syntheses of **1** and **2** and EPR measurements. B.E. performed the pulsed EPR experiments on **1Cu<sub>0.001%</sub>**. S.-D.J. carried out all magnetic measurements. P.N. coordinated and participated in pulsed EPR experiments. J.v.S. designed and supervised the work and wrote the manuscript with contributions from all authors.

## Additional information

**Supplementary Information** accompanies this paper at <http://www.nature.com/naturecommunications>

**Competing financial interests:** The authors declare no competing financial interests.

**Reprints and permission** information is available online at <http://npg.nature.com/reprintsandpermissions/>

**How to cite this article:** Bader, K. et al. Room temperature quantum coherence in a potential molecular qubit. *Nat. Commun.* 5:5304 doi: 10.1038/ncomms6304 (2014).

**COMMENTED PAPER 3**

**P. Neugebauer, M. Orlita, C. Faugeras, A.-L. Barra and M.Potemski**  
How perfect can graphene be?

*Phys. Rev. Lett.*, 103, 136403 (2009).



## How Perfect Can Graphene Be?

P. Neugebauer,<sup>1</sup> M. Orlita,<sup>1,2,3,\*</sup> C. Faugeras,<sup>1</sup> A.-L. Barra,<sup>1</sup> and M. Potemski<sup>1</sup>

<sup>1</sup>*Grenoble High Magnetic Field Laboratory, CNRS, BP 166, F-38042 Grenoble Cedex 09, France*

<sup>2</sup>*Institute of Physics, Charles University, Ke Karlovu 5, CZ-121 16 Praha 2, Czech Republic*

<sup>3</sup>*Institute of Physics, ASCR, Cukrovarnická 10, CZ-162 53 Praha 6, Czech Republic*

(Received 27 May 2009; published 25 September 2009; publisher error corrected 29 September 2009)

We have identified the cyclotron resonance response of the purest graphene ever investigated, which can be found in nature on the surface of bulk graphite, in the form of decoupled layers from the substrate material. Probing such flakes with Landau level spectroscopy in the THz range at very low magnetic fields, we demonstrate a superior electronic quality of these ultralow density layers ( $n_0 \approx 3 \times 10^9 \text{ cm}^{-2}$ ) expressed by the carrier mobility in excess of  $10^7 \text{ cm}^2/(\text{V} \cdot \text{s})$  or scattering time of  $\tau \approx 20 \text{ ps}$ . These parameters set new and surprisingly high limits for intrinsic properties of graphene and represent an important challenge for further developments of current graphene technologies.

DOI: [10.1103/PhysRevLett.103.136403](https://doi.org/10.1103/PhysRevLett.103.136403)

PACS numbers: 71.70.Di, 76.40.+b, 81.05.Uw

The fabrication of graphene structures has triggered a vast research effort focused on the properties of two-dimensional systems with massless Dirac fermions. Nevertheless, further progress in exploring this quantum electrodynamics system in solid-state laboratories seems to be limited by the insufficient electronic quality of man-made structures, and the crucial question arises as to whether existing technologies have reached their limit or major advances are in principle possible. The substrate, and more generally any surrounding medium, has been recently identified as a dominant source of extrinsic scattering mechanisms, which effectively degrade the electronic quality of currently available graphene samples [1,2]. Despite significant advances in technology, including the fabrication of suspended specimens [3,4], the realistic limits of the scattering time and mobility in graphene, achievable after elimination of major extrinsic scattering sources, remain an open issue. Experiments call for higher quality samples, which are almost certainly crucial for possible verification of interesting predictions concerning basic phenomena of quantum electrodynamics (e.g., Zitterbewegung) or observation of the effects of interactions between Dirac fermions, (resulting, e.g., in the appearance of the fractional quantum Hall effect). Even more simple effects such as lifting the degeneracy of the spin and/or pseudospin degree of freedom in very high magnetic fields indicate the strong influence of the sample quality on the information that can be deduced from experiments [5,6].

Recently, well-defined graphene flakes have been discovered in the form of sheets, decoupled from, but still located on the surface of bulk graphite which naturally serves as a well-matched substrate for graphene [7]. In this Letter, we report on response from these flakes in microwave magneto-absorption experiments and show that their Dirac-like electronic states are quantized into Landau levels (LLs) in magnetic fields down to 1 mT and at elevated

temperatures up to 50 K. The deduced unprecedented quality of the studied electronic system sets surprisingly high limits for the intrinsic scattering time and the corresponding carrier mobility in graphene.

The cyclotron resonance (CR) has been measured in a high-frequency EPR setup in double-pass transmission configuration, using the magnetic-field-modulation technique. A flake of natural graphite was placed in the variable temperature insert of the superconducting solenoid and via quasioptics exposed to the linearly polarized microwave radiation emitted by a Gun diode at frequencies 283.2 or 345 GHz (1.171 or 1.427 meV). The absorbed radiation has been followed by either heterodyne detection (283.2 GHz) or by the bolometer (345 GHz). To enhance the relatively weak response of graphene flakes, the modulation amplitude ( $\Delta B \sim 0.5 \text{ mT}$ ) had to be chosen close to the CR width, which broadens resonances observed at lower fields. All spectra have been corrected for the remanent field of the magnet.

Our main experimental finding is illustrated in Fig. 1. The traces in this figure represent the magneto-absorption response of the natural graphite specimen at different temperatures, measured as a function of the magnetic field at fixed microwave frequency. They correspond to the derivative of the absorption strength with respect to the magnetic field since the field modulation technique has been applied. Strong at 7.5 K, but rapidly vanishing with temperature lines marked with numbered arrows in Fig. 1 can be easily recognized as CR harmonics of  $K$  point electrons in bulk graphite. A possible origin of the temperature dependent transition marked with the star will be discussed later on. The features of primary interest, which we argue are due to decoupled graphene sheets on the graphite surface, are seen at very low fields, within the yellow highlighted area of Fig. 1.

The interpretation of these low-field data is schematically illustrated in Fig. 2. The observed spectral lines

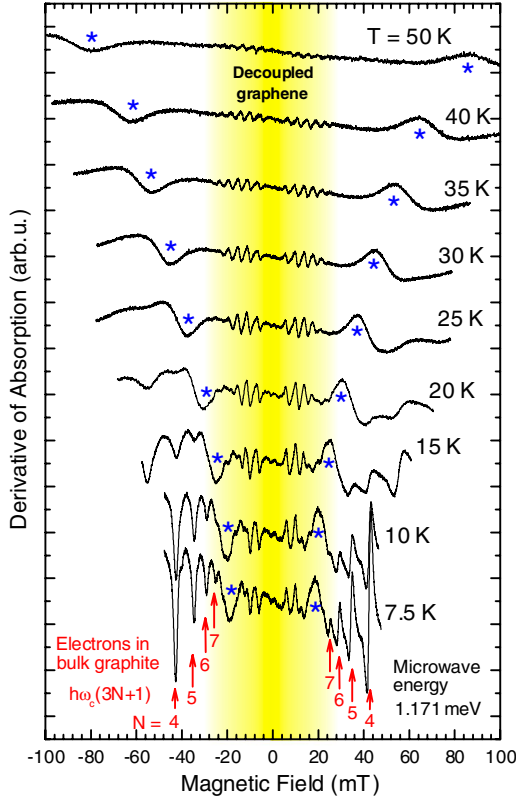


FIG. 1 (color online). Magneto-absorption spectra (detected with field modulation technique) of natural graphite specimen taken in the temperature interval 7.5–50 K at fixed microwave energy  $\hbar\omega = 1.171$  meV. The response of low electron concentration graphene layers decoupled from bulk graphite is seen within the yellow highlighted area. High CR harmonics of  $K$  point electrons in bulk graphite [21], with basic CR frequency  $\omega_c$  corresponding to the effective mass  $m = 0.054m_0$  [20] are shown by numbered arrows. The origin of features denoted by stars is discussed in the text.

[Fig. 2(a)] are assigned to cyclotron resonance transitions between adjacent LLs ( $|\Delta n| = 1$ ) with energies:  $E_n = \text{sign}(n)\tilde{c}\sqrt{2e\hbar B|n|} = \text{sign}(n)E_1\sqrt{|n|}$  [8,9], characteristic of massless Dirac fermions in graphene sheets with an effective Fermi velocity  $\tilde{c}$ . This velocity is the only adjustable parameter required to match the energies of the observed and calculated CR transitions. A best match is found for  $\tilde{c} = (1.00 \pm 0.02) \times 10^6 \text{ m} \cdot \text{s}^{-1}$  in fair agreement with values found in multilayer epitaxial graphene [10,11] or exfoliated graphene on Si/SiO<sub>2</sub> substrate [12–14]. As can be seen from Figs. 2(b) and 2(c), the multimode character of the measured spectra is directly related to thermal distribution of carriers among different LLs. The intensity of a given transition is proportional to the difference in thermal occupation of the involved LLs. Roughly speaking, the strongest transitions imply LLs in the vicinity of the Fermi level, which fixes  $E_F$  at around 6–7 meV from the Dirac point.

To reproduce the experimental data, we assume the absorption strength is proportional to the longitudinal con-

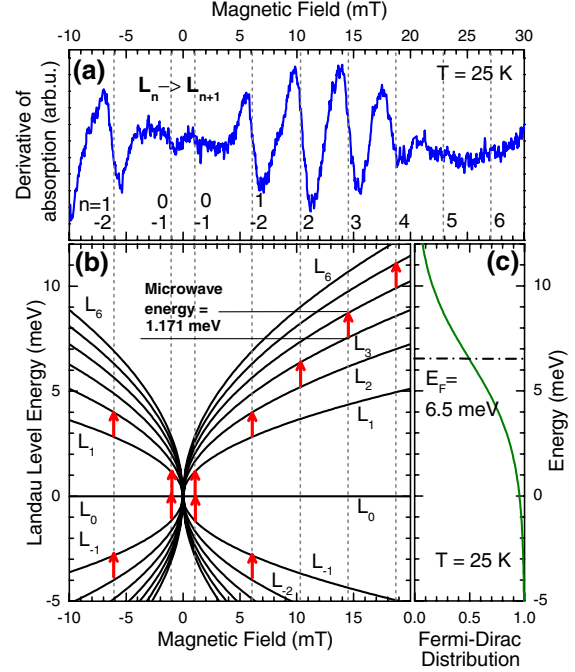


FIG. 2 (color online). Magneto-absorption spectrum (after removing a weak linear background seen in the raw data of Fig. 1) measured at  $T = 25$  K and microwave frequency  $\hbar\omega = 1.171$  meV (a) in comparison with the LL fan chart (b), where the observed cyclotron resonance (CR) transitions are shown by arrows. The occupation of individual LLs is given by the Fermi-Dirac distribution plotted in the part (c). For simplicity, we considered only  $n$ -type doping with  $E_F = 6.5$  meV. The dashed lines show positions of resonances assuming  $\tilde{c} = 1.00 \times 10^6 \text{ m} \cdot \text{s}^{-1}$ .

ductivity of the system:

$$\sigma_{xx}(\omega, B) \propto (B/\omega) \sum_{m,n} M_{m,n} \frac{f_n - f_m}{E_m - E_n - (\hbar\omega + i\gamma)},$$

where  $f_n$  is the occupation of the  $n$ -th LL, and  $M_{m,n} = \alpha \delta_{|m|,|n|\pm 1}$  with  $\alpha = 2$  for  $n$  or  $m$  equal to 0, otherwise  $\alpha = 1$  [10,15]. The calculated traces in Fig. 3 have been drawn taking  $\gamma = 35 \mu\text{eV}$  for the line broadening,  $\tilde{c} = 1.00 \times 10^6 \text{ m} \cdot \text{s}^{-1}$  and  $E_F = 6.5$  meV. To directly simulate the measured traces, the derivative of the absorption with respect to the magnetic field has been calculated taking account of the field modulation  $\Delta B = 0.5$  mT used in the experiment. In spite of its simplicity, our model is more than in a qualitative agreement with our experimental data, see Fig. 3. The calculation fairly well reproduces the experimental trends: the multimode character of the spectra, the intensity distribution among the lines, as well as its evolution with temperature; and it allows us to estimate the characteristic broadening of the CR transitions.

Our modeling could be further improved but at the expense of additional complexity which we want to avoid here. Assuming magnetic-field and/or LL index dependence of the broadening parameter  $\gamma$  and taking into account the possible fluctuation of the Fermi level within

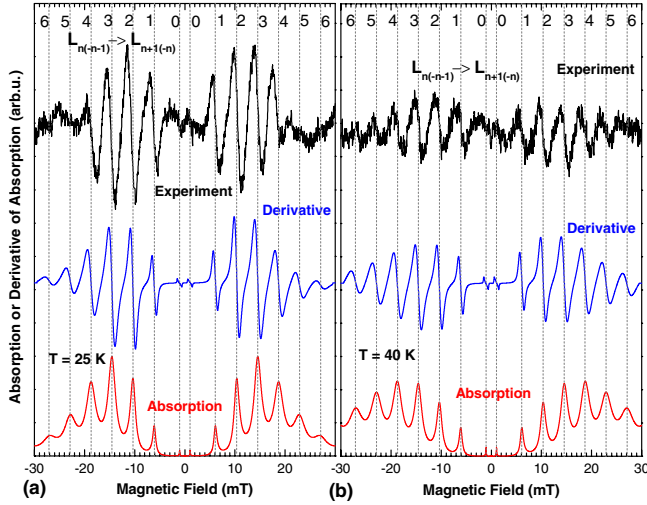


FIG. 3 (color online). Background-removed magneto-absorption spectra from experiment at  $T = 25$  and  $40$  K (black curves) in comparison to the response at the microwave frequency  $\hbar\omega = 1.171$  meV calculated for parameters  $\tilde{c} = 1.00 \times 10^6$  m  $\cdot$  s $^{-1}$ ,  $\gamma = 35$   $\mu$ eV, and  $E_F = 6.5$  meV. The dashed lines show the calculated positions of the CR transitions.

the ensemble of probed flakes would improve the agreement between experiment and theory, particularly at low temperatures. Comparing both, the measured and simulated traces, we are also more confident in the spectacular observation of the CR transition (involving the  $n = 0$  LL) at a magnetic field as low as 1 mT. Bearing in mind the small value of the extracted broadening parameter, one may conclude that LL quantization should survive in studied graphene layers down to the field of  $B = (\gamma/E_1)^2 \approx 1$   $\mu$ T. Hence, the magnetic field of the Earth of  $\sim 50$   $\mu$ T is no longer negligibly small. Instead, it can open an energy gap at the Dirac point up to  $\Delta \approx 0.3$  meV, depending on the sample orientation.

To crosscheck our interpretation, we have also measured the spectra using a different (higher) microwave energy  $\hbar\omega = 1.427$  meV, see Fig. 4. Despite the weaker sensitivity of the experimental setup at this frequency, we can clearly identify the same set of inter-LL transitions simply shifted to higher magnetic fields.

The finite Fermi energy  $E_F \approx 6$ – $7$  meV, corresponding to a carrier density of  $n_0 \approx 3 \times 10^9$  cm $^{-2}$ , indicates that the probed layers are in thermodynamical contact with the surrounding material, which supplies these carriers. On the other hand, we find no signs of electrical coupling of these graphene layers to bulk graphite. Our experiments show that any possible energy gap opened due to this interaction at the Dirac point cannot exceed a few hundred  $\mu$ eV. The absence of this gap convincingly confirms that we are indeed dealing with decoupled graphene and not with the  $H$  point of bulk graphite, where Dirac-like fermions are also present [16] but a (pseudo)gap of a few meV is expected [17] and indeed observed [18]. The temperature evolution of the measured spectra is another important

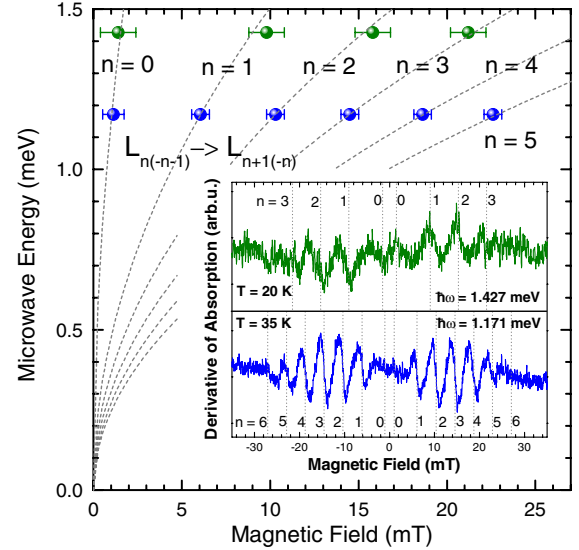


FIG. 4 (color online). Positions of CRs at microwave energies  $\hbar\omega = 1.171$  and  $1.427$  meV. Each position represents an average value obtained at different temperatures. One background-removed CR spectrum at each microwave frequency with a high number of observed CRs is shown in the inset. The grey curves show positions of CRs for  $\tilde{c} = 1.00 \times 10^6$  m  $\cdot$  s $^{-1}$ .

indication allowing us to discriminate between the graphene and bulk graphite contributions. No (or very weak) temperature broadening of CR transitions is expected for graphene [3,11,19], whereas the response of bulk graphite should follow the relatively strong decrease of the carrier scattering time, expressed by the average mobility, which reaches up to  $10^6$  cm $^2$ /(V  $\cdot$  s) at low temperatures, but falls down by 1 order of magnitude at  $T \approx 50$  K [20]. Indeed, this behavior is observed in Fig. 1. Whereas the CR harmonics of  $K$  point electrons in bulk graphite [21] seen in the spectra at  $|B| \geq 20$  mT, disappear very rapidly upon increasing  $T$ , the graphenelike features survive and their intensity is simply following the vanishing difference in the occupation between the adjacent LLs. It is worth noticing that the graphenelike signal, although always substantially weaker than the response from bulk graphite, has been observed for a number of different specimens of natural graphite. Mechanical scratching of the sample surface and the fast thermal cooling have been found to enhance the signal from decoupled graphene compared to bulk graphite, likely helping in detaching graphene sheets from the graphite crystal.

Since the well-defined LL quantization in our graphene flakes is observed down to  $|B| = 1$  mT, see Fig. 2, we obtain via the semiclassical LL quantization condition  $\mu B > 1$  the carrier mobility  $\mu > 10^7$  cm $^2$ /(V  $\cdot$  s), almost 2 orders of magnitude higher in comparison with suspended [2–4] or epitaxial graphene [11]. The LL broadening  $\gamma$ , obtained via comparison of our experiment with the simulated traces, allows us to estimate the scattering time  $\tau \approx 20$  ps ( $\tau = \hbar/\gamma$ ), which significantly exceeds those reported in any kind of man-made graphene samples,

see, e.g., Refs. [2,3], and gives an independent estimation for the mobility  $\mu = e\tau\tilde{c}^2/E_F \approx 3 \times 10^7 \text{ cm}^2/(\text{V} \cdot \text{s})$  in good agreement with the estimate above. Even though we cannot verify this estimate by a direct electrical measurement, a near correspondence of the scattering time derived from CR measurements and transport scattering time was recently verified on samples with a significantly lower mobility [12]. Moreover, the estimated mobility should not decrease with temperature, as no broadening of CRs is observed up to  $T = 50 \text{ K}$ , when CR intensities become comparable with the noise. This extremely high value of mobility combines two effects: the long scattering time  $\tau$  and a very small effective mass  $m = E_F/\tilde{c}^2 \approx 2 \times 10^{-4} m_0 E_F [\text{meV}]$ . Remarkably, the same scattering time in a moderate density sample ( $n_0 = 10^{11} \text{ cm}^{-2}$ ), would imply the mobility still remaining high, around  $\mu \approx 5 \times 10^6 \text{ cm}^2/(\text{V} \cdot \text{s})$ , and comparable to best mobilities of two-dimensional electron gas in GaAs structures at these densities.

The model we used here to describe the magneto-absorption response of Dirac fermions is amazingly simple, based on a one-particle approximation, and it is perhaps surprising that it is so well applicable to simulate the experimental data, particularly in context of the outstanding quality of the electronic system studied. At first sight, the observation of collective excitations, due to, e.g., magneto-plasmons, could be expected in our experiments, and only preliminary theoretical work addresses the surprising approximate validity of Kohn's theorem in graphene [22,23]. Also, size-confined magneto-plasmons are apparent in the microwave-absorption spectra of two-dimensional gas of massive electrons [24], but apparently not seen in our experiments on graphene. This perhaps points out the qualitative difference in the plasmon behavior in systems with quadratic and linear dispersion relations [25,26]. On the other hand, we speculate that the transition, marked with stars in Fig. 1, has a character of a collective excitation. The energy of this excitation softens with temperature and can be deduced to scale roughly as  $B/T$ , which points towards its magnetic origin. For example,  $B/T$  energy scaling is typical of a ferromagnetic resonance, see, e.g., Ref. [27]. Nevertheless, the origin of this spectral feature remains an intriguing puzzle. We see this feature repeatedly on different samples, but at slightly different energies, each time however characteristically evolving with temperature. With its apparent magnetic characteristics, one should seek its origin in impurities [28], structural defects [29], or edge states [30] in graphene, but possibly also on the surface of bulk graphite [31].

To conclude, graphene layers decoupled from bulk graphite have been probed in CR experiment, which offers unambiguous evidence of extremely high carrier mobility in graphene exceeding  $10^7 \text{ cm}^2/(\text{V} \cdot \text{s})$ . This measurement significantly shifts the limits of intrinsic mobility in gra-

phene [19] and poses a quest for further development in the technology of its fabrication. Graphene samples with mobilities comparable to the best GaAs samples [32] thus seem to be achievable.

This work has been supported by EuroMAGNET II under the EU contract, by projects PCR CNRS-CNRC, PICS-4340, MSM0021620834, KAN400100652, and Barrande No. 19535NF, by the Contract No. ANR-06-NANO-019.

\*orlita@karlov.mff.cuni.cz

- [1] J. Martin *et al.*, Nature Phys. **4**, 144 (2008).
- [2] Y.-W. Tan *et al.*, Phys. Rev. Lett. **99**, 246803 (2007).
- [3] K. I. Bolotin *et al.*, Phys. Rev. Lett. **101**, 096802 (2008).
- [4] X. Du *et al.*, Nature Nanotech. **3**, 491 (2008).
- [5] D. A. Abanin *et al.*, Phys. Rev. Lett. **98**, 196806 (2007).
- [6] Z. Jiang *et al.*, Phys. Rev. Lett. **99**, 106802 (2007).
- [7] G. Li, A. Luican, and E. Y. Andrei, Phys. Rev. Lett. **102**, 176804 (2009).
- [8] K. S. Novoselov *et al.*, Nature (London) **438**, 197 (2005).
- [9] Y. B. Zhang *et al.*, Nature (London) **438**, 201 (2005).
- [10] M. L. Sadowski *et al.*, Phys. Rev. Lett. **97**, 266405 (2006).
- [11] M. Orlita *et al.*, Phys. Rev. Lett. **101**, 267601 (2008).
- [12] Z. Jiang *et al.*, Phys. Rev. Lett. **98**, 197403 (2007).
- [13] R. S. Deacon *et al.*, Phys. Rev. B **76**, 081406(R) (2007).
- [14] Z. Li *et al.*, Nature Phys. **4**, 532 (2008).
- [15] V. P. Gusynin, S. G. Sharapov, and J. P. Carbotte, Phys. Rev. Lett. **98**, 157402 (2007).
- [16] M. Orlita *et al.*, Phys. Rev. Lett. **100**, 136403 (2008).
- [17] A. Grüneis *et al.*, Phys. Rev. B **78**, 205425 (2008).
- [18] W. W. Toy, M. S. Dresselhaus, and G. Dresselhaus, Phys. Rev. B **15**, 4077 (1977).
- [19] S. V. Morozov *et al.*, Phys. Rev. Lett. **100**, 016602 (2008).
- [20] N. B. Brandt, S. M. Chudinov, and Y. G. Ponomarev, *Semimetals I: Graphite and its Compounds*, Modern Problems in Condensed Matter Sciences (North-Holland, Amsterdam, 1988), Vol. 20.1.
- [21] P. Nozières, Phys. Rev. **109**, 1510 (1958).
- [22] Y. A. Bychkov and G. Martinez, Phys. Rev. B **77**, 125417 (2008).
- [23] K. Asano and T. Ando (private communication).
- [24] S. J. Allen, D. C. Tsui, and R. A. Logan, Phys. Rev. Lett. **38**, 980 (1977).
- [25] E. H. Hwang and S. Das Sarma, Phys. Rev. B **75**, 205418 (2007).
- [26] M. Polini, A. MacDonald, and G. Vignale, arXiv:0901.4528.
- [27] X. Liu and J. K. Furdyna, J. Phys. Condens. Matter **18**, R245 (2006).
- [28] B. Uchoa *et al.*, Phys. Rev. Lett. **101**, 026805 (2008).
- [29] O. V. Yazyev and L. Helm, Phys. Rev. B **75**, 125408 (2007).
- [30] L. Yang, M. L. Cohen, and S. G. Louie, Phys. Rev. Lett. **101**, 186401 (2008).
- [31] J. Červenka and C. F. J. Flipse, Nature Phys. (to be published).
- [32] E. H. Hwang and S. Das Sarma, Phys. Rev. B **77**, 235437 (2008).

**COMMENTED PAPER 4**

M. Orlita, **P. Neugebauer**, C. Faugeras, A.-L. Barra, M. Potemski, F. M. D. Pellegrino,  
and D. M. Basko

Cyclotron motion in the vicinity of Lifshitz transition in graphite

*Phys. Rev. Lett.*, 108, 017602 (2012).

## Cyclotron Motion in the Vicinity of a Lifshitz Transition in Graphite

M. Orlita,<sup>1,2</sup> P. Neugebauer,<sup>1</sup> C. Faugeras,<sup>1</sup> A.-L. Barra,<sup>1</sup> M. Potemski,<sup>1</sup> F. M. D. Pellegrino,<sup>3,4</sup> and D. M. Basko<sup>5</sup>

<sup>1</sup>Laboratoire National des Champs Magnétiques Intenses, CNRS-UJF-UPS-INSA, Grenoble, France

<sup>2</sup>Charles University, Faculty of Mathematics and Physics, Ke Karlovu 5, 121 16 Praha 2, Czech Republic

<sup>3</sup>Dipartimento di Fisica e Astronomia, Università di Catania, Via S. Sofia 64, I-95123 Catania, Italy

<sup>4</sup>CNISM, UdR Catania, I-95123 Catania, Italy

<sup>5</sup>Université Grenoble 1/CNRS, LPMMC UMR 5493, B.P. 166, 38042 Grenoble, France

(Received 21 September 2011; published 4 January 2012)

Graphite, a model (semi)metal with trigonally warped bands, is investigated with a magnetoabsorption experiment and viewed as an electronic system in the vicinity of the Lifshitz transition. A characteristic pattern of up to 20 cyclotron resonance harmonics has been observed. This large number of resonances, their relative strengths and characteristic shapes trace the universal properties of the electronic states near a separatrix in momentum space. Quantum-mechanical perturbative methods with respect to the trigonal warping term hardly describe the data which are, on the other hand, fairly well reproduced within a quasiclassical approach and conventional band structure model. Trigonal symmetry is preserved in graphite in contrast to a similar system, bilayer graphene.

DOI: 10.1103/PhysRevLett.108.017602

PACS numbers: 76.40.+b, 71.70.Di, 73.22.Pr, 81.05.uf

A Lifshitz transition [1] (also known as electronic topological transition) is a change in the Fermi surface topology occurring upon a continuous change of some external parameter, such as pressure [2], magnetic field [3] or, most naturally, doping [4]. This transition does not involve symmetry breaking, like conventional phase transitions of the Landau type, but still leads to observable singularities in thermodynamics, electron transport, sound propagation, and magnetic response of metals [5]. Saddle points in electronic dispersion, often apparent in complex metals, have only recently been visualized with the spectroscopy method of angle-resolved photoemission [6]. In this Letter, we show how the proximity to a Lifshitz transition manifests itself in cyclotron resonance (CR) absorption experiments on graphite, a model system with saddle points due to the trigonal warping of electronic bands [7].

Classically, CR can be understood from the equation of motion for an electron in a magnetic field  $\mathbf{B}$  [8]:

$$d\mathbf{p}/dt = (e/c)[\mathbf{v} \times \mathbf{B}], \quad (1)$$

where  $\mathbf{p} = \hbar\mathbf{k}$  is the electron quasimomentum,  $e = -|e|$  the electron charge, and  $\mathbf{v} = \partial\epsilon(\mathbf{p})/\partial\mathbf{p}$  is the electron velocity, determined by the dispersion  $\epsilon(\mathbf{p})$ . Since both the energy  $\epsilon$  and the momentum component  $p_z$  along  $\mathbf{B}$  are conserved, the motion occurs along cyclotron orbits in the  $(p_x, p_y)$  plane, determined by the condition  $\epsilon(p_x, p_y, p_z) = \text{const}$ . This motion is periodic, and its period,  $2\pi/\omega_c$ , being proportional to the cyclotron mass, defines the cyclotron frequency  $\omega_c = \omega_c(\epsilon, p_z)$ . When an electric field, oscillating at frequency  $\omega$ , is applied, the electron can absorb energy. Absorption becomes resonant when the perturbation frequency  $\omega$  matches the cyclotron frequency  $\omega_c$  or its integer multiple.

In good metals, the incoming radiation is efficiently screened and penetrates the sample only within a thin skin layer. CR absorption is then a surface effect, observed mainly when the magnetic field is parallel to the surface [9,10]. This makes CR for good metals a less efficient tool for probing the Fermi surface, as compared to other methods, such as, e.g., the de Haas-van Alphen effect. The resonant absorption is also often smeared by the dependence of  $\omega_c$  on  $p_z$ , which is an additional disadvantage.

We have applied the CR absorption technique to study the cyclotron motion in the vicinity of the Lifshitz transition in graphite. The low-temperature in-plane conductivity of this material is relatively low,  $\sigma \sim 10^7\text{--}10^8 (\Omega \cdot \text{m})^{-1}$ , and it quickly decreases upon the application of a magnetic field [7,11]. The skin depth thus reaches tens of nanometers and greatly exceeds the spacing between adjacent graphene layers. Moreover, graphite is a highly anisotropic crystal with rather flat electronic dispersion in the  $z$  direction (perpendicular to the layers). It appears as a suitable material for CR studies of the electronic system near the Lifshitz transition driven by the trigonal warping of electronic bands.

CR absorption was measured using the setup routinely applied to high-frequency electron paramagnetic resonance experiments [12]. A flake of natural graphite (50  $\mu\text{m}$  thick, area 1  $\text{mm}^2$ ) was placed in a Fabry-Perot cavity mounted inside a superconducting coil. The magnetic field was applied perpendicular to the graphene layers. Linearly polarized microwave radiation from a Gunn diode tripled to a frequency of 283.2 GHz (1.171 meV) was delivered to the sample via quasi-optics waveguides. The field-modulation technique was applied to enhance the detection sensitivity. The modulation

amplitude was chosen in a way to maximize the signal but to not distort the measured line shapes.

A representative experimental spectrum (raw data) is shown in Fig. 1(a). This trace represents the response of the natural graphite specimen measured as a function of the magnetic field at fixed microwave frequency. Because of the field-modulation technique, it corresponds to the derivative of the absorbed power with respect to  $B$ . The magnetoabsorption response of graphite is expected to be mostly sensitive to singularities in the electronic joint density of states, located at the  $K$  and  $H$  points of the graphite Brillouin zone. A number of the observed resonances can be easily identified as being due to electronic states at the  $K$  point, along the results of previous similar studies [13–18]. Holes at the  $H$  point as well as decoupled sheets of graphene on the surface of graphite give rise to resonances at a different spectral range (much lower magnetic fields) [19,20].

To a very first approximation, the  $K$  point electrons of graphite have parabolic dispersion. Their effective mass, most frequently reported to be in the range from  $m = 0.057m_0$  to  $0.060m_0$  [7] ( $m_0$  free electron mass), fixes the cyclotron frequency at  $\hbar\omega_{c0} \approx 2 \times B[\text{T}]$  meV. Then, the broad but still visible resonance at  $|B| \approx 0.6$  T is attributed to the fundamental CR absorption. All other observed resonances are higher harmonics of the fundamental one. This is evidenced in Fig. 1(b) where the spectrum from Fig. 1(a) is replotted against  $\omega/\omega_{c0}$  (i.e., versus  $B^{-1}$  instead of  $B$ ).  $\hbar\omega_{c0}$  is eventually set at  $2.05 \times B[\text{T}]$  meV.

In agreement with previous reports [13], the observed harmonics follow two series:  $\omega \approx |3k \pm 1|\omega_{c0}$ , where  $k = 0, \pm 1, \pm 2, \dots$ .

The superior quality of the present data (due to higher frequencies applied and perhaps a better quality of graphite specimens) allows us to uncover more and intriguing spectral features. Our key observations, that we interpret in the following, are (i) the appearance of a large number (up to 20) of CR harmonics, (ii) an enhanced strength of  $3k + 1$  harmonics as compared to the strength of the  $3k - 1$  series at  $B > 0$  (and vice versa at  $B < 0$ ), and finally, (iii) a very characteristic, asymmetric broadening of the observed resonances, enhanced on the low-frequency (high-field) sides of the absorption peaks. These features are clearly seen in the raw data and also in Fig. 1(c) in which we reproduce the actual absorption spectrum, as derived from the numerical integration, over the magnetic field, of the measured (differential) signal.

The appearance of  $n$  harmonics with  $n = 3k \pm 1$  is usually understood as being due to breaking of the isotropy of the electronic spectrum in the layer plane by the trigonal warping. For isotropic bands, only the  $k = 0$  fundamental transition is allowed, whereas the  $n = 3k \pm 1$  harmonic appears in the  $|k|$ th order of the perturbation theory with respect to the trigonal warping term [16,21]. The spectrum in Fig. 1 contains many harmonics which start to fall off only at large indices  $n \geq 7$ . Clearly, the perturbation theory is not applicable to interpret these data. Instead, we will use the quasiclassical approximation.

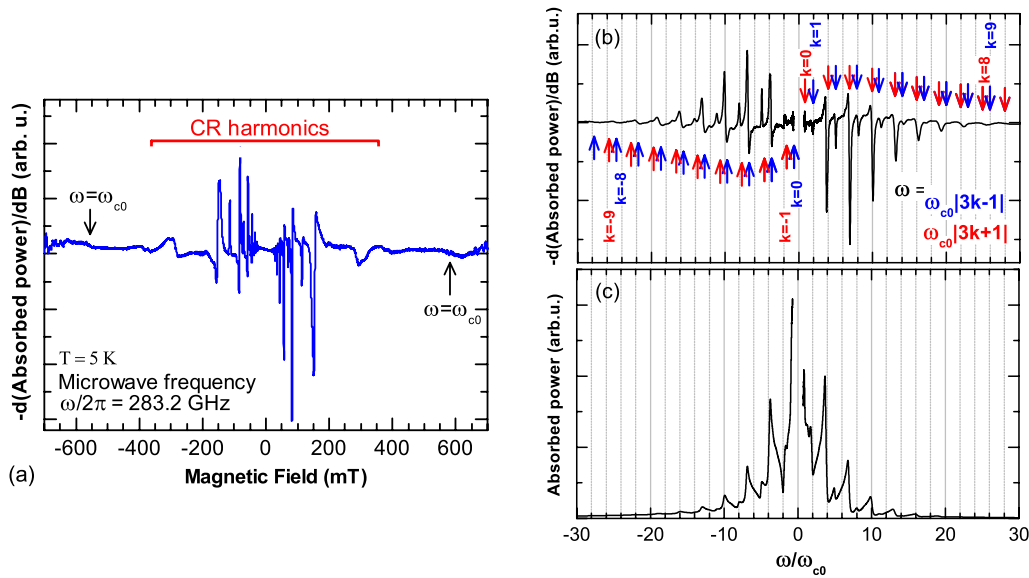


FIG. 1 (color online). Magnetoabsorption spectra of natural graphite measured at a fixed microwave excitation energy  $\hbar\omega = 1.171$  meV and detected with the help of the field-modulation technique at temperature of 5 K. Harmonics of fundamental CR frequency  $\omega_{c0} = eB/m_{c0}$  ( $m_{c0} = 0.057m_0$ ) are observed down to fields of 20 mT. (a) Derivative of the absorption with respect to the magnetic field  $B$ , as a function of  $B$ . (b) The same plotted as a function of  $\omega/\omega_{c0}$ , so that individual harmonics at frequencies of  $|3k \pm 1|\omega_{c0}$ ,  $k = 0, \pm 1, \pm 2, \dots$ , are clearly seen, as marked by vertical arrows. (c) Absorption as a function of  $\omega/\omega_{c0}$  obtained by the numerical integration of the curve presented in part (a) with respect to  $B$ .

Equation (1) can be cast in the Hamiltonian form in the phase space  $(p_x, p_y)$ :  $dp_x/dt = -\partial\mathcal{H}(p_x, p_y)/\partial p_y$ ,  $dp_y/dt = \partial\mathcal{H}(p_x, p_y)/\partial p_x$ , with the Hamiltonian  $\mathcal{H}(p_x, p_y) = -(eB/c)\epsilon(p_x, p_y)$  (we omitted  $p_z$ , which enters as a parameter). Generally, classical Hamiltonian systems exhibit a very rich behavior. However, they share some universal features when the energy  $\epsilon$  is close to that of a saddle point of the Hamiltonian,  $\epsilon = \epsilon_{sp}$ , as is well known in the classical nonlinear physics [22]. (i) The cyclotron motion in the vicinity of a saddle point is slow and its period diverges logarithmically,  $\omega_c(\epsilon) \rightarrow 0$  for  $\epsilon \rightarrow \epsilon_{sp}$ . (ii) The Fourier spectrum of this motion contains many harmonics and their number diverges when  $\epsilon \rightarrow \epsilon_{sp}$ . This second fact provides an obvious hint for the interpretation of the experimental data.

The experimentally probed electronic states are those around the Fermi level  $\epsilon_F$ . Thus, the effects discussed above are important if  $\epsilon_F \approx \epsilon_{sp}$ . This is the case of graphite, as illustrated in Fig. 2 using standard calculations based on the Slonczewski-Weiss-McClure (SWM) model [23] in the two-band approximation (see Supplemental Information [24]). Here we used the standard values of the SWM parameters [7]:  $\gamma_0 = 3150$  meV,  $\gamma_1 = 375$  meV,  $\gamma_2 = -20$  meV,  $\gamma_3 = 315$  meV,  $\gamma_4 = 44$  meV,

$\gamma_5 = 38$  meV,  $\Delta = -8$  meV. The band dispersion has six saddle points at two different energies  $\epsilon_{e-sp}$  and  $\epsilon_{h-sp}$ , which define two separatrices—isoenergetic lines separating regions with different topology. Fermi level crossing these saddle points would imply the change in the topology of the Fermi surface, which actually corresponds to the Lifshitz transition of the neck-collapsing type. The Fermi level is close to the upper separatrix, on which we focus our attention hereafter,  $\epsilon_{sp} \equiv \epsilon_{e-sp}$ . The single electron pocket around the  $K$  point at  $\epsilon_F > \epsilon_{sp}$ , splits into four disconnected pockets when  $\epsilon_F$  goes below  $\epsilon_{sp}$ . Figure 2(d) shows the classical cyclotron frequency for the SWM dispersion at  $k_z = 0$ , which vanishes at  $\epsilon = \epsilon_{sp}$ .

In the language of quantum mechanics, the  $k_z = 0$  energy spectrum consists of discrete Landau levels (LLs)  $\epsilon_l$ . In the quasiclassical approximation,  $\epsilon_l$  can be found from the Bohr-Sommerfeld quantization rule. The  $n$ th CR harmonic corresponds to the transition over  $n$  levels,  $n\hbar\omega_c \approx \epsilon_{l+n} - \epsilon_l$ , to the leading order in  $\hbar$ . The decrease of  $\omega_c(\epsilon)$  at  $\epsilon \rightarrow \epsilon_{sp}$  corresponds to an accumulation of LLs. Nevertheless,  $\Delta\epsilon$  does not approach zero, since the condition of the validity of the quasiclassical quantization,  $|\omega_c(\epsilon + \hbar\omega_c) - \omega_c(\epsilon)| \ll \omega_c(\epsilon)$ , holds only if  $\epsilon$  is not too close to  $\epsilon_{sp}$ . LLs always remain discrete, see Fig. 2(d).

As we will show later,  $\epsilon_F - \epsilon_{sp}$  is about 6 meV; i.e., it is 5 times larger than the microwave frequency,  $\hbar\omega = 1.171$  meV. Our classical approximation is justified in this case. As a matter of fact, the quasiclassical approximation works better, the smaller  $\omega$  is. However, if microwave frequency is too small, the harmonic structure will be smeared by broadening of electronic states. The optimal frequency, used in the experiment, is thus determined by an appropriate compromise between these two competing conditions.

Assuming that the absorbed power is proportional to the real part of the conductivity,  $\text{Re}\sigma_{xx}(\omega)$ , and calculating the latter from the standard kinetic equation [8] in the simplest relaxation time approximation for the collision integral (see Supplemental Information [24]), we obtain

$$\text{Re}\sigma_{xx}(\omega) = \frac{e^2}{\pi^2\hbar} \sum_{n=-\infty}^{\infty} \int \left( -\frac{\partial f}{\partial \epsilon} \right) \frac{\Gamma m_c |v_{x,n}|^2 dk_z d\epsilon}{\hbar^2(\omega - n\omega_c)^2 + \Gamma^2}, \quad (2)$$

where the  $k_z$  integration is from  $-\pi/(2a_z)$  to  $\pi/(2a_z)$ . Both the cyclotron frequency,  $\omega_c$ , and the cyclotron mass,  $m_c = -eB/(c\omega_c)$ , depend on  $\epsilon$  and  $k_z$ . The basic frequency  $\omega_{c0}$ , introduced earlier, is  $\omega_{c0} = \omega_c(\epsilon = \epsilon_F, k_z = 0)$ .  $\mathbf{v}_n = \mathbf{v}_n(\epsilon, k_z)$  is the Fourier harmonic of the electron velocity, corresponding to the term  $\propto e^{-in\omega_c t}$ , determined from the solution of the unperturbed equation of motion, Eq. (1). Finally,  $\Gamma$  accounts for relaxation, and  $f(\epsilon)$  is the Fermi function.

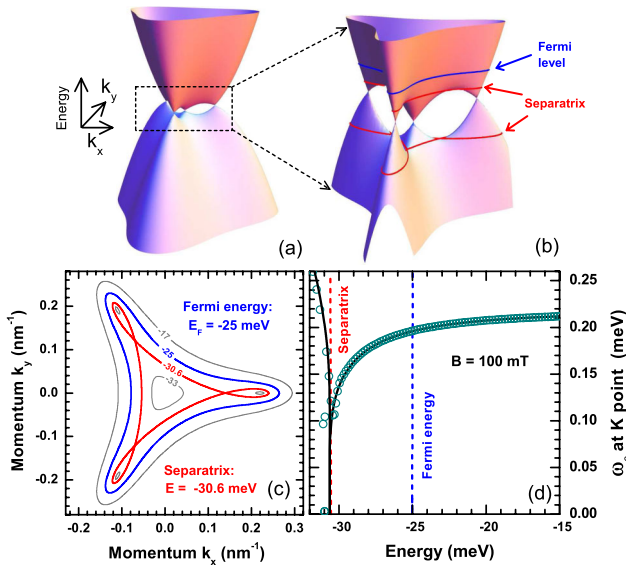


FIG. 2 (color online). (a),(b) Electronic structure near the  $K$  point of graphite ( $k_z = 0$ ). Two separatrix lines pass through six saddle points. The Fermi level is located about 6 meV above the upper separatrix. (c) Constant energy contours in the  $(k_x, k_y)$  plane for  $k_z = 0$  for  $\epsilon = -17$ ,  $\epsilon = -25$  (Fermi level),  $\epsilon = -30.6$  (upper separatrix), and  $\epsilon = -33$  meV. (d) Classical cyclotron frequency  $\hbar\omega_c(\epsilon, k_z = 0)$  at  $B = 100$  mT in the relevant energy interval.  $\omega_c$  vanishes at the saddle point. Open circles show the LL spacing,  $\Delta\epsilon_l = \epsilon_{l+1} - \epsilon_l$ , as a function of  $\epsilon_l$ , derived from the SWM model. Roughly 1 meV away from the saddle point, the circles fall on the classical curve,  $\Delta\epsilon_l \approx \hbar\omega_c(\epsilon_l)$ .

Even without solving Eq. (1), it is easy to see that the triangular symmetry of  $\epsilon(\mathbf{p})$  in the  $(p_x, p_y)$  plane fixes  $v_n = 0$  for  $n = 3k$ ,  $k = \pm 1, \pm 2, \dots$ . In Fig. 1(b), the resonances at  $n = 3k$  are absent, which demonstrates that the triangular symmetry is not broken in graphite. This is in contrast with recent reports for a bilayer graphene [25–28], even though it is formally described by the same single-particle Hamiltonian (for a fixed  $k_z$ ) [29]. The same symmetry fixes  $v_{n,x}$  to be real and  $v_{n,y} = \pm i v_{n,x}$  for  $n = 3k \pm 1$ , so the peaks at  $n = 3k + 1$  and  $n = 3k - 1$  are seen in the opposite circular polarizations of the microwave field. This helps us to understand the observed difference in the intensities of the  $n = 3k + 1$  and  $n = 3k - 1$  series. Indeed, for  $B > 0$ , when the electron moves along the Fermi surface, shown in Fig. 2(b), in the overall counterclockwise direction, it should be more strongly coupled to the counterclockwise polarized radiation. As both circular polarizations are equally present in the incoming linearly polarized radiation, the spectrum is fairly symmetric with respect to  $B \rightarrow -B$ .

The present studies are restricted to bulk graphite, a system with fixed Fermi level but in an apparent proximity to the Lifshitz transition. An obvious experimental challenge would be to trace the CR response when changing the Fermi level with respect to the separatrix energy, with an attempt to tune the proximity to Lifshitz transition in graphitic structures. This can be in principle envisaged for electrostatically gated bilayer graphene [27,28] and/or for bulk graphite under hydrostatic pressure [30]. Importantly, such experiments require no degradation of the quality of the sample, which likely excludes the experiments on, for example, chemically doped structures.

Besides the large number of harmonics, typical of a classical motion near a saddle point, the proximity to the Lifshitz transition also leads to some lowering of the cyclotron frequency. Indeed, the fundamental cyclotron frequency determined from the period in  $B^{-1}$  of the spectrum,  $\hbar\omega_{c0}/B = 2.05$  meV/T, is slightly lower than its parabolic-band limit at  $k_z = 0$ , 2.24 meV/T. The latter value, however, relies on the specific values of the parameters of the SWM model. More apparent effects are deduced from the analysis of the peak shapes (which are determined by the integration over  $k_z$ ).

As seen from Fig. 1(c), each peak has an abrupt cutoff on the high-frequency side and a tail on the low-frequency side. This contradicts the first intuition, based on the well-known fact that the parabolic part of the bands becomes steeper as  $k_z$  increases from the  $K$  point towards the  $H$  point. This pushes the LLs upwards as  $k_z$  increases and would result in a tail on the high-frequency side of each peak in the absorption spectrum  $\mathcal{A}(\omega, B)$  [31]. However, the bottom of the conduction band [defined as  $\epsilon(\mathbf{p} = 0, k_z)$ ] and the saddle point  $\epsilon_{sp}(k_z)$  shift upwards upon increasing  $k_z$ , as  $\epsilon(\mathbf{p} = 0, k_z) = 2\gamma_2 \cos k_z a_z$ ,  $\gamma_2 < 0$ . Thus, the Fermi level approaches the saddle point as  $k_z$

moves away from the  $k_z = 0$  point and  $\omega_c(\epsilon_F, k_z)$  decreases simultaneously, see Fig. 2(d). This provides a tail on the low-frequency side of the peaks. Thus, the suppression of  $\omega_c$  near the Lifshitz transition is crucial to interpret the peak asymmetry.

The spectrum derived from Eq. (2) is shown in Fig. 3, with  $\epsilon_F$  and  $\Gamma$  as the only adjustable parameters—the parameters of the SWM model were fixed [7]. The best agreement is obtained for  $\epsilon_F = -25$  meV. If  $\epsilon_F = -24$  meV, the peaks have no asymmetry, since  $\omega_c(\epsilon_F = -24$  meV,  $k_z)$  has a significant upturn on increasing  $k_z$ . When  $\epsilon_F = -26$  meV the falloff of large- $n$  harmonics is noticeably slower than the experimental one. In other words, the closer  $\epsilon_F$  is to  $\epsilon_{sp}$ , the more harmonics are seen in the spectrum. The frequency  $\omega_c(\epsilon_F = -25$  meV,  $k_z = 0)/B = 2.03$  meV/T agrees with the experimental value, 2.05 meV/T. The value  $\epsilon_F = -25$  meV is also in good agreement with the one determined independently from the charge neutrality condition (see Supplemental Information [24]),  $\epsilon_F = -24$  meV. A constant value of  $\Gamma = 20$   $\mu$ eV was assumed for the curve in Fig. 3(a). Apparently, this does not describe well the amplitudes of peaks at  $n = 1, 2$ : the theoretical peaks are narrower and thus more intense than the experimental ones. Better agreement is obtained under the assumption that  $\Gamma \propto \sqrt{B}$  (see Ref. [32] and Supplemental Information [24]). Notably, the curve in Fig. 3(b) with  $\Gamma = 0.1\sqrt{B[\text{T}]}$  meV corresponds to the zero-field relaxation rate  $\hbar/\tau_{B=0} = 40$   $\mu$ eV. The extracted value of  $\tau_{B=0}$  provides the zero-field dc conductivity  $\sigma = 1.2 \times 10^8$  ( $\Omega \cdot \text{m}$ )<sup>-1</sup> (see Supplemental Information [24]). This is fully consistent with typical literature data [7,11] and implies a mean electron free path of 6  $\mu$ m, which is, notably, comparable or even longer than the corresponding values reported for strictly 2D graphene-based structures [27,33,34].

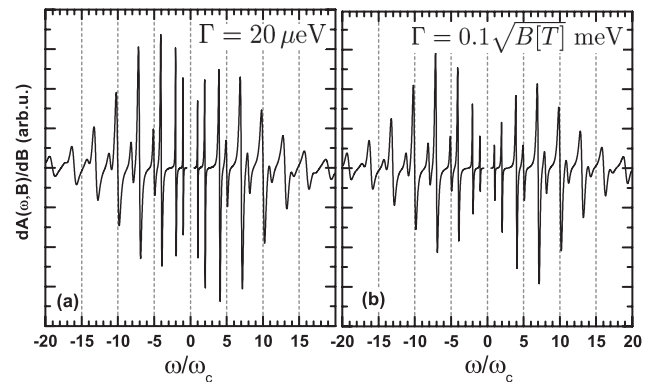


FIG. 3. Derivative of the absorption with respect to  $B$ , as calculated using Eq. (2) for different electronic broadenings  $\Gamma$ . (a) a constant broadening  $\Gamma = 20$   $\mu$ eV and (b)  $\Gamma = 0.1\sqrt{B[\text{T}]}$  meV.

To conclude, we have introduced CR experiments as a new tool to study Lifshitz transitions. We have shown how the proximity to the Lifshitz transition manifests itself in the CR spectrum of a model system, bulk graphite. Namely, we have observed a multimode response, where the basic CR mode is accompanied by many harmonics. Using the standard SWM model for the electronic band structure of graphite to analyze the data, we have determined the Fermi energy and estimated the electronic broadening. The similarity between the band structure of graphite near the  $K$  point and that of a bilayer graphene logically suggests to probe Lifshitz transition in the latter system by CR methods, and to shed more light on the currently debated issue of spontaneous symmetry breaking in bilayer graphene [25–28].

We thank M.-O. Goerbig and J.-N. Fuchs for collaboration on the early stages of this work, and V.F. Gantmakher and Yu. I. Latyshev for helpful discussions. Part of this work was supported by RTRA DISPOGRAPH project. M. O. acknowledges support from GACR P204/10/1020 and GRA/10/E006 (EPIGRAT). F.M.D.P. thanks LPMMC for hospitality.

- 
- [1] I. M. Lifshitz, Zh. Eksp. Teor. Fiz. **38**, 1565 (1960).
  - [2] V.I. Makarov and Bar'yakhtar, Zh. Eksp. Teor. Fiz. **48**, 1717 (1965), and references therein; C.W. Chu, T.F. Smith, and W.E. Gardner, Phys. Rev. B **1**, 214 (1970); B.K. Godwal *et al.*, Phys. Rev. B **57**, 773 (1998).
  - [3] P.M.C. Rourke *et al.*, Phys. Rev. Lett. **101**, 237205 (2008); J. Wosnitza *et al.*, Physica (Amsterdam) **403B**, 1219 (2008).
  - [4] D. Yoshizumi *et al.*, J. Phys. Soc. Jpn. **76**, 063705 (2007); Y. Okamoto, A. Nishio, and Z. Hiroi, Phys. Rev. B **81**, 121102(R) (2010); S.E. Sebastian *et al.*, Proc. Natl. Acad. Sci. U.S.A. **107**, 6175 (2010); M.R. Norman, J. Lin, and A.J. Millis, Phys. Rev. B **81**, 180513(R) (2010); D. LeBoeuf *et al.*, Phys. Rev. B **83**, 054506 (2011).
  - [5] Y.M. Blanter *et al.*, Phys. Rep. **245**, 159 (1994).
  - [6] C. Liu *et al.*, Nature Phys. **6**, 419 (2010).
  - [7] N.B. Brandt, S.M. Chudinov, and Y.G. Ponomarev, *Semimetals I: Graphite and Its Compounds* (North-Holland, Amsterdam, 1988).
  - [8] A. A. Abrikosov, *Fundamentals of the Theory of Metals* (North-Holland, Amsterdam, 1988).
  - [9] M. Ya. Azbel' and E. A. Kaner, Zh. Eksp. Teor. Fiz. **30**, 811 (1956).
  - [10] M. S. Khaikin, Zh. Eksp. Teor. Fiz. **41**, 1773 (1961) [Sov. Phys. JETP **14**, 1260 (1962)].
  - [11] X. Du *et al.*, Phys. Rev. Lett. **94**, 166601 (2005).
  - [12] P. Neugebauer and A.-L. Barra, Appl. Magn. Reson. **37**, 833 (2010).
  - [13] J. K. Galt, W. A. Yager, and H. W. Dail, Jr., Phys. Rev. **103**, 1586 (1956); S. J. Williamson *et al.*, Solid State Commun. **4**, 37 (1966); H. Suematsu and S. Tanuma, J. Phys. Soc. Jpn. **33**, 1619 (1972).
  - [14] B. Lax and H.J. Zeiger, Phys. Rev. **105**, 1466 (1957).
  - [15] P. Nozières, Phys. Rev. **109**, 1510 (1958).
  - [16] M. Inoue, J. Phys. Soc. Jpn. **17**, 808 (1962).
  - [17] G. Dresselhaus, Phys. Rev. B **10**, 3602 (1974).
  - [18] R. E. Doezema *et al.*, Phys. Rev. B **19**, 4224 (1979).
  - [19] M. Orlita *et al.*, Phys. Rev. Lett. **100**, 136403 (2008).
  - [20] P. Neugebauer *et al.*, Phys. Rev. Lett. **103**, 136403 (2009).
  - [21] D. S. L. Abergel and V. I. Fal'ko, Phys. Rev. B **75**, 155430 (2007); L. A. Falkovsky, Phys. Rev. B **84**, 115414 (2011).
  - [22] R.Z. Sagdeev, D.A. Usikov, and G.M. Zaslavsky, *Nonlinear Physics: From the Pendulum to Turbulence and Chaos* (Harwood Academic Publishers, New York, 1988).
  - [23] J.W. McClure, Phys. Rev. **108**, 612 (1957); J.C. Slonczewski and P.R. Weiss, *ibid.* **109**, 272 (1958).
  - [24] See Supplemental Material at <http://link.aps.org/supplemental/10.1103/PhysRevLett.108.017602> for details of the SWM model as well as performed calculations of the optical conductivity.
  - [25] O. Vafek and K. Yang, Phys. Rev. B **81**, 041401 (2010).
  - [26] Y. Lemonik *et al.*, Phys. Rev. B **82**, 201408(R) (2010).
  - [27] A. S. Mayorov *et al.*, Science **333**, 860 (2011).
  - [28] M. Mucha-Kruczyński, I.L. Aleiner, and V.I. Fal'ko, Phys. Rev. B **84**, 041404 (2011).
  - [29] M. Orlita *et al.*, Phys. Rev. Lett. **102**, 166401 (2009).
  - [30] E. Mendez, A. Misu, and M. S. Dresselhaus, Phys. Rev. B **21**, 827 (1980).
  - [31] P. Kossacki, C. Faugeras, M. Kühne, M. Orlita, A. A. L. Nicolet, J. M. Schneider, D. M. Basko, Yu. I. Latyshev, and M. Potemski, Phys. Rev. B **84**, 235138 (2011).
  - [32] T. Ando, J. Phys. Soc. Jpn. **38**, 989 (1975).
  - [33] K. I. Bolotin *et al.*, Phys. Rev. Lett. **101**, 096802 (2008).
  - [34] S. A. Mayorov *et al.*, Nano Lett. **11**, 2396 (2011).

**COMMENTED PAPER 5**

L. Gregoli, C. Danieli, A.-L. Barra, **P. Neugebauer**, G.Pellegrino, G.Poneti, R. Sessoli and A. Cornia  
Magnetostructural Correlations in Tetrairon(III) Single-Molecule Magnets

*Chem. Eur. J.*, 15, 6456 - 6467 (2009).

## Magnetostructural Correlations in Tetrairon(III) Single-Molecule Magnets

Luisa Gregoli,<sup>[a]</sup> Chiara Danieli,<sup>[a]</sup> Anne-Laure Barra,<sup>[b]</sup> Petr Neugebauer,<sup>[b]</sup>  
Giovanna Pellegrino,<sup>[c]</sup> Giordano Poneti,<sup>[d]</sup> Roberta Sessoli,<sup>[d]</sup> and Andrea Cornia\*<sup>[a]</sup>

**Abstract:** We report three novel tetrairon(III) single-molecule magnets with formula  $[\text{Fe}_4(\text{L})_2(\text{dpm})_6]$  ( $\text{Hdpm} = 2,2,6,6$ -tetramethylheptane-3,5-dione), prepared by using pentaerythritol monoether ligands  $\text{H}_3\text{L} = \text{R}'\text{OCH}_2\text{C}(\text{CH}_2\text{OH})_3$  with  $\text{R}' =$  allyl (**1**), (*R,S*)-2-methyl-1-butyl (**2**), and (*S*)-2-methyl-1-butyl (**3**), along with a new crystal phase of the complex containing  $\text{H}_3\text{L} = 11$ -(acetylthio)-2,2-bis(hydroxymethyl)-undecan-1-ol (**4**). High-frequency EPR (HF-EPR) spectra at low temperature were collected on powder samples in

order to determine the zero-field splitting (zfs) parameters in the ground  $S = 5$  spin state. In **1–4** and in other eight isostructural compounds previously reported, a remarkable correlation is found between the axial zfs parameter  $D$  and the pitch  $\gamma$  of the propeller-like structure. The relationship is directly demonstrated by **1**, which features both

structurally and magnetically inequivalent molecules in the crystal. The dynamics of magnetization has been investigated by ac susceptometry, and the results analyzed by master-matrix calculations. The large rhombicities of **2** and **3** were found to be responsible for the fast magnetic relaxation observed in the two compounds. However, complex **3** shows an additional faster relaxation mechanism which is unaccounted for by the set of spin Hamiltonian parameters determined by HF-EPR.

**Keywords:** EPR spectroscopy • iron • magnetic properties • single-molecule magnets • tripodal ligands

### Introduction

Slow magnetic relaxation in molecular entities is a lively research area which straddles the interface between chemistry, physics, and materials science. This phenomenon is observed in two main families of compounds: single-molecule magnets (SMMs) and single-chain magnets (SCMs).<sup>[1]</sup> The persistence of magnetization in such systems is limited to the

low-temperature regime (below about 4.2 K), but can be in principle exploited for breakthrough applications in the field of magnetic storage and information processing.<sup>[2]</sup> Many families of SMMs have been thus far synthesized and thoroughly characterized, including  $\text{Ni}_4$ ,<sup>[3]</sup>  $\text{Mn}_4$ ,<sup>[4]</sup>  $\text{Mn}_6$ ,<sup>[5]</sup> and  $\text{Mn}_{12}$ <sup>[6]</sup> species. Single-molecule magnet behavior is also often found in tetrairon(III) complexes with a propeller-like structure and an  $S = 5$  ground state, known as ferric stars.<sup>[7–13]</sup> Ferric stars can be very conveniently assembled by using 2,2,6,6-tetramethylheptane-3,5-dionate ( $\text{dpm}^-$ ) ligands combined with simple alkoxides ( $\mu\text{-OMe}$ ,  $\mu\text{-OEt}$ ) or triply deprotonated trimethylol derivatives  $\text{RC}(\text{CH}_2\text{OH})_3$  (see Table 1). Their axial zero-field splitting (zfs) parameter  $D$ , as determined by high-frequency EPR (HF-EPR), is invariably negative and ranges from  $-0.445 \text{ cm}^{-1}$  in **5** to  $-0.206 \text{ cm}^{-1}$  in **12**. By comparing the structural and magnetic properties of **5**, **8**, **11**, and **12**, we previously showed that the  $D$  value correlates with the helical pitch of the propeller-like structure.<sup>[8]</sup>

We herein significantly extend the  $\text{Fe}_4$  SMM family by reporting three new derivatives **1–3** prepared by using pentaerythritol monoethers  $\text{H}_3\text{L}^i = \text{R}'\text{OCH}_2\text{C}(\text{CH}_2\text{OH})_3$ , with  $\text{R}' =$  allyl ( $\text{H}_3\text{L}^1$ ), (*R,S*)-2-methyl-1-butyl ( $\text{H}_3\text{L}^2$ ), and (*S*)-2-methyl-1-butyl ( $\text{H}_3\text{L}^3$ ). In addition, we describe a novel crystal phase of the complex containing  $\text{H}_3\text{L}^4 = 11$ -(acetylthio)-

[a] Dr. L. Gregoli, Dr. C. Danieli, Prof. Dr. A. Cornia  
Department of Chemistry and INSTM Research Unit  
University of Modena and Reggio Emilia  
Via G. Campi 183, 41100 Modena (Italy)  
Fax: (+39)059-373543  
E-mail: andrea.cornia@unimore.it

[b] Dr. A.-L. Barra, P. Neugebauer  
Grenoble High Magnetic Field Laboratory  
CNRS, BP 166, 25 Avenue des Martyrs  
38042 Grenoble Cedex 9 (France)

[c] Dr. G. Pellegrino  
Department of Chemistry and INSTM Research Unit  
University of Catania, Viale A. Doria 6, 95125 Catania (Italy)

[d] G. Poneti, Prof. Dr. R. Sessoli  
Department of Chemistry and INSTM Research Unit  
University of Florence, Via della Lastruccia 3  
50019 Sesto Fiorentino (FI) (Italy)

Supporting information for this article is available on the WWW under <http://dx.doi.org/10.1002/chem.200900483>.

Table 1. Structural data (determined by single-crystal X-ray diffraction and averaged assuming  $D_3$  symmetry) and magnetic parameters (determined by HF-EPR and ac susceptometry) for tetrairon(III) propellers.

Compound	$\gamma, \phi, \theta$ [°]	$D, E, 10^5 B_4^0$ [cm <sup>-1</sup> ]	$U_{\text{eff}}/k_B, U/k_B^{[e]}$ [K]
[Fe <sub>4</sub> (L) <sub>2</sub> (dpm) <sub>6</sub> ] series <sup>[a]</sup>			
5, R = Me	70.8, 29.2, 54.1	-0.445, 0.0, 1.0	17.0, 16.0 <sup>[8,11]</sup>
6, R = (CH <sub>2</sub> ) <sub>2</sub> CH=CH <sub>2</sub>	69.7, 30.8, 54.2	-0.434, 0.020, 1.0 <sup>[c]</sup>	15.9, 15.6 <sup>[9a]</sup>
7, R = CH <sub>2</sub> OPh	68.8, 32.3, 54.5	-0.433, 0.014, 1.5	15.7, 15.6 <sup>[12]</sup>
8, R = Ph	68.8, 32.3, 54.2	-0.418, 0.023, 0.8 <sup>[c]</sup>	15.6, 15.0 <sup>[8]</sup>
9, R = 4-Cl-Ph	68.1, 33.5, 54.4	-0.411, 0.010, 1.1	-, 14.8 <sup>[13a]</sup>
10, R = CH <sub>2</sub> O(CH <sub>2</sub> ) <sub>4</sub> (C <sub>16</sub> H <sub>9</sub> )	67.1, 35.1, 54.5	-0.409, 0.008, 2.4	13.7, 14.7 <sup>[13b,c]</sup>
[Fe <sub>4</sub> (L')(OEt) <sub>3</sub> (dpm) <sub>6</sub> ] (11) <sup>[b]</sup>	65.9, 35.0, 56.1	-0.27, 0.0, <0.5 <sup>[d]</sup>	5.95, 9.6 <sup>[8]</sup>
[Fe <sub>4</sub> (OMe) <sub>6</sub> (dpm) <sub>6</sub> ] (12)	63.2, 37.7, 57.3	-0.206, 0.010, -1.1 <sup>[d]</sup>	3.5, 7.4 <sup>[7,8]</sup>

[a] H<sub>3</sub>L = RC(CH<sub>2</sub>OH)<sub>3</sub>. [b] H<sub>3</sub>L' = *t*BuC(CH<sub>2</sub>OH)<sub>3</sub>. [c] Molecules with slightly different parameters were detected in the lattice. [d] For the dominant species in the lattice. [e] Calculated as  $(|D|/k_B)S^2$ .

2,2-bis(hydroxymethyl)undecan-1-ol ligands (**4**), the first SMM to show magnetic hysteresis at gold surfaces.<sup>[9]</sup> High-yield synthetic procedures are reported, along with the results of thorough characterization by single-crystal XRD, dc and ac magnetic measurements, and HF-EPR, which lend firm support to the above-mentioned magnetostructural correlation.

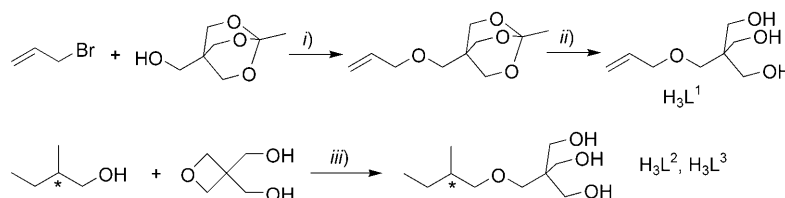
## Results and Discussion

**Synthesis:** Trimethylol derivatives RC(CH<sub>2</sub>OH)<sub>3</sub> have been widely used as versatile ligands for the construction of polynuclear metal complexes.<sup>[10a]</sup> Recently, it has been shown that they act as site-specific ligands toward tetrairon(III) SMMs with a propeller-like structure.<sup>[8,9,10b,c,11–13]</sup> This property has been exploited to bind Fe<sub>4</sub> SMMs to a silicon surface decorated with trimethylol receptors,<sup>[13a]</sup> as well as to functionalize tetrairon(III) complexes with surface-binding groups suitable for gold substrates<sup>[9]</sup> or carbon nanotubes.<sup>[13c]</sup> These tripodal ligands can be prepared by different synthetic pathways. Base-catalyzed Tollens condensation between the appropriate functionalized acetaldehyde RCH<sub>2</sub>CHO and formaldehyde is the linear synthesis most exploited in this field.<sup>[14a–c]</sup> Even though this procedure is often successful, yields are seriously lowered owing to the formation of formylated or partially hydroxylated byproducts, whose separation is not trivial.<sup>[14d]</sup> A complementary route is malonic ester synthesis, in which dialkyl malonate is first alkylated to introduce the R group and then hydroxymethylated with formaldehyde.<sup>[14e,f]</sup> The subsequent reduction step requires protection of the hydroxymethyl group and is usually carried out with LiAlH<sub>4</sub> under rather drastic conditions that narrow the synthetic scope of the method.<sup>[14e]</sup> A similar procedure entails alkylation of sodium triethyl methane tricarboxylate<sup>[14g]</sup> followed by reduc-

tion, which can interfere with other functional groups. A completely different approach, based on convergent synthesis, can be envisaged to afford trimethylol derivatives with formula R'HNC(CH<sub>2</sub>OH)<sub>3</sub> and R'OCH<sub>2</sub>C(CH<sub>2</sub>OH)<sub>3</sub> starting from easily available and cheap reagents like 2-amino-2-(hydroxymethyl)-1,3-propanediol (TRIS) and 2,2-bis(hydroxymethyl)-1,3-propanediol (pentaerythritol), respectively. Functionalization of the amino group of TRIS requires mild

conditions, and no protection of the hydroxyl groups is necessary.<sup>[15a–d]</sup> The synthesis of pentaerythritol monoethers requires protection of OH groups by formation of mono- or bicyclic derivatives. Use of bicyclic ortho esters of pentaerythritol such as pentaerythritol orthoacetate first involves Williamson-type reaction between the free OH group and the appropriate alkyl, allyl, or benzyl halide under mild conditions. Deprotection is then carried out by acid hydrolysis followed by saponification.<sup>[15e–h]</sup> Alternatively, acid- or base-catalyzed ring-opening of 3,3-bis(hydroxymethyl)oxetane by alcohols or phenols can be exploited to prepare pentaerythritol monoethers in one step. However, due to the low ring strain of oxetanes, the reaction requires rather drastic conditions.<sup>[12,15i–m]</sup> Other strategies include nucleophilic substitution on 3-hydroxymethyl-3-bromomethyloxetane followed by acid hydrolysis<sup>[12,16a,b]</sup> or use of 1,3-dioxanes as protecting groups for pentaerythritol. The latter route has been mainly exploited for different functionalization of at least two hydroxyl groups of pentaerythritol, rather than for the synthesis of monoethers.<sup>[16c,d]</sup>

The new derivatives used in this work were prepared as described in Scheme 1. Allyl derivative H<sub>3</sub>L<sup>1</sup> was obtained from allyl bromide and pentaerythritol orthoacetate, by following a literature method.<sup>[15g,h]</sup> The chiral ligands H<sub>3</sub>L<sup>2</sup> (racemic form) and H<sub>3</sub>L<sup>3</sup> (enantiopure *S* form) were prepared by base-catalyzed opening of 3,3-bis(hydroxymethyl)oxetane with (*R,S*)-2-methyl-1-butanol and (*S*)-2-methyl-1-butanol, respectively. In this case, the alcohol was used both as a reactant and as solvent. Crystalline samples of tetrairon(III) complexes **1–3** were then obtained in moderate to good



Scheme 1. Synthesis of ligands H<sub>3</sub>L<sup>1–3</sup>. Experimental conditions: i) KOH, DMSO, room temperature, 45 min, 85 %; ii) HCl, Na<sub>2</sub>CO<sub>3</sub>, MeOH/H<sub>2</sub>O, 96 %;<sup>[15g,h]</sup> iii) sodium 2-methyl-1-butoxide, 2-methyl-1-butanol, reflux, overnight, 30–32 %.

yield (43–88 %) by treating **12** with an excess of ligands  $H_3L^{1-3}$  (2.7–5.1 equiv) in dry diethyl ether and by subsequent vapor diffusion of dry methanol into the reaction mixture. With ligand  $H_3L^4$ , the reaction mixture was left undisturbed to allow slow evaporation of the solvent. The microcrystalline material was then extensively washed with methanol and recrystallized from DME to give **4** as large, X-ray quality, orange-yellow blocks in 78 % yield. The product has identical chemical composition to the poorly crystalline solid phase obtained by slow evaporation of DME/Et<sub>2</sub>O.<sup>[9a]</sup>

**Crystal and molecular structures:** Crystallographic data and refinement parameters for **1–4** are presented in Table 2, and molecular structures are

shown in Figures 1–3. Complete structural data are provided as Supporting Information. As the crystal lattice contains no free solvent molecules, samples are completely air-stable. The four compounds are isostructural and differ only in the substituents on the tripodal ligands. Their Fe/O core approaches idealized  $D_3$  symmetry, with a threefold axis perpendicular to the tetrairon plane and a twofold axis passing through the central iron ion and each of the peripheral metal ions. All compounds are 1:1 mixtures of  $\Lambda$  and  $\Delta$  pro-

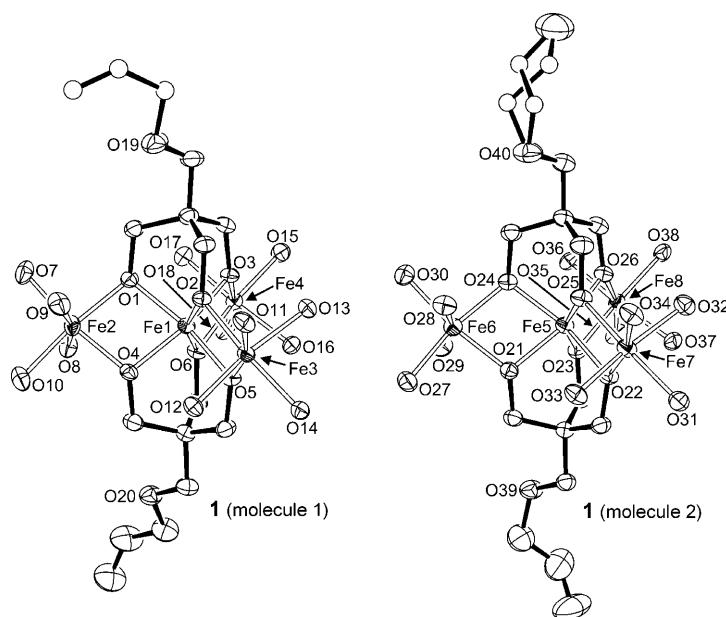


Figure 1. ORTEP of the two crystallographically-independent molecules in crystals of **1** ( $\Lambda$  isomers). One alkyl chain in molecule 2 is disordered over two approximately equally populated positions. Thermal ellipsoids are drawn at 50 % probability. All hydrogen atoms and the carbon atoms of  $dpm^-$  ligands have been omitted for clarity.

PELLER isomers, although only **1**, **2**, and **4** crystallize in centric space groups.

Compound **1**, which contains allyl-substituted ligand  $H_3L^1$ , crystallizes in monoclinic space group  $P2_1/c$  with two whole tetrairon(III) molecules in the asymmetric unit (Figure 1). The crystallographic molecular symmetry is  $C_1$ , although an approximate twofold symmetry is found along Fe1–Fe2 in molecule 1 and Fe5–Fe6 in molecule 2 if the allyl substituents are disregarded.

Compound **2**, which entails the chiral tripodal ligand  $H_3L^2$  in racemic form, crystallizes in monoclinic space group  $P2/n$ . The asymmetric unit comprises half a tetrametallic complex, which develops around a twofold axis and has rigorous crystallographic  $C_2$  symmetry along the Fe1–Fe2 direction. The alkyl chain of the tripodal ligand is disordered over two positions with occupancies of 0.60 and 0.40 corresponding to the two enantiomers of  $H_3L^2$ . In the  $\Lambda$  isomer, the two components correspond to the *S* and *R* enantiomers of the ligand, represented by solid and open bonds, respectively, in Figure 2. We argue that the  $\Lambda$  ( $\Delta$ ) propeller isomer has a

Table 2. Crystallographic data and refinement parameters for **1–4**.<sup>[a]</sup>

	<b>1</b>	<b>2</b>	<b>3</b>	<b>4</b>
formula	C <sub>82</sub> H <sub>140</sub> Fe <sub>4</sub> O <sub>20</sub>	C <sub>86</sub> H <sub>152</sub> Fe <sub>4</sub> O <sub>20</sub>	C <sub>86</sub> H <sub>152</sub> Fe <sub>4</sub> O <sub>20</sub>	C <sub>96</sub> H <sub>168</sub> Fe <sub>4</sub> O <sub>20</sub> S <sub>2</sub>
formula weight	1669.34	1729.48	1729.48	1929.82
crystal system	monoclinic	monoclinic	monoclinic	monoclinic
space group	$P2_1/c$	$P2/n$	$P2$	$C2/c$
<i>a</i> [Å]	38.1036(12)	17.0632(7)	17.1169(3)	27.5893(6)
<i>b</i> [Å]	15.9282(5)	15.5838(7)	15.6485(3)	20.7460(5)
<i>c</i> [Å]	30.3692(9)	19.5691(8)	19.3862(4)	19.2973(4)
$\beta$ [°]	91.1410(10)	110.600(1)	110.517(1)	98.2990(10)
<i>V</i> [Å <sup>3</sup> ]	18428.1(10)	4870.9(4)	4863.29(16)	10929.5(4)
<i>Z</i>	8	2	2	4
$\rho_{\text{calcd}}$ [g cm <sup>-3</sup> ]	1.203	1.179	1.181	1.173
$\mu$ [mm <sup>-1</sup> ]	0.679	0.644	0.645	0.618
crystal size [mm]	0.56 × 0.37 × 0.30	0.62 × 0.30 × 0.22	0.50 × 0.25 × 0.22	0.69 × 0.40 × 0.23
$2\theta_{\text{max}}$ [°]	27.53	27.54	27.52	27.53
reflins collected	175 713	49 295	50 142	51 344
indep. reflins ( <i>R</i> <sub>int</sub> )	42 146 (0.0377)	11 197 (0.0234)	17 440 (0.0224)	12 470 (0.0305)
data/restraints/parameters	42 146/348/2199	11 197/16/511	17 440/25/1024	12 470/31/549
<i>R</i> <sub>1</sub> , <i>wR</i> <sub>2</sub> ( <i>I</i> > 2 $\sigma$ ( <i>I</i> ))	0.0662, 0.1666	0.0379, 0.0996	0.0319, 0.0840	0.0603, 0.1525
<i>R</i> <sub>1</sub> , <i>wR</i> <sub>2</sub> (all data)	0.1051, 0.1991	0.0482, 0.1072	0.0411, 0.0888	0.0987, 0.1867
largest diff. peak and hole [e Å <sup>-3</sup> ]	1.729/−0.716	0.627/−0.520	0.379/−0.257	0.769/−0.715

[a] All measurements carried out at 120(2) K with MoK $\alpha$  radiation ( $\lambda = 0.71073$  Å).

slightly greater tendency to combine with the *S* (*R*) enantiomer. Of course, due to the centrosymmetric space group, the crystal contains  $\Lambda$  and  $\Delta$  isomers, as well as *R* and *S* ligands, in exactly equal amounts.

Compound **3** features the chiral ligand  $H_3L^3$  in enantiopure *S* form and crystallizes in noncentrosymmetric monoclinic space group *P2* (Figure 2). The asymmetric unit comprises two half tetrametallic clusters, which develop around twofold axes and consequently have rigorous crystallographic  $C_2$  symmetry along the Fe1–Fe2 and Fe4–Fe5 directions, respectively. As expected, all tripodal ligands display the same absolute configuration. The absolute structure could be unambiguously determined through anomalous dispersion effects, and confirmed the expected *S* absolute configuration for  $H_3L^3$ . The two crystallographically distinct molecules in the crystal have different core configurations, corresponding to the  $\Lambda$  (molecule 1) and  $\Delta$  (molecule 2) isomers. Due to the chiral nature of both the tripodal ligand and the cluster core, they can be regarded as diastereoisomers. This result shows that the enantiopure triol is not efficient as a resolving agent for the tetrairon(III) propellers, since the two diastereoisomers crystallize together in the same lattice. To the best of our knowledge, the only homochiral tetrairon(III) propeller so far isolated is  $[Fe_4(L'')_6]$  based on the achiral ligand  $H_2L'' = N$ -benzyl-diethanolamine.<sup>[10d]</sup>

Compound **4**, which contains the long-chain alkyl derivative  $H_3L^4$ , crystallizes in space group *C2/c* with half a tetrametallic complex in the asymmetric unit (Figure 3). The crystals are excellent X-ray diffractors in spite of the long and flexible alkyl chains, which are disordered over three positions with occupancies of 0.36, 0.28, and 0.36. Notably, the S...S distance in each molecule is as large as 2.6–2.9 nm.

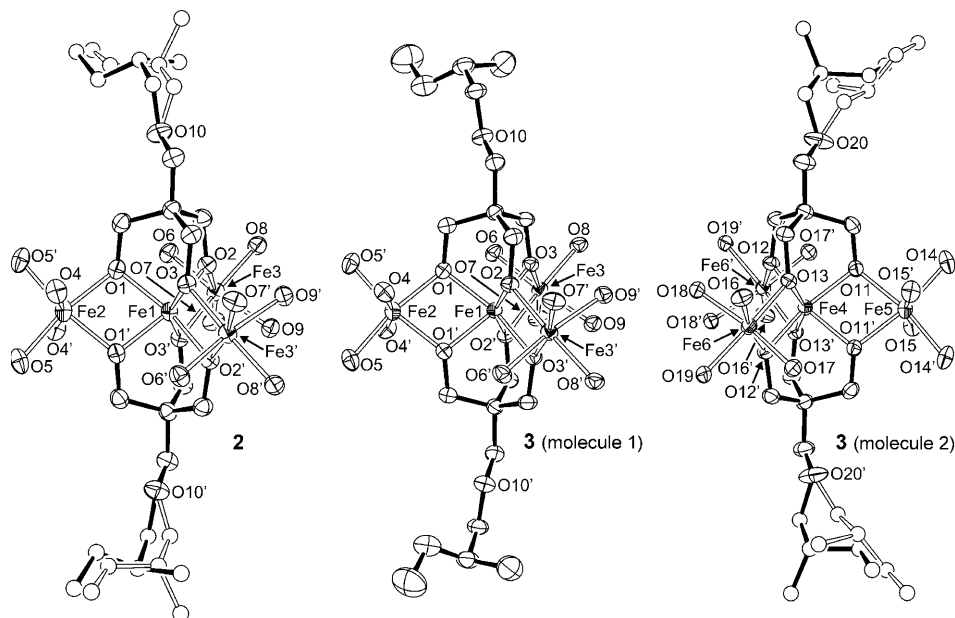


Figure 2. Left: ORTEP of **2** ( $\Lambda$  isomer), with bound tripodal ligands in *S* form (solid bonds) and *R* form (open bonds). Right: ORTEP plot of the two crystallographically independent molecules in crystals of compound **3** ( $\Lambda$  and  $\Delta$  isomers). Thermal ellipsoids are drawn at 50% probability. All hydrogen atoms and the carbon atoms of  $dpm^-$  ligands have been omitted for clarity.

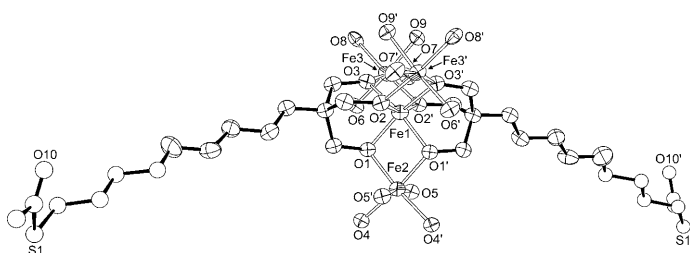


Figure 3. ORTEP of **4** ( $\Lambda$  isomer) with thermal ellipsoids at 30% probability. All hydrogen atoms and the carbon atoms of  $dpm^-$  ligands have been omitted for clarity. Only one component of the disordered SAc-terminated alkyl chain is shown.

Selected structural parameters for complexes **1–4** are gathered in Table 3 for the sake of comparison. They were averaged under the assumption of idealized  $D_3$  symmetry and include the Fe–O distances for the central ( $Fe_c$ ) and peripheral metal centers ( $Fe_p$ ), the  $Fe_c$ –O– $Fe_p$  angles at the bridging alkoxide ligands, and the angular parameters  $\alpha$ ,  $\beta$ ,  $\theta$ ,  $\phi$ , and  $\gamma$  (see Figure 4 for definition). The values of  $\theta$  and  $\phi$  can be easily calculated from the (average) interbond angles  $\alpha$  and  $\beta$  by using Equations (1) and (2).

$$\cos\theta = \sqrt{\frac{1 + 2\cos\alpha}{3}} \quad (1)$$

$$\cos\frac{\phi}{2} = \sqrt{\frac{3(1 + \cos\beta)}{4(1 - \cos\alpha)}} \quad (2)$$

The angle  $\theta$  describes the distortion by trigonal compression [ $\theta > 54.74 = \arccos(1/3)^{1/2}$ ] or elongation ( $\theta < 54.74$ ),

whereas a departure of  $\phi$  from the octahedral value ( $60^\circ$ ) indicates distortion by trigonal rotation. Finally, the angle  $\gamma$  is the “pitch” of the propeller structure, evaluated as the dihedral angle between the  $Fe_cO_2Fe_p$  and  $Fe_4$  planes. By straightforward trigonometric arguments it can be shown that the three angles  $\theta$ ,  $\phi$ , and  $\gamma$  are related by Equation (3)

$$\cos\gamma = \frac{\sin(\phi/2)}{[\sin^2(\phi/2) + \cot^2\theta]^2} \quad (3)$$

Thus, the propeller pitch can be altered in two ways: either  $\theta$  is kept constant and the extent of trigonal rotation  $\phi$  is varied, or  $\phi$  is kept constant and  $\gamma$  is changed by varying  $\theta$ . From the definition of the dif-

Table 3. Selected geometrical and magnetic parameters for complexes **1–4**. Fe<sub>c</sub> and Fe<sub>p</sub> denote the central and peripheral metal centers, respectively. Geometrical parameters have been averaged under the assumption of D<sub>3</sub> symmetry, and the numbers in parentheses are the associated standard deviations.

	<b>1</b>	<b>2</b>	<b>3</b>	<b>4</b>
Fe <sub>c</sub> –O [Å]	1.986(8) <sup>[a]</sup> 1.988(5) <sup>[b]</sup>	1.987(8)	1.986(10) <sup>[a]</sup> 1.987(14) <sup>[b]</sup>	1.983(5)
Fe <sub>p</sub> –O [Å]	1.998(17) <sup>[a]</sup> 1.996(16) <sup>[b]</sup>	1.993(17)	1.993(17) <sup>[a]</sup> 1.994(17) <sup>[b]</sup>	1.991(13)
Fe <sub>c</sub> –O–Fe <sub>p</sub> [°]	102.2(1.0) <sup>[a]</sup> 102.6(5) <sup>[b]</sup>	102.4(4)	102.5(5) <sup>[a]</sup> 102.6(3) <sup>[b]</sup>	101.7(3)
O1–Fe <sub>c</sub> –O2 = α [°]	89.9(9) <sup>[a]</sup> 89.3(3) <sup>[b]</sup>	89.1(3)	89.1(2) <sup>[a]</sup> 89.2(4) <sup>[b]</sup>	89.62(12)
O1–Fe <sub>c</sub> –O1' = β [°]	77.6(9) <sup>[a]</sup> 77.12(19) <sup>[b]</sup>	77.23(8)	77.18(18) <sup>[a]</sup> 77.14(18) <sup>[b]</sup>	78.13(17)
θ [°]	54.7 <sup>[a]</sup> 54.2 <sup>[b]</sup>	54.1	54.1 <sup>[a]</sup> 54.2 <sup>[b]</sup>	54.5
φ [°]	34.4 <sup>[a]</sup> 31.0 <sup>[b]</sup>	30.6	30.4 <sup>[a]</sup> 30.7 <sup>[b]</sup>	34.9
γ [°]	67.3(5) <sup>[a]</sup> 69.5(4) <sup>[b]</sup>	70.0(2)	70.0(4) <sup>[a]</sup> 69.9(6) <sup>[b]</sup>	67.3(4)
J <sub>1</sub> , J <sub>2</sub> [cm <sup>-1</sup> ] <sup>[c]</sup>	17.65(4), 0.49(2)	17.23(5), 0.30(3)	15.56(2), -0.11(1)	15.93(10), 0.31(7)
D [cm <sup>-1</sup> ] <sup>[d]</sup>	-0.417 <sup>[a]</sup> -0.435 <sup>[b]</sup>	-0.449	-0.442	-0.412
E [cm <sup>-1</sup> ] <sup>[d]</sup>	0.015 <sup>[a]</sup> 0.009 <sup>[b]</sup>	0.030	0.031	0.006
10 <sup>5</sup> B <sub>4</sub> <sup>0</sup> [cm <sup>-1</sup> ] <sup>[d]</sup>	1.3 <sup>[a]</sup> 0.9 <sup>[b]</sup>	2.4	1.6	1.8
U <sub>eff</sub> /k <sub>B</sub> [K]	15.93(6)	11.9(3)	12.9(4), 9.5(18)	16.10(5)
U/k <sub>B</sub> [K] <sup>[e]</sup>	15.0 <sup>[a]</sup> 15.6 <sup>[b]</sup>	16.2	15.9	14.8
10 <sup>8</sup> τ <sub>0</sub> [s]	4.05(11)	6.0(9)	15(3), 9(5)	7.45(19)

[a] Molecule 1. [b] Molecule 2. [c] From magnetic susceptibility vs. *T* data at *T* ≥ 10 K. [d] From HF-EPR spectra (the uncertainty on *D* and *E* is ±1 in the last digit; the uncertainty on B<sub>4</sub><sup>0</sup> is ±5 in the last digit). [e] Calculated as (|*D*|/k<sub>B</sub>)*S*<sup>2</sup>.

ferent angles in Figure 4, it follows that increasing either φ or θ results in a smaller helical pitch.

In the isostructural series **1–10**, θ spans a very limited range (from 54.1 to 54.7°), and its closeness to the octahedral value (54.74°) indicates only small trigonal elongation (see Tables 1 and 3). The essentially constant θ value is likely a consequence of the fixed bite angle of the tripodal ligands. By contrast, important differences stand out when the φ and γ values are analyzed in detail. The smallest φ angle and the largest pitch are found in **5**,<sup>[8,11]</sup> and the largest φ value and smallest pitch in **10**.<sup>[13c]</sup> The two crystallographically independent molecules in **1** have quite different φ and γ values, although they contain the same achiral ligand H<sub>3</sub>L<sup>1</sup>. On the other hand, the two diastereoisomers of **3** display quite similar geometries, despite the expectedly different interaction of the enantiopure chiral ligand H<sub>3</sub>L<sup>3</sup> with the two propeller isomers Λ (molecule 1) and Δ (molecule 2). These findings suggest that not only intramolecular factors but also crystal-packing effects may be responsible for the observed differences in trigonal distortion and helical pitch. The same conclusion can be reached by examining the magnetic properties of the two crystal phases of **4** (see below).

In the series **1–10** a straightforward correlation exists between γ and φ (Figure 4), as expected because of the small differences in θ. Indeed, the observed data points are well

reproduced by Equation (3) (dashed line) when θ is fixed at the value observed in **5**, which exhibits the largest helical pitch. Thus, the observed changes in γ are mainly triggered by different trigonal rotations. The small departures from the calculated curve originate from the fact that as φ is increased the θ angle increases slightly (see inset in Figure 4) and thus contributes to a small extra reduction of helical pitch. The data points corresponding to **11** and **12** do not follow the previously discussed trend owing to the significantly larger θ values of these two complexes. This structural feature and the consequent decrease of helical pitch must ultimately be ascribed to the relaxation of bite angle constraints caused by the replacement of one (**11**) or two (**12**) tripodal ligands with monodentate alkoxides.

#### Magnetism and HF-EPR spectroscopy: Compounds **1–4**

were magnetically characterized by measuring the temperature dependence of the molar magnetic susceptibility χ<sub>m</sub> in low fields (1–10 kOe) and the isothermal field dependence of magnetization at low temperature (1.9, 2.5, and 4.5 K). All complexes display very similar behavior and we herein restrict our attention to compound **1** as a representative example (details on **2–4** can be found in the Supporting Information). The χ<sub>m</sub>*T* versus *T* plot for **1** (Figure 5) is characteristic of ferric stars, in which the dominant antiferromagnetic interaction between the central and peripheral high-spin iron(III) centers generates an *S* = 5 ground state.<sup>[7,8,11]</sup> Quantitative fitting of the data at *T* ≥ 10 K by using a Heisenberg spin Hamiltonian with nearest-neighbor (*J*<sub>1</sub>) and next-nearest-neighbor (*J*<sub>2</sub>) coupling constants gives *J*<sub>1</sub> = 17.65(4) cm<sup>-1</sup>, *J*<sub>2</sub> = 0.49(2) cm<sup>-1</sup>, and *g* = 2.0123(8); differences between the two inequivalent tetrairon molecules in the lattice were neglected. The isothermal molar magnetization versus field data for **1**, plotted in Figure 5 (inset) as *M*<sub>m</sub> versus *H*/*T*, could be accurately fitted only with a negative *D* parameter (*D* = -0.438(9) cm<sup>-1</sup>, *g* = 2.043(6), and *S* = 5).

The fine structure of the ground *S* = 5 state for all compounds was studied in detail by HF-EPR spectroscopy on pressed powder samples at 190 and 230 GHz and at three temperatures (5, 10, and 20 K). All compounds gave spectra characteristic of quasi-axial systems with an easy-axis anisotropy. We herein discuss 230 GHz spectra, while data at

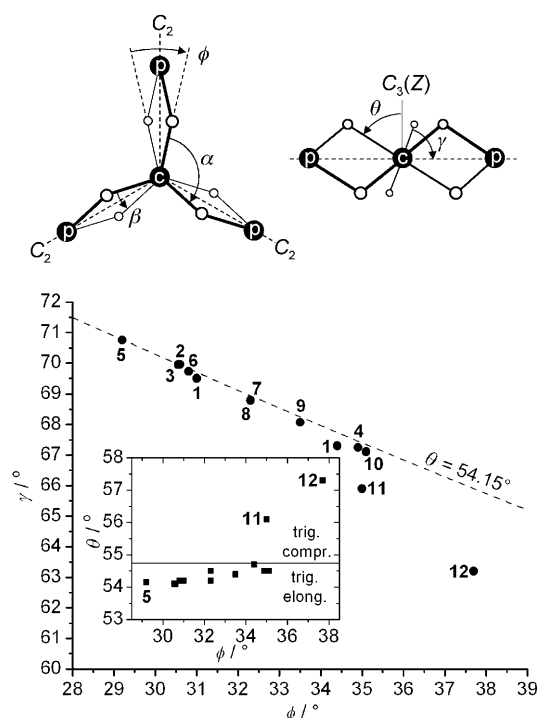


Figure 4. Top: Definition of the angles  $\theta$ ,  $\phi$ ,  $\gamma$ ,  $\alpha$ , and  $\beta$  used in the structural analysis of tetrairon(III) propellers, assuming idealized  $D_3$  symmetry. The dashed lines lie in the plane defined by the four metal centers. Bottom:  $\gamma$  versus  $\phi$  plot for tetrairon(III) propellers **1–12**. The two data points for complex **1** correspond to the two inequivalent molecules in the lattice. Average structural parameters were used for the two crystallographically inequivalent molecules in **3**. The inset shows a  $\theta$  versus  $\phi$  plot. See text for details on the structural model represented by the dashed trace.

190 GHz can be found in the Supporting Information. For convenience, we first discuss the spectra of **2**. Experimental traces recorded at 230 GHz and 20 K display four well-resolved parallel transitions, marked by an asterisk in Figure 6. Extrapolation of the pattern toward the central resonance field, drawn with a vertical dashed line ( $H_0 = 82.1$  kOe), shows that five resonances lie at  $H < H_0$ , as expected for an  $S = 5$  state. The parallel resonance observed at lowest field (ca. 40 kOe) gains intensity upon cooling and must consequently be assigned to the  $M_S = -4 \leftarrow -5$  transition of an easy-axis system ( $D < 0$ ). Furthermore, careful

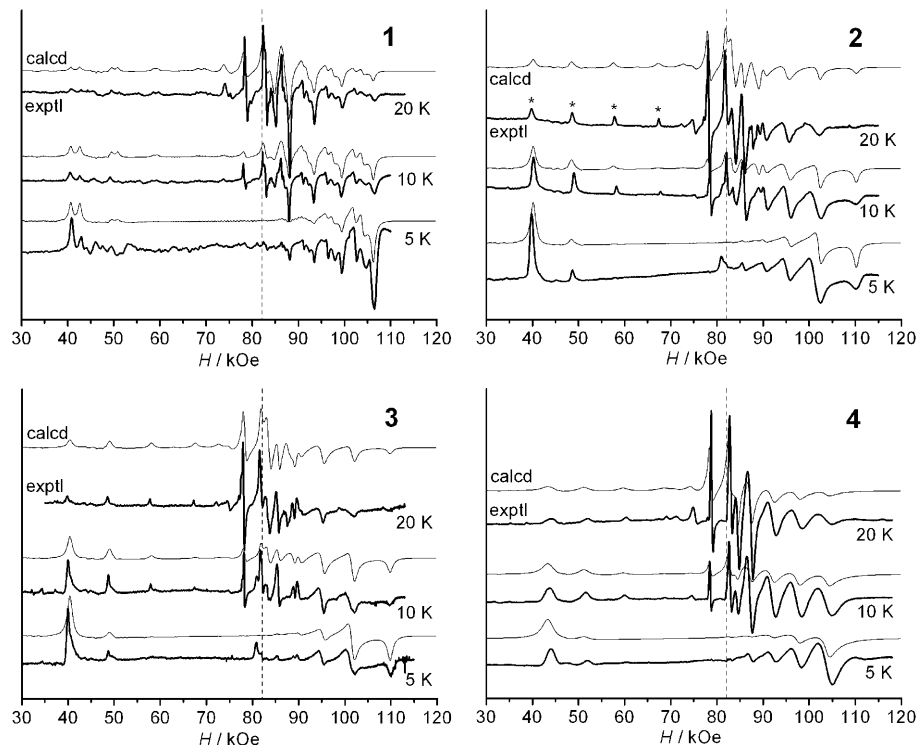


Figure 6. HF-EPR spectra of **1–4** recorded on pressed powder samples at 230 GHz and at three temperatures. The asterisks in the spectra of **2** label parallel transitions, while the dashed vertical line indicates the central resonance field ( $H_0 = 82.1$  kOe).

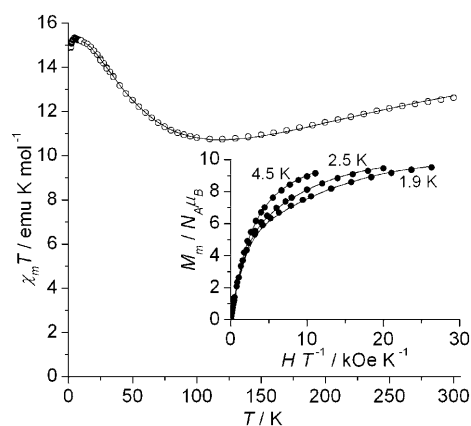


Figure 5. Direct-current magnetic properties of **1**. The solid lines are the best fit to the experimental data, as described in detail in the text.

inspection of the parallel region reveals that the line-to-line separation increases smoothly when moving to higher fields, thus pointing to the presence of fourth-order axial anisotropy terms of opposite sign with respect to the  $D$  term. More detailed fitting of the spectra was based on a spin Hamiltonian [Eq. (4)]<sup>[1a,17]</sup> that includes second-order ( $D$ ) and fourth-order ( $B_4^0$ ) axial terms along with a second-order transverse term  $E$ , which is permitted by the nonaxial crystallographic symmetry of all the compounds.

$$\hat{H}_{\text{EPR}} = \mu_{\text{B}} \hat{\mathbf{S}} \cdot \mathbf{g} \cdot \hat{\mathbf{H}} + D[\hat{S}_z^2 - \frac{1}{3}S(S+1)] + \frac{E}{2}(\hat{S}_+^2 + \hat{S}_-^2) + B_4^0 \hat{O}_4^0 \quad (4)$$

Transverse fourth-order terms were not included, as the rather broad line widths of the perpendicular transitions precluded the determination of such terms. The best-fit parameters thus obtained are gathered in Table 3. The spectra of **3** are very similar and can be fitted with essentially the same parameters, although important differences have been observed in the spin dynamics of the two compounds (vide infra). In spite of the disordered alkyl chains in **2** and **3** and the two structurally inequivalent molecules which compose the crystal lattice of **3**, the EPR signals do not exhibit any resolvable splitting, that is, the different stereoisomers in the crystal lattice are magnetically equivalent within experimental resolution. Complex **4** displays a slightly lower axial anisotropy than **2** and **3**, since the  $M_S = -4 \leftarrow -5$  transition is found at higher field (44 vs. 40 kOe, see Figure 6). This compound also exhibits a smaller rhombicity, which is reflected by the smaller extension of the perpendicular pattern at  $H > H_0$ . The axial anisotropy ( $D = -0.412 \text{ cm}^{-1}$ ) is significantly lower than in a previously reported poorly crystalline phase of the same compound ( $D = -0.435 \text{ cm}^{-1}$ ).<sup>[9a]</sup> Compound **1** has unique spectral features. Both parallel and perpendicular bands exhibit an apparent splitting which reveals the presence of at least two magnetically inequivalent molecules. One component gives rise to a parallel  $M_S = -4 \leftarrow -5$  signal at about 41 kOe, and consequently its axial anisotropy is only slightly lower than those of **2** and **3**. A second component at about 43 kOe is clearly visible in the spectra, which could be satisfactorily reproduced in both the parallel and perpendicular regions with the parameters reported in Table 3 by setting a 1:1 ratio between the two inequivalent species. Since this compound does not contain any solvent of crystallization, distortions due to partial solvent loss cannot be invoked to explain the observed line splittings. Indeed, as shown in the previous section, the lattice of **1** contains two crystallographically inequivalent molecules with significantly different structural parameters  $\phi$  and  $\gamma$ .

**Alternating-current magnetic studies:** The magnetization dynamics of polycrystalline powder samples of **1–4** was investigated by means of ac susceptibility measurements in zero static applied field. The analysis was performed as a function of temperature (from 1.8 K) and frequency of the oscillating field ( $\nu = 100\text{--}25\,000 \text{ Hz}$ ). While simple paramagnets do not show any imaginary (out-of-phase) component  $\chi''$  of the complex susceptibility, SMMs are characterized by freezing of the magnetization and appearance of a nonzero, frequency-dependent out-of-phase response.<sup>[1a]</sup> All complexes investigated showed frequency-dependent maxima in their  $\chi''$  versus  $T$  plots (see the Supporting Information). At constant frequency, the temperature at which  $\chi''$  has a maximum ( $T_{\text{max}}$ ) was found to decrease in the order  $\mathbf{4} > \mathbf{1} > \mathbf{2} \approx \mathbf{3}$ . Within the Debye model commonly employed to analyze the ac response of SMMs, a maximum in  $\chi''$  is observed when the relaxation time  $\tau$  equals  $(2\pi\nu)^{-1}$ . The temperature

dependence of the relaxation time is then often determined by measuring  $T_{\text{max}}$  at different frequencies.<sup>[1a]</sup> However, a more rigorous procedure is to analyze the frequency dependence of the ac susceptibility at constant temperature by using Debye model [Eqs. (5) and (6)],

$$\chi'(\omega) = \chi_{\text{S}} + (\chi_{\text{T}} - \chi_{\text{S}}) \frac{1 + (\omega\tau)^{1-\alpha} \sin(\alpha\pi/2)}{1 + 2(\omega\tau)^{1-\alpha} \sin(\alpha\pi/2) + (\omega\tau)^{2-2\alpha}} \quad (5)$$

$$\chi''(\omega) = (\chi_{\text{T}} - \chi_{\text{S}}) \frac{(\omega\tau)^{1-\alpha} \cos(\alpha\pi/2)}{1 + 2(\omega\tau)^{1-\alpha} \sin(\alpha\pi/2) + (\omega\tau)^{2-2\alpha}} \quad (6)$$

where  $\omega = 2\pi\nu$ , and  $\chi_{\text{T}}$  and  $\chi_{\text{S}}$  are the isothermal and adiabatic susceptibilities, that is, the susceptibilities observed in the two limiting cases  $\nu \rightarrow 0$  and  $\nu \rightarrow \infty$ , respectively. This allows not only to extract the relaxation time but also to evaluate the distribution of relaxation times, as described by the  $\alpha$  parameter. The model is completely satisfactory for **1**, **2**, and **4**, and affords  $\alpha$  values which approach 0.25 at the lowest temperatures and decrease toward zero at high temperature (see Supporting Information). However, it fails to reproduce the ac response of **3**. Indeed, an Argand diagram obtained by plotting  $\chi''_{\text{m}}$  versus  $\chi'_{\text{m}}$  clearly suggests the presence of two relaxation processes, as reflected in the two overlapping semicircles in Figure 7a. The susceptibility versus frequency data are well reproduced by considering the convolution of two different relaxation processes, each involving 50% of the molecules in the sample (while normally only  $\chi''$  is fitted, for **3** both  $\chi'$  and  $\chi''$  have been fitted to reduce over-parameterization, as shown in the Supporting Information).

The relaxation times obtained from this analysis are shown in an Arrhenius plot in Figure 7b. The two datasets for compound **3** reflect the two above-described relaxation processes; however, the fast-relaxing species is affected by a larger uncertainty. The linear  $\ln \tau$  versus  $1/T$  plots indicate a thermally activated relaxation mechanism which follows the Arrhenius law [Eq. (7)].

$$\tau = \tau_0 \exp(U_{\text{eff}}/k_{\text{B}} T) \quad (7)$$

The parameters  $U_{\text{eff}}/k_{\text{B}}$  and  $\tau_0$ , evaluated by a linear fit, are gathered in Table 3, along with the anisotropy barrier calculated as the energy difference between  $M_S = \pm 5$  and  $M_S = 0$  states ( $U/k_{\text{B}} = (|D|/k_{\text{B}})S^2$ , since for  $S = 5$  accidentally no contribution arises from the  $B_4^0$  parameter). Careful inspection of these values and those collected in Table 1 reveals that for the isostructural complexes **1**, **4**, **5–8**, and **10** the observed energy barrier  $U_{\text{eff}}$  is comparable with  $U$ . By contrast, a substantial reduction of the effective barrier to below 13 K is detected in **2** and **3**, although the  $D$  parameters of the two compounds are close to that of **5**, which has  $U_{\text{eff}}/k_{\text{B}} = 17.0 \text{ K}$ . The lowered barriers in **2** and **3** indicate greater effectiveness of underbarrier (tunneling) relaxation, which is promoted by transverse anisotropy terms.<sup>[18]</sup> Indeed, **2** and **3** have the largest rhombic anisotropy in the series, with  $|E/D| \approx 0.07$ . To better understand the origin of

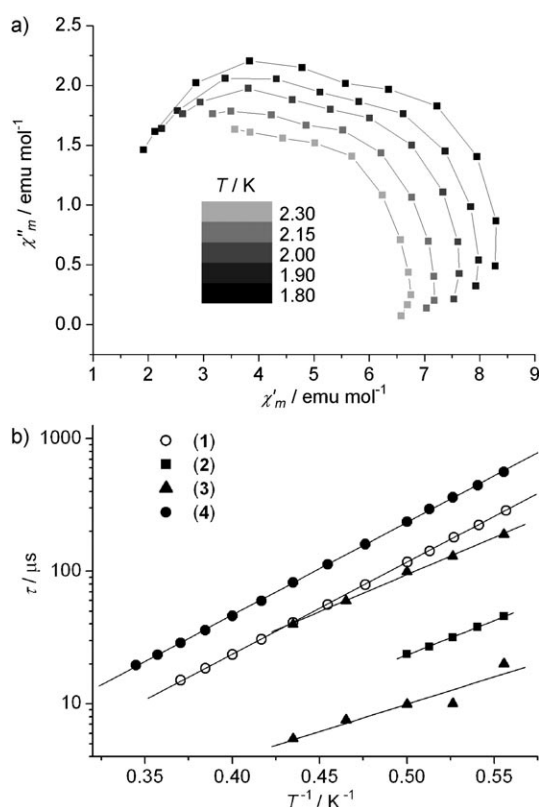


Figure 7. a) Argand diagram highlighting the occurrence of two relaxation dynamics in compound **3**. b) Arrhenius plot of compounds **1–4** extracted from ac measurements by using the Debye model.

this striking difference the energy barrier was estimated from the temperature dependence of the relaxation time, calculated by a master-matrix approach.<sup>[19]</sup> Briefly, this consists of calculating the energy and wavefunction of the spin sublevels of the  $S=5$  ground state according to the spin-Hamiltonian parameters and successive evaluation of the transition probabilities by considering coupling with the phonon bath.<sup>[1a]</sup> Spin-phonon coupling is mediated by a coefficient which is not known a priori and is usually considered as an adjustable parameter. However, it only acts as an offset on the calculated relaxation times and does not affect the height of the barrier. We calculated the dependence of  $U_{\text{eff}}$  on the  $E$  parameter while keeping all other spin-Hamiltonian parameters fixed at the values observed in **3**. As reported in the Supporting Information, the barrier heights observed in **2** (11.9 K) and in the slow-relaxing species of **3** (12.9 K) are well reproduced by setting  $|E/D|=0.07$ . On the other hand, modeling the barrier height of the fast-relaxing species in **3** (9.5 K) requires an  $E$  parameter about three times larger than estimated from HF-EPR. Such a large rhombicity would be easily visible in HF-EPR spectra, as confirmed by spectral simulation (see the Supporting Information). To gain additional insight into this unusually fast relaxation, we considered the effect of higher-order transverse anisotropy terms.<sup>[6a]</sup> The fourth-order term which is compatible with the idealized trigonal symmetry of the cluster has the form of Equation (8).<sup>[17]</sup>

$$B_4^3 \hat{O}_4^3 = \frac{1}{4} B_4^3 [\hat{S}_z (\hat{S}_+^3 + \hat{S}_-^3) + (\hat{S}_+^3 + \hat{S}_-^3) \hat{S}_z] \quad (8)$$

Calculations by the master-matrix approach showed that a  $B_4^3$  value as large as  $7 \times 10^{-3} \text{ cm}^{-1}$  is required to reproduce the observed  $U_{\text{eff}}$ . Again, such a value would hardly escape detection by HF-EPR (see the Supporting Information). At present, we have no explanation for finding two relaxation processes in **3**, since its EPR spectra do not show any line splittings nor anomalous broadening and are virtually identical to those of **2**. We can only suspect that higher order anisotropy terms, although undetectable by HF-EPR, play a significant role in the reduction of  $U_{\text{eff}}$  for one of the diastereoisomers cocrystallized in **3**. Note that although the two nonequivalent sets of molecules in **1** are clearly distinguished in HF-EPR spectra, a single relaxation time is detected.

**Magnetostructural correlations:** The  $D$  parameters for complexes **1–12** are plotted in Figure 8 as a function of  $\gamma$ . For compound **1** we attribute the smaller anisotropy ( $D = -0.417 \text{ cm}^{-1}$ ) to molecule 1 [ $\gamma = 67.3(5)^\circ$ ] and the larger ani-

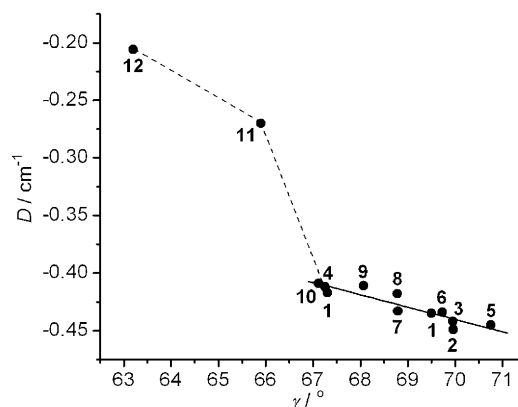


Figure 8.  $D$  versus  $\gamma$  plot for the twelve tetrairon(III) propellers so far characterized. The solid line provides the best fit to all data except for **11** and **12**. The dashed lines are simply a guide to the eye.

sotropy ( $D = -0.435 \text{ cm}^{-1}$ ) to molecule 2 [ $\gamma = 69.5(4)^\circ$ ]. Notwithstanding the limited range of  $\gamma$  spanned by the series (less than  $4^\circ$ ), in complexes **1–10** the  $D$  value is a linear function of propeller pitch. Clearly, adopting an inverted assignment for the magnetically inequivalent molecules in **1** would result in large deviations of the corresponding data points from the linear correlation. Note also that the  $D$  parameters for the two crystal phases of **4** ( $D = -0.435 \text{ cm}^{-1}$ <sup>[9a]</sup> and  $-0.412 \text{ cm}^{-1}$ ) span a large fraction (ca. 60%) of the total  $D$  range found in  $[\text{Fe}_4(\text{L})_2(\text{dpm})_6]$  complexes ( $-0.449$  to  $-0.409 \text{ cm}^{-1}$ ). Beside intramolecular factors of electronic or steric nature, crystal packing effects may therefore play an important role in determining the observed structural and magnetic features.

The trend is qualitatively followed by compounds **11** and **12** as well, although their anisotropy is significantly smaller than predicted by linear extrapolation of the  $D$  versus  $\gamma$  plot for **1–10**. Such a correlation was first suggested by examin-

ing a very limited series compounds (**5**, **8**, **11**, and **12**)<sup>[8]</sup> and here finds firm support over twelve complexes.

The data in Figure 8 can be most simply analyzed in the framework of the strong-exchange approximation, that is, by assuming that exchange interactions are dominant over anisotropic contributions responsible for zfs.<sup>[20]</sup> As first proposed elsewhere,<sup>[8]</sup> the ground-state  $D$  parameter for  $D_3$  molecular symmetry (unique axis  $Z$ ) is related to dipolar and single-ion anisotropy terms through Equation (9)

$$D = \frac{5}{39}D_c + \frac{51}{182} [D_p(3\cos^2\beta' - 1) + 3E_p\sin^2\beta'\cos 2\gamma'] + D_{\text{dip}} \quad (9)$$

where  $D_{\text{dip}}$  is the dipolar anisotropy projected on the  $S=5$  state, which is of easy-axis type, that is,  $D_{\text{dip}} < 0$ . Its value calculated in the point-dipole approximation amounts to only a small fraction of the observed anisotropy. Furthermore, because of the very similar Fe...Fe distances, it is almost constant in the series of tetrairon(III) propellers, spanning the range from  $-0.0345 \text{ cm}^{-1}$  in **12** to  $-0.0371 \text{ cm}^{-1}$  in **10** (these two compounds have the largest and the shortest Fe...Fe separation in the series, respectively). We argue that molecular anisotropy in the series is largely determined by single-ion contributions. These are described in Equation (9) by four parameters:  $D_c$  is the axial zfs parameter of the central iron(III) ion, which lies on the threefold axis  $Z$  and must consequently have a rigorously axial anisotropy;  $D_p$  and  $E_p$  are the axial and rhombic zfs parameters of peripheral metal centers, whose anisotropy tensors  $\mathbf{D}_p$  are not independent, but related by a threefold rotation around  $Z$ ; and the Eulerian angles  $\beta'$  and  $\gamma'$  define the orientation of  $\mathbf{D}_p$  in the molecular reference frame (the third Eulerian angle rotates all  $\mathbf{D}_p$  tensors simultaneously around  $Z$  and has no influence on  $D$ ). In  $D_3$  symmetry the  $\text{Fe}_p\text{-Fe}_c$  direction coincides with a twofold axis and must correspond to one of the principal directions of  $\mathbf{D}_p$  (i.e.,  $\gamma' = 0$  or  $90^\circ$ ). In previous work, the anisotropy observed in **5**, the sole compound with rigorous  $D_3$  symmetry, was analyzed by using a  $D_c$  value estimated from DFT calculations ( $-0.61 \text{ cm}^{-1}$ ) and the known anisotropy parameters of the  $(\mu\text{-MeO})_2\text{Fe}(\text{dbm})_2$  fragment (Hdbm = 1,3-diphenylpropane-1,3-dione;  $D_p = 0.770(3) \text{ cm}^{-1}$ ,  $E_p = 0.090(3) \text{ cm}^{-1}$ ).<sup>[8]</sup> From Equation (9), the contribution of  $\text{Fe}_c$  amounts to only  $-0.08 \text{ cm}^{-1}$ , and hence about 75 % of the observed anisotropy is due to  $\text{Fe}_p$ . Since  $D_p$  is positive, the hard axis of  $\mathbf{D}_p$  must lie roughly perpendicular to the molecular axis  $Z$ . An anisotropy parameter  $D = -0.41 \text{ cm}^{-1}$  is indeed calculated by setting  $\beta' = 90^\circ$  and  $\gamma = 90^\circ$ , that is, assuming the easy axis of  $\mathbf{D}_p$  to be exactly parallel to  $Z$ .<sup>[8]</sup>

According to Equation (9), a variation in  $D$  can be triggered by two main mechanisms: 1) modulation of the  $D_c$  parameter and 2) modulation of the magnitude and/or orientation of the anisotropy tensors for the peripheral metal ions. In the series **1–10**, the observed changes in helical pitch are mainly due to different trigonal rotations, and are accompanied only by small variations in  $\theta$  (Figure 4). According to

ligand-field calculations with the angular overlap model,<sup>[21]</sup> distortions by trigonal rotation or trigonal elongation generate an easy-axis anisotropy in pseudo-octahedral high-spin iron(III) complexes.<sup>[7,22]</sup> We thus expect that the increase in helical pitch is accompanied by an enhancement of the easy-axis anisotropy of the central ion. Notice that a concomitant slight enhancement of trigonal elongation is observed (see inset in Figure 4), which also reinforces the easy-axis anisotropy. By contrast, the trigonal compression exhibited by **11** and **12**, which have the smallest helical pitch in the series, is known to result in hard-axis anisotropy<sup>[7,22]</sup> and thus contributes to further reduce the magnitude of the  $D_c$  parameter. However, the observed  $D$  modulation (from  $-0.45$  to  $-0.21 \text{ cm}^{-1}$ ) cannot be ascribed solely to the anisotropy of the central ion. In fact, it would imply an unrealistically large variation of zfs for a  $^6\text{S}$  ion (ca.  $2 \text{ cm}^{-1}$ ). It follows that the  $\mathbf{D}_p$  tensors undergo significant changes in the series, so that their projection along  $Z$  is progressively reduced with decreasing helical pitch. Such modulation can be most simply described as a reorientation of  $\mathbf{D}_p$  along the Fe–Fe direction, that is, a change in  $\beta'$  in Equation (9).<sup>[8]</sup>

Magnetostructural correlations were previously inferred not only for the  $D$  value but also for the fourth-order axial anisotropy parameter  $B_4^0$  in complexes **5**, **8**, **11**, and **12** based on either single-crystal (**11**, **12**) or powder (**5**, **8**) HF-EPR spectra.<sup>[8]</sup> Thus,  $B_4^0$  was found to be negative in **12**, vanishingly small in **11**, and positive in  $[\text{Fe}_4(\text{L})_2(\text{dpm})_6]$  species **5** and **8**. Additionally, such a trend was shown to be consistent with the effect of reorientation of  $\mathbf{D}_p$  tensors.<sup>[8]</sup> It is now rewarding to find that all complexes of the  $[\text{Fe}_4(\text{L})_2(\text{dpm})_6]$  series have a positive  $B_4^0$  parameter, as expected from their very similar helical pitch.<sup>[8]</sup> The large apparent variations observed (from  $0.8 \times 10^{-5}$  to  $2.4 \times 10^{-5} \text{ cm}^{-1}$ , see Tables 1 and 3) must be taken with great care. In fact, the  $B_4^0$  estimates based on simulation of powder data are subject to large uncertainties ( $\pm 0.5 \times 10^{-5} \text{ cm}^{-1}$ ) because of the small spin value ( $S=5$ ) and strong correlation with the  $D$  parameter. A reliable analysis of the  $B_4^0$  versus  $\gamma$  relationship requires a complete series of single-crystal studies, which lies beyond the scope of this work.

## Conclusions

We have reported the synthesis and structural and magnetic characterization of four new tetrairon(III) propellers **1–4**. In particular, we developed a route to chiral tripodal ligands which afforded for the first time a  $\text{Fe}_4$  cluster containing enantiopure organic ligands (**3**). HF-EPR analysis allowed us to corroborate the dependence of the axial anisotropy parameter  $D$  on propeller pitch over a series of twelve complexes. The relationship is directly demonstrated by **1**, the first  $\text{Fe}_4$  cluster to feature both structurally and magnetically (according to EPR) inequivalent molecules in the crystal. Measurement of the magnetization dynamics by ac susceptibility confirmed SMM behavior for **1–4** and revealed enhanced underbarrier tunneling in **2** and **3**, which have the

largest rhombic  $E$  parameter. Interestingly, a single relaxation time was detected for **1**, **2**, and **4** within experimental resolution. By contrast, two relaxation mechanisms were resolved for **3**, which consists of two cocrystallized diastereoisomers that cannot be distinguished in EPR spectra. Simulations of the temperature dependence of the relaxation time by a master-matrix approach found a rewarding consistency between the effective barrier observed in compounds **2** and **3** (slow-relaxing species) and the spin-Hamiltonian parameters evaluated by HF-EPR. However, even assuming unresolved differences in fourth-order transverse anisotropy terms, the occurrence of a fast-relaxing species in **3** could not be accounted for by such calculations. Our results suggest that higher order anisotropy terms, which escape detection in HF-EPR spectra, may play a significant role in the dynamics of these tetrairon(III) SMMs.

## Experimental Section

**Synthesis:** All compounds were of commercial grade and used as received. Compound **12**,<sup>[8]</sup> 3,3-bis(hydroxymethyl)oxetane,<sup>[15]</sup> 2-allyloxy-methyl-2-hydroxymethylpropane-1,3-diol ( $H_3L^1$ ),<sup>[15g,h]</sup> and 11-(acetylthio)-2,2-bis(hydroxymethyl)undecan-1-ol ( $H_3L^4$ )<sup>[9a]</sup> were prepared by literature methods. Diethyl ether from a freshly opened can was pretreated with  $CaCl_2$  overnight, filtered, and distilled from sodium/benzophenone shortly before use. Methanol was carefully dried by treatment with  $Mg/I_2$  and distilled prior to use.<sup>[23]</sup> 1,2-Dimethoxyethane (DME) was distilled from NaH. Elemental analysis was carried out on a CE Instruments EA1110 analyzer. NMR spectra were recorded with a Bruker FT-DPX200 NMR spectrometer.

**(*R,S*)-2-Hydroxymethyl-2-(2-methyl-butoxymethyl)propane-1,3-diol ( $H_3L^2$ ):** A solution of 3,3-bis(hydroxymethyl)oxetane (0.600 g, 5.08 mmol) in (*R,S*)-2-methyl-1-butanol (2.6 mL) was added dropwise to a stirred solution of sodium (*R,S*)-2-methyl-1-butoxide, obtained by dissolving sodium metal (0.050 g, 2.2 mmol) in (*R,S*)-2-methyl-1-butanol (4.0 mL) under  $N_2$ . The reaction was refluxed under  $N_2$  overnight and cooled to room temperature. Excess alcohol was removed under reduced pressure and the crude material was purified by column chromatography on silica gel ( $CH_2Cl_2$ :MeOH 9:1) to yield  $H_3L^2$  as a colorless oil (0.330 g, 32%).  $^1H$  NMR (200 MHz,  $CDCl_3$ , 30 °C, TMS):  $\delta$  = 0.85 (d,  $^3J(H,H)$  = 6.6 Hz, 3H,  $CH_3CH$ ), 0.86 (t,  $^3J(H,H)$  = 7.4 Hz, 3H,  $CH_3CH_2$ ), 1.01–1.47 (m, 2H,  $CH_2CH_2$ ), 1.53–1.69 (m, 1H,  $CH_3CH$ ), 3.18 (dd,  $^2J(H,H)$  = 9.2 Hz,  $^3J(H,H)$  = 5.7 Hz, 1H,  $OCH_2CH$ ), 3.26 (dd,  $^2J(H,H)$  = 9.2 Hz,  $^3J(H,H)$  = 6.4 Hz, 1H,  $OCH_2CH$ ), 3.37 (brs, 3H,  $CH_2OH$ ), 3.40 (s, 2H,  $C^{IV}CH_2O$ ), 3.66 ppm (s, 6H,  $CH_2OH$ );  $^{13}C$  NMR (200 MHz,  $CDCl_3$ , 30 °C, TMS)  $\delta$  = 77.33 ( $OCH_2CH$ ), 73.72 ( $C^{IV}CH_2O$ ), 64.15 ( $CH_2OH$ ), 45.14 ( $C^{IV}$ ), 34.89 (CH), 26.31 ( $CH_2CH_3$ ), 16.65 ( $CH_3CH$ ), 11.35 ppm ( $CH_3CH_2$ ).

**(*S*)-2-Hydroxymethyl-2-(2-methyl-butoxymethyl)propane-1,3-diol ( $H_3L^3$ ):** The same procedure as above using (*S*)-2-methyl-1-butanol afforded  $H_3L^3$  as a colorless oil (0.314 g, 30%) showing identical NMR features.

**[ $Fe_4(L^1)_2(dpm)_6$ ] (**1**):** Compound **12** (0.061 g, 0.041 mmol) was dissolved in dry  $Et_2O$  (25 mL) to give a yellow solution. A solution of triol  $H_3L^1$  (0.037 g, 0.21 mmol) in dry methanol (0.2 mL) was added while stirring. Vapor diffusion of dry methanol (40 mL) into the clear yellow solution afforded yellow-orange prisms of **1**, which were washed with the external diffusion mixture, then with dry methanol, and vacuum dried (0.056 g, 82%). Elemental analysis calcd (%) for  $C_{82}H_{140}Fe_4O_{20}$ : C 59.00, H 8.45; found: C 59.13, H, 8.74.

**[ $Fe_4(L^2)_2(dpm)_6$ ] (**2**):** Compound **12** (0.060 g, 0.040 mmol) was dissolved in dry  $Et_2O$  (25 mL) to give a yellow solution. A solution of triol  $H_3L^2$  (0.022 g, 0.11 mmol) was added while stirring and the product was crystallized by slow vapor diffusion of dry methanol (40 mL) into the clear yellow solution. Yellow-orange rods of **2** were isolated as described for **1**

(0.061 g, 88%). Elemental analysis calcd (%) for  $C_{86}H_{152}Fe_4O_{20}$ : C 59.72, H 8.86; found: C 59.52, H, 9.14.

**[ $Fe_4(L^3)_2(dpm)_6$ ] (**3**):** The product was synthesized in 43% yield as described for **2** by using ligand  $H_3L^3$ . Elemental analysis calcd (%) for  $C_{86}H_{152}Fe_4O_{20}$ : C 59.72, H 8.86; found: C 59.43, H, 9.09.

**[ $Fe_4(L^4)_2(dpm)_6$ ] (**4**):** Compound **12** (0.120 g, 0.0795 mmol) was dissolved in dry  $Et_2O$  (50 mL) to give a yellow solution. Triol  $H_3L^4$  (0.065 g, 0.21 mmol) was added and the solution was stirred until complete dissolution. Complete evaporation of the solvent over 4 days afforded a poorly crystalline solid, which was extensively washed with dry methanol until the washings were colorless and dried under vacuum (0.133 g). The solid was dissolved in dry DME (1.5 mL) and the solution was left undisturbed to allow slow evaporation of the solvent over two weeks. The large yellow-orange prisms thus obtained were washed with DME: MeOH (1:5 and 1:10 v/v) and dried under nitrogen flux (0.120 g, 78%). Elemental analysis calcd (%) for  $C_{96}H_{168}Fe_4O_{20}S_2$ : C 59.75, H 8.77, S 3.32; found: C 60.06, H 8.92, S 3.47.

**X-ray structures:** Structure determinations on **1–4** were carried out at 120(2) K on a four-circle Bruker-Nonius X8 APEX diffractometer, equipped with  $Mo_{K\alpha}$  radiation and a Kryoflex nitrogen flow cryostat. The structures were solved by direct methods using the SIR92<sup>[24a]</sup> program. Full-matrix (or block-matrix for **1**) least-squares refinement on  $F_o^2$  was performed with the SHELXL-97 program<sup>[24b]</sup> implemented in the WINGX suite.<sup>[24c]</sup> All non-hydrogen atoms were refined anisotropically, with the exception of few disordered moieties. Hydrogen atoms were treated as riding contributors with isotropic displacement parameters. These were fixed to  $U_H = pU_{iso}(C)$  where  $p = 1.2$  for methine, aromatic, and trimethylol hydrogen atoms, and  $p = 1.5$  for the remaining H atoms. Restraints were applied to the geometry and displacement parameters of some disordered moieties. Refinement of the Flack parameter for **3** afforded 0.020(11) and 0.763(14) for the normal and inverted models, respectively, and unambiguously proved the correctness of the absolute structure, which entails tripodal ligands in the  $S$  form. Structure refinement of **1** was particularly challenging and is herein described in detail. The unit cell was found to be metrically monoclinic within experimental error ( $a = 38.1028(11)$ ,  $b = 15.9276(5)$ ,  $c = 30.3680(9)$  Å,  $\alpha = 90.000(1)$ ,  $\beta = 91.140(1)$ ,  $\gamma = 90.007(1)^\circ$  on 8126 reflections with no metrical constraints). The diffraction pattern averaged satisfactorily to  $2/m$  symmetry with  $R(\text{int}) = 0.0377$ . Reflections appeared as very narrow and free of any resolvable splittings. The analysis of systematic absences pointed clearly to monoclinic space group  $P2_1/c$ . Structure solution showed the presence of two independent molecules in the asymmetric unit (Fe1–Fe4 and Fe5–Fe8). Refinement gave  $wR2 = 0.2847$  and  $R1 = 0.0934$ , with three large electron-density residuals (5.7–2.2) close to three iron atoms of an  $Fe_4$  molecule (Fe1–Fe4), and several additional peaks greater than  $1 e \text{ \AA}^{-3}$ . Attempts to individuate possible pseudomerohedral twinning laws using the program ROTAX<sup>[24d]</sup> were unsuccessful. A careful examination of  $\Delta F$  maps also showed the presence of residuals close to oxygen atoms of  $\beta$ -diketonate ligands, suggesting the occurrence of major disorder effects. Preliminary fitting of the largest residuals showed about 10–15% of molecule Fe1–Fe4 to be disordered, with the minority component being approximately obtained from Fe5–Fe8 by inversion around (0.75, 0.50, 0.75). Due to its extensive overlap with Fe1–Fe4, this minority component (Fe9–Fe12) was then restrained to have the same geometry as Fe5–Fe8, with allowed deviations of 0.01 and 0.02 Å for 1–2 and 1–3 interatomic distances, respectively. For simplicity, isotropic displacement parameters in molecule Fe9–Fe12 were held fixed to values comparable to those observed for corresponding atoms in Fe5–Fe8. Final refinement afforded  $wR2 = 0.1991$  and  $R1 = 0.0662$ .

CCDC-721125, CCDC-721126, CCDC-721127, and CCDC-721128 contain the supplementary crystallographic data for this paper. These data can be obtained free of charge from The Cambridge Crystallographic Data Centre via [www.ccdc.cam.ac.uk/data\\_request/cif](http://www.ccdc.cam.ac.uk/data_request/cif).

**Physical techniques:** Magnetic data for polycrystalline samples of **1** (20.80 mg), **2** (14.82 mg), **3** (11.38 mg), and **4** (11.20 mg) were recorded on a Cryogenic S600 SQUID magnetometer. Magnetic susceptibilities were measured in applied fields of 1 kOe from 1.9 to 30 K and 10 kOe from 30 K to 300 K. Magnetization was also measured at 1.9, 2.5, and

4.5 K in fields up to 50 kOe. Data reduction was carried out by using the following molecular weights and diamagnetic contributions (estimated from Pascal's constants): for **1**, 1669.3 and  $-952 \times 10^{-6}$  emu mol<sup>-1</sup>; for **2** and **3**, 1729.5 and  $-1023 \times 10^{-6}$  emu mol<sup>-1</sup>; for **4**, 1929.8 and  $-1147 \times 10^{-6}$  emu mol<sup>-1</sup>. Alternating-current susceptibility was measured on microcrystalline powder samples using an Oxford Instruments MAGLAB platform equipped with a laboratory-developed probe based on the inductance between a primary and a secondary coil. HF-EPR spectra were recorded at the Grenoble High Magnetic Field Laboratory on a home-built spectrometer working in single-pass configuration at temperatures ranging from 5 to 30 K. Gunn diodes operating at 95 or 115 GHz, equipped with a frequency doubler, were used as source excitation. The polycrystalline samples used for the experiments were pressed into a pellet to avoid orientation effects. Simulation of HF-EPR spectra and spin-Hamiltonian calculations were carried out with dedicated software, as described elsewhere.<sup>[9a,25]</sup>

### Acknowledgements

The work was financed by NE MAGMANET (FP6-NMP3-CT-2005-515767), EC-RTN QuEMolNa (FP6-CT-2003-504880), ERANET project "NanoSci-ERA: NanoScience in the European Research Area" (SMMTRANS), as well as by Italian PRIN and FIRB grants. Dr. L. Sorace and Dr. F. Pineider are acknowledged for assistance in HF-EPR spectra simulation and in magnetic characterization, respectively.

- [1] a) D. Gatteschi, R. Sessoli, J. Villain, *Molecular Nanomagnets*, Oxford University Press, Oxford, **2006**; b) *Single-Molecule Magnets and Related Phenomena, Structure and Bonding Book Series, Vol. 122* (Ed.: R. E. P. Winpenny), Springer, Berlin, **2006**.
- [2] L. Bogani, W. Wernsdorfer, *Nat. Mater.* **2008**, *7*, 179–186.
- [3] a) J. Lawrence, E.-C. Yang, R. Edwards, M. M. Olmstead, C. Ramsey, N. S. Dalal, P. K. Gantzel, S. Hill, D. N. Hendrickson, *Inorg. Chem.* **2008**, *47*, 1965–1974; b) E.-C. Yang, W. Wernsdorfer, L. N. Zakharov, Y. Karaki, A. Yamaguchi, R. M. Isidro, G.-D. Lu, S. Wilson, A.-L. Rheingold, H. Ishimoto, D. N. Hendrickson, *Inorg. Chem.* **2006**, *45*, 529–546; c) A. Wilson, J. Lawrence, E. C. Yang, M. Nakano, D. N. Hendrickson, S. Hill, *Phys. Rev. B* **2006**, *74*, 140403(R)/1–4; d) E.-C. Yang, C. Kirman, J. Lawrence, L. N. Zakharov, A. L. Rheingold, S. Hill, D. N. Hendrickson, *Inorg. Chem.* **2005**, *44*, 3827–3836.
- [4] a) W. Wernsdorfer, N. Aliaga-Alcade, D. N. Hendrickson, G. Christou, *Nature* **2002**, *416*, 406–409; b) S. Hill, R. S. Edwards, N. Aliaga-Alcade, G. Christou, *Science* **2003**, *302*, 1015–1018.
- [5] a) C. J. Milios, A. Vinslava, W. Wernsdorfer, S. Moggach, S. Parsons, S. P. Perlepes, G. Christou, E. K. Brechin, *J. Am. Chem. Soc.* **2007**, *129*, 2754–2755; b) C. J. Milios, R. Inglis, A. Vinslava, R. Bagai, W. Wernsdorfer, S. Parsons, S. P. Perlepes, G. Christou, E. K. Brechin, *J. Am. Chem. Soc.* **2007**, *129*, 12505–12511.
- [6] a) A.-L. Barra, A. Caneschi, A. Cornia, D. Gatteschi, L. Gorini, L.-P. Heiniger, R. Sessoli, L. Sorace, *J. Am. Chem. Soc.* **2007**, *129*, 10754–10762; b) N. E. Chakov, S.-C. Lee, A. G. Harter, P. L. Kuhns, A. P. Reyes, S. Hill, N. S. Dalal, W. Wernsdorfer, K. A. Abboud, G. Christou, *J. Am. Chem. Soc.* **2006**, *128*, 6975–6989; c) A. Cornia, R. Sessoli, L. Sorace, D. Gatteschi, A.-L. Barra, C. Daiguebonne, *Phys. Rev. Lett.* **2002**, *89*, 257201/1–4.
- [7] A.-L. Barra, A. Caneschi, A. Cornia, F. Fabrizi de Biani, D. Gatteschi, C. Sangregorio, R. Sessoli, L. Sorace, *J. Am. Chem. Soc.* **1999**, *121*, 5302–5310.
- [8] S. Accorsi, A.-L. Barra, A. Caneschi, G. Chastanet, A. Cornia, A. C. Fabretti, D. Gatteschi, C. Mortalò, E. Olivieri, F. Parenti, P. Rosa, R. Sessoli, L. Sorace, W. Wernsdorfer, L. Zoppi, *J. Am. Chem. Soc.* **2006**, *128*, 4742–4755.
- [9] a) A.-L. Barra, F. Bianchi, A. Caneschi, A. Cornia, D. Gatteschi, L. Gorini, L. Gregoli, M. Maffini, F. Parenti, R. Sessoli, L. Sorace, A. M. Talarico, *Eur. J. Inorg. Chem.* **2007**, 4145–4152; b) M. Mannini, F. Pineider, P. Saintavit, L. Joly, A. Fraile-Rodriguez, M.-A. Arrio, C. Cartier dit Moulin, W. Wernsdorfer, A. Cornia, D. Gatteschi, R. Sessoli, *Adv. Mater.* **2009**, *21*, 167–171; c) M. Mannini, F. Pineider, P. Saintavit, C. Danieli, E. Otero, C. Sciancalepore, A. M. Talarico, M.-A. Arrio, A. Cornia, D. Gatteschi, R. Sessoli, *Nat. Mater.* **2009**, *8*, 194–197.
- [10] a) E. K. Brechin, *Chem. Commun.* **2005**, 5141–5153; b) M. Moragues-Cánovas, E. Rivière, L. Ricard, C. Paulsen, W. Wernsdorfer, G. Rajaraman, E. K. Brechin, T. Mallah, *Adv. Mater.* **2004**, *16*, 1101–1105; c) C. Schlegel, J. van Slageren, M. Manoli, E. K. Brechin, M. Dressel, *Phys. Rev. Lett.* **2008**, *101*, 147203/1–4; d) R. W. Saalfrank, I. Bernt, M. M. Chowdhry, F. Hampel, G. B. M. Vaughan, *Chem. Eur. J.* **2001**, *7*, 2765–2769; e) N. T. Madhu, J.-K. Tang, I. J. Hewitt, R. Clérac, W. Wernsdorfer, J. van Slageren, C. E. Anson, A. K. Powell, *Polyhedron* **2005**, *24*, 2864–2869; f) R. W. Saalfrank, A. Scheurer, I. Bernt, F. W. Heinemann, A. V. Postnikov, V. Schöne-mann, A. X. Trautwein, M. S. Alam, H. Rupp, P. Müller, *Dalton Trans.* **2006**, 2865–2874.
- [11] A. Cornia, A. C. Fabretti, P. Garrisi, C. Mortalò, D. Bonacchi, D. Gatteschi, R. Sessoli, L. Sorace, W. Wernsdorfer, A.-L. Barra, *Angew. Chem.* **2004**, *116*, 1156–1159; *Angew. Chem. Int. Ed.* **2004**, *43*, 1136–1139.
- [12] A. Cornia, L. Gregoli, C. Danieli, A. Caneschi, R. Sessoli, L. Sorace, A.-L. Barra, W. Wernsdorfer, *Inorg. Chim. Acta* **2008**, *361*, 3481–3488.
- [13] a) G. G. Condorelli, A. Motta, G. Pellegrino, A. Cornia, L. Gorini, I. L. Fragalà, C. Sangregorio, L. Sorace, *Chem. Mater.* **2008**, *20*, 2405–2411; b) Unpublished data; c) L. Bogani, C. Danieli, E. Biavardi, N. Bendiab, A.-L. Barra, E. Dalcanele, W. Wernsdorfer, A. Cornia, *Angew. Chem.* **2009**, *121*, 760–764; *Angew. Chem. Int. Ed.* **2009**, *48*, 746–750.
- [14] a) O. C. Dermer, P. W. Solomon, *J. Am. Chem. Soc.* **1954**, *76*, 1697–1699; b) L. Beaufort, L. Delaude, A. F. Noels, *Tetrahedron* **2007**, *63*, 7003–7008; c) J. Haldar, P. Kondaiah, S. Bhattacharya, *J. Med. Chem.* **2005**, *48*, 3823–3831; d) T. J. Dunn, W. L. Neumann, M. M. Rogic, S. R. Woulfe, *J. Org. Chem.* **1990**, *55*, 6368–6373; e) Y. Ozoe, M. Eto, *Agric. Biol. Chem.* **1982**, *46*, 411–418; f) P. Schober, G. Huttner, L. Zsolnai, A. Jacobi, *J. Organomet. Chem.* **1998**, *571*, 279–288; g) G. R. Newkome, Z. Yao, G. R. Baker, V. K. Gupta, *J. Org. Chem.* **1985**, *50*, 2003–2004.
- [15] a) J. W. Han, K. I. Hardcastle, C. L. Hill, *Eur. J. Inorg. Chem.* **2006**, 2598–2603; b) X. Qian, F. Liu, *Tetrahedron Lett.* **2003**, *44*, 795–799; c) G. R. Newkome, G. R. Baker, S. Arai, M. J. Saunders, P. S. Russo, K. J. Theriot, C. N. Moorefield, L. E. Rogers, J. E. Miller, *J. Am. Chem. Soc.* **1990**, *112*, 8458–8465; d) Y.-F. Song, D.-L. Long, L. Cronin, *Angew. Chem. Int. Ed.* **2007**, *46*, 3900–3904; e) I. A. Gorodetskaya, T.-L. Choi, R. H. Grubbs, *J. Am. Chem. Soc.* **2007**, *129*, 12672–12673; f) M. Lee, Y.-S. Jeong, B.-K. Cho, N.-K. Oh, W.-C. Zin, *Chem. Eur. J.* **2002**, *8*, 876–883; g) R. A. Findeis, L. H. Gade, *Dalton Trans.* **2003**, 249–254; h) J. A. Camerano, M. A. Casado, M. A. Ciriano, F. J. Lahoz, L. A. Oro, *Organometallics* **2005**, *24*, 5147–5156; i) H. Reiff, D. Dietrich, R. Braden, H. Ziemann, *Justus Liebig's Ann. Chem.* **1973**, 365–374; j) J. Cheymol, P. Chabrier, J. Seyden-Penne, *Bull. Soc. Chim. Fr.* **1959**, 1184–1185; k) C. H. Issidorides, A. I. Matar, *J. Am. Chem. Soc.* **1955**, *77*, 6382–6383.
- [16] a) C. Schaal, *Bull. Soc. Chim. Fr.* **1969**, *6*, 2136–2140; b) J. Cheymol, P. Chabrier, J. Seyden-Penne, C. Schaal, *Compt. Rend.* **1965**, *260*, 2836–2838; c) Z.-X. Jiang, Y. B. Yu, *J. Org. Chem.* **2007**, *72*, 1464–1467; d) I. García-Álvarez, G. Corrales, E. Doncel-Pérez, A. Muñoz, M. Nieto-Sampedro, A. Fernández-Mayoralas, *J. Med. Chem.* **2007**, *50*, 364–373.
- [17] A. Abragam, B. Bleaney, *Electron Paramagnetic Resonance of Transition Ions*, Dover, New York, **1986**.
- [18] D. Gatteschi, R. Sessoli, *Angew. Chem.* **2003**, *115*, 278–309; *Angew. Chem. Int. Ed.* **2003**, *42*, 268–297.
- [19] a) F. Hartmann-Boutron, P. Politi, J. Villani, *Int. J. Mod. Phys. B* **1996**, *10*, 2577–2637; b) J. Villain, F. Hartmann-Boutron, R. Sessoli, A. Rettori, *Europhys. Lett.* **1994**, *27*, 159–164.

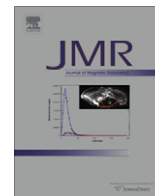
- [20] A. Bencini, D. Gatteschi, *EPR of Exchange Coupled Systems*, Springer, Berlin, **1990**.
- [21] a) C. E. Schäffer, *Struct. Bonding (Berlin)* **1968**, 5, 68–95; b) A. Bencini, I. Ciofini, M. G. Uytterhoeven, *Inorg. Chim. Acta* **1998**, 274, 90–101.
- [22] D. Gatteschi, L. Sorace, *J. Solid State Chem.* **2001**, 159, 253–261.
- [23] A. I. Vogel, *Practical Organic Chemistry*, Longman, London, **1959**.
- [24] a) A. Altomare, G. Cascarano, C. Giacovazzo, A. Guagliardi, *J. Appl. Crystallogr.* **1993**, 26, 343–350; b) G. M. Sheldrick, SHELX97, Programs for Crystal Structure Analysis (Release 97-2), University of Göttingen, Göttingen, Germany, **1997**; c) L. J. Farrugia, *J. Appl. Crystallogr.* **1999**, 32, 837–838; d) R. I. Cooper, R. O. Gould, S. Parsons, D. J. Watkin, *J. Appl. Crystallogr.* **2002**, 35, 168–174.
- [25] C. J. H. Jacobsen, E. Pedersen, J. Villadsen, H. Weihe, *Inorg. Chem.* **1993**, 32, 1216–1221.

Received: February 21, 2009  
Published online: May 21, 2009

**COMMENTED PAPER 6**

F. El Hallak, **P. Neugebauer**, A.-L. Barra, J. van Slageren, M. Dressel, A. Cornia  
Torque-detected ESR of a tetrairon(III) single molecule magnet

*J. Magn. Reson.*, 223, 55 - 60 (2012).



## Torque-detected ESR of a tetrairon(III) single molecule magnet

Fadi El Hallak<sup>a</sup>, Petr Neugebauer<sup>b,1</sup>, Anne-Laure Barra<sup>b</sup>, Joris van Slageren<sup>c</sup>, Martin Dressel<sup>a</sup>, Andrea Cornia<sup>d,\*</sup>

<sup>a</sup> 1. Physikalisches Institut, Universität Stuttgart, D-70550 Stuttgart, Germany

<sup>b</sup> LNCMI-CNRS and Université Joseph Fourier, F-38042 Grenoble, Cedex 9, France

<sup>c</sup> Institut für Physikalische Chemie, Universität Stuttgart, D-70569 Stuttgart, Germany

<sup>d</sup> Department of Chemical and Geological Sciences & INSTM Research Unit, University of Modena and Reggio Emilia, via G. Campi 183, I-41125 Modena, Italy

### ARTICLE INFO

#### Article history:

Received 10 July 2012

Available online 21 August 2012

#### Keywords:

Single molecule magnets

Torque magnetometry

ESR spectroscopy

Magnetic anisotropy

### ABSTRACT

Single-crystal studies on anisotropic ESR-active materials can be conveniently carried out using torque-detected (TD) ESR, a novel technique which brings to ESR the sensitivity typical of torque magnetometry (TM). This method, which is easily operated in high magnetic fields and in a wide range of frequencies, was applied to investigate magnetic anisotropy in crystals of a tetrairon(III) single-molecule magnet with an  $S = 5$  ground state. TDESER was supported by TM measurements carried out in situ and provided an accurate estimate of the second-order axial anisotropy parameter  $D$  and of the longitudinal fourth-order contribution  $B_4^0$ . The results were validated through a parallel angle-resolved investigation by traditional high-frequency ESR on the same material.

© 2012 Elsevier Inc. All rights reserved.

### 1. Introduction

Magnetic anisotropy is an essential ingredient of the behavior of many magnetic materials, including molecules known as Single Molecule Magnets (SMMs). In these materials, an axial Ising-type anisotropy produces an energy barrier to magnetic moment reversal and results in slow magnetic relaxation at low temperatures ( $T$ ) [1]. Transverse anisotropy components also play a key role in causing tunneling through the barrier in a strongly field- and symmetry-dependent fashion [2]. To date the most powerful method to investigate magnetic anisotropy in SMMs is electron spin resonance (ESR) operated at high frequencies and in high fields (HFESR) to fully reveal the fine structure of the ground spin state [3–6]. Sensitivity and accessible frequency ranges are crucial parameters for HFESR. Cavity perturbation techniques can be used to detect magnetic resonance transitions on single crystal samples at frequencies up to 700 GHz, but these spectrometers are limited to discrete frequencies or very narrow frequency ranges [7,8]. On the other hand, broad band methods, such as frequency domain magnetic resonance spectroscopy (FDMRS) [9–11] suffer from their low sensitivity. Indeed, measurements performed on single crystals of SMMs using FDMRS are very rare, and only studies on single-crystal mosaics have been published [12,13].

As an alternative, magnetic resonance transitions can be detected by measuring magnetization changes induced by the absorption of radiation [10], a technique introduced more than 40 years ago [14]. To this aim, different magnetic sensors were used to probe the effect of microwave irradiation off and on resonance, including SQUIDs [15], micro-SQUIDs [16], and Hall bars [17,18]. SQUIDs and micro-SQUIDs are highly sensitive but they have a slow response time and, in addition, cannot be operated in very high magnetic field (above 8 T for SQUIDs and much less for micro-SQUIDs). On the contrary, Hall bars are highly sensitive and have a fast response time. In any case, use of these setups was so far limited to either single frequencies or very narrow frequency ranges.

We have now combined our experience in FDMRS and torque magnetometry to develop a novel tool for magnetic characterization which has been named torque-detected ESR (TDESER). Technical details have been already presented elsewhere [19]. Torque magnetometry (TM) measures the mechanical couple experienced by a magnetic sample in a homogeneous magnetic field ( $\mathbf{H}$ ) due to the noncollinearity between  $\mathbf{H}$  and the magnetization ( $\mathbf{M}$ ), i.e. due to the presence of transverse magnetization [20]. When the sample has a permanent magnetic moment, the torque signal allows measuring the magnetization directly. For a paramagnet, the appearance of a transverse magnetization is a consequence of magnetic anisotropy. In a paramagnetic molecule with  $N$  thermally accessible spin states, the component of the torque signal along a given axis  $\alpha$  is:

$$\tau_{\alpha} = \frac{\sum_{i=1}^N \tau_{i,\alpha} \exp(-E_i/k_B T)}{\sum_{i=1}^N \exp(-E_i/k_B T)} \quad (1)$$

\* Corresponding author. Fax: +39 059 373543.

E-mail address: [acornia@unimore.it](mailto:acornia@unimore.it) (A. Cornia).

<sup>1</sup> Present address: Institute of Physical and Theoretical Chemistry, Goethe University Frankfurt, Max-von-Laue-Str. 7, D-60438 Frankfurt am Main, Germany.

where  $E_i$  is the energy of the  $i$ th spin state (in general, a function of the spin Hamiltonian parameters and of the applied magnetic field),  $k_B$  is the Boltzmann constant and:

$$\tau_{i,z} = - \left( \frac{\partial E_i}{\partial \theta_z} \right)_{\mathbf{H}} \quad (2)$$

is the contribution provided to the torque by the  $i$ th state. Here,  $\theta_z$  is the angle used to describe the rotation of the sample around the  $z$ -axis. Resonant absorption of microwave (MW) radiation changes the population of the states with respect to Boltzmann distribution in a way which depends on the transition probabilities, on the MW power, and on the spin–lattice relaxation time. It consequently leads to a change in the torque signal, which can be used to detect magnetic resonance transitions. The torque signal was measured here by using a highly sensitive CuBe cantilever, which enables studying very small single crystals. The cantilever response is fast compared with commercial SQUIDS, and the device can be operated up to high magnetic fields and in a broad frequency range. Furthermore, the MW radiation has virtually no effect on the measured torque values off resonance. Finally, conventional torque measurements performed in advance on the crystal of interest “in situ” provide an initial estimate of the magnitude and orientation of the anisotropy tensor. As a disadvantage, the torque signal – and consequently the sensitivity of TDESr – is strongly dependent upon the applied field direction because all torque components vanish whenever the field lies along a principal magnetic direction [20]. Under these special conditions the technique cannot be used. However, by properly adjusting the field orientation, TDESr can be made several orders of magnitude more sensitive than FDMRS.

We herein present a combined study by TM, TDESr and HFESr on a single crystal of  $[\text{Fe}_4(\text{L})_2(\text{dpm})_6]$  (**1**) where Hdpm is 2,2,6,6-tetramethyl-3,5-heptanedione (also known as dipivaloylmethane) and  $\text{H}_3\text{L}$  is the tripodal ligand (*R,S*)-2-hydroxymethyl-2-(2-methyl-butoxymethyl)propane-1,3-diol [21]. Among SMMs of the  $\text{Fe}_4$  family, this particular derivative was chosen because it exhibits very narrow lines in the HFESr spectra recorded on a powder sample [21]. Moreover, all molecules in the crystal are magnetically equivalent and iso-oriented, a most favorable situation for single-crystal studies (see below).

The crystal structure of **1**, as determined by single-crystal X-ray diffraction at 120(2) K [21], has monoclinic symmetry and belongs to space group  $P2_1/n$  with  $a = 17.0632(7)$ ,  $b = 15.5838(7)$ ,  $c = 19.5691(8)$  Å and  $\beta = 110.600(1)^\circ$ . The molecular structure viewed perpendicular to the metal plane and along the **b** crystal axis is shown in Fig. 1a and b, respectively. The system consists of four  $\text{Fe}^{3+}$  ions ( $s_f = 5/2$ ) that are antiferromagnetically coupled to give a ground total spin state of  $S = 5$ . Regarding the 2-methyl-butoxymethyl residues on tripodal ligands, the molecule has approximate axial ( $D_3$ ) symmetry along the normal to the metal plane (**n**), which is thus expected to be close to the unique (easy) magnetic axis of the system.

The crystallographic symmetry, however, is  $C_2$  and the twofold axis is directed along the line joining Fe1 and Fe2, which is parallel to the **b** axis of the unit cell. Therefore,  $\text{Fe1} \cdots \text{Fe2}$  must represent a principal direction ( $y$ ) for the second-order anisotropy tensor of the  $S = 5$  state, the easy axis ( $z$ ) and the third principal direction ( $x$ ) being forced to lie in the **ac** plane. HFESr spectra recorded on a polycrystalline sample have been previously [21] used to determine the anisotropy parameters appearing in the spin Hamiltonian of Eq. (3) and gathered in Table 1 (entry 1):

$$\hat{H} = \mu_0 \mu_B g \hat{\mathbf{S}} \cdot \hat{\mathbf{H}} + D[\hat{S}_z^2 - S(S+1)/3] + E(\hat{S}_x^2 - \hat{S}_y^2) + B_4^0 \hat{O}_4^0 \quad (3)$$

In Eq. (3),  $D$  and  $E$  are the zero-field splitting parameters that describe second-order axial and rhombic components of anisotropy (the nonaxial molecular symmetry permits  $E \neq 0$ ).  $B_4^0$  is associated with the fourth-order axial operator [1]:

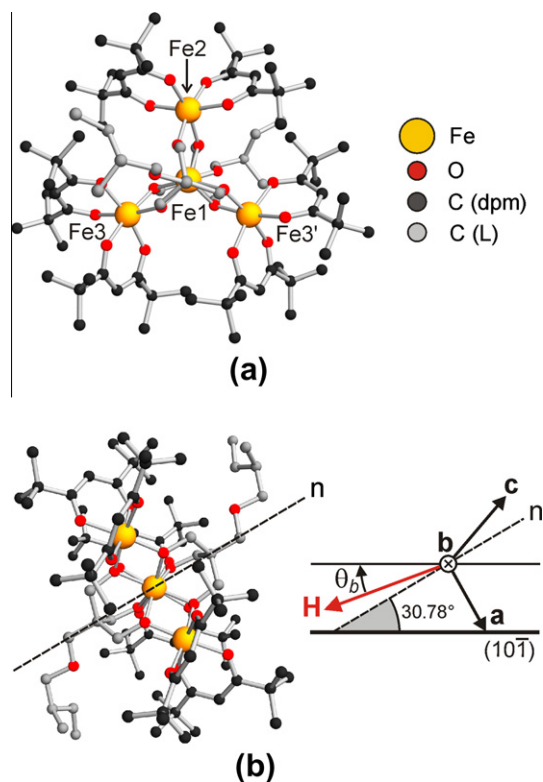


**Fig. 1.** Molecular structure of **1** viewed normal to the metal plane (a) and along the **b** axis (b). Metal centers Fe3 and Fe3' are symmetry related through a crystallographic twofold axis directed along  $\text{Fe1} \cdots \text{Fe2}$ . Hydrogen atoms and disorder effects on the alkyl substituents of tripodal ligands are omitted for clarity. Part (b) includes the unit cell axes (**a–c**) along with the normal to the metal plane (**n**, dashed line), the trace of the (101) face of the crystal (bold line) and the definition of the angle  $\theta_b$  used to describe the rotation of the crystal around the **b** axis. According to the crystal structure, at  $\theta_b = 30.78^\circ$  the field lies along **n**.

$$\hat{O}_4^0 = 35\hat{S}_z^4 + [25 - 30S(S+1)]\hat{S}_z^2 + 3S^2(S+1)^2 - 6S(S+1) \quad (4)$$

The negative  $D$  value and the small  $|E/D|$  ratio (0.067) point to a dominant easy-axis anisotropy, as required for a SMM, while the positive  $B_4^0$  value results in a “compressed” parabolic shape for the anisotropy barrier, as detailed in Ref. [22].

We have investigated a single crystal of **1** using TM to accurately determine the orientation of the easy magnetic axis, and subsequently using TDESr. Magnetic resonance transitions detected as a function of field and frequency have been used to extract the anisotropy parameters of the  $S = 5$  ground state. In the third part of the work, we have studied a single-crystal sample by HFESr, applying the magnetic field along the easy axis and in the hard plane. The parameter sets obtained by the different techniques are in excellent agreement with each other and provide an accurate characterization of magnetic anisotropy in this SMM.

## 2. Experimental

Well-formed monoclinic crystals of **1** were prepared as described in Ref. [21]. The crystals grow as rod-like prisms developed along the [101] zone axis, with (010),  $(\bar{1}01)$ ,  $(0\bar{1}0)$  and  $(10\bar{1})$  as main crystal faces. Technical details of the TDESr setup, which operates in the frequency range 30–1440 GHz ( $1\text{--}48\text{ cm}^{-1}$ ) in fields up to 8 T and at temperatures down to 1.7 K, can be found elsewhere [19]. For the TM and TDESr measurements, a face-indexed single crystal of approximately 100  $\mu\text{m}$

**Table 1**  
Spin Hamiltonian parameters of **1** obtained using different techniques.<sup>a</sup>

Entry	Technique	$g$	$D$ (cm <sup>-1</sup> )	$E$ (cm <sup>-1</sup> )	$10^2 B_4^0$ (cm <sup>-1</sup> )
1	HFESR (powder) <sup>b</sup>	2.00	-0.449(1)	0.030(1) <sup>c</sup>	2.4(5)
2	TM ( $\theta$ dependence) <sup>d</sup>	2.00	-0.4059(2)	0	1.00(3)
3	TM ( $\theta$ dependence) <sup>d</sup>	2.00	-0.4502(2)	-0.038	0.97(3)
4	TM ( $T$ dependence) <sup>d</sup>	2.00	-0.4051(4)	0	1.21(6)
5	TM ( $T$ dependence) <sup>d</sup>	2.00	-0.4490(3)	-0.038	1.42(5)
6	TDES <sup>d</sup>	1.989(2)	-0.4457(7)	0	1.6(1)
7	HFESR (crystal) <sup>d</sup>	2.00	-0.447(3)	-0.038(1)	1.6(6)

<sup>a</sup> Numbers in parentheses are estimated standard deviations (esds) supplied by the least-squares fitting routines (parameters with no esd have been held fixed).

<sup>b</sup> Ref. [21].

<sup>c</sup> Absolute value.

<sup>d</sup> This work.

mass was fixed on the cantilever with vacuum grease and visually aligned using an optical microscope. The accuracy of alignment was estimated to be  $\pm 1^\circ$ . The crystal was oriented with its (10 $\bar{1}$ ) face lying flat on the cantilever and the (010) face perpendicular to the rotation axis of the goniometer. In this way, the rotation was performed around the crystallographic **b** axis and the magnetic field **H** was applied orthogonal to the rotation axis, i.e. in the **ac** plane. The sample orientation is described using the angle  $\theta_b$ , being  $\theta_b = 0$  when the [101] zone axis is parallel to the magnetic field (Fig. 1). In this configuration, the cantilever detects the *b*-component of the torque vector ( $\tau_b$ ) and positive  $\tau_b$  values indicate a tendency of the sample to rotate clockwise in Fig. 1b.

HFESR measurements on a face-indexed single crystal of **1** were performed with the Quasi-Optical setting of the spectrometer, operating in double pass transmission. The exciting frequency of 230 GHz is propagated in the cryostat with a corrugated guide which ends on a taper. A recently developed one-axis rotating holder [23] is attached to the taper, with a flat mirror placed below the sample for the reflection of the exciting frequency. The main feature of the rotating holder results from the use of a rotating piezoelectric micropositioner. It allows rotating over  $\sim 340^\circ$  with an absolute measurement of the angle through the use of a resistive encoder. The transmitted light is then detected with a hot-electron InSb bolometer. The sample was visually oriented and fixed on the support using vacuum grease. The accuracy of initial alignment was estimated to be  $\pm 1^\circ$ . Fitting of the spectra was carried out using a dedicated software [24,25].

### 3. Results and discussion

Angle resolved measurements by TM and TDES have been carried out on face-indexed single crystals of **1** by applying the magnetic field in the **ac** plane and rotating the sample around **b**. The rotation angle ( $\theta_b$ ) was defined as the angle between the magnetic field and the [101] zone axis (Fig. 1b). In Fig. 2a we report the results obtained at  $\mu_0 H = 0.5$  T and  $T = 1.65$  K for a full rotation of the sample. The torque oscillates with a  $180^\circ$  period and vanishes at  $90^\circ$  intervals of  $\theta_b$  when the field lies along the principal magnetic directions in the **ac** plane. The angles of zero torque are reproduced by the expression  $33.4(3)^\circ + n \times 90^\circ$  ( $n = \text{integer}$ ), the intercept being close to the orientation of **n** calculated from the crystal structure ( $\theta_b = 30.78^\circ$ ). Furthermore, the positive  $\tau_b$  value measured at  $\theta_b = 0$  indicates that the sample tends to rotate so as to bring **n** along the applied field. Hence, considering the precision with which the crystal was visually aligned ( $\pm 1^\circ$ ), the easy axis (*z*) is very close to **n** and the *x* direction consequently lies essentially in the plane of the metals.

Isothermal torque curves were also measured for fields up to 8 T applied close to the hard plane. This arrangement is convenient as

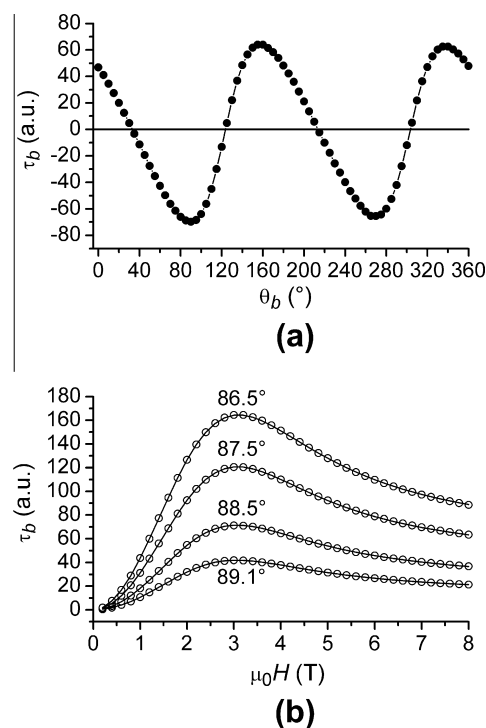


**Fig. 2.** (a) Angular variation of the torque signal recorded at 0.5 T and 1.65 K. The rotation was performed along the crystallographic **b** axis and the rotation angle is defined in Fig. 1b (a.u. = arbitrary units). (b) Field-dependent torque curves measured at 1.63 K by applying the magnetic field in the **ac** plane at different angles ( $\theta$ ) from the easy axis. The solid traces are best fit curves obtained with the parameters of Table 1 (entry 3).

it leads to a characteristic peak in the torque signal, which can be used to accurately determine magnetic anisotropy [26]. As a further advantage, when the angle ( $\theta$ ) between the magnetic field and the easy axis approaches  $90^\circ$ , isofield values of  $\tau_b/(90 - \theta)$  for different  $\theta$  settings fall on the same curve.

Hence, changing crystal orientation leads to a simple rescaling of the torque curve. If the cantilever is operated in the linear response regime (e.g. for small flexion), a *single* scale factor can then be refined to account for instrumental calibration constant, sample mass and inaccuracies in crystal orientation, while information on magnetic anisotropy is extracted *only* from the field dependence of the torque signal [26]. Fig. 2b presents field dependent torque curves recorded at  $T = 1.63$  K and four different  $\theta$  values (nominally,  $89.1^\circ$ ,  $88.5^\circ$ ,  $87.5^\circ$  and  $86.5^\circ$ ). In low fields, the torque signal first increases approximately as  $H^2$ , reaches a maximum around 3.0 T (hereafter denoted as the “breaking field”,  $H_{br}$ ) and then decreases in high fields. This behavior reflects the competition

between Zeeman energy and magnetic anisotropy energy. As explained in detail elsewhere [20], in low fields the magnetic anisotropy dominates over the Zeeman effect and the torque signal is proportional to  $H^2(\chi_{zz}-\chi_{xx})$ , where  $\chi_{zz}$  and  $\chi_{xx}$  are the low-field susceptibilities along  $z$  and  $x$ , respectively. By contrast, high  $H$  values cause the magnetic moment to flip along the applied field, affording a strong decrease of the torque signal. The curves were subject to least-squares fitting using spin Hamiltonian in Eq. (3). In the least-squares routine,  $D$  and  $B_4^0$  were treated as adjustable parameters along with an overall scale factor and with the  $\theta$  value for all crystal orientations except one ( $89.1^\circ$ ), to avoid correlation with the overall scale factor. The Landé factor  $g$  was held fixed at 2.00, as appropriate for high-spin iron(III). Since both  $D$  and  $E$  contribute to magnetic anisotropy in the **ac** plane in a highly correlated fashion, we imposed  $E = 0$  to obtain a rough estimate of the  $D$  parameter. Differences between nominal and best fit  $\theta$  values did not exceed  $0.3^\circ$ , while the resulting  $D$  and  $B_4^0$  parameters (Table 1, entry 2) were found comparable, although not identical, with those provided by HFESR on a powder sample (Table 1, entry 1). It is rewarding that torque data clearly point to a positive  $B_4^0$ , consistent with powder HFESR.

Fig. 3a displays the field dependence of the torque signal recorded at six different temperatures for  $\theta = 88.5^\circ$ . Here  $H_{br}$  was found to increase with increasing temperature, as plotted in Fig. 3b, and its  $T$  dependence already provided a rough estimate  $D = -0.40(2) \text{ cm}^{-1}$  for  $E = B_4^0 = 0$ .

The curves in Fig. 3a were again fitted to Eq. (3), treating  $D$  and  $B_4^0$  as adjustable parameters with  $g = 2.00$  and  $E = 0$ . A scale factor was also refined at each temperature to account for small possible changes in the response of the cantilever. The best fit parameters gathered in Table 1 (entry 4) compare well with those extracted from Fig. 2b, though with a slightly larger  $B_4^0$ .

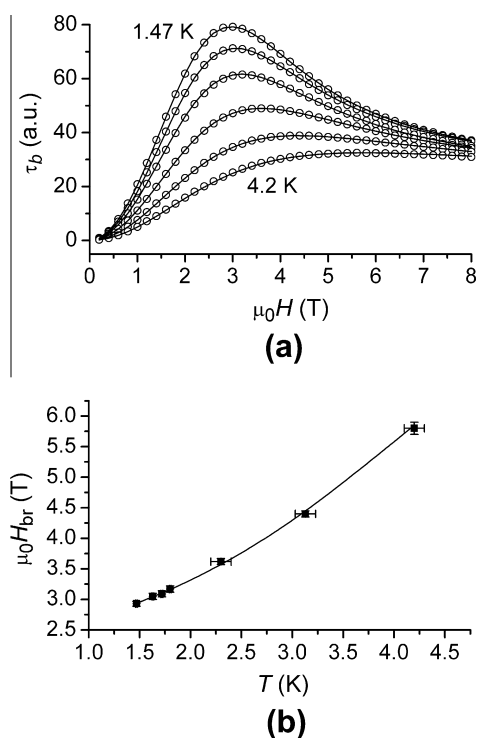


**Fig. 3.** (a) Field-dependent torque curves recorded at different temperatures (1.47, 1.63, 1.81, 2.35, 3.13 and 4.2 K) by applying the magnetic field in the **ac** plane at  $88.5^\circ$  from the easy axis. The solid traces are best fit curves obtained with the parameters of Table 1 (entry 5). (b) Values of the breaking field  $H_{br}$  as a function of temperature, along with the best fit curve calculated with  $D = -0.40(2) \text{ cm}^{-1}$  and  $E = B_4^0 = 0$ .

Both entries 2 and 4 in Table 1 feature  $D$  values ca. 10% smaller in absolute value than found by powder HFESR, as a likely consequence of neglecting rhombic anisotropy. In fact, according to Eq. (3) for a positive (negative)  $E$  parameter  $x$  is the hard (intermediate) axis and the magnetic anisotropy in the **ac** plane is increased (decreased) with respect to a purely axial system with the same  $D$ . Therefore, neglecting  $E$  leads to an overestimation (underestimation) of  $|D|$ . Based on our data, we then argue that the **ac** plane contains the easy and intermediate axes, while **b** is the hard axis. The correctness of this conclusion was fully confirmed by single-crystal HFESR (see below), which showed that  $E = -0.038(1) \text{ cm}^{-1}$ . Indeed, when the  $E$  parameter was set to  $-0.038 \text{ cm}^{-1}$  in our analysis the best-fit  $D$  parameter was found to agree with the value determined by the other techniques (see Table 1, entries 3 and 5).

We have used the same single crystal to perform the TDESER measurements. The **ac** magnetic field component of the MW radiation was oriented perpendicular to both the externally applied field and the easy axis. Therefore the selection rules of “perpendicular” ESR apply ( $\Delta M = \pm 1$ ). Fig. 4a gives the TDESER spectra recorded at 20 K at two different magnetic fields (4.0 and 4.5 T) applied in the **ac** plane at  $\theta = 5^\circ$ , i.e. close to the easy axis. The frequency was swept in the range 110–260 GHz and the signal  $\Delta\tau_b$  defined as the difference between the torques measured with and without MW irradiation. Notice that because the spectra were recorded at constant field and temperature, the torque signal without irradiation is also constant. Five sharp peaks, roughly evenly-spaced in frequency, are detected in this frequency range. The lines shift to higher frequencies as the magnetic field is increased from 4.0 to 4.5 T, thus proving that they are of magnetic resonance origin. In fact, when the field was further increased to 4.8 T, a sixth resonance line was observed [19]. The line-to-line separation is ca. 26.3 GHz, to be compared with the frequency spacing of parallel

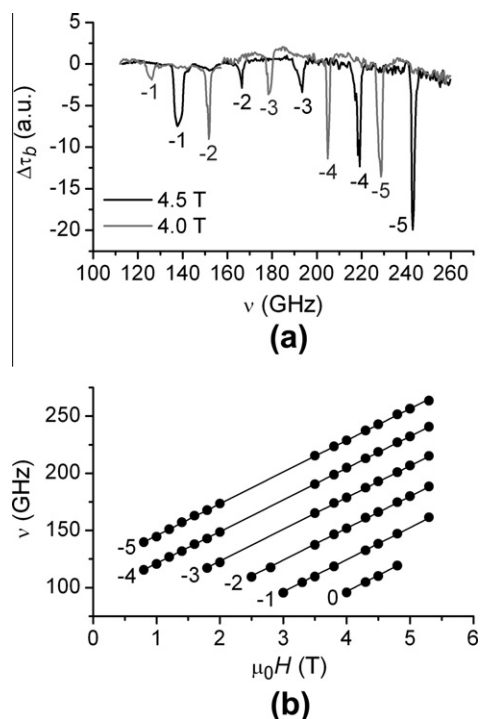


**Fig. 4.** (a) TDESER spectra recorded at 20 K by applying magnetic fields of 4.0 (gray trace) and 4.5 T (black trace) at  $\theta = 5^\circ$  from the easy axis. (b) Resonance frequencies extracted from field-dependent TDESER spectra, along with best-fit calculation with the parameters reported in Table 1 (entry 6). The resonances involve the strong-field spin states  $M$  and  $M + 1$  and are labeled with the  $M$  quantum number in both panels.

transitions that can be calculated using the  $D$  parameter reported in Ref. [21],  $2|D|/h = 26.9$  GHz.

A closer inspection of Fig. 4a reveals that the line-to-line separation decreases smoothly with increasing frequency, as expected when  $B_4^0$  and  $D$  have opposite signs. The best-fit parameters obtained by fitting the frequency and field dependence of resonance lines (Fig. 4b) are given in Table 1 (entry 6). Due to the small angle between the magnetic field and the easy axis, the measurements did not provide reliable information on the  $E$  term, which was therefore fixed to zero for simplicity. However,  $D$  and  $B_4^0$  could be precisely determined from the observed resonances. Calculated data included in Fig. 4b clearly show the outstanding quality of the fit. Notice that the broad frequency range which can be accessed allows spanning a wide portion of the energy spectrum for the system.

Magnetic resonances in anisotropic systems are expected to depend on magnetic field direction, as confirmed by Fig. 5a. When the magnetic field is applied in the **ac** plane at different  $\theta$  angles, the intensity of the peaks undergoes pronounced variations which largely reflect the angular dependence of the torque signal itself. More relevant to the present study is the observed shift of resonant peaks, which can be clearly resolved even for a small angular change thanks to the narrow lines. Such an angular dependence is plotted in Fig. 5b for the  $-5 \rightarrow -4$  and  $-4 \rightarrow -3$  transitions and allows determining the spin Hamiltonian parameters in Eq. (3), like in angle-resolved experiments by conventional ESR. The best-fit parameters so obtained ( $D = -0.444(7)$  cm<sup>-1</sup>,  $B_4^0 = 1.1(4) \times 10^{-5}$  cm<sup>-1</sup>,  $g = 1.99(5)$  and  $E = 0.00(3)$  cm<sup>-1</sup>) are in excellent agreement with those provided by constant-angle TDES (Table 1, entry 6).

To validate the results of TM and TDES spectroscopy and to obtain a definitive proof of the magnitude and orientation of in-plane anisotropy, HFESR spectra were recorded at 230 GHz and 10 K on a

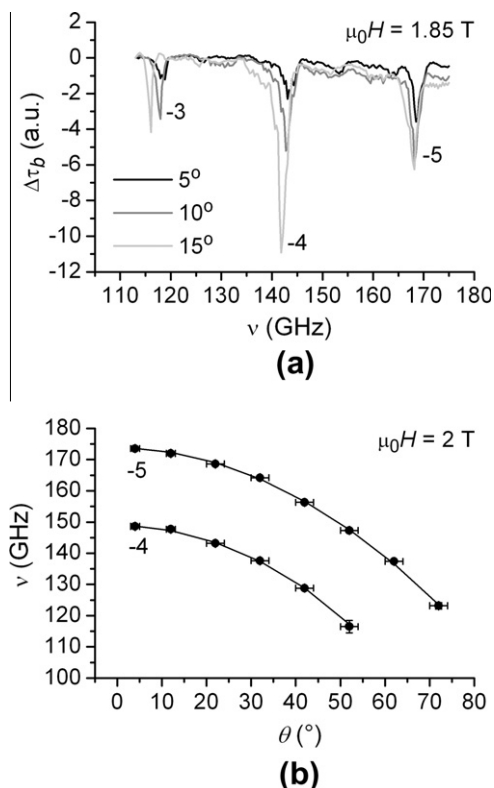


**Fig. 5.** (a) TDES spectra recorded at 20 K by applying the magnetic field at different angles ( $\theta$ ) from the easy axis. The labeling of the peaks is the same as in Fig. 4. (b) Angular dependence of resonance frequencies along with best-fit calculation with the parameters reported in the text.

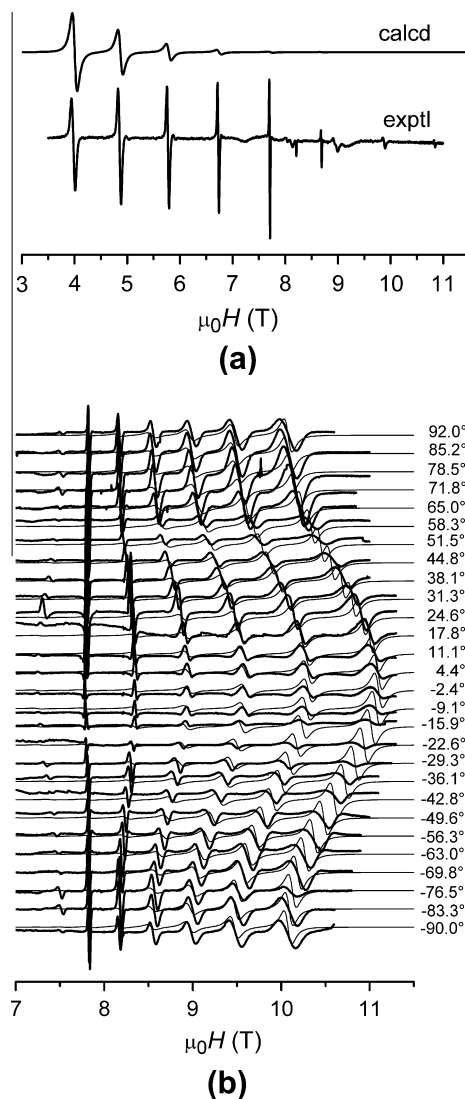


**Fig. 6.** HFESR spectra at 10 K and 230 GHz with the field applied along the easy axis (a) and in the hard plane, at different angles from the **b** axis of the monoclinic unit cell (b). Experimental (bold) and simulated traces have been vertically shifted for a better visualization. A linewidth of 500 G has been used for all simulations with the parameters reported in Table 1 (entry 7).

face-indexed crystal of **1** (Fig. 6). The magnetic field was applied along the easy axis and in the hard plane, at different angles from the **b** axis of the monoclinic cell. The easy axis spectrum (Fig. 6a) features a set of almost equally spaced transitions similar to those observed by frequency-swept TDES (Fig. 4a). With decreasing field, the spacing diminishes confirming opposite signs for  $D$  and  $B_4^0$ . The reported rotation in the hard plane (Fig. 6b) directly shows that perpendicular resonances move toward larger field values as the field approaches **b**. Simultaneous fitting of the spectra with isotropic  $g = 2.00$  gave  $D = -0.447(3)$ ,  $E = -0.038(1)$  and  $B_4^0 = 1.6(6) \times 10^{-5}$  cm<sup>-1</sup> (Table 1, entry 7), thus proving that the twofold axis through Fe1 and Fe2 ( $y$ ) is the *hard* magnetic axis of the tetra-iron(III) system.

#### 4. Conclusions

We applied a novel torque-detected (TD) ESR technique along with traditional torque magnetometry to determine the spin Hamiltonian parameters in the ground  $S = 5$  state of an Fe<sub>4</sub> single

molecule magnet. Torque measurements on a single crystal of the compound were carried out at constant  $H$  and  $T$  as a function of field orientation, so as to individuate the principal magnetic directions. As expected, the easy magnetic axis was found to lie within a few degrees from the normal to the metal plane. Field-swept torque curves were also collected at different  $T$  and field orientations and afforded reasonably accurate estimates of the axial anisotropy parameters  $D$  and  $B_4^0$ . TDESr studies, carried out in situ on the same single crystal as a function of  $H$ , field orientation and frequency, revealed well-resolved resonances that allowed a spectroscopic-quality determination of  $D$  and  $B_4^0$ . The results were validated through a parallel investigation of the material by angle-resolved high-frequency ESR. Our work demonstrates that TDESr may represent an important addition to the pool of experimental techniques available for the characterization of anisotropic, ESR-active materials. It is a versatile and technically simple method which supplies ESR-quality information but offers the sensitivity typical of torque magnetometry. For this reason, it potentially enables the investigation of single crystals with mass in the microgram range. As a further advantage, it can be operated in high magnetic fields and in a broad range of frequencies, thus allowing to explore wide portions of the field-dependent energy spectrum of the system.

### Acknowledgments

This work was financially supported by Italian MIUR through a PRIN2008 project, by the German DFG and by Université Joseph Fourier through a visiting professorship to A.C. We thank Dr. L. Gregoli for preparing the single-crystal samples used in this work during her postdoctoral fellowship at University of Modena and Reggio Emilia.

### References

- [1] D. Gatteschi, R. Sessoli, J. Villain, *Molecular Nanomagnets*, Oxford University Press, Oxford, 2006.
- [2] S. Hill, S. Datta, J. Liu, R. Inglis, C.J. Milios, P.L. Feng, J.J. Henderson, E. del Barco, E.K. Brechin, D.N. Hendrickson, Magnetic quantum tunneling: insights from simple molecule-based magnets, *Dalton Trans.* 39 (2010) 4693–4707 (and references therein).
- [3] D. Gatteschi, A.-L. Barra, A. Caneschi, A. Cornia, R. Sessoli, L. Sorace, EPR of molecular nanomagnets, *Coord. Chem. Rev.* 250 (2006) 1514–1529 (and references therein).
- [4] A.-L. Barra, A. Caneschi, A. Cornia, D. Gatteschi, L. Gorini, L.-P. Heiniger, R. Sessoli, L. Sorace, The origin of transverse anisotropy in axially symmetric single molecule magnets, *J. Am. Chem. Soc.* 129 (2007) 10754–10762.
- [5] G. de Loubens, A.D. Kent, V. Krymov, G.J. Gerfen, C.C. Beedle, D.N. Hendrickson, High frequency EPR on dilute solutions of the single molecule magnet  $\text{Ni}_4$ , *J. Appl. Phys.* 103 (2008) 07B910.
- [6] Z. Wang, J. van Tol, T. Taguchi, M.R. Daniels, G. Christou, N.S. Dalal,  $\text{Mn}_7$  species with an  $S = 29/2$  ground state: high-frequency EPR studies of a species at the classical/quantum spin interface, *J. Am. Chem. Soc.* 133 (2011) 17586–17589.
- [7] S. Takahashi, S. Hill, Rotating cavity for high-field angle-dependent microwave spectroscopy of low-dimensional conductors and magnets, *Rev. Sci. Instrum.* 76 (2005) 023114.
- [8] G.W. Morley, L.-C. Brunel, J. van Tol, A multifrequency high-field pulsed electron paramagnetic resonance/electron-nuclear double resonance spectrometer, *Rev. Sci. Instrum.* 79 (2008) 064703.
- [9] J. van Slageren, S. Vongtragool, B. Gorshunov, A.A. Mukhin, N. Karl, J. Krzystek, J. Telsler, A. Müller, C. Sangregorio, D. Gatteschi, M. Dressel, Frequency-domain magnetic resonance spectroscopy of molecular magnetic materials, *Phys. Chem. Chem. Phys.* 5 (2003) 3837–3843.
- [10] J. Van Slageren, New directions in electron paramagnetic resonance spectroscopy on molecular nanomagnets, *Top. Curr. Chem.* 321 (2012) 199–234 (and references therein).
- [11] A. Schnegg, J. Behrends, K. Lips, R. Bittl, K. Holldack, Frequency domain Fourier transform THz-EPR on single molecule magnets using coherent synchrotron radiation, *Phys. Chem. Chem. Phys.* 11 (2009) 6820–6825.
- [12] J. van Slageren, S. Vongtragool, B. Gorshunov, M. Mukhin, M. Dressel, Frequency-domain magnetic-resonance spectroscopic investigations of the magnetization dynamics in  $\text{Mn}_{12}\text{Ac}$  single crystals, *Phys. Rev. B* 79 (2009) 224406.
- [13] S. Vongtragool, B. Gorshunov, M. Dressel, J. Krzystek, D.M. Eichhorn, J. Telsler, Direct observation of fine structure transitions in a paramagnetic nickel(II) complex using far-infrared magnetic spectroscopy: a new method for studying high-spin transition metal complexes, *Inorg. Chem.* 42 (2003) 1788–1790.
- [14] G.A. Candela, Influence of paramagnetic resonance on the static susceptibility. Spin-lattice relaxation time of cupric sulfate pentahydrate, *J. Chem. Phys.* 42 (1965) 113–117.
- [15] B. Cage, S.E. Russek, D. Zipse, N.S. Dalal, Advantages of superconducting quantum interference device-detected magnetic resonance over conventional high-frequency electron paramagnetic resonance for characterization of nanomagnetic materials, *J. Appl. Phys.* 97 (2005) 10M507.
- [16] W. Wernsdorfer, A. Mueller, D. Mailly, B. Barbara, Resonant photon absorption in the low-spin molecule  $\text{V}_{15}$ , *Europhys. Lett.* 66 (2004) 861–867.
- [17] E. del Barco, A.D. Kent, E.C. Yang, D.N. Hendrickson, Quantum superposition of high spin states in the single molecule magnet  $\text{Ni}_4$ , *Phys. Rev. Lett.* 93 (2004) 157202.
- [18] K. Petukhov, S. Bahr, W. Wernsdorfer, A.-L. Barra, V. Mosser, Magnetization dynamics in the single-molecule magnet  $\text{Fe}_8$  under pulsed microwave irradiation, *Phys. Rev. B* 75 (2007) 064408.
- [19] F. El Hallak, J. van Slageren, M. Dressel, Torque detected broad band electron spin resonance, *Rev. Sci. Instrum.* 81 (2010) 095105.
- [20] A. Cornia, D. Gatteschi, R. Sessoli, New experimental techniques for magnetic anisotropy in molecular materials, *Coord. Chem. Rev.* 219–221 (2001) 573–604.
- [21] L. Gregoli, C. Danieli, A.-L. Barra, P. Neugebauer, G. Pellegrino, G. Poneti, R. Sessoli, A. Cornia, Magnetostructural correlations in tetrairon(III) single-molecule magnets, *Chem. Eur. J* 15 (2009) 6456–6467.
- [22] S. Accorsi, A.-L. Barra, A. Caneschi, G. Chastanet, A. Cornia, A.C. Fabretti, D. Gatteschi, C. Mortalò, E. Olivieri, F. Parenti, P. Rosa, R. Sessoli, L. Sorace, W. Wernsdorfer, L. Zoppi, Tuning anisotropy barriers in a family of tetrairon(III) single-molecule magnets with an  $S = 5$  ground state, *J. Am. Chem. Soc.* 128 (2006) 4742–4755.
- [23] P. Neugebauer, A.-L. Barra, New cavity design for broad-band quasi-optical HF-EPR spectroscopy, *Appl. Magn. Reson.* 37 (2010) 833–843.
- [24] C.J.H. Jacobsen, E. Pedersen, J. Villadsen, H. Weihe, ESR Characterization of  $\text{trans-V}^{\text{II}}(\text{py})_4\text{X}_2$  and  $\text{trans-Mn}^{\text{II}}(\text{py})_4\text{X}_2$  ( $\text{X} = \text{NCS}, \text{Cl}, \text{Br}, \text{I}$ ;  $\text{py} = \text{pyridine}$ ), *Inorg. Chem.* 32 (1993) 1216–1221.
- [25] S. Mossin, H. Weihe, A.-L. Barra, Is the axial zero-field splitting parameter of tetragonally elongated high-spin manganese(III) complexes always negative?, *J. Am. Chem. Soc.* 124 (2002) 8764–8765.
- [26] A. Cornia, M. Affronte, A.G.M. Jansen, D. Gatteschi, A. Caneschi, R. Sessoli, Magnetic anisotropy of  $\text{Mn}_{12}$ -acetate nanomagnets from high-field torque magnetometry, *Chem. Phys. Lett.* 322 (2000) 477–482.

**COMMENTED PAPER 7**

Y. Rechkemmer, J.E. Fischer, R. Marx, M. Dörfel, **P. Neugebauer**, S. Horvath, M. Gysler, T. Brock-Nannestad, W. Frey, M.F. Reid, J. van Slageren  
Comprehensive Spectroscopic Determination of the Crystal Field Splitting in an Erbium Single-Ion Magnet

*J. Am. Chem. Soc.*, 137, 13114-13120 (2015).

# Comprehensive Spectroscopic Determination of the Crystal Field Splitting in an Erbium Single-Ion Magnet

Yvonne Rechkemmer,<sup>†</sup> Julia E. Fischer,<sup>†,‡</sup> Raphael Marx,<sup>†</sup> María Dörfel,<sup>†</sup> Petr Neugebauer,<sup>†</sup> Sebastian Horvath,<sup>‡</sup> Maren Gysler,<sup>†</sup> Theis Brock-Nannestad,<sup>§</sup> Wolfgang Frey,<sup>||</sup> Michael F. Reid,<sup>‡</sup> and Joris van Slageren<sup>\*,†</sup>

<sup>†</sup>Institut für Physikalische Chemie, Universität Stuttgart, Pfaffenwaldring 55, D-70569 Stuttgart, Germany

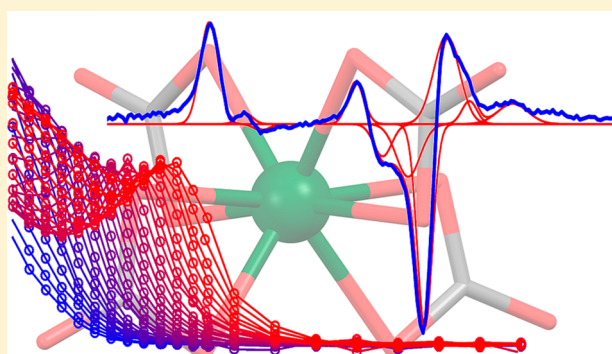
<sup>‡</sup>Department of Physics and Astronomy, University of Canterbury, Christchurch 8140, New Zealand

<sup>§</sup>Department of Chemistry, University of Copenhagen, Universitetsparken 5, 2100 Copenhagen, Denmark

<sup>||</sup>Institut für Organische Chemie, Universität Stuttgart, Pfaffenwaldring 55, D-70569 Stuttgart, Germany

## Supporting Information

**ABSTRACT:** The electronic structure of a novel lanthanide-based single-ion magnet,  $\{C(NH_2)_3\}_5[Er(CO_3)_4] \cdot 11H_2O$ , was comprehensively studied by means of a large number of different spectroscopic techniques, including far-infrared, optical, and magnetic resonance spectroscopies. A thorough analysis, based on crystal field theory, allowed an unambiguous determination of all relevant free ion and crystal field parameters. We show that inclusion of methods sensitive to the nature of the lowest-energy states is essential to arrive at a correct description of the states that are most relevant for the static and dynamic magnetic properties. The spectroscopic investigations also allowed for a full understanding of the magnetic relaxation processes occurring in this system. Thus, the importance of spectroscopic studies for the improvement of single-molecule magnets is underlined.



## 1. INTRODUCTION

The vision that molecules may one day be used to store information at unprecedentedly high densities has been a major driver for research in a number of different areas. In molecular nanomagnetism, it has led to a search for molecules that display magnetic bistability; i.e., their magnetic moments can be either positive or negative and are stable for long periods of time in zero external magnetic field.<sup>1,2</sup> The name single-molecule magnets (SMMs) has been coined for such molecules.<sup>3</sup> Mononuclear SMMs are also known as single-ion magnets (SIMs). The characteristics required are a large magnetic moment and a large magnetic anisotropy that stabilizes states with large  $z$ -components of the magnetic moment. Together, these generate an energy barrier toward inversion of the magnetic moment. For polynuclear transition metal complexes, this energy barrier has remained below the 100 K mark.<sup>4</sup> Much larger energy barriers, of up to ca. 1000 K, have been reported for molecular compounds of lanthanide ions, especially of dysprosium(III).<sup>5–7</sup> In lanthanide complexes, the origin of the magnetic anisotropy is the crystal field splitting (CFS) of the microstates of the lowest total angular momentum ( $J$ ) multiplet. For ions with odd numbers of unpaired electrons (Kramers ions), the minimum degeneracy of the crystal field (CF) states is 2-fold (Kramers doublets) in the absence of an external magnetic field. However, a vast majority of lanthanide

complexes do not actually show any magnetic bistability at all, which would be evidenced by sizable coercivity in the magnetic hysteresis curve. The reason for this lack of bistability can be found in the occurrence of efficient underbarrier relaxation processes, such as quantum tunneling. Slowly, strategies are emerging to remedy this issue. First, the implementation of strong magnetic coupling in polynuclear systems can lead to effective quenching of tunneling of the magnetization. For the lanthanides, strong magnetic coupling can only be achieved by means of radical bridging ligands, leading to highly air- and moisture-sensitive species.<sup>8–11</sup> Second, careful engineering of the crystal field (by judicious choice of ligands) can lead to CF eigenstates that are highly “axial”, i.e., contain little or no contribution from states with small  $m_j$  quantum numbers. As a consequence all transitions between microstates with opposite orientations of the magnetic moment are strongly suppressed.<sup>12</sup> One method to create a strongly axial crystal field is by the use of only two ligands that are placed strictly *trans* to each other.<sup>13,14</sup> This is quite a formidable synthetic challenge. Fortunately, complexes with lower symmetries can also possess axial CF eigenstates,<sup>12,15</sup> and bistability has been found in mononuclear complexes.<sup>16</sup> To make rational progress toward

Received: August 7, 2015

Published: September 22, 2015

improving magnetic bistability in lanthanide-based SMMs, the electronic structure and its relation to the molecular structure needs to be understood much better, because the bistability is critically dependent on the detailed nature of the CF eigenstates. So far, all attempts to design novel materials have been based on *ab initio* calculations, and more in-depth experimental study of the CFS is clearly warranted. A second, more technical reason for detailed study of the CFS is for the fit of the temperature dependence of the relaxation time. Often, the high-temperature part of the curve is fit to an exponential function. However, only one (Orbach) of the possible relaxation mechanisms (tunneling, direct, Orbach, and Raman processes) actually has an exponential temperature dependence. Indeed the experimentally derived effective energy barrier often does not correspond to the energy gap to an existing excited CF state as determined by *ab initio* calculations. Because both magnetometry and *ab initio* calculations have finite accuracies,<sup>17</sup> the origins of this discrepancy remain unclear.

Attempts to determine the CFS parameters from powder SQUID magnetometry invariably lead to hopelessly overparametrized situations. Although advanced magnetic measurement methods such as single crystal SQUID and torque magnetometries yield some information on the CFS,<sup>18,19</sup> in-depth information can only be gained from spectroscopic measurements. For these reasons, an increase in spectroscopic measurements has been called for in recent literature.<sup>20,21</sup> A number of spectroscopic methods have been used to study the crystal field splitting in lanthanide SMMs, such as electron paramagnetic resonance,<sup>22–24</sup> far-infrared spectroscopy,<sup>17,23,25</sup> inelastic neutron scattering,<sup>26–28</sup> and luminescence spectroscopy.<sup>29–33</sup> All these studies have been limited to the Russell–Saunders ground multiplet. From these studies, an accurate estimate of the gap between the ground and first excited microstates may be obtained. However, for a detailed understanding of the *nature* of the CF eigenstates, investigation of the ground multiplet alone does not suffice.<sup>34</sup> The precise composition of the lowest CF eigenstates determines the static and dynamic magnetic properties of lanthanide SIMs. Of particular importance is that some CF parameters are highly sensitive to the energies of specific transitions that do not necessarily end in the ground multiplet. Investigation of all the states arising from the  $4f^n$  configuration of the lanthanide ion requires extensive spectroscopic measurements, where not only transitions that end in the ground multiplet are considered.

Here we present the first such in-depth spectroscopic investigation of the CF splitting in a lanthanide-based SIM. We employ a combination of far-infrared, magnetic circular dichroism, optical absorption, luminescence, and multifrequency EPR spectroscopies. We have elected to investigate the novel SIM  $\{\text{C}(\text{NH}_2)_3\}_5[\text{Er}(\text{CO}_3)_4]\cdot 11\text{H}_2\text{O}$  (**1**),<sup>35</sup> because there are no ligand-based or charge-transfer transitions in the near-UV, visible, or near-infrared regions of the spectrum. Ligand-based transitions precluded in-depth investigations in the case of the complexes  $(\text{NBu}_4)[\text{LnPc}_2]$ .<sup>17</sup> We demonstrate that a comprehensive determination of the CFS and the nature of the eigenstates can be achieved in this manner. This allows for a full understanding of the processes relevant for the relaxation of the magnetization.

## 2. EXPERIMENTAL METHODS

**Synthesis of 1.**  $\{\text{C}(\text{NH}_2)_3\}_5[\text{Er}(\text{CO}_3)_4]\cdot 11\text{H}_2\text{O}$  (**1**) was synthesized according to a slightly modified literature procedure.<sup>35</sup> Guanidine carbonate (9.016 g, 50.0 mmol) was dissolved in 20 mL of doubly

distilled water, giving a saturated solution. To this was added  $\text{Er}(\text{NO}_3)_3\cdot 5\text{H}_2\text{O}$  (1.099 g, 2.5 mmol) in doubly distilled water. A white precipitate formed which was filtered off using a  $0.45\ \mu\text{m}$  syringe filter, and the resulting clear solution was stored at  $5\ ^\circ\text{C}$  yielding pale pink crystals after several weeks. Elemental analysis: found (calcd for  $\text{C}_9\text{H}_{52}\text{ErN}_{15}\text{O}_{23}$ )/%: C 11.97 (11.93), H 5.80 (5.79), N 23.12 (23.19). Further characterization data can be found in the [Supporting Information](#).

**Magnetic and Spectroscopic Measurements.** Magnetic measurements were performed using a Quantum Design MPMS-XL7 SQUID magnetometer. Far-infrared (FIR) spectra were recorded on a Bruker IFS 113v FTIR spectrometer equipped with an Oxford Instruments Spectromag SM4000 optical cryomagnet and an Infrared Laboratories pumped Si bolometer. Optical absorption and magnetic circular dichroism (MCD) spectra were recorded on samples of **1** dispersed into Baysilone vacuum grease on an Aviv 42 CD spectrometer equipped with an Oxford Instruments Spectromag 10 T optical cryomagnet and photomultiplier and InGaAs detectors. Luminescence spectra were recorded on a Horiba FluoroLog3 luminescence spectrometer equipped with an Oxford Instruments helium flow optical cryostat and photomultiplier and InGaAs detectors. X-Band EPR spectra were recorded on a Bruker EMX EPR spectrometer equipped with an Oxford Instruments continuous flow cryostat. High-frequency EPR (HF-EPR) spectra were recorded on a home-built spectrometer featuring an Anritsu signal generator, a VDI amplifier-multiplier chain, a Thomas Keating quasioptical bridge, an Oxford Instruments 15/17 T solenoid cryomagnet, and a QMC Instruments InSb hot electron bolometer.

**Analysis and Calculations.** Magnetic data were corrected for diamagnetic contributions using Pascal's constants,<sup>36</sup> and simulations were performed using the simulation software CONDON.<sup>37</sup> The crystal field analysis was carried out by means of the f-shell program package.<sup>38</sup> The program pycf was used to calculate g tensors from the f-shell output.<sup>39</sup> EPR spectra were simulated by using the Easyspin program.<sup>40</sup> The reported uncertainty values were estimated in the following manner: We have taken the standard deviations given by the output of the f-shell program, and modified these by assessing the effect of parameter value modification on the EPR spectra, to give realistic estimates of the parameter uncertainties.

## 3. RESULTS AND DISCUSSION

Complex **1** was synthesized by means of a facile reaction between aqueous solutions of guanidinium carbonate and erbium(III) nitrate pentahydrate,<sup>35</sup> and characterized by conventional methods (Figure S 1, Figure S 3, Table S 1). X-ray crystallographic analysis (Figure 1, Table S 2) reveals that **1** crystallizes as a hendecahydrate in the monoclinic space group  $P2_1/n$ , forming a hydrogen bonded network. The  $[\text{Er}(\text{CO}_3)_4]^{5-}$  anion has  $C_1$  site symmetry. To assess the presence of any

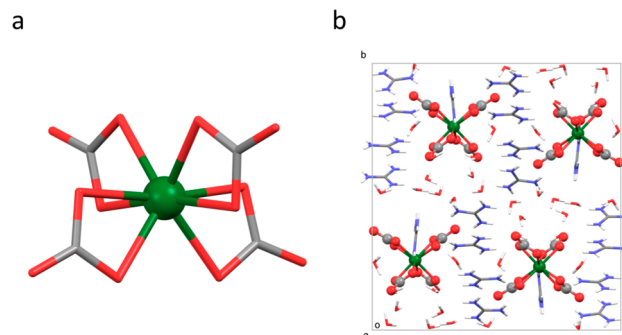


**Figure 1.** (a) Crystallographically determined molecular structure of the  $[\text{Er}(\text{CO}_3)_4]^{5-}$  anion of **1** viewed perpendicularly to the pseudo- $C_2$ -axis. (b) Packing diagram of **1**: erbium, dark green; oxygen, red; nitrogen, blue; carbon, gray; hydrogen, white.

approximate higher symmetry, it is helpful to consider the distances between the carbonate carbon atoms. For perfect tetrahedral symmetry, all these distances should be equal. In practice three sets of distances are found (Figure S 2, all distances in Å): 3.970/4.030, 4.318/4.352, 5.043/5.069. Hence, the approximate symmetry of the coordination geometry is  $C_{2v}$  and we have used this symmetry for the analysis of the spectroscopic data (see below). The real symmetry is not only determined by the positions of the coordinating atoms, but also by the rest of the ligand.<sup>17,41</sup> In  $C_{2v}$  symmetry the CF is parametrized by 9 independent parameters (see below).<sup>42</sup>

We carried out a magnetic characterization of **1** by means of comprehensive direct current (dc) and alternating current (ac) magnetic susceptibility and magnetization measurements. The dc  $\chi T$  value of **1** is  $\chi T = 10.82 \text{ cm}^3 \text{ K mol}^{-1}$  at room temperature (cf. the  $^4I_{15/2}$  free ion value of  $11.48 \text{ cm}^3 \text{ K mol}^{-1}$ ), decreasing to  $3.75 \text{ cm}^3 \text{ K mol}^{-1}$  at low temperatures (Figure 2).

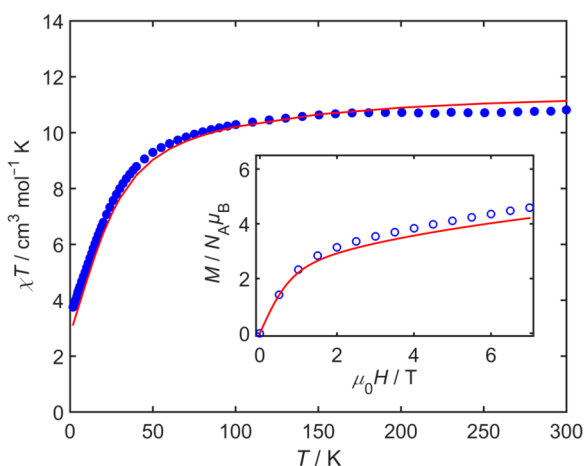


**Figure 2.** Product of magnetic susceptibility and temperature ( $\chi T$ ) as a function of temperature, recorded on a powder pellet of **1** mixed with a minimal amount of vacuum grease, at an applied field of 1000 Oe. The inset shows the magnetization curve recorded on the same sample at 1.8 K. Symbols are experimental data, and solid lines are simulations (see text).

We attribute this decrease to the influence of the CFS of the  $^4I_{15/2}$  Russell–Saunders ground multiplet of erbium(III). The molecular magnetization reaches a value of  $4.59 \mu_B$  at 1.8 K and 7 T. Without spectroscopic data, attempts to extract the 9 CF parameters from these data would not be fruitful. Alternating susceptibility measurements in an applied field of  $H_{dc} = 1000 \text{ Oe}$  display a clear out-of-phase susceptibility signal (Figure S 4), proving that **1** is a (field induced) SIM. Extensive ac measurements at different frequencies and temperatures (Figure S 5) enabled us to generate Argand plots of the out-of-phase ( $\chi''$ ) as a function of the in-phase component ( $\chi'$ ) of the ac susceptibility (Figure 3). The two clearly visible semicircles reveal the presence of two distinct relaxation processes. These data were fitted with generalized Debye equations to extract relaxation times and their distributions (Table S 3). The distribution of relaxation times of the fast process is rather broad ( $\alpha = 0.1$  to  $\alpha = 0.3$ ), but that of the slow process is quite narrow ( $\alpha \leq 0.04$ ). The relaxation times extracted are displayed as an Arrhenius plot of  $\ln \tau$  as a function of inverse temperature  $T^{-1}$  (Figure 4), resulting in a strongly curved dependence for the slow process, and a largely temperature independent fast

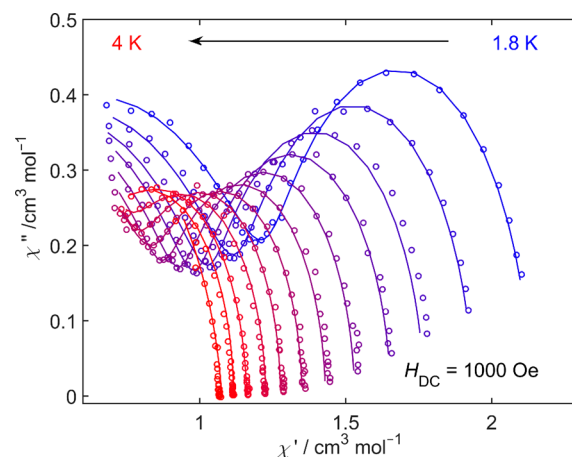


**Figure 3.** Argand diagram of the out-of-phase component of the alternating current (ac) susceptibility ( $\chi''$ ) as a function of the real component ( $\chi'$ ) derived from measurements at different temperatures as indicated. Symbols are experimental data points; lines are fits (see text).

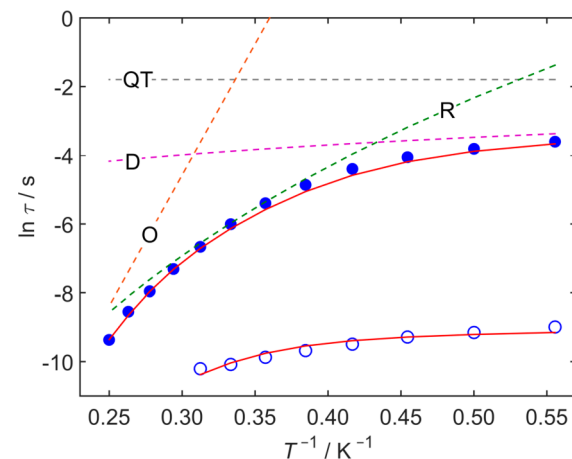


**Figure 4.** Arrhenius plot of  $\ln \tau$  as a function of  $T^{-1}$ . Filled symbols are points derived from experimental data for the slow relaxation process; open symbols are for the fast relaxation process. Dashed lines are the different contributions to the slow relaxation process: D = direct, O = Orbach, QT = quantum tunnelling, R = Raman. The solid line is the sum of these contributions.

process. The temperature dependence of the four relaxation mechanisms is given by eq 1:<sup>43</sup>

$$\tau^{-1} = \frac{B_1}{1 + B_2 H^2} + \frac{A H^{n_1} T}{\text{direct}} + \frac{C T^{n_2}}{\text{Raman}} + \tau_0^{-1} \exp(-\Delta_{CF}/k_B T)_{\text{Orbach}} \quad (1)$$

Here  $H$  is the applied field, and  $T$  is the temperature. The parameters  $B_1$ ,  $B_2$ ,  $A$ ,  $C$ , and  $\tau_0$  all cannot be determined by other than purely empirical means. For the parameters  $n_1$  and  $n_2$ , explicit values have been derived for different conditions,<sup>44</sup> but other values are also regularly reported.<sup>45,46</sup> The parameter  $\Delta_{CF}$  is a real intermediate CF state, typically the first or second, or, in a few cases, higher CF excited state.<sup>47,48</sup> Clearly, this is a severely overparametrized problem. By working at very low temperatures (in practice at  $T = 1.8 \text{ K}$ ), it can be assumed that the two-phonon processes (Raman, Orbach) are not operative.

From the dc field dependence of the relaxation rate at  $T = 1.8$  K (Figure S 6, Figure S 7, Figure S 8, Table S 4), we have derived the parameter values  $A = 1621 \text{ T}^{-2} \text{ K}^{-1} \text{ s}^{-1}$ ,  $B_1 = 25.2 \text{ s}^{-1}$ ,  $B_2 = 318 \text{ T}^{-2}$  for the slow process and  $A = 19 \times 10^4 \text{ T}^{-2} \text{ K}^{-1} \text{ s}^{-1}$ ,  $B_1 = 50 \times 10^{15} \text{ s}^{-1}$ ,  $B_2 = 3 \times 10^{14} \text{ T}^{-2}$  for the fast process. Here  $n_1$  has been fixed to the theoretical value of  $n_1 = 2$  for a Kramers doublet in the presence of hyperfine interactions.<sup>44</sup> No sensible straight line can be drawn through the points in Figure 4; consequently, the remaining parameters  $C$ ,  $n_2$ ,  $\tau_0$ , and  $\Delta_{\text{CF}}$  cannot be unequivocally determined at this stage. As will be shown below, the first CF excited doublet is located at  $52 \text{ cm}^{-1}$ . Using this as the value for  $\Delta_{\text{CF}}$  and fixing  $n_2$  to the value derived for Kramers ions in the low-temperature limit ( $n_2 = 9$ ), we find the following parameter values:  $C = 0.57 \text{ K}^{-9} \text{ s}^{-1}$  and  $\tau_0 = 0$  for the fast process and  $C = 0.02 \text{ K}^{-9} \text{ s}^{-1}$  and  $\tau_0 = 1.2 \times 10^{-12} \text{ s}$  for the slow process.

To find out the exact composition of the eigenstates that determine the static and dynamic properties and to determine the energies of the CF levels ( $\Delta_{\text{CF}}$ ), we have embarked on an extensive spectroscopic study of **1**. First, we have recorded far-infrared (FIR) spectra at 9 K and at different magnetic fields (Figure S 9). The application of an external field allows separating the field dependent CF excitations from field independent excitations such as vibrations that occur in the same frequency range. The CF excitations can be made more evident by normalization of the spectra by division of the in-field spectra by the 6 T spectrum. We observed three CF excitations, namely, at 52, 84, and  $105 \text{ cm}^{-1}$ . The splitting of the middle feature is an artifact, which we have observed more often in FIR spectra whenever CF and vibrational transitions overlap. The last of these is at the edge of our spectral window, and the assignment to a CF transition on the basis of this measurement alone would not be beyond doubt. However, the CF analysis (see below) shows that there must be a CF level at this position, and we have therefore used this energy.

Luminescence spectroscopy is a second method that furnishes information on the CFS of the ground multiplet. Erbium(III) is well-known for the near-infrared (NIR) luminescent transition from the  $^4I_{13/2}$  first excited to the  $^4I_{15/2}$  ground multiplet,<sup>49</sup> used in fiber optic telecommunication amplifiers, but also transitions from higher lying states to the ground multiplet occur.<sup>50</sup> However, the low-temperature emission spectrum of **1** ( $\lambda_{\text{exc}} = 290 \text{ nm}$ ) merely showed a broad emission band attributed to ligand luminescence. Intriguingly, superimposed on this broad luminescence band are sharp dips, whose energies correspond to the optical absorption bands (Figure S 10). This phenomenon has been observed before,<sup>51,52</sup> and we attribute this to resonant reabsorption of the ligand emission by the lanthanide ion. No ff-luminescence in the visible or near-infrared was observed for any excitation wavelength.

We were, however, able to record a wealth of UV-vis-NIR-absorption and -MCD-spectra (Figure 5, Figures S 11–20). We obtained best results for samples dispersed into transparent vacuum grease. The absorption spectra were calibrated against pure vacuum grease. Because the MCD signal is a signed quantity, often a higher resolution than in the corresponding absorption spectrum is achieved. In absorption, we have observed CF split transitions from the  $^4I_{15/2}$  ground state to the  $^4I_{9/2}$ ,  $^4F_{9/2}$ ,  $^4S_{3/2}$ ,  $^2H_{11/2}$ ,  $^4F_{7/2}$ ,  $^4F_{5/2}$ ,  $^4F_{3/2}$ ,  $^2H_{9/2}$ , and  $^4G_{11/2}$  multiplets, whereas MCD spectra allowed the observation of transitions to  $^4I_{13/2}$ ,  $^4F_{9/2}$ ,  $^2H_{11/2}$ ,  $^4F_{7/2}$ ,  $^4F_{5/2}$ ,  $^4F_{3/2}$ , and  $^4H_{11/2}$ .<sup>53</sup> Further transitions were observed, but either they

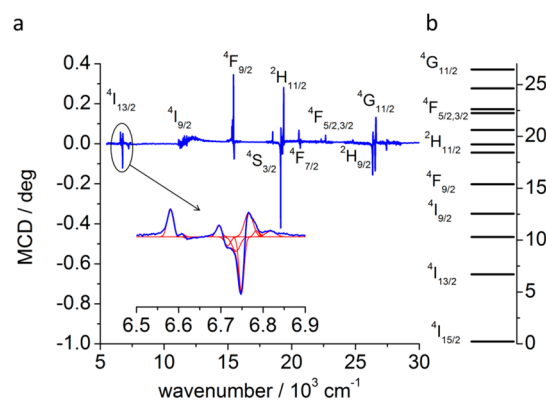


**Figure 5.** (a) Complete magnetic circular dichroism (MCD) spectrum, composed of several separate scans, recorded on a mull of **1** in transparent vacuum grease. The inset shows a zoom of the  $^4I_{15/2} \rightarrow ^4I_{13/2}$  transition. (b) Energy level diagram showing the calculated energetic positions (in  $10^3 \text{ cm}^{-1}$ ) of the multiplets.

were too weak or no usable CF splitting was observed, so they were not taken into account in the analysis. All spectra were carefully deconvoluted into sums of Gaussian lines. Often more lines would be observed than expected on the basis of the multiplicity of the final state. These are attributed to vibronic excitations that occur because ff electric dipole transitions are Laporte-forbidden, and can gain intensity through coupling with ungerade vibrational modes.<sup>42</sup> In the analysis, we have almost always used the lower-energy component. From the FIR and optical data together, we were able to determine the positions of no fewer than 48 independent energy levels (Table S 5).

For the magnetic properties, the lowest-lying Kramers doublets (KDs) are of the most interest. A technique that can be exquisitely sensitive to the precise composition of the lowest KDs is (high-frequency) EPR.<sup>23</sup> We have therefore recorded EPR spectra on **1** at X-band (9.5 GHz) and at high frequencies around 300 GHz (Figure 6). Especially in the latter,

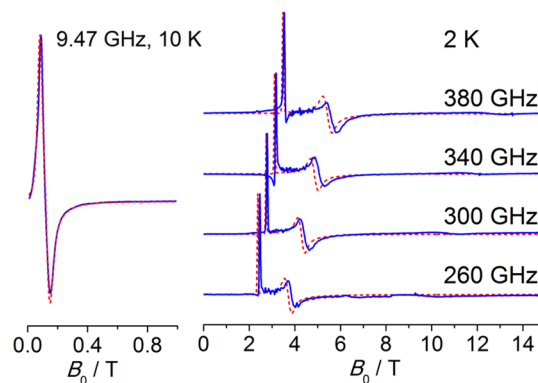


**Figure 6.** Experimental (blue, solid) and simulated (red, dashed) X-band EPR (left, 10 K) and high-frequency EPR (right, 2 K) spectra recorded on mulls of **1** in Fluorolube.

two clear and one weaker resonance line can be clearly observed. Within the  $S = 1/2$  pseudospin approximation we find effective  $g$ -values  $g_1 = 7.64$ ,  $g_2 = 4.85$ , and  $g_3 = 1.94$ .

The Hamiltonian that describes the electronic structure of a  $C_{2v}$ -symmetric lanthanide complex in the space of the  $4f^7$  configuration is given in eq 2:<sup>42</sup>

$$\begin{aligned}
 \mathcal{H} &= \mathcal{H}_{\text{free ion}} + \mathcal{H}_{\text{crystal field}} \\
 \mathcal{H}_{\text{free ion}} &= E_{\text{ave}} + \sum_{k=2,4,6} F^k f_k + \zeta_{4f} A_{\text{SO}} + \alpha L(L+1) \\
 &\quad + \beta G(G_2) + \gamma G(R_7) + \sum_{i=2,3,4,6,7,8} T^i t_i \\
 &\quad + \sum_l M^l m_l + \sum_k P^k p_k \\
 \mathcal{H}_{\text{crystal field}} &= -e[B_{20}C_0^2 + B_{22}(C_{-2}^2 + C_2^2) + B_{40}C_0^4 \\
 &\quad + B_{42}(C_{-2}^4 + C_2^4) + B_{44}(C_{-4}^4 + C_4^4) \\
 &\quad + B_{60}C_0^6 + B_{62}(C_{-2}^6 + C_2^6) \\
 &\quad + B_{64}(C_{-4}^6 + C_4^6) + B_{66}(C_{-6}^6 + C_6^6)] \quad (2)
 \end{aligned}$$

Here  $E_{\text{ave}}$  is the spherical contribution to the energy,  $F^k f_k$  are the electrostatic repulsion integrals, and  $\zeta_{4f}$  is the spin-orbit coupling constant. The remaining terms of  $\mathcal{H}_{\text{free ion}}$  are two and three particle, as well as spin-spin and spin-orbit corrections. These parameters have little influence on the spectroscopically observed splittings and were fixed to literature mean values during the fitting procedure.<sup>42</sup> The crystal field Hamiltonian  $\mathcal{H}_{\text{crystal field}}$  is expressed in the Wybourne notation. Here,  $B_{kq}$  are the adjustable parameters, and  $C_q^k$  are spherical tensor operators. Note that  $C_q^k$  are not formulated in terms of the Stevens operators typical for analyses in the basis of the Russell-Saunders ground multiplet. We have used this Hamiltonian in the full basis of all 364 states arising from the  $4f^{11}$  configuration.

The fit followed the following procedure: First, the experimentally determined data (FIR, optical absorption, MCD) were ranked according to energy. In case more excitations were observed than expected on the basis of the multiplicity of the relevant final state, some excitations were tentatively assigned to vibronic excitations and temporarily discarded. Subsequently, the 14 parameters were fit to these levels. On the basis of the results, the energy levels were reassigned, and the process was repeated in the search of the global minimum. Once a reasonable fit (root-mean-square error less than  $20 \text{ cm}^{-1}$ ) was obtained, its quality was assessed by simulating the HFEP spectra on the basis of this parameter set. After a lengthy iterative process, we finally arrived at a robust and consistent parameter set (parameter set 1, Table 1),

**Table 1. Free Ion and Crystal Field Parameters Derived for 1**

param	value/ $\text{cm}^{-1}$
$E_{\text{ave}}$	$35\,469 \pm 10$
$F^2$	$95\,991 \pm 100$
$F^4$	$69\,046 \pm 105$
$F^6$	$51\,686 \pm 170$
$\zeta_{4f}$	$2355 \pm 2$
$B_{20}$	$145 \pm 50$
$B_{22}$	$40 \pm 25$
$B_{40}$	$0 \pm 50$
$B_{42}$	$930 \pm 30$
$B_{44}$	$-386 \pm 30$
$B_{60}$	$350 \pm 30$
$B_{62}$	$440 \pm 20$
$B_{64}$	$620 \pm 15$
$B_{66}$	$330 \pm 50$

with a final rms error of ca.  $17 \text{ cm}^{-1}$  (Table S 5), which also allows excellent simulations of the susceptibility, magnetization, and HFEP spectra (Figure 2, Figure 6). The obtained parameters were transformed, so that they lie in the standard range for which  $0 \leq B_{22}/B_{20} \leq (1/6)^{1/2}$ .<sup>54</sup> The deviations of the energies of the KDs of the ground multiplet with those directly measured by FIR spectroscopy are less than  $10 \text{ cm}^{-1}$  (Table 2).

**Table 2. Energies of the Lowest  $^4I_{15/2}$  Multiplet Directly Measured by FIR Spectroscopy and Those Derived from the Crystal Field Analysis**

$E_{\text{exp}}/\text{cm}^{-1}$ (FIR)	$E_{\text{CF}}/\text{cm}^{-1}$
0	0
52	44
84	91
105	112
	280
	325
	437
	462

We can now inspect the composition of the ground KD (Table S 6), which is decisive for the low-temperature magnetic properties. Although we have carried out the analysis in the complete basis of the  $4f^{11}$  configuration, we find that the ground KD only contains contributions from the  $^4I_{15/2}$  Russell-Saunders ground multiplet:  $|KD1\rangle = \sum c_i |^{2S+1}L_J m_J\rangle_i = \sum c_i |m_J\rangle_i = 0.50|-13/2\rangle - 0.50|-5/2\rangle + 0.42|11/2\rangle - 0.36|3/2\rangle - 0.27|15/2\rangle - 0.27|-1/2\rangle - 0.20|-9/2\rangle$ , with the second component of the doublet the mirror image of the first. Hence, the ground Kramers doublet is extraordinarily mixed in character and contains contributions from functions with low  $m_J$  values, and also contributions with both positive and negative  $m_J$  components. This leads to efficient relaxation of the magnetization explaining the relatively poor performance of **1** as a single-molecule magnet.<sup>43</sup> It will be interesting to investigate the crystal field splitting of erbium single molecule magnets where more axial KDs are expected, such as  $\text{Er}[\text{N}(\text{SiMe}_3)_2]_3$ ,<sup>55</sup> by the methodology described in this paper.

An important point is the following: If the CF parameters are fit to the experimentally derived (FIR, optical absorption, MCD) energy levels *without* taking into account the EPR data, a parameter set with a smaller rms error ( $13 \text{ cm}^{-1}$ ) can be found (parameter set 2, Table S 8). This parameter set features rather different CF splitting parameters and predicts the ground KD to have smaller contributions from functions with small values of  $m_J$  (Table S 9, Figure S 23). However, this parameter set does not allow for reasonable fits of the magnetic and EPR data (Figure S 21, Figure S 22), and therefore must be wrong. This leads to the important conclusion that an analysis of the CF splitting on the basis of optical data alone is not necessarily sufficient to correctly determine the composition of the lowest Kramers doublets that are crucially important for the dc and ac magnetic properties. Similar effects may explain unexpected discrepancies between experimental and calculated susceptibility data reported recently.<sup>21</sup>

## CONCLUSIONS

We have presented an in-depth analysis of the magnetic properties and the electronic structure of a novel lanthanide-based single-ion magnet. The study has allowed for a full understanding of the magnetization dynamics. Importantly, we

have presented the first comprehensive electronic structure determination of a lanthanide single-molecule magnet. We have shown that, for a correct description of the states relevant for the magnetic properties, including the results from electron paramagnetic resonance measurements is crucial. We are convinced that detailed understanding of the electronic structure of lanthanide-based single-molecule magnets, such as that achieved in the present paper, is essential for rational design of novel such systems with improved properties.

## ■ ASSOCIATED CONTENT

### 📄 Supporting Information

The Supporting Information is available free of charge on the ACS Publications website at DOI: 10.1021/jacs.5b08344.

Detailed information on synthesis and characterization, equipment used, magnetic and spectroscopic measurements, data analysis, and calculations (PDF)

## ■ AUTHOR INFORMATION

### Corresponding Author

\*slageren@ipc.uni-stuttgart.de

### Present Address

<sup>†</sup>Max Planck Institute for Chemical Physics of Solids, Nöthnitzer Straße 40, D-01187 Dresden, Germany.

### Notes

The authors declare no competing financial interest.

## ■ ACKNOWLEDGMENTS

We thank Claudio Eisele (University of Stuttgart) for experimental contributions, Pierre Eckold (University of Stuttgart) for powder X-ray diffraction measurements, Martin Dressel (University of Stuttgart) for access to the SQUID magnetometer and FIR spectrometer, George S. Goff (Los Alamos National Laboratory) for useful discussions, as well as DFG (INST 41/863-1, 41/864-1, SPP1601, SL104/S-1) and COST CM1006 Eufen for funding.

## ■ REFERENCES

- Gatteschi, D.; Sessoli, R.; Villain, J. *Molecular Nanomagnets*; Oxford University Press: Oxford, 2006.
- Sessoli, R.; Gatteschi, D.; Caneschi, A.; Novak, M. A. *Nature* **1993**, *365*, 141.
- Aubin, S. M. J.; Wemple, M. W.; Adams, D. M.; Tsai, H. L.; Christou, G.; Hendrickson, D. N. *J. Am. Chem. Soc.* **1996**, *118*, 7746.
- Milios, C. J.; Vinslava, A.; Wernsdorfer, W.; Moggach, S.; Parsons, S.; Perlepes, S. P.; Christou, G.; Brechin, E. K. *J. Am. Chem. Soc.* **2007**, *129*, 2754.
- Woodruff, D. N.; Winpenny, R. E. P.; Layfield, R. A. *Chem. Rev.* **2013**, *113*, 5110.
- Ishikawa, N.; Sugita, M.; Ishikawa, T.; Koshihara, S.; Kaizu, Y. *J. Phys. Chem. B* **2004**, *108*, 11265.
- Ishikawa, N.; Mizuno, Y.; Takamatsu, S.; Ishikawa, T.; Koshihara, S. *Y. Inorg. Chem.* **2008**, *47*, 10217.
- Rinehart, J. D.; Fang, M.; Evans, W. J.; Long, J. R. *J. Am. Chem. Soc.* **2011**, *133*, 14236.
- Rinehart, J. D.; Fang, M.; Evans, W. J.; Long, J. R. *Nat. Chem.* **2011**, *3*, 538.
- Demir, S.; Zadrozny, J. M.; Nippe, M.; Long, J. R. *J. Am. Chem. Soc.* **2012**, *134*, 18546.
- Demir, S.; Nippe, M.; Gonzalez, M. I.; Long, J. R. *Chem. Sci.* **2014**, *5*, 4701.
- Ungur, L.; Chibotaru, L. F. *Phys. Chem. Chem. Phys.* **2011**, *13*, 20086.
- Chilton, N. F. *Inorg. Chem.* **2015**, *54*, 2097.

- Chilton, N. F.; Goodwin, C. A. P.; Mills, D. P.; Winpenny, R. E. P. *Chem. Commun.* **2015**, *51*, 101.
- Aravena, D.; Ruiz, E. *Inorg. Chem.* **2013**, *52*, 13770.
- Ungur, L.; Le Roy, J. J.; Korobkov, I.; Murugesu, M.; Chibotaru, L. F. *Angew. Chem., Int. Ed.* **2014**, *53*, 4413.
- Marx, R.; Moro, F.; Dörfel, M.; Ungur, L.; Waters, M.; Jiang, S. D.; Orlita, M.; Taylor, J.; Frey, W.; Chibotaru, L. F.; van Slageren, J. *Chem. Sci.* **2014**, *5*, 3287.
- Cucinotta, G.; Perfetti, M.; Luzon, J.; Etienne, M.; Car, P. E.; Caneschi, A.; Calvez, G.; Bernot, K.; Sessoli, R. *Angew. Chem., Int. Ed.* **2012**, *51*, 1606.
- Perfetti, M.; Cucinotta, G.; Boulon, M.-E.; El Hallak, F.; Gao, S.; Sessoli, R. *Chem. - Eur. J.* **2014**, *20*, 14051.
- Sorace, L.; Benelli, C.; Gatteschi, D. *Chem. Soc. Rev.* **2011**, *40*, 3092.
- Karbowiak, M.; Rudowicz, C.; Ishida, T. *Inorg. Chem.* **2013**, *52*, 13199.
- Lucaccini, E.; Sorace, L.; Perfetti, M.; Costes, J.-P.; Sessoli, R. *Chem. Commun.* **2014**, *50*, 1648.
- Moreno Pineda, E.; Chilton, N. F.; Marx, R.; Dorfel, M.; Sells, D. O.; Neugebauer, P.; Jiang, S.-D.; Collison, D.; van Slageren, J.; McInnes, E. J. L.; Winpenny, R. E. P. *Nat. Commun.* **2014**, *5*, 5243.
- Ghosh, S.; Datta, S.; Friend, L.; Cardona-Serra, S.; Gaita-Ariño, A.; Coronado, E.; Hill, S. *Dalton Trans.* **2012**, *41*, 13697.
- Haas, S.; Heintze, E.; Zapf, S.; Gorshunov, B.; Dressel, M.; Bogani, L. *Phys. Rev. B: Condens. Matter Mater. Phys.* **2014**, *89*, 174409.
- Pedersen, K. S.; Ungur, L.; Sigrist, M.; Sundt, A.; Schau-Magnussen, M.; Vieru, V.; Mutka, H.; Rols, S.; Weihe, H.; Waldmann, O.; Chibotaru, L. F.; Bendix, J.; Dreiser, J. *Chem. Sci.* **2014**, *5*, 1650.
- Kofu, M.; Yamamuro, O.; Kajiwara, T.; Yoshimura, Y.; Nakano, M.; Nakajima, K.; Ohira-Kawamura, S.; Kikuchi, T.; Inamura, Y. *Phys. Rev. B: Condens. Matter Mater. Phys.* **2013**, *88*, 064405.
- Klokishner, S. I.; Ostrovsky, S. M.; Reu, O. S.; Pali, A. V.; Tregenna-Piggott, P. L. W.; Brock-Nannestad, T.; Bendix, J.; Mutka, H. *J. Phys. Chem. C* **2009**, *113*, 8573.
- Flanagan, B. M.; Bernhardt, P. V.; Krausz, E. R.; Lüthi, S. R.; Riley, M. J. *Inorg. Chem.* **2002**, *41*, 5024.
- Long, J.; Rouquette, J.; Thibaud, J.-M.; Ferreira, R. A. S.; Carlos, L. D.; Donnadiou, B.; Vieru, V.; Chibotaru, L. F.; Konczewicz, L.; Haines, J.; Guari, Y.; Larionova, J. *Angew. Chem., Int. Ed.* **2015**, *54*, 2236.
- Pointillart, F.; Guennic, B. L.; Maury, O.; Golhen, S.; Cador, O.; Ouahab, L. *Inorg. Chem.* **2013**, *52*, 1398.
- Shintoyo, S.; Murakami, K.; Fujinami, T.; Matsumoto, N.; Mochida, N.; Ishida, T.; Sunatsuki, Y.; Watanabe, M.; Tsuchimoto, M.; Mrozinski, J.; Coletti, C.; Re, N. *Inorg. Chem.* **2014**, *53*, 10359.
- Pedersen, K. S.; Dreiser, J.; Weihe, H.; Sibille, R.; Johannessen, H. V.; Sørensen, M. A.; Nielsen, B. E.; Sigrist, M.; Mutka, H.; Rols, S.; Bendix, J.; Piligkos, S. *Inorg. Chem.* **2015**, *54*, 7600.
- Karbowiak, M.; Rudowicz, C. *Polyhedron* **2015**, *93*, 91.
- Goff, G. S.; Cisneros, M. R.; Kluk, C.; Williamson, K.; Scott, B.; Reilly, S.; Runde, W. *Inorg. Chem.* **2010**, *49*, 6558.
- Bain, G. A.; Berry, J. F. *J. Chem. Educ.* **2008**, *85*, 532.
- Schilder, H.; Lueken, H. J. *Magn. Mater.* **2004**, *281*, 17.
- Reid, M. F. *F-Shell Empirical Programs*; University of Canterbury: Christchurch, New Zealand.
- Horvath, S.; Reid, M. F. *pcyf*; <https://bitbucket.org/sebastianhorvath/pycf/>, 2015.
- Stoll, S.; Schweiger, A. *J. Magn. Reson.* **2006**, *178*, 42.
- Petit, S.; Pilet, G.; Luneau, D.; Chibotaru, L. F.; Ungur, L. *Dalton Trans.* **2007**, 4582.
- Görller-Walrand, C.; Binnemans, K. In *Handbook on the Physics and Chemistry of Rare Earths*; Gschneidner, K. A., Eyring, L., Eds.; Elsevier: Amsterdam, 1996; Vol. 23.
- Liddle, S. T.; van Slageren, J. *Chem. Soc. Rev.* **2015**, *44*, 6655.
- Abraham, A.; Bleaney, B. *Electron Paramagnetic Resonance of Transition Ions*; Dover Publications, Inc.: New York, 1986.

(45) Boulon, M. E.; Cucinotta, G.; Luzon, J.; Degl'Innocenti, C.; Perfetti, M.; Bernot, K.; Calvez, G.; Caneschi, A.; Sessoli, R. *Angew. Chem., Int. Ed.* **2013**, *52*, 350.

(46) Herchel, R.; Váhovská, L.; Potočňák, I.; Trávníček, Z. *Inorg. Chem.* **2014**, *53*, 5896.

(47) Blagg, R. J.; Ungur, L.; Tuna, F.; Speak, J.; Comar, P.; Collison, D.; Wernsdorfer, W.; McInnes, E. J. L.; Chibotaru, L. F.; Winpenny, R. E. P. *Nat. Chem.* **2013**, *5*, 673.

(48) Singh, S. K.; Gupta, T.; Shanmugam, M.; Rajaraman, G. *Chem. Commun.* **2014**, *50*, 15513.

(49) Comby, S.; Bünzli, J. C. G. In *Handbook on the Physics and Chemistry of Rare Earths, Vol 37: Optical Spectroscopy*; Gschneidner, K. A., Bünzli, J.-C. G., Pecharsky, V. K., Eds.; Elsevier: Amsterdam, 2007; Vol. 37, p 217.

(50) Bünzli, J.-C. G. *Chem. Rev.* **2010**, *110*, 2729.

(51) Kang, J. G.; Kim, T. J.; Park, K. S.; Kang, S. K. *Bull. Korean Chem. Soc.* **2004**, *25*, 373.

(52) Martín-Ramos, P.; Coutinho, J. T.; Ramos Silva, M.; Pereira, L. C. J.; Lahoz, F.; da Silva, P. S. P.; Lavin, V.; Martín-Gil, J. *New J. Chem.* **2015**, *39*, 1703.

(53) Dieke, G. H. *Spectra and Energy Levels of Rare Earth Ions in Crystals*; Interscience Publishers: New York, 1968.

(54) Rudowicz, C.; Chua, M.; Reid, M. F. *Phys. B* **2000**, *291*, 327.

(55) Zhang, P.; Zhang, L.; Wang, C.; Xue, S. F.; Lin, S. Y.; Tang, J. K. *J. Am. Chem. Soc.* **2014**, *136*, 4484.

**COMMENTED PAPER 8**

**P. Neugebauer**, J. G. Krummenacker, V. P. Denysenkov, G. Parigi, C. Luchinat, T. F. Prisner  
Liquid state DNP of water at 9.2 T: an experimental access to saturation

*Phys. Chem. Chem. Phys.*, 15, 6049 - 6056 (2013).

# Liquid state DNP of water at 9.2 T: an experimental access to saturation†

Cite this: *Phys. Chem. Chem. Phys.*, 2013, **15**, 6049

Petr Neugebauer,<sup>a</sup> Jan G. Krümmenacker,<sup>a</sup> Vasyl P. Denysenkov,<sup>a</sup> Giacomo Parigi,<sup>b,c</sup> Claudio Luchinat<sup>b,c</sup> and Thomas F. Prisner<sup>\*a</sup>

We have performed liquid state ("Overhauser") Dynamic Nuclear Polarization (DNP) experiments at high magnetic field (9.2 T, corresponding to 260 GHz EPR and 400 MHz <sup>1</sup>H-NMR resonance frequency) on aqueous solutions of <sup>14</sup>N-TEMPOL nitroxide radicals. Integrated signal enhancements exceeding –80 were observed for the water protons at microwave superheated temperatures (160 °C) and still –14 at ambient temperatures (45 °C) relevant to biological applications. Different contributions contributing to the DNP enhancement such as saturation factor, leakage factor and sample temperature under microwave irradiation could be determined independently for a high spin concentration of 1 M, allowing the calculation of the coupling factors as a function of temperature and a quantitative comparison of this parameter with values derived from field dependent relaxation measurements or predictions from MD simulation.

Received 11th December 2012,  
Accepted 15th February 2013

DOI: 10.1039/c3cp44461a

www.rsc.org/pccp

## Introduction

Improving sensitivity is a key issue in Nuclear Magnetic Resonance (NMR) spectroscopy. Even a small signal enhancement by a factor of 2 shortens the acquisition time by a factor of 4. One way of tackling the sensitivity issue is hyperpolarization by Dynamic Nuclear Polarization (DNP). In DNP, hyperpolarization of nuclei is achieved by microwave (MW) irradiation of the unpaired electron spin of radicals (polarizing agents), which are part of the sample under study, to transfer their larger Boltzmann polarization to the nuclei.<sup>1–3</sup> At high magnetic fields, pioneering work has been performed in the solid state,<sup>4,5</sup> leading to a surge of new developments and applications.<sup>6–9</sup> More recently, high field DNP in the liquid state has become a field of study, with new developments at *e.g.* 3.4 T<sup>10–13</sup> and 9.2 T.<sup>14–17</sup> In the liquid state, the active DNP mechanism is the Overhauser effect.

The Overhauser enhancement can be written as

$$\epsilon_{\text{OE}} = \frac{\langle I_z \rangle - I_0}{I_0} = \frac{\gamma_e}{\gamma_n} \cdot f \cdot s \cdot \zeta \quad (1)$$

<sup>a</sup> Institute of Physical and Theoretical Chemistry and Center for Biomolecular Magnetic Resonance, Goethe-University, Max-von-Laue-Str. 7, 60438, Frankfurt am Main, Germany. E-mail: prisner@chemie.uni-frankfurt.de

<sup>b</sup> Department of Chemistry, University of Florence, via della Lastruccia 3, 50019, Sesto Fiorentino, FI, Italy

<sup>c</sup> CERM, University of Florence, Via Luigi Sacconi 6, 50019, Sesto Fiorentino, FI, Italy

† Electronic supplementary information (ESI) available. See DOI: 10.1039/c3cp44461a

where  $\gamma_e$  and  $\gamma_n$  are the gyromagnetic ratios of the electron and the nucleus, respectively, *i.e.*  $\gamma_e/\gamma_n \approx -660$  for protons,<sup>18</sup>  $f = 1 - T_{1R}/T_{1W}$  is the leakage factor, which can be determined from the nuclear  $T_1$  in the presence ( $T_{1R}$ ) and in the absence of radicals in the solution ( $T_{1W}$ ), and reflects the influence of radicals on the nuclear relaxation rate of the used solvent. The factor  $s$  denotes the saturation factor, which describes how well the electron transition is saturated by the MW irradiation. It ranges from 0 for no saturation, *i.e.* thermal population, to 1 for a fully saturated electron spin transition with equalized populations. The last parameter is called the coupling factor  $\zeta$ . While the optimization of  $f$  and  $s$  is rather a technical issue, the coupling factor reflects the nature of the polarization transfer between the electron and nuclear spins and cannot be easily controlled. If the magnetic dipole-dipole coupling is the dominant mechanism, as usually the case for protons of target molecules in liquids, the coupling factor ranges between 0 and 0.5. This yields a maximal theoretical enhancement ( $\zeta = 0.5$ ,  $s = 1$ ,  $f = 1$ ) of –330. The coupling factor and its temperature dependence were independently determined from the field dependence of the solvent water proton relaxivity (also called Nuclear Magnetic Relaxation Dispersion – NMRD) profiles<sup>12,19–22</sup> and compared with the values obtained using DNP.

## Experimental

### DNP measurements

The DNP experiments were performed on a setup, which consists of a commercial 400 MHz NMR spectrometer (Bruker Avance),

equipped with a home built MW bridge operating at 260 GHz for Electron Paramagnetic Resonance (EPR) excitation, and a home built double resonance DNP probe (260 GHz/400 MHz).<sup>23</sup>

The DNP probe consists of a helix coil for NMR excitation and detection made of a copper tape, which serves as the body of a TE<sub>011</sub> cylindrical resonator for the EPR excitation at the same time (double resonance structure), as depicted in Fig. 1. The probe further contains a Radio Frequency (RF) tuning setup and the metal–dielectric MW waveguide (Institute of Radiophysics and Electronics – IRE, Ukraine) to propagate the MW. The leads of the helix coil are connected to the RF circuit tuned to 400 MHz NMR frequency. The MW resonance mode is maintained inside of the helix coil between two plungers made of MACOR (Corning Inc.) with silver coated caps. This MW resonance structure is coupled to the MW waveguide in the middle of the helix coil through an elliptical iris (0.4 mm by 0.25 mm). For MW cavity tuning, one of the plungers can be moved from the outside of the probe *via* gears and a driving rod. The RF of the NMR circuit can be tuned in the range from 390 to 400 MHz; its conversion factor is 0.17 mT W<sup>-1/2</sup> and its quality factor  $Q_{RF}$  is about 70. The MW resonance of the cavity can be tuned between 256 and 260 GHz, typically reaching a conversion factor of 0.45 mT W<sup>-1/2</sup> and a quality factor  $Q_{MW}$  of approximately 400.<sup>15</sup> The necessary MW power for a DNP experiment at 260 GHz is produced using a high power (20 W) gyrotron source (Gycom, Russia). Power transmission to the MW bridge is achieved *via* a corrugated waveguide transmission line (Gycom) with a total length of 12 m. The MW bridge consists of oversized waveguides, calibrated attenuators, a beam splitter (all IRE, Ukraine) and two zero-bias Schottky diodes (VDI-WR3ZBD-S027C, Virginia Diodes) used for incident power monitoring and cavity tuning. The total MW losses from the gyrotron to the DNP probe are approximately 4 dB. For more details concerning the DNP spectrometer see the work of Denysenkov *et al.*<sup>15,23</sup>

For DNP measurements the liquid sample is put into a quartz capillary (Polymicro) of 50, 30 or 20 μm inner diameter (ID) with the same 150 μm outer diameter (OD). The capillary is sealed with wax on both ends and placed along the axis of the cylindrical double resonance cavity. The size of the MW cavity is approximately 1.6 mm, which leads to effective sample volumes of 3, 1.1 or 0.5 nl for 50, 30 or 20 μm ID capillaries, respectively.

For typical NMR experiments not requiring a double resonance structure, such as  $T_{1n}$  measurements, a commercial 400 MHz liquid state probehead was used (Bruker BBI).

Both probeheads can be equipped with a temperature control unit (BCU 05, Bruker), bringing the sample to a set temperature using a stream of gas.

The DNP enhancements were determined by taking the <sup>1</sup>H FT-NMR spectra of the samples in the MW cavity (Fig. 1) with and without continuous wave (CW) MW irradiation of the (central) hyperfine line of the <sup>14</sup>N-TEMPOL nitroxide radicals, respectively. The proton NMR lines are then integrated to determine the signal strength, while the integrated enhancement is calculated using eqn (1).

CW-EPR measurements were performed with our home built pulsed high field EPR spectrometer operating at 180 GHz.<sup>24</sup> For measurements at temperatures higher than 25 °C an additional resistive heater was used. The sample temperature was monitored using a platinum thermometer attached to the body of the MW cavity.

## NMRD measurements

Longitudinal relaxation rates at magnetic fields ranging from 0.01 to 40 MHz proton Larmor frequency were measured using the field cycling technique with a high sensitivity Stellar Spinmaster FFC-2000-1T. Errors in the measurement of the relaxation rates are below 1%. Proton relaxivity is calculated by subtracting the relaxation rates of the buffer from the relaxation rate of the <sup>14</sup>N-TEMPOL solution, and normalizing to the radical concentration. High frequency relaxation rates at 250, 400, 500 and 950 MHz were measured on corresponding NMR spectrometers.

The paramagnetic enhancement of the solvent nuclear relaxation rate is described using the inner-sphere and the outer-sphere models,<sup>19,20,25,26</sup> which take into account the contributions to relaxation from the dipole–dipole coupled electron and nuclear spins when positioned at a fixed distance  $r$  ( $R_1^{\text{inner}}$ ) or when the nucleus in the solvent molecules is freely diffusing around the paramagnetic molecule, down to a distance of closest approach,  $d$  ( $R_1^{\text{outer}}$ ), respectively.

In the inner-sphere model, if the solvent nucleus exchanges between a position where it is bound to the paramagnetic molecule and a position where it is free in solution on a time scale shorter than its relaxation time in the bound position (fast exchange regime), the paramagnetic contribution to relaxation is given by<sup>25,26</sup>

$$R_1^{\text{inner}} = k(7J(\omega_s, \tau_c) + 3J(\omega_n, \tau_c))$$

where

$$k = f_M \frac{2}{15} \left( \frac{\mu_0}{4\pi} \right)^2 \frac{\gamma_1^2 g^2 \mu_B^2 S(S+1)}{r^6},$$

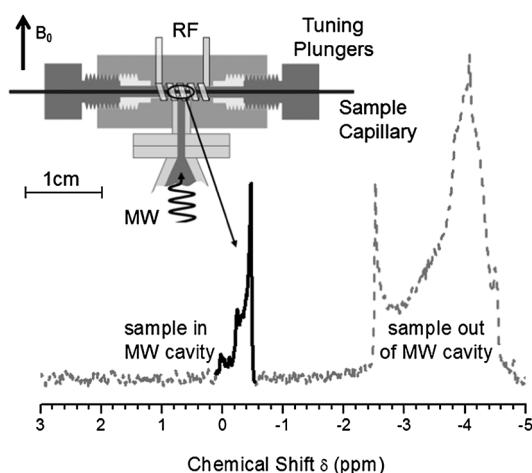


**Fig. 1** Schematic drawing of the double resonance structure used for <sup>1</sup>H-NMR at 400 MHz and EPR at 260 GHz simultaneously (top left) and a typical <sup>1</sup>H-NMR spectrum of water obtained with this setup. The peak at -0.4 ppm corresponds to the sample inside of the MW cavity, while the large signal between -2.5 and -4.5 ppm is due to the sample outside of the MW cavity.

$J(\omega, \tau)$  is the Lorentzian spectral density functions in the form of

$$J(\omega, \tau) = \frac{\tau}{1 + \omega^2 \tau^2},$$

where  $\tau_c$  is the correlation time for the dipolar interaction,  $f_M$  is the mole fraction of ligand nuclei in bound positions (equal to  $2 \times 10^{-3}/111$  assuming one water molecule bound to each paramagnetic molecule),  $\omega_I$  and  $\omega_S$  are the proton and electron Larmor frequencies multiplied by  $2\pi$ , respectively,  $S$  is the electron spin quantum number,  $\gamma_I$  is the proton gyromagnetic ratio,  $\mu_B$  is the electron Bohr magneton,  $g_e$  is the electron  $g$  factor, and  $\mu_0$  is the permeability of vacuum.

In the outer-sphere model, the translational diffusion of the ligand molecules causes a paramagnetic contribution to relaxation given by<sup>20</sup>

$$R_1^{\text{outer}} = k'(7\tilde{J}(\omega_S, \tau_D) + 3\tilde{J}(\omega_I, \tau_D))$$

where

$$k' = \frac{32\,000\pi}{405} \left(\frac{\mu_0}{4\pi}\right)^2 \frac{N_A [M] \gamma_I^2 g_e^2 \mu_B^2 S(S+1)}{dD},$$

$$\tilde{J}(\omega, \tau) = \frac{1 + 5z/8 + z^2/8}{1 + z + z^2/2 + z^3/6 + 4z^4/81 + z^5/81 + z^6/648},$$

$z = (2\omega\tau_D)^{0.5}$ ,  $N_A$  is Avogadro's constant,  $D$  is the sum of the diffusion coefficients of the solvent molecule and of the paramagnetic molecule, and  $[M]$  represents the molar concentration of the paramagnetic moiety (expressed in  $\text{mol dm}^{-3}$ ). This model was developed in the hypothesis of spherical molecules, with the unpaired electron in the center of the molecule. A diffusional correlation time  $\tau_D$  is defined, which depends on the diffusion coefficients and on the distance of closest approach  $d$  between solvent protons and electron spins:

$$\tau_D = \frac{d^2}{D}.$$

Finally, the coupling factor results

$$\xi = \frac{5}{7} \left[ 1 - \frac{3kJ(\omega_I, \tau_c) + 3k'\tilde{J}(\omega_I, \tau_D)}{R_1^{\text{inner}} + R_1^{\text{outer}}} \right].$$

## Results and discussion

The DNP experiments were performed over a broad range of  $^{14}\text{N}$ -TEMPOL radical concentrations in water, ranging from 5 mM up to 1 M, and in 3 different capillary sizes.

Fig. 2 shows a DNP experiment performed on a water sample doped with 1 M of  $^{14}\text{N}$ -TEMPOL in a 30  $\mu\text{m}$  ID capillary. The irradiation MW power was approximately 600 mW, corresponding to a  $B_1$  field of 3.5 G. The figure shows a strongly negatively enhanced signal in the MW cavity. It yields an enhancement factor of  $-83$ , the negative sign is caused by an electron–nuclear dipolar interaction typical for liquid state DNP experiments. Notably, while the signal from outside of the MW cavity remains unchanged at the same position at approximately  $-7$  ppm, the

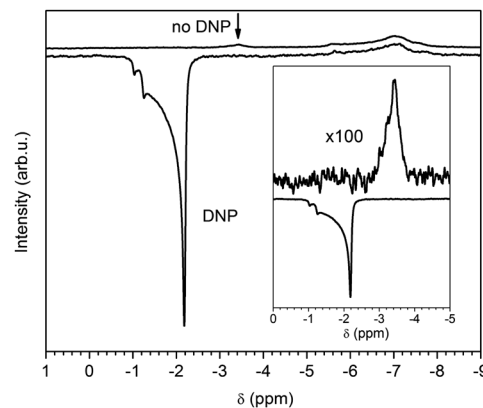


**Fig. 2** Normalized  $^1\text{H}$ -NMR spectra to single scan of 1 M  $^{14}\text{N}$ -TEMPOL in water with (lower spectrum – 64 scans) and without (upper spectrum – 512 scans) MW irradiation of the sample, respectively. An integrated enhancement of  $-83$  can be observed in the water proton signal. The inset shows the reference spectrum without irradiation enlarged by a factor of 100 for comparison.

DNP enhanced signal significantly changes its position with respect to the reference signal indicated by the arrow. This shift is caused by a combination of MW heating and the suppression of the strong paramagnetic shift of the 1 M radical concentration sample by the microwave irradiation.<sup>27</sup> Both contributions to the chemical shift change are important for a proper understanding of the DNP experiments and help to quantitatively analyze the parameters involved in eqn (1), which are discussed in detail in the following text.

### Sample temperature calibration

The sample temperature is an important parameter involved in almost every aspect of Overhauser DNP from relaxation rates to lineshapes and molecular motion. As a consequence, for a quantitative analysis, keeping track of the sample temperature is critical. Unfortunately, the sample temperature in our DNP experiment cannot be accessed directly, *e.g.* with a thermometer. Also, accessing the sample temperature *via* the temperature dependence of the chemical shift can be problematic, because the shift is strongly dependent on the experimental configuration of the probe<sup>28</sup> and thus prone to error.

Therefore, we calibrated the temperature with a method similar to the use of neat ethylene glycol as a “chemical shift thermometer”,<sup>29–31</sup> using a reference sample consisting of 90% water and 10% ethylene glycol. In this sample, the relative shift between the water proton peak and the  $\text{CH}_2$  peak of ethylene glycol exhibits a strong temperature dependence, which was calibrated. The calibration was performed using gas heating in both the standard Bruker BBI and the DNP probeheads, yielding the same calibration curve (see ESI†). This shows that unlike the approach relying on the absolute chemical shift this approach is insensitive to experimental configurations. To obtain the sample temperature under DNP conditions at a given MW power, the DNP sample is replaced by the reference water sample containing 10% ethylene glycol, which is irradiated with the same MW power. The relative shift then provides the reference sample temperature. Assuming the dielectric losses

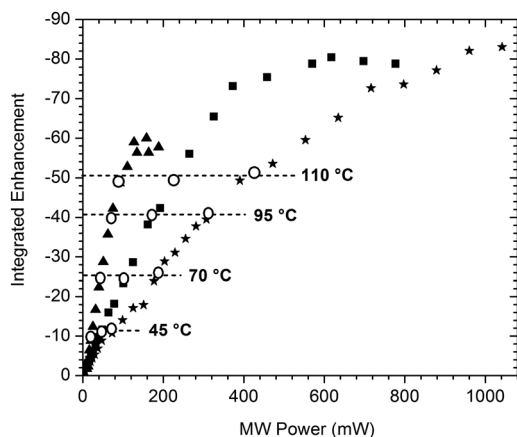


**Fig. 3** The DNP enhancement plotted against the incident MW power for a 1 M  $^{14}\text{N}$ -TEMPO in water sample for three capillary sizes: 50 ( $\blacktriangle$ ), 30 ( $\blacksquare$ ) and 20 ( $\blackstar$ )  $\mu\text{m}$  ID. The temperature increase is indicated by hollow circles ( $\circ$ ) for each capillary, dashed lines connect these points into virtual isotherms.

in water and the water–ethylene glycol mixture are the same, this temperature corresponds to the temperature of the DNP sample. To confirm this assumption the experiment was repeated using only 5% of ethylene glycol yielding the same temperature value.

Varying the sample size (capillary radius) results in varying dielectric losses in the MW resonator and thus in a variation of sample temperature for a given incident MW power. The result is shown in Fig. 3. As shown and proven by the above calibrations, the MW heating of the sample in the capillary leads to temperatures far beyond 100 °C which is well known as “superheated water”,<sup>32</sup> before further increasing the MW power destroys the sample in the MW cavity. Furthermore, our DNP probe (*i.e.* the MW cavity) has an inhomogeneous irradiation profile over the DNP sample (see ESI<sup>†</sup>), which leads to a temperature gradient across the sample. At low irradiation power the temperature gradient is low, whereas at high irradiation power it becomes more significant.<sup>14</sup> However, higher sample diffusion rates can smooth the temperature gradient effect. Since we monitor NMR peak positions, the stated temperatures represent the highest temperature in the sample and should therefore be considered as lower boundaries for possible  $\varepsilon$  values.

For more details concerning the DNP sample temperature see Fig. S1 of the ESI.<sup>†</sup>

### Leakage factor $f$

The leakage factor, which reflects the introduction of a strong relaxation pathway by adding radicals to the solution was measured for all mentioned radical concentrations and in a broad temperature range from room temperature, *i.e.* 25 °C to 95 °C, *i.e.* just below the boiling point of water. An excerpt of this is displayed in Table 1.

Being in the extreme narrowing limit,  $T_1$  becomes longer with increasing temperature. Typically, nuclear  $T_1$  of water spans values from 3 s to 10 s in a temperature range from 25 °C to 95 °C. However, the strongly temperature dependent effects on  $T_1$  in the presence and in the absence of radicals

**Table 1** Measured leakage factor  $f$  as a function of  $^{14}\text{N}$ -TEMPO concentration and the sample temperature

	200 mM	100 mM	40 mM	20 mM	5 mM
25 °C	0.99	0.98	0.95	0.90	0.66
95 °C	0.99	0.98	0.94	0.89	0.64

almost cancel out completely in the ratio, so the leakage factor turns out to be almost independent of the temperature of our experiment. Because adding radicals to the solution adds a strong relaxation pathway and thus shortens nuclear  $T_1$ , the leakage factor shows a monotonic increase with radical concentration. Already at 40 mM  $^{14}\text{N}$ -TEMPO concentration, the leakage factor has reached 0.95 and at 200 mM it is 0.99 and therefore practically at its theoretical maximum of 1.

The concentration dependence of the leakage factor therefore dominates the fast rise of the observed DNP enhancements up to 100 mM (Fig. 4). A further increase in the enhancement can be attributed to Heisenberg (spin) exchange, collapsing the three EPR lines of  $^{14}\text{N}$ -TEMPO into a single line at high concentration (Fig. 5), making saturation easier. The spread of the DNP enhancements for a given isotherm in Fig. 4 is due to the capillary change between consecutive measurements, which leads to slightly different MW couplings and thus sample temperatures.

### Saturation factor $s$

The saturation factor  $s$  in a DNP experiment is in general hard to access experimentally, especially at high magnetic fields, by EPR methods, as for example ELDOR,<sup>33</sup> due to very short electron spin relaxation times  $T_{1e}$  and  $T_{2e}$  of nitroxide radicals in liquid solution. Also, extrapolating the experimentally observed DNP enhancements to full saturation by a power curve<sup>18</sup> will not work well as the MW irradiation of the sample always results in a change of the sample temperature. Since the extrapolation to infinite MW power is unstable in the first place, the temperature deviation prevents the power curve method from giving a result with a reasonable error.

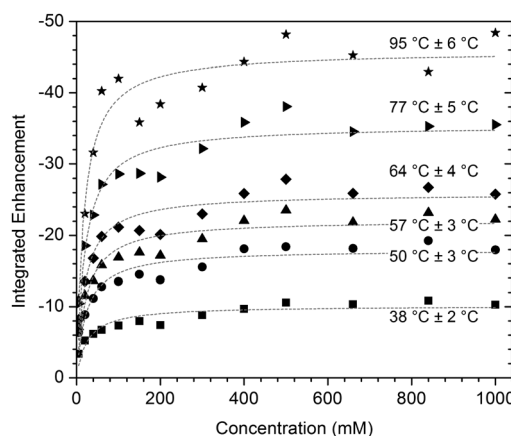


**Fig. 4** Dependence of the integrated DNP enhancement on the  $^{14}\text{N}$ -TEMPO concentration for various irradiation powers and hence sample temperatures, as indicated in the figure. The experiment was performed using 30  $\mu\text{m}$  ID capillaries.

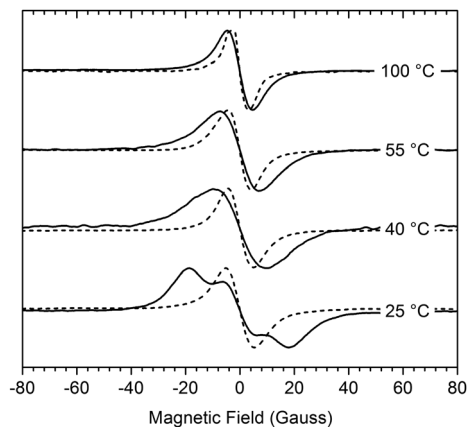


**Fig. 5** 180 GHz CW-EPR spectra of  $^{14}\text{N}$ -TEMPOL in water samples with 100 mM (solid lines) and 1 M (dotted lines) radical concentration, respectively, at various temperatures ranging from room temperature (bottom) to the boiling point (top). In this regime both elevated temperature and radical concentration narrow the EPR line, making saturation easier.

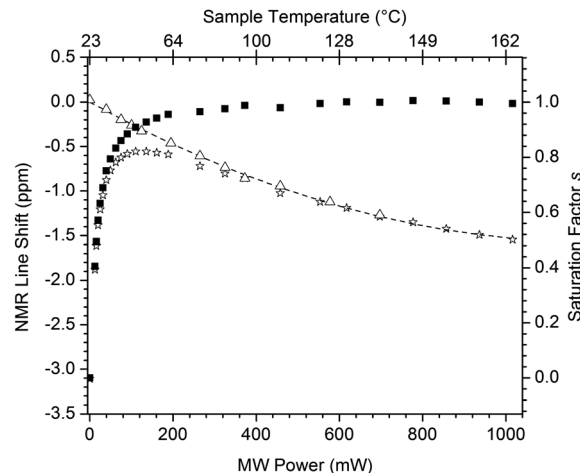


**Fig. 6** NMR line shifts of the peak of a pure water sample ( $\Delta$ ) and a 1 M  $^{14}\text{N}$ -TEMPOL in water sample ( $\star$ ), plotted against the incident MW power. Through the microwave heating calibration each irradiation power can be assigned a sample temperature (temperature scale on top). By subtracting the temperature shift from the total NMR shift the pure paramagnetic shift is obtained, which can be scaled to yield the saturation factor ( $\blacksquare$ , scale on the right).

Consequently, we explored a method where  $s$  is accessed *via* the paramagnetic shift. This idea to determine the saturation of the EPR line has been already presented in the work of Wind *et al.*<sup>34</sup> reducing the Knight shift in a fluoranthenyl radical anion salt one-dimensional crystal, and by Gafurov *et al.* for DNP measurements in aqueous solutions of Fremy's salt.<sup>14</sup> In a DNP sample in a static magnetic field, the nuclei experience a certain paramagnetic shift, depending on the radical concentration and on the interaction of the radicals with the solvent.<sup>27</sup> If the electron spin transition is now saturated, the electron spin polarization is diminished. In consequence, the paramagnetic shift is diminished as well. At full saturation, *i.e.* equalized electron spin populations and no polarization left, the paramagnetic shift has disappeared altogether. If the temperature effect on the chemical shift and the variation of the paramagnetic shift can be distinguished well, monitoring the NMR peak position gives a direct access to  $s$ . By subtracting the temperature dependent chemical shift of a reference sample without radicals from the total NMR shift of the DNP sample the pure paramagnetic shift is obtained. This allows determining the saturation factor  $s$ .

Because the paramagnetic shift scales linearly with the radical concentration, high concentrations are required to apply this method. For a sample with 1 M concentration of  $^{14}\text{N}$ -TEMPOL in water the paramagnetic shift is large enough to do so, as can be seen in Fig. 6.

Fig. 6 shows that for a 20  $\mu\text{m}$  ID capillary a MW power of roughly 100 mW is sufficient to achieve  $>0.9$  saturation. For MW powers above 200 mW the saturation factor  $s$  does not improve anymore, but the sample is heated further. As a consequence, the NMR line shift of the DNP sample follows the temperature shift of the pure water.

The dependence of the saturation factor  $s$  on the applied MW power can be better understood from the CW-EPR spectra of the DNP samples. The narrower the EPR linewidth of the respective spectrum, the easier it is to saturate the

corresponding EPR transition. The EPR spectrum is determined by the radical concentration and by the temperature through the MW heating during the DNP experiment. As can be seen in Fig. 5, both an elevated temperature and a higher concentration make the Heisenberg (spin) exchange rate higher, which causes the three hyperfine lines of  $^{14}\text{N}$ -TEMPOL to collapse into one. For the 1 M sample the spin exchange rate at 25  $^{\circ}\text{C}$  is large enough, so the temperature effect on the linewidth is less pronounced than in the case of the 100 mM sample. This linewidth dependence on radical concentration and temperature also affects the DNP enhancement for low concentration samples (Fig. 4).

### Coupling factor $\xi$ from NMRD

The relaxation profiles of a 40 mM TEMPOL solution were acquired from 25  $^{\circ}\text{C}$  to 80  $^{\circ}\text{C}$ , and normalized to 1 mM radical concentration after subtraction of the pure water relaxation rates. The profiles, reported in Fig. 7, show that relaxivity is almost constant at low fields and then decreases (according to the spectral density functions previously reported) to approach the smaller high field values, when the  $J(\omega_s, \tau_c)$  and  $\tilde{J}(\omega_s, \tau_D)$  terms approach zero. This decrease in relaxivity is called dispersion. The dispersion is centred at the proton Larmor frequency with a relaxivity value equal to the average between the low field value and the high field value with the  $J(\omega_s, \tau_c)$  and  $\tilde{J}(\omega_s, \tau_D)$  terms approaching zero. Fig. 7 shows that the centre of the dispersion for the profiles acquired at different temperatures is positioned at higher fields with increasing temperature. This is a clear indication of the expected decrease with temperature of the correlation time of the motions modulating the water proton–unpaired electron hyperfine interaction.<sup>26</sup> In turn, this indicates that the coupling factor increases with temperature, as expected.<sup>19</sup> The profiles were fitted according to the outer-sphere and inner-sphere relaxation models, *i.e.*, as

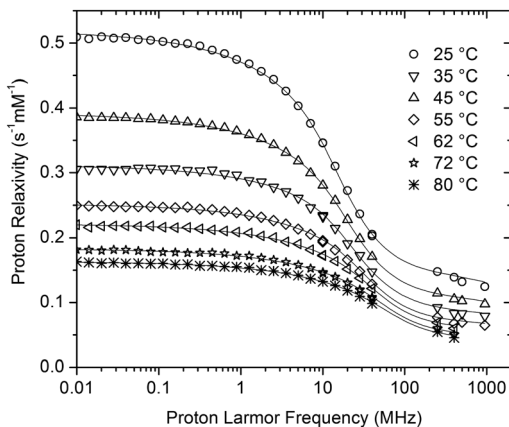


**Fig. 7** Solvent water  $^1\text{H}$  relaxivity profiles for solutions of  $^{14}\text{N}$ -TEMPOL at different temperatures ranging from 25 to 80  $^\circ\text{C}$ . Best fit profiles are shown as lines.

the sum of the contributions to relaxation from the translational diffusion of water molecules freely diffusing around the radical, and from water protons bound to the radical at a fixed distance,  $r$ , from the paramagnetic center, and in fast exchange with the bulk solvent.

A very good fit was indeed obtained with a unique value of  $r$  and of the distance of closest approach,  $d$ . The resulting best fit parameters are reported in Table 2. From the standard deviation of the best fit parameters, the error of the correlation time values can be estimated to be between 5 and 10%. Although the effect of possible local motions faster than the global reorientation time of the complex is not taken into account explicitly in the present model, the quality of the fits was very good. Therefore, the inclusion of further parameters related to these fast motions would not permit us to obtain accurate estimates of the fitting parameters due to their large covariance. The contribution from the inner-sphere term amounts to about 30% of the total relaxivity at low fields for the profile at 25  $^\circ\text{C}$ . The diffusion coefficient  $D$  at 25  $^\circ\text{C}$  is in agreement with the expectations and with previous results for the same and similar nitroxide molecules.<sup>12,19,22</sup> It increases with temperature in very good agreement with the  $T/\eta$  dependence (where  $\eta$  is the viscosity). The correlation time in the inner-sphere term results in a smaller value compared to the diffusional correlation time. Since the former is ascribed to the reorientation time of the molecule, this indicates that the paramagnetic molecule rotates significantly in the time it takes for the solvent water

**Table 2** Best fit parameters of the field dependent relaxation profiles and corresponding coupling factors at 400 MHz

$T$ ( $^\circ\text{C}$ )	$\tau_c$ (ps)	$r$ ( $\text{\AA}$ )	$d$ ( $\text{\AA}$ )	$D$ ( $10^{-9} \text{ m}^2 \text{ s}^{-1}$ )	$\tau_D$ (ps)	$\zeta_{400}$ (MHz)
25	17.3	2.78	2.88	2.74	30.3	0.008
35	12.9			3.61	22.3	0.012
45	11.2			4.74	17.5	0.018
55	7.84			5.46	15.2	0.026
62	6.12			5.92	14.0	0.031
72	4.60			6.95	11.9	0.042
80	3.90			7.66	10.8	0.050

molecules to approach the paramagnetic molecule. Furthermore, it should be considered that the unpaired electron is not located at the center of the radical. This causes a rotational contribution to relaxation that is not accounted for by the translational diffusion model. Therefore, the inner-sphere term may not represent a real water molecule actually bound to the radical with a lifetime longer than  $\tau_c$ , but may simply report such a rotational effect occurring during solvent diffusion. Because of the non-central position of the unpaired electron in the radical,  $d$  has a value related to the weighted average of the distances of closest approach for the different directions along which the water molecules approach the radical.<sup>19</sup>

The NMRD coupling factors at 400 MHz proton Larmor frequency have been calculated from the above parameters and the equations are reported in the Experimental section, as a function of temperature, and shown in Fig. 8 (also reported in Table 2). The coupling factor increases by more than a factor of 5 on passing from 25  $^\circ\text{C}$  ( $\zeta = 0.008$ ) to 80  $^\circ\text{C}$  ( $\zeta = 0.050$ ).

### Coupling factor $\zeta$ from DNP experiments

Having determined the leakage factor (Table 1), the saturation factor (Fig. 6) and the experimental DNP enhancement as a function of temperature (Fig. 3), eqn (1) can now be used to calculate the concentration independent coupling factor  $\zeta$  from the DNP experiments for the respective sample temperature. This is depicted in Fig. 8 for several experiments and sample sizes, yielding a plot of coupling factor as a function of sample temperature. The figure shows that the data are well reproducible, even for different sample sizes and hence different heating and saturation behaviour, *i.e.* our procedure accurately extracts  $f$ ,  $s$  and the temperature. Referring to biomolecular applications at physiological temperatures (*e.g.* 45  $^\circ\text{C}$ ), the maximum DNP enhancement will be  $-14$  at full saturation of

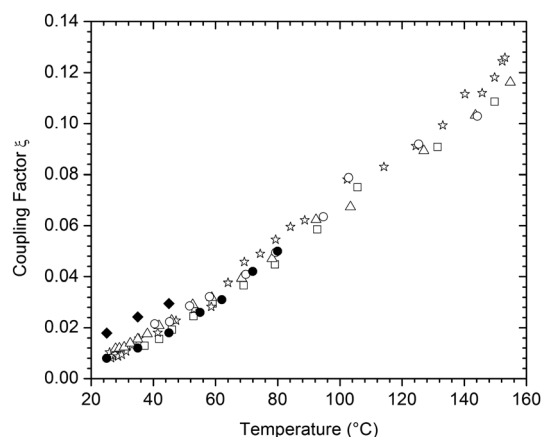


**Fig. 8** Coupling factor (enhancement) between the  $^{14}\text{N}$ -TEMPOL radicals and the water protons *versus* the sample temperature. The DNP experiments were performed using 30  $\mu\text{m}$  ( $\square$ ,  $\circ$ ,  $\triangle$ ) and 20  $\mu\text{m}$  ( $\star$ ) ID capillaries. The spread of the experimental data points indicates the statistical errors in enhancement and heating reproducibility. Coupling factors determined through the field dependent relaxation measurements ( $\bullet$ ) as well as by molecular dynamics<sup>34</sup> ( $\blacklozenge$ ) are also shown for comparison.

EPR transition, as calculated from the expected coupling factor of 0.02.

## Conclusions

We were able for the first time to determine the saturation factor  $s$  of high field DNP measurements, exploiting the paramagnetic shift induced by a high concentration of our polarizing agent ( $^{14}\text{N}$ -TEMPOL). For a high radical concentration (1 M) full saturation could be achieved already with moderate microwave power (200 mW). We determined the elevated sample temperature under MW irradiation by using an ethylene glycol doped reference sample, which exhibits a temperature dependent relative chemical shift. For high MW power (1 W) surprisingly high temperatures of up to 160 °C could be reached.

With knowledge of the saturation factor  $s$ , leakage factor  $f$  as well as the sample temperature during the experiment, the coupling factor  $\xi$ , which is concentration independent, could be calculated from the experimental data as a function of temperature (Fig. 8).

The value obtained for the coupling factor  $\xi$  at 45 °C from the DNP experiments is slightly lower than the value of  $\xi = 0.03$  predicted by molecular dynamics simulations (MD) for 9.2 T (260 GHz) at this temperature<sup>35</sup> and it compares rather well to the  $\xi$  values predicted from NMR relaxation dispersion curves for this and similar nitroxide radicals in water.<sup>12,19,22,36,37</sup> The increase with temperature is nicely reproduced in both cases (MD and NMRD). Although the possible presence of fast local motions may cause an underestimation of the coupling factor at high magnetic fields, when calculated from the NMRD profiles and analyzed using the hard sphere model,<sup>40</sup> the value derived for the present system at 9.2 T (400 MHz proton Larmor frequency) is rather close to the experimentally observed value.

Alternatively, our experimentally observed DNP enhancement of  $\varepsilon = -11$  obtained at 9.2 T and 45 °C can be compared to the experimentally determined DNP enhancements of  $\varepsilon = -50$ <sup>10</sup> and  $-63$ <sup>11</sup> obtained at a somewhat lower magnetic field of 3.4 T (95 GHz/W-band). Taking the theoretically predicted field dependence of  $\xi \sim B_0^{-2}$  for rotational motion<sup>18,38</sup> and  $\xi \sim B_0^{-3/2}$  (ref. 35 and 39) for translational motion, respectively, these values compare again rather well with our data, taking into account the different experimental setups used and the uncertainties for  $\varepsilon$ ,  $T$  and  $s$ .

We observe very large integrated enhancements of up to  $-83$  in aqueous solutions of 1 M  $^{14}\text{N}$ -TEMPOL at temperatures of about 160 °C. Therefore the very high enhancements observed for TEMPOL and Fremy's salt<sup>14</sup> are partly due to very high temperatures achieved in the tiny sample capillaries by microwave heating. A second effect which may be important in producing higher coupling factors than expected from the magnetic field dependence can be related to additional dynamic modes, which were observed in MD simulations, and in the case of the TEMPOL–water system can be modelled within the classical force-free model<sup>41</sup> by inclusion of fast reorientation times and the associated order parameters.<sup>42</sup> Taking both effects into account permits us to achieve coupling

parameters derived from NMRD experiments similar to coupling parameters calculated from MD simulations and in good quantitative agreement with the experimentally observed DNP enhancements at 9.2 T. Despite the fact that the maximum enhancements were obtained for samples with very high radical concentrations (to observe the paramagnetic shift) and very high temperatures (to saturate the electron spin system), reasonable good enhancements of  $\varepsilon \approx -14$  can be achieved at 9.2 T magnetic field for a sample with a moderate radical concentration of 20 mM (corresponding to a leakage factor  $f = 0.9$ ) and at a temperature of 45 °C, if full saturation of the electron spin transition is achieved.

## Outlook

A new resonator design<sup>40</sup> will render much larger sample volumes, improve the NMR performance (sensitivity and linewidth) and lessen the problem of MW heating. Together with sufficiently large enhancements at high magnetic fields and at ambient temperature this leads the way towards applications of this new approach towards analytics of size restricted samples such as for example biofluids or for biomolecular structural research.

## Acknowledgements

This work was supported by the DIP program from the German Research Council (DFG), the Center for Biomolecular Magnetic Resonance Frankfurt (BMRZ), the European Commission, contract Bio-NMR no. 261863, and the COST Action TD1103. We thank Burkhard Endeward, Andriy Marko, Marat Gafurov, Johanna Baldus, Frank Löhr and Christian Richter from the Goethe University for experimental support and Shimon Vega from the Weizmann Institute for stimulating discussions. Also, we gratefully acknowledge technical support from Bernhard Thiem, Manfred Strupf, Bernhard Klug and the mechanical workshop of the Institute of Physical Chemistry in Frankfurt.

## References

- 1 A. W. Overhauser, *Phys. Rev.*, 1953, **92**, 411–415.
- 2 T. R. Carver and C. P. Slichter, *Phys. Rev.*, 1953, **92**, 212–213.
- 3 T. R. Carver and C. P. Slichter, *Phys. Rev.*, 1956, **102**, 975–980.
- 4 L. R. Becerra, G. J. Gerfen, R. J. Temkin, D. J. Singel and R. G. Griffin, *Phys. Rev. Lett.*, 1993, **71**, 3561–3564.
- 5 J. H. Ardenkjaer-Larsen, B. Fridlund, A. Gram, G. Hansson, L. Hansson, M. H. Lerche, R. Servin, M. Thaning and K. Golman, *Proc. Natl. Acad. Sci. U. S. A.*, 2003, **100**, 10158–10163.
- 6 K. Golman, R. i. t. Zandt, M. Lerche, R. Pehrson and J. H. Ardenkjaer-Larsen, *Cancer Res.*, 2006, **66**, 10855–10860.
- 7 C. Song, K.-N. Hu, C.-G. Joo, T. M. Swager and R. G. Griffin, *J. Am. Chem. Soc.*, 2006, **128**, 11385–11390.
- 8 M. Reese, D. Lennartz, T. Marquardsen, P. Höfer, A. Tavernier, P. Carl, T. Schippmann, M. Bennati,

- T. Carlomagno, F. Engelke and C. Griesinger, *Appl. Magn. Reson.*, 2008, **34**, 301–311.
- 9 S. Hu, M. Zhu, H. A. I. Yoshihara, D. M. Wilson, K. R. Keshari, P. Shin, G. Reed, C. von Morze, R. Bok, P. E. Z. Larson, J. Kurhanewicz and D. B. Vigneron, *Magn. Reson. Imaging*, 2011, **29**, 1035–1040.
- 10 P. J. M. van Bentum, G. H. A. van der Heijden, J. A. Villanueva-Garibay and A. P. M. Kentgens, *Phys. Chem. Chem. Phys.*, 2011, **13**, 17831–17840.
- 11 E. V. Kryukov, K. J. Pike, T. K. Y. Tam, M. E. Newton, M. E. Smith and R. Dupree, *Phys. Chem. Chem. Phys.*, 2011, **13**, 4372–4380.
- 12 P. Höfer, G. Parigi, C. Luchinat, P. Carl, G. Guthausen, M. Reese, T. Carlomagno, C. Griesinger and M. Bennati, *J. Am. Chem. Soc.*, 2008, **130**, 3254–3255.
- 13 M.-T. Türke, I. Tkach, M. Reese, P. Höfer and M. Bennati, *Phys. Chem. Chem. Phys.*, 2010, **12**, 5893–5901.
- 14 M. Gafurov, V. Denysenkov, M. Prandolini and T. Prisner, *Appl. Magn. Reson.*, 2012, **43**, 119–128.
- 15 V. Denysenkov, M. J. Prandolini, M. Gafurov, D. Sezer, B. Endeward and T. F. Prisner, *Phys. Chem. Chem. Phys.*, 2010, **12**, 5786–5790.
- 16 M. J. Prandolini, V. P. Denysenkov, M. Gafurov, B. Endeward and T. F. Prisner, *J. Am. Chem. Soc.*, 2009, **131**, 6090–6092.
- 17 M. J. Prandolini, V. P. Denysenkov, M. Gafurov, S. Lyubenova, B. Endeward, M. Bennati and T. F. Prisner, *Appl. Magn. Reson.*, 2008, **34**, 399–407.
- 18 K. H. Hausser and D. Stehlik, *Adv. Magn. Reson.*, 1968, **3**, 79–139.
- 19 M. Bennati, C. Luchinat, G. Parigi and M.-T. Türke, *Phys. Chem. Chem. Phys.*, 2010, **12**, 5902–5910.
- 20 L.-P. Hwang and J. H. Freed, *J. Chem. Phys.*, 1975, **63**, 4017–4025.
- 21 R. A. Wind and J.-H. Ardenkjaer-Larsen, *J. Magn. Reson.*, 1999, **141**, 347–354.
- 22 M.-T. Türke, G. Parigi, C. Luchinat and M. Bennati, *Phys. Chem. Chem. Phys.*, 2012, **14**, 502–510.
- 23 V. P. Denysenkov, M. J. Prandolini, A. Krahn, M. Gafurov, B. Endeward and T. F. Prisner, *Appl. Magn. Reson.*, 2008, **34**, 289–299.
- 24 M. Rohrer, O. Brüggmann, B. Kinzer and T. Prisner, *Appl. Magn. Reson.*, 2001, **21**, 257–274.
- 25 I. Solomon, *Phys. Rev.*, 1955, **99**, 559–565.
- 26 I. Bertini, C. Luchinat and G. Parigi, *Adv. Inorg. Chem.*, 2005, **57**, 105–172.
- 27 I. Bertini, C. Luchinat and G. Parigi, in *Solution NMR of Paramagnetic Molecules*, Elsevier, 2001, vol. 2.
- 28 R. E. Hoffman, *J. Magn. Reson.*, 2006, **178**, 237–247.
- 29 A. L. Van Geet, *Anal. Chem.*, 1968, **40**, 2227–2229.
- 30 M. L. Kaplan, F. A. Bovey and H. N. Cheng, *Anal. Chem.*, 1975, **47**, 1703–1705.
- 31 C. Ammann, P. Meier and A. Merbach, *J. Magn. Reson.*, 1982, **46**, 319–321.
- 32 L. J. Briggs, *J. Appl. Phys.*, 1955, **26**, 1001–1003.
- 33 M.-T. Türke and M. Bennati, *Phys. Chem. Chem. Phys.*, 2011, **13**, 3630–3633.
- 34 R. A. Wind, H. Lock and M. Mehring, *Chem. Phys. Lett.*, 1987, **141**, 283–288.
- 35 D. Sezer, M. J. Prandolini and T. F. Prisner, *Phys. Chem. Chem. Phys.*, 2009, **11**, 6626–6637.
- 36 C. Griesinger, M. Bennati, H. M. Vieth, C. Luchinat, G. Parigi, P. Höfer, F. Engelke, S. J. Glaser, V. Denysenkov and T. F. Prisner, *Prog. Nucl. Magn. Reson. Spectrosc.*, 2012, **64**, 4–28.
- 37 M. Reese, M.-T. Türke, I. Tkach, G. Parigi, C. Luchinat, T. Marquardsen, A. Tavernier, P. Höfer, F. Engelke, C. Griesinger and M. Bennati, *J. Am. Chem. Soc.*, 2009, **131**, 15086–15087.
- 38 W. Müller-Warmuth and K. Meise-Gresch, *Adv. Magn. Reson.*, 1983, **11**, 1–45.
- 39 Y. Ayant, E. Belorizky, J. Aluzon and J. Gallice, *J. Phys.*, 1975, **36**, 991–1004.
- 40 V. Denysenkov and T. Prisner, *J. Magn. Reson.*, 2012, **217**, 1–5.
- 41 D. Sezer, *Phys. Chem. Chem. Phys.*, 2013, **15**, 526–540.
- 42 G. Lipari and A. Szabo, *J. Am. Chem. Soc.*, 1982, **104**, 4546–4559.

**COMMENTED PAPER 9**

**P. Neugebauer**, J. G. Krummenacker, V. P. Denysenkov, C. Helmling, C. Luchinat, G. Parigi and T. F. Prisner

High-field liquid state NMR hyperpolarization: a combined DNP/NMRD approach

*Phys. Chem. Chem. Phys.*, 16, 18781-18787 (2014).



Cite this: *Phys. Chem. Chem. Phys.*,  
2014, 16, 18781

## High-field liquid state NMR hyperpolarization: a combined DNP/NMRD approach†

Petr Neugebauer,<sup>a</sup> Jan G. Krummenacker,<sup>a</sup> Vasyl P. Denysenkov,<sup>a</sup>  
Christina Helmling,<sup>a</sup> Claudio Luchinat,<sup>b</sup> Giacomo Parigi<sup>\*b</sup> and Thomas F. Prisner<sup>\*a</sup>

Here we show how fast dynamics between radicals and solvent molecules in liquid solutions can be detected by comparison of coupling factors determined by nuclear magnetic relaxation dispersion (NMRD) measurements and dynamic nuclear polarization (DNP) enhancement measurements at high magnetic field (9.2 T). This is important for a theoretical understanding of the Overhauser DNP mechanism at high magnetic fields and thus for optimization of the DNP agent/target system for high resolution liquid state NMR applications. Mixtures of the solution of TEMPOL radicals in water, toluene, acetone and DMSO have been investigated. The results are compared to the classical hard-sphere model and molecular dynamic simulations. Our results clearly indicate that fast sub-ps dynamics, which are not related to classical rotational or translational motion of the molecules, significantly contribute to the Overhauser DNP mechanism at high magnetic fields.

Received 4th June 2014,  
Accepted 15th July 2014

DOI: 10.1039/c4cp02451f

www.rsc.org/pccp

### Introduction

It has been shown that dynamic nuclear polarization (DNP) can significantly enhance NMR signals in solids even at high magnetic fields.<sup>1</sup> The mechanisms responsible for this polarization transfer in solids are the solid effect in the case of a spin  $S = 1/2$ ,  $I = 1/2$  system and the cross effect if two radicals couple simultaneously to the nuclear spin. Fast dissolution of the solid after DNP polarization transfer allows one to use this hyperpolarization for <sup>13</sup>C MRI and MRS applications in liquids.<sup>2</sup> Subsequently also surprisingly large DNP enhancements have been observed in liquids at magnetic fields of 9.2 T (corresponding to 400 MHz proton NMR frequency).<sup>3,4</sup> In this case the DNP enhancement is based on the unbalance of the cross-relaxation rates (zero-quantum and double quantum) between nuclear and electron spin and the mechanism is called Overhauser effect.<sup>5</sup> The Overhauser enhancement can be written as

$$\epsilon_{\text{OE}} = \frac{\langle I_z \rangle - I_0}{I_0} = \frac{\gamma_e}{\gamma_n} \cdot f \cdot s \cdot \xi \quad (1)$$

where  $\gamma_e$  and  $\gamma_n$  are the gyromagnetic ratios of the electron and the nucleus, respectively, *i.e.*  $\gamma_e/\gamma_n \approx -660$  for a proton spin, and  $f = 1 - T_{1S}/T_{1I}$  is the leakage factor, which can be

determined from the nuclear  $T_1$  relaxation time in the presence ( $T_{1S}$ ) or absence ( $T_{1I}$ ) of radicals in the solution. It denotes how much of the relaxation of the nuclear spin is caused by the radicals ( $f = 1$  for 100%,  $f = 0$  for 0%). The saturation factor  $s$  describes how well the electron spin system is saturated by the resonant microwave (MW) irradiation, ranging again from 0 (no saturation) to 1 (full saturation). The last parameter  $\xi$  is called the coupling factor. While  $f$  can be optimized by varying the concentration of the radical and  $s$  by applying enough microwave power, the coupling factor  $\xi$  depends on the strength and dynamics of the coupling between electron and nuclear spin and cannot be easily controlled. For magnetic dipole-dipole coupling, which is usually the dominant coupling for radicals and proton nuclear spins of solvent molecules, the maximum coupling factor is  $\xi = 0.5$ . This yields a maximal theoretical enhancement of  $-330$  for proton nuclear spins. Whereas the leakage factor  $f$  can be easily determined by NMR experiments, the saturation factor  $s$  is more difficult to access at high magnetic fields in solutions. We found recently that for high radical concentrations the quenching of the paramagnetic shift can be used to determine this value.<sup>6</sup> The coupling factor  $\xi$  can be calculated from the spectral density function  $J(\omega)$  of the dipolar interaction by

$$\xi = \frac{5J(\omega_s)}{3J(\omega_I) + 7J(\omega_s)} \quad (2)$$

where  $\omega_s$  and  $\omega_I$  are the electron and nuclear spin Larmor frequencies, respectively. Within the force-free hard sphere

<sup>a</sup> Institute of Physical and Theoretical Chemistry and Center for Biomolecular Magnetic Resonance (BMRZ), Goethe-University, Max-von-Laue-Str. 7, 60438, Frankfurt am Main, Germany. E-mail: prisner@chemie.uni-frankfurt.de

<sup>b</sup> Magnetic Resonance Center (CERM) and Department of Chemistry, University of Florence, Via L. Sacconi 6, Florence, Italy. E-mail: parigi@cern.unifi.it

† Electronic supplementary information (ESI) available. See DOI: 10.1039/c4cp02451f

model<sup>7</sup> the spectral density function for translational diffusion can be expressed by

$$\tilde{J}(\omega, \tau) = \frac{1 + 5z/8 + z^2/8}{1 + z + z^2/2 + z^3/6 + 4z^4/81 + z^5/81 + z^6/648} \quad (3)$$

with  $z = (2\omega \tau_D)^{1/2}$  and the diffusion correlation time  $\tau_D$  given by

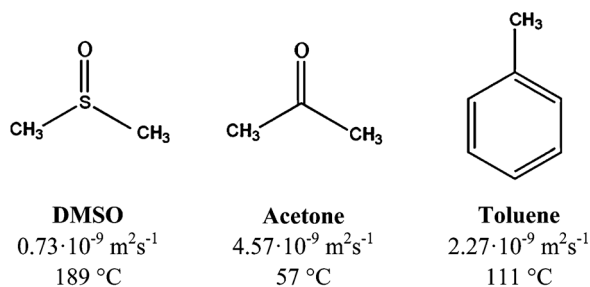
$$\tau_D = \frac{d^2}{D} \quad (4)$$

with  $D$  being the sum of the diffusion coefficients of the radical and the solvent molecule and  $d$  the distance of closest approach between electron and nuclear spin. More sophisticated models also include an inner-sphere contribution from the rotation of the transient radical–solvent complex with a rotational correlation time  $\tau_R$ .<sup>8</sup> The respective correlation times can be determined from the field dependence of the solvent proton relaxation dispersion (NMRD) profiles.<sup>8,9</sup>

Recently we could show that the DNP enhancement at a magnetic field of 9.2 T of a solution of TEMPOL in water could be quantitatively modelled by the translational motion of nitroxide and water molecules and an additional contribution arising from a fast motion, which could be modelled within the classical force-free hard-sphere model by a fast inner-sphere rotation of the complex.<sup>6</sup> Molecular dynamic simulations of TEMPOL in water also suggested contributions from fast local dynamics of the TEMPOL–water complex.<sup>10</sup> Here we extended this study to the solvents acetone, toluene and DMSO. Despite the fact that these solvents have rather different viscosities and diffusion rates, substantial DNP enhancements have been observed for all solvents. Comparison of the high field DNP enhancements with the NMRD measurements allows us to conclude that additional fast dynamics of the radical–solvent complex contribute substantially to the coupling factor at high magnetic fields.

## Results and discussion

Solutions of TEMPOL (4-hydroxy-2,2,6,6-tetramethylpiperidin-1-oxyl) radicals with the solvents shown in Scheme 1 were prepared with different radical concentrations (5 mM–1 M). Samples were filled in the respective capillaries for NMR, EPR or DNP experiments without degassing.



**Scheme 1** Solvent molecules used in this study together with their diffusion coefficients at 25 °C and their boiling points in °C.

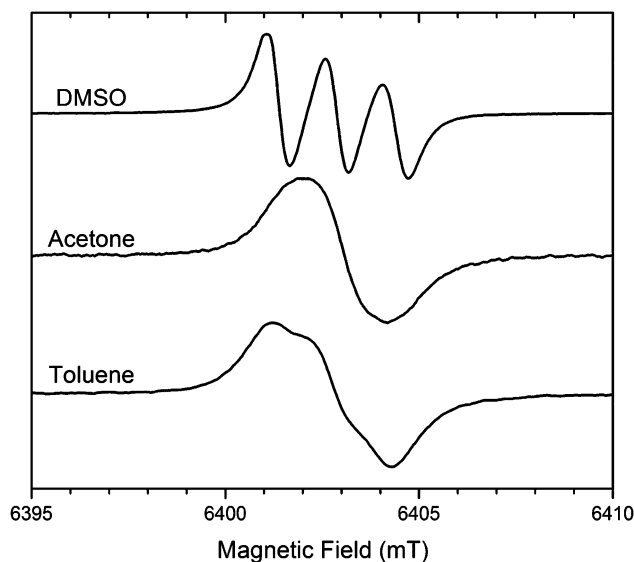


**Fig. 1** 180 GHz CW-EPR spectra of 40 mM <sup>14</sup>N-TEMPOL in DMSO, acetone and toluene samples (not degassed) recorded at room temperature. The picture shows the varied line shape broadening for all three solvents, due to the different Heisenberg exchange rates.

Because of the rather different diffusion coefficients of the solvents, different EPR spectra and DNP enhancements are expected at high magnetic fields. Fig. 1 shows CW-EPR spectra taken at 180 GHz (G-band) for 40 mM <sup>14</sup>N-TEMPOL concentrations recorded at a temperature of 25 °C.

The linewidth is affected by the presence of paramagnetic oxygen in the sample. Whereas in the case of DMSO the amount of dissolved oxygen is negligible (0.034 ml O<sub>2</sub> ml<sup>-1</sup> solvent)<sup>11</sup> this is not the case for acetone (0.207 ml O<sub>2</sub> ml<sup>-1</sup> solvent)<sup>12</sup> and toluene (0.186 ml O<sub>2</sub> ml<sup>-1</sup> solvent).<sup>13</sup> However at high fields the contribution of oxygen to the linewidth is less pronounced than at 9 GHz (X-band) frequencies where even a small amount of paramagnetic oxygen affects the linewidth strongly. The main difference of the line shape for the different solvents thus comes from Heisenberg spin exchange, demonstrating the rather different translational dynamics of the different solutions. We extracted spin exchange rates from linewidth broadening as a function of radical concentration at X- and G-band frequencies. Values for the exchange rate of  $k_H = (2.7 \pm 0.1) \times 10^{-9} \text{ M}^{-1} \text{ s}^{-1}$ ,  $(11.2 \pm 0.2) \times 10^{-9} \text{ M}^{-1} \text{ s}^{-1}$  and  $(8.8 \pm 0.3) \times 10^{-9} \text{ M}^{-1} \text{ s}^{-1}$  for DMSO, acetone and toluene, respectively, were determined at 25 °C. At higher temperature and concentration the three lines collapse into a single line which narrows further before finally dipolar line broadening occurs at very high concentrations (see ESI†).

The DNP experiments were performed over a broad range of <sup>14</sup>N-TEMPOL radical concentrations: from 5 mM up to 1 M in the case of DMSO and acetone or up to 200 mM in the case of toluene. Fig. 2 shows DNP experiments performed on a sample doped with 1 M <sup>14</sup>N-TEMPOL in DMSO (Fig. 2A, 30 μm ID capillary size), in acetone (Fig. 2B, 20 μm ID capillary size) and in toluene (Fig. 2C, 50 μm ID capillary size). The irradiation MW power was approximately 450 mW in all experiments,

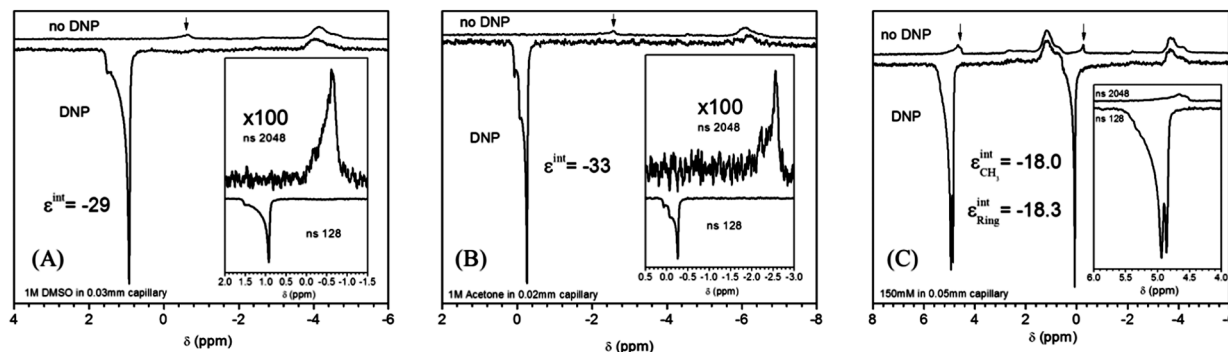


Fig. 2 Normalized  $^1\text{H}$ -NMR spectra to single scan of 1 M  $^{14}\text{N}$ -TEMPOL in DMSO (A), acetone (B) and toluene (C) with (lower spectrum –128 scans) and without (upper spectrum –2048 scans) MW irradiation of the sample. Spectral intensities are normalized to number of scans. An integrated enhancement of  $-29$ ,  $-33$  and  $-18.3$  can be observed on the corresponding proton signals. The inset shows the reference spectrum without irradiation enlarged by a factor of 100 for comparison, except toluene (C) where the detail of the enhanced aromatic ring is shown. The peak at  $-4$  ppm arises from solvent outside of the MW-resonator and is therefore not enhanced.

corresponding to a  $B_1$  field of 3 G. All microwave pumped signals show a strong negative enhancement, as expected for dipolar coupling. Enhancement factors  $\varepsilon$  are  $-29$ ,  $-33$  and  $-18$  for DMSO, acetone and toluene, respectively.

Notably, while the signal from outside of the MW cavity remains unchanged at the same position, the DNP enhanced signal significantly changes its position with respect to the reference signal as indicated by the arrows in the figure. This shift, as already explained in our previous work on water,<sup>6</sup> is caused by a combination of MW heating and strong paramagnetic shift<sup>14</sup> induced by the high radical concentration. Therefore it is important to know temperature as well as the saturation factor for a quantitative evaluation of the DNP results. Whereas in DMSO and acetone we resolved only the signal from the methyl groups, in the case of the toluene sample (Fig. 2C) we were able to resolve all three signals, even if the resolution of the DNP probe is not optimal yet. We observed two signals from hydrogens bound to the aromatic ring and one signal from the methyl group (aliphatic hydrogens). The overall integrated enhancement of the ring protons is slightly larger compared to that of the methyl groups (Fig. 2C). In Fig. 3, the measured NMR signal enhancements for all three samples are shown as a function of applied microwave power.

In all cases the enhancement rises monotonically with increasing microwave power, due to the increased temperature

of the sample. Saturation of the EPR transition is achieved for these concentrations of radicals already much earlier, as reflected by the suppression of the paramagnetic shift as a function of microwave power (see ESI<sup>†</sup>). Therefore the saturation factor is  $s \approx 1$ .

The leakage factor was measured for all solvents and concentrations in the temperature range where DNP experiments were performed. Table 1 shows leakage factors at room temperature ( $25^\circ\text{C}$ ). Despite the fact that again all solvents exhibit different concentration dependence of the leakage factor, for concentrations above 100 mM the leakage factor under DNP conditions is  $f \approx 1$  for all solvents and experimental temperatures (more information in ESI<sup>†</sup>). The estimation of the saturation factor and the leakage factor is important (see eqn (1)) for determining the coupling factors related to the measured DNP enhancements  $\varepsilon$ . In this way, the coupling factors obtained from DNP and NMRD measurements can be quantitatively compared.

Table 1 Measured leakage factor  $f$  as a function of  $^{14}\text{N}$ -TEMPOL concentration at  $25^\circ\text{C}$  for organic solvents used as well as for water

	200 mM	100 mM	40 mM	20 mM	5 mM
DMSO	0.99	0.98	0.95	0.89	0.69
Acetone	0.98	0.93	0.85	0.62	0.26
Toluene $\text{CH}_3/\text{ring}$	0.98/0.99	0.96/0.98	0.91/0.94	0.85/0.89	0.58/0.67
Water	0.99	0.98	0.95	0.90	0.66

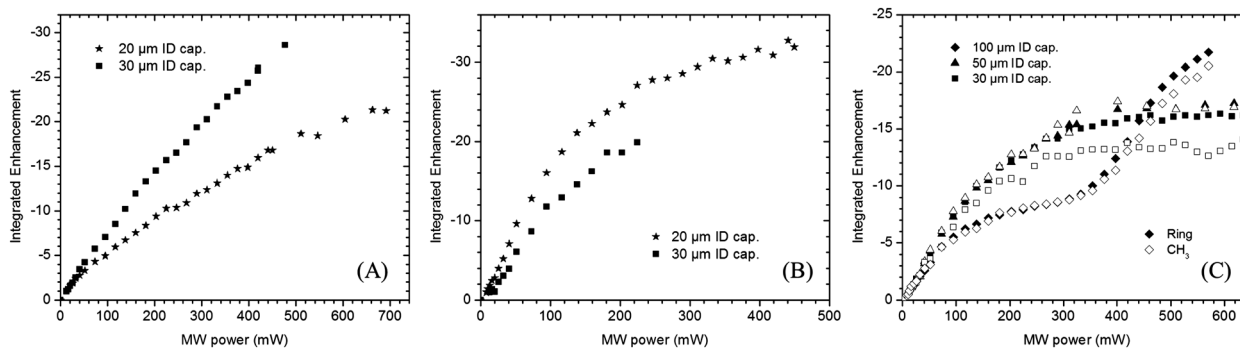


Fig. 3 The DNP enhancement plotted against the incident MW power for 1 M  $^{14}\text{N}$ -TEMPOL in DMSO (A) and acetone (B), and 200 mM  $^{14}\text{N}$ -TEMPOL in toluene (C) samples. Capillary sizes: 100 (◆), 50 (▲), 30 (■) and 20  $\mu\text{m}$  (★).

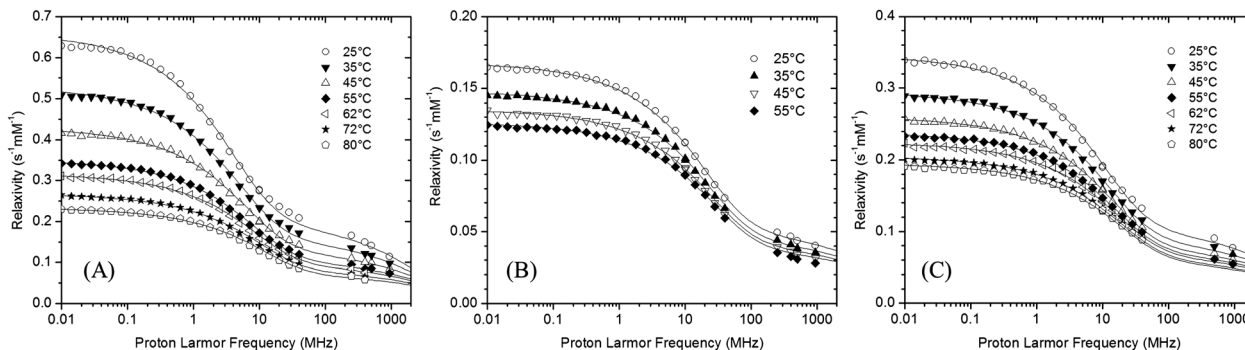


Fig. 4 Solvent  $^1\text{H}$  relaxivity profiles for solutions of  $^{14}\text{N}$ -TEMPOL in DMSO (A), acetone (B) and toluene (C) are shown at different temperatures ranging from 25 to 80 °C. Best fit profiles from the outer-sphere model are also shown as lines.

NMRD measurements performed at temperatures ranging from 25 °C to boiling temperature for all three solvents are shown in Fig. 4.

All dispersion profiles were fitted in a first step by using outer-sphere relaxation only. In this case the free parameter is the translational correlation time  $\tau_D$  and the relaxivity is given by

$$\frac{R_1}{c} = C(7J(\omega_I, \tau_D) + 3J(\omega_S, \tau_D)) \quad (5)$$

with  $c$  being the concentration of radicals,  $C$  a constant<sup>8</sup> and  $R_1$  the longitudinal nuclear spin relaxation rate. The fits to the experimental dispersion curves are rather good, although not perfect for DMSO and toluene. The resulting fit parameter  $\tau_D$  is reported in Table 2 for all solvents and two temperatures (model A). Slightly better fits for DMSO and toluene could be achieved by introducing an additional spectral density from inner-sphere contributions of the transiently formed radical-solvent complex (model B, data and fits shown in the ESI†). The rather small differences in the NMRD fits for these two solvents mainly show up in the region between 20 and 200 MHz proton Larmor frequencies. Note that the data points above 100 MHz are taken in a non-classical way by relaxation measurements on NMR spectrometers at the respective proton Larmor frequencies, leading to larger variations and errors of these data points. For the inner-sphere contributions a Lorentzian spectral density with a correlation time  $\tau_c$  was considered, with a temperature dependence given by

$$\tau_c = A \cdot \exp(B/T) \quad (6)$$

The values for outer-sphere diffusion correlation time  $\tau_D$  and inner-sphere correlation time  $\tau_c$  are reported under model B in Table 2. All best fit parameters are reported in the ESI.† Notably, the diffusion coefficients obtained from the best fit of the NMRD profiles (see Tables S1–S3, ESI†) are in agreement with the values expected for the different solvents. For comparison also the values for water as solvent are given in Table 2. For water satisfactory fits of the NMRD dispersion curves could only be obtained by taking also inner-sphere dynamics into account.<sup>6</sup> For all solvents a strong decrease of both correlation times  $\tau_D$  and  $\tau_c$  (about a factor of 2–3) could be observed by an

Table 2 Fit parameters of the NMRD profiles. Model A represents fits with only outer-sphere diffusional motion with correlation time  $\tau_D$ , model B with additional inner-sphere complex motion with an additional correlation time  $\tau_c$ . In model B, the increase in the paramagnetic enhancement is proportional to  $\sum_i n_i/r_i^6$ , where  $n_i$  is the number of protons at distance  $r_i$  from the paramagnetic center. Due to the six-power dependence, protons at the shortest distance are those providing the largest contribution. Further data are given in the ESI

Solvent molecule	Model	Temperature [K]	Trans. corr. time $\tau_D$ [ps]	Inner sphere corr. time $\tau_c$ [ps]
DMSO	A	298	115	—
DMSO	A	353	41	—
DMSO	B	298	129	1.57
DMSO	B	353	46	0.55
DMSO	C	298	127	3.71
DMSO	C	353	46	0.29
Acetone	A	298	23	—
Acetone	A	328	17	—
Toluene	A	289	43	—
Toluene	A	353	24	—
Toluene	B	298	49	1.54
Toluene	B	353	28	0.92
Water	B	298	30	17
Water	B	353	11	4

increase of the temperature by 55 °C. For acetone, because of the low boiling temperature, only a temperature increase of 30 °C could be achieved, resulting in a much lower factor of 1.35 only. Thus, increasing the temperature by heating strongly affects the coupling factor  $\zeta$  and therefore the achievable DNP enhancement  $\epsilon$ , as a result of the decrease in the correlation times.

The comparison of the coupling factors predicted from the fits of the NMR dispersion curves and from the DNP enhancements (by taking the saturation factor  $s$  and the leakage factor  $f$  explicitly into account) is shown for DMSO, acetone and toluene in Fig. 5.

Interestingly, while for the low viscosity solvent acetone the coupling factors extracted from DNP and NMRD measurements agree very well without taking into account any effect from fast  $\tau_c$  inner-sphere contributions, for the higher viscosity solvents DMSO and toluene inner-sphere fast dynamics of the complex must be explicitly taken into account. However, in the case of DMSO, the NMRD predicted coupling factors are clearly somewhat larger than the DNP determined coupling factors. We have then fit

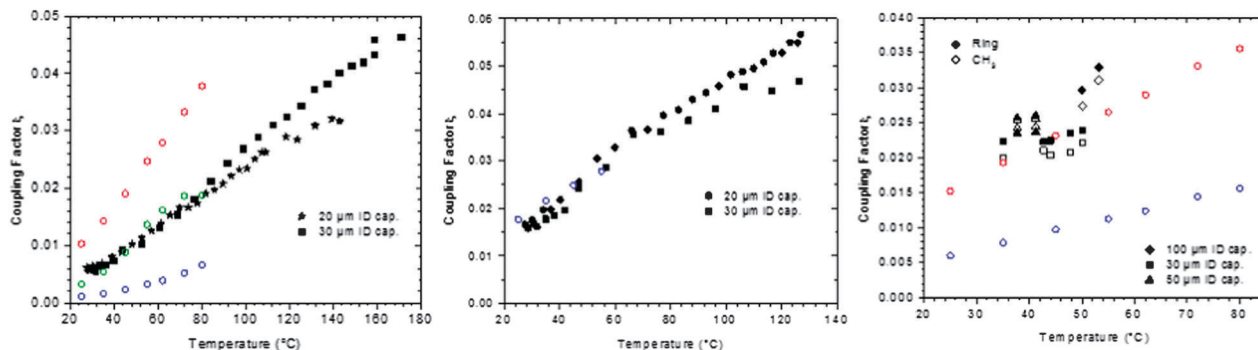


Fig. 5 Comparison of coupling factors  $\zeta$  calculated from DNP enhancement (in black) and from NMRD (outer-sphere model A in blue, outer-sphere and inner-sphere model B in red, model C as explained in the text in green) as a function of temperature. Left panel: DMSO, middle panel: acetone, right panel: toluene.

the NMRD profiles without imposing eqn (6) and found that an almost equally good fit can be obtained (see model C in Tables S5–S7 and Fig. S13 and S14, ESI†) providing NMRD-derived coupling factors in nice agreement with the DNP data (Fig. 5A). In summary, for DMSO and toluene the fast dynamics of the solvent–radical complex compensate the much lower efficiency of the diffusional dynamics, and contribute significantly to the overall coupling factor and therefore DNP enhancement observed for these solvents. Despite the fact that this high frequency dynamics only contribute rather weakly to the NMR dispersion curves they are essential to explain the high enhancements observed for these two solvents and to get consistent interpretation of DNP and NMRD experiments.

It is interesting to compare the coupling factors  $\zeta$  calculated from experimental magnetic resonance experiments with the ones extracted from MD simulations.<sup>15,16</sup> For toluene solutions at room temperature MD simulations predict a coupling factor of 0.019 to 0.02 at a magnetic field of 9.2 T for methyl and ring protons, respectively. These values agree very well with the coupling factors calculated from DNP enhancements and from the values predicted from NMRD measurements assuming outer-sphere and inner-sphere relaxation. The small difference of 10% between ring and methyl protons is beyond the accuracy of the DNP measurements, but indeed a slightly larger enhancement could be observed for the ring proton peaks (Fig. 2). Higher DNP enhancement of the ring protons has also been experimentally observed at lower magnetic fields of 0.3 T<sup>17</sup> and 3.4 T.<sup>18</sup> At low radical concentrations (<5 mM) and low magnetic field (0.3 T) higher enhancements were found in toluene compared to water as solvent. The reason is favourable saturation and leakage factors for toluene under these experimental conditions, whereas the extracted coupling factor at such magnetic fields was found to be about 30% lower for toluene compared with water, in good agreement with predictions from our NMRD measurements and MD simulations.<sup>16</sup> Interestingly the situation is opposite at a high magnetic field of 9.2 T: here the leakage and saturation factors at 5 mM radical concentration are slightly less favorable in toluene, whereas the coupling factor is higher for toluene compared to water. This demonstrates that different dynamics contribute to the DNP enhancement at different magnetic field strengths. At low magnetic fields translational diffusion (see Scheme 1 for rates) plays the dominant role, leading to a larger coupling factor for water

compared to toluene. At high magnetic fields the very fast inner-sphere dynamics of the nitroxide–toluene complex (compared to the nitroxide–water solution) contributes significantly to the coupling factor (Table 2 and ESI†). The rotational correlation times for nitroxide radicals in toluene extracted from cw-EPR spectra recorded at 9 and 260 GHz are longer than the inner-sphere correlation times necessary to explain our coupling factors at 260 GHz (see ESI†). DNP measurements performed at 94 GHz (3.4 T magnetic field)<sup>18</sup> achieved a maximal enhancement of  $-45$ , again in rather good agreement with the respective coupling factors extracted from NMRD or MD<sup>16</sup> data (assuming  $f = 1$  and  $s = 1$ ).

Also for DMSO as solvent very fast inner-sphere dynamics are essential to explain the DNP enhancements at high magnetic fields. In this case inner-sphere correlation times somewhat different from those obtained from the best fit to the NMRD profiles have to be assumed to achieve satisfactory agreement with NMRD and DNP data simultaneously. Nevertheless also these correlation times are much shorter than the rotational correlation times extracted from cw-EPR measurements (see ESI†). Similar discrepancies between rotational correlation times and inner-sphere dynamics have also been observed for TEMPOL in ethanol at 3.4 T magnetic field.<sup>19</sup> It can be speculated that low frequency vibrational or librational dynamics of the transient radical–solvent complex might be the source of these fast dynamics modulating the electron–nuclear spin hyperfine interaction on a short ps to sub-ps time scale, which are especially important for the DNP coupling factor at high magnetic fields and which are not modeled well within the approximations made by the force-free hard-sphere model.<sup>16</sup> Molecular dynamic simulations might allow obtaining a more atomistic understanding of such fast local dynamics.

## Experimental

CW-EPR measurements were performed with our home built G-band EPR spectrometer operating at a frequency of 180 GHz and a magnetic field of 6.4 T.<sup>20</sup>

DNP experiments were performed on a setup consisting of a commercial 400 MHz NMR spectrometer (Bruker Avance) equipped with a home built EPR bridge operating at 260 GHz

for electron spin excitation.<sup>21</sup> The samples were filled in quartz capillaries (Polymicro) with 100, 50, 30 or 20  $\mu\text{m}$  inner diameter (ID) and an outer diameter of 150  $\mu\text{m}$  and sealed with wax at both ends. They were placed inside a home built double resonance DNP probe with a cylindrical  $\text{TE}_{011}$  microwave resonator which also acts as a resonant helical coil for the NMR excitation (260 GHz/400 MHz). The length of the MW cavity is approximately 1.6 mm, leading to effective sample volumes of 13, 3, 1.1 or 0.5 nl respectively. Microwave excitation with power of up to 500 mW was achieved by a gyrotron source. The DNP enhancements were determined by taking the  $^1\text{H}$  FT-NMR spectra of the samples with and without continuous wave (CW) MW irradiation of the central hyperfine line of the  $^{14}\text{N}$ -TEMPOL nitroxide spectra. Integrated proton NMR signals were used to calculate the DNP enhancement factor  $\varepsilon$ . The temperature is a critical parameter in the DNP experiments because of sample heating by the microwave excitation. We determined the sample temperature of the tiny DNP samples under microwave irradiation by the temperature dependent chemical shift difference ( $\Delta\delta$ ) between the  $\text{CH}_2$  and OH groups of ethylene glycol.<sup>6</sup> We added 10% of ethylene glycol to pure solvent samples and recorded the shift difference ( $\Delta\delta$ ) as a function of temperature using the Bruker BBI probe. Subsequently,  $\Delta\delta$  was monitored in the DNP resonator under microwave irradiation, allowing determination of the sample temperature at a given microwave power. We observed a very strong MW heating in the case of acetone (similar to water) and smaller microwave heating with the other two solvents. We estimated the error in the temperature determination by this method to be less than 10%. While we could use ethylene glycol as a “chemical shift thermometer” in the case of DMSO, acetone and water, this method failed in the case of toluene, because of insolubility. Unfortunately, also methanol as a substitute for ethylene glycol could not be used successfully because NMR signals outside the MW resonator overlapped with the methanol lines. However toluene, among all the above mentioned solvents, has the lowest dielectric constant and therefore very low MW heating. Together with the knowledge gained on the other solvents we could estimate the temperature of toluene to be below 60  $^\circ\text{C}$  even under high microwave excitation power. This was also confirmed by DNP experiments performed with different ID capillaries (as shown in Fig. 2C). For the two smaller capillaries (30 and 50  $\mu\text{m}$ ) we observed the same rise of the enhancement upon applied MW power, demonstrating that we observe a rise due to the change in the saturation factor and not due to elevated temperature for such capillary sizes. In the largest capillary (100  $\mu\text{m}$ ) we saw a step in the enhancement curve which is also observable in the paramagnetic NMR shift measurements (see ESI<sup>†</sup>). This might be due to detuning of the microwave resonant cavity by heating or convection flow in the larger capillary. Due to the larger dielectric losses in DMSO and acetone, we performed all the DNP experiments in 20  $\mu\text{m}$  and 30  $\mu\text{m}$  ID capillaries (Fig. 2A and B). DMSO shows the expected trend, where the enhancement in the larger capillary rises faster than in the smaller one, due to heating. However this is not the case with acetone, where we see an opposite effect due to different saturation behaviour (see ESI<sup>†</sup>).

Relaxation time measurements were performed using a commercial 400 MHz liquid state probe (Bruker BBI). Longitudinal

relaxation rates at magnetic fields ranging from 0.01 to 40 MHz proton Larmor frequency were measured using the field cycling technique with a high sensitive relaxometer (Stelar Spinmaster FFC-2000-1T). Errors in the measurement of the relaxation rates were below 1%. Proton relaxivity was calculated by subtraction of the relaxation rates of the buffer from the relaxation rate of the  $^{14}\text{N}$ -TEMPOL solution, and normalization to the radical concentration. High frequency relaxation rates at higher frequencies (250, 400, 500 and 950 MHz) were measured on separate NMR spectrometers.

## Conclusion

DNP and NMRD experiments on solutions of TEMPOL radicals in DMSO, acetone and toluene have been performed. The coupling factors  $\xi$  extracted from these measurements range between 0.005 and 0.02 at room temperature, despite their order of magnitude different viscosities and diffusion constants. Thus, large proton Overhauser DNP enhancements in the range of 10–50 have been observed for all three solvents. This is in line with experimental results on the polarization transfer efficiency from TEMPOL to water<sup>6</sup> or other molecules such as pyruvate, lactate and acetate in aqueous solution.<sup>22</sup> In all these cases substantial DNP enhancements could be observed at a high magnetic field of 9.2 T. A combination of the two methods allows one to highlight and quantify the significant contribution of fast dynamics of the radical–solvent complex to the coupling factor at high magnetic fields not related to viscosity and translational diffusion coefficient of the solvent and the radical molecule. Molecular dynamic simulations might give more insight into the molecular origins of these fast dynamics and allow one to make predictions for optimization of the DNP agent/target system for a given magnetic field strength. These findings also allow one to speculate that liquid state Overhauser DNP polarization transfer might be efficient and useable at even higher magnetic field strengths, provided the technical problems related to MW sample heating can be solved.

## Acknowledgements

This work was supported by the DIP program from the German Research Council (DFG), the Center for Biomolecular Magnetic Resonance (BMRZ), Frankfurt, the European Commission (Bio-NMR) and the COST Action (TD1103). We would like to thank Juan Carlos Lagomacini for checking the temperature calibration procedure, Burkhard Endeward, Johanna Baldus, Christian Richter, and Frank Löhr for experimental assistance and Shimon Vega for scientific discussion. Also, we gratefully acknowledge technical support from Bernhard Thiem, Manfred Strupf and Bruker Biospin.

## References

- 1 L. R. Becerra, G. J. Gerfen, R. J. Temkin, D. J. Singel and R. G. Griffin, *Phys. Rev. Lett.*, 1993, **71**, 3561–3564.
- 2 J. H. Ardenkjær-Larsen, B. Fridlund, A. Gram, G. Hansson, L. Hansson, M. H. Lerche, R. Servin, M. Thaning and

- K. Golman, *Proc. Natl. Acad. Sci. U. S. A.*, 2003, **100**, 10158–10163.
- 3 M. J. Prandolini, V. P. Denysenkov, M. Gafurov, B. Endeward and T. F. Prisner, *J. Am. Chem. Soc.*, 2009, **131**, 6090–6092.
- 4 C. Griesinger, M. Bennati, H. M. Vieth, C. Luchinat, G. Parigi, P. Höfer, F. Engelke, S. J. Glaser, V. Denysenkov and T. F. Prisner, *Prog. Nucl. Magn. Reson. Spectrosc.*, 2012, **64**, 4–28.
- 5 A. W. Overhauser, *Phys. Rev.*, 1953, **92**, 411–415.
- 6 P. Neugebauer, J. G. Krummenacker, V. P. Denysenkov, G. Parigi, C. Luchinat and T. F. Prisner, *Phys. Chem. Chem. Phys.*, 2013, **15**, 6049–6056.
- 7 L.-P. Hwang and J. H. Freed, *J. Chem. Phys.*, 1975, **63**, 4017–4025.
- 8 M.-T. Turke, G. Parigi, C. Luchinat and M. Bennati, *Phys. Chem. Chem. Phys.*, 2012, **14**, 502–510.
- 9 I. Bertini, C. Luchinat and G. Parigi, *Adv. Inorg. Chem.*, 2005, **57**, 105–172.
- 10 D. Sezer, M. J. Prandolini and T. F. Prisner, *Phys. Chem. Chem. Phys.*, 2009, **11**, 6626–6637.
- 11 W. R. Baird and R. T. Foley, *J. Chem. Eng. Data*, 1972, **17**, 355–357.
- 12 S. Glasstone, *Textbook of Physical Chemistry*, Macmillan & Co Ltd, London, 1951.
- 13 R. Battino, T. R. Rettich and T. Tominaga, *J. Phys. Chem. Ref. Data*, 1983, **12**, 163–178.
- 14 I. Bertini, C. Luchinat and G. Parigi, *Solution NMR of Paramagnetic Molecules*, Elsevier, 2001, vol. 2.
- 15 D. Sezer, *Phys. Chem. Chem. Phys.*, 2013, **15**, 526–540.
- 16 D. Sezer, *Phys. Chem. Chem. Phys.*, 2014, **16**, 1022–1032.
- 17 N. Enkin, G. Liu, I. Tkach and M. Bennati, *Phys. Chem. Chem. Phys.*, 2014, **16**, 8795–8800.
- 18 E. V. Kyukov, M. E. Newton, K. J. Pike, D. R. Bolton, R. M. Kowalczyk, A. P. Howes, M. E. Smith and R. Dupree, *Phys. Chem. Chem. Phys.*, 2010, **12**, 5757–5767.
- 19 G. H. A. van der Heijden, A. P. M. Kentgens and P. J. M. van Bentum, *Phys. Chem. Chem. Phys.*, 2014, **16**, 8493–8502.
- 20 M. H. Hertel, V. Denysenkov, M. Bennati and T. F. Prisner, *Magn. Reson. Chem.*, 2005, **43**, 248–255.
- 21 V. P. Denysenkov, M. J. Prandolini, M. Gafurov, D. Sezer, B. Endeward and T. F. Prisner, *Phys. Chem. Chem. Phys.*, 2010, **12**, 5786–5790.
- 22 J. Krummenacker, V. Denysenkov and T. F. Prisner, *Appl. Magn. Reson.*, 2012, **43**, 139–146.

## 8 REFERENCES

1. C. Boesch, *J. Magn. Reson. Imag.*, 2004, **20**, 177-179.
2. E. K. Zavoisky, *Zh. Eksp. Teor. Fiz.*, 1945, **15**, 253.
3. E. M. Purcell, H. C. Torrey and R. V. Pound, *Phys. Rev.*, 1946, **69**, 37-38.
4. E. L. Hahn, *Phys. Rev.*, 1950, **80**, 580-594.
5. R. J. Blume, *Phys. Rev.*, 1958, **109**, 1867-1873.
6. J. P. Gordon and K. D. Bowers, *Phys. Rev. Lett.*, 1958, **1**, 368-370.
7. D. E. Kaplan, M. E. Browne and J. A. Cowen, *Rev. Sci. Instrum.*, 1961, **32**, 1182-1186.
8. G. Feher, *Bell Syst. Tech. J.*, 1957, **36**, 449-484.
9. M. A. Ondar, A. A. Dubinskii, O. Ya. Grinberg, J. A. Grigor'ev, L. B. Volodarskii and Y. S. Lebedev, *Zhurnal Strukturnoi Khimii*, 1981, **22**.
10. H. C. Box, E. E. Budzinski, H. G. Freund and W. R. Potter, *J. Chem. Phys.*, 1979, **70**, 1320-1325.
11. E. Haindl, K. Möbius and H. Oloff, *Z. Naturforsch.*, 1985, **40a**, 169-172.
12. W. B. Lynch, K. A. Earle and J. H. Freed, *Rev. Sci. Instrum.*, 1988, **59**, 1345-1351.
13. R. T. Weber, J. A. J. M. Disselhorst, L. J. Prevo, J. Schmidt and W. T. H. Wenckebach, *J. Magn. Reson.*, 1989, **81**, 129-144.
14. F. Muller, M. A. Hopkins, N. Coron, M. Grynberg, L. C. Brunel and G. Martinez, *Rev. Sci. Instrum.*, 1989, **60**, 3681-3684.
15. A. L. Barra, L. C. Brunel and J. B. Robert, *Chem. Phys. Lett.*, 1990, **165**, 107-109.
16. T. F. Prisner, S. Un and R. G. Griffin, *Israel Journal of Chemistry*, 1992, **32**, 357-363.
17. L. R. Becerra, G. J. Gerfen, R. J. Temkin, D. J. Singel and R. G. Griffin, *Phys. Rev. Lett.*, 1993, **71**, 3561-3564.
18. D. A. Hall, D. C. Maus, G. J. Gerfen, S. J. Inati, L. R. Becerra, F. W. Dahlquist and R. G. Griffin, *Science*, 1997, **276**, 930-932.
19. A. D. Milov, A. B. Ponomarev and Y. D. Tsvetkov, *Chem. Phys. Lett.*, 1984, **110**, 67-72.
20. G. Jeschke and Y. Polyhach, *Phys. Chem. Chem. Phys.*, 2007, **9**, 1895-1910.
21. M. Bennati and T. F. Prisner, *Reports on Progress in Physics*, 2005, **68**, 411.
22. M. Rohrer, O. Brüggemann, B. Kinzer and T. F. Prisner, *Appl Magn Reson*, 2001, **21**, 257-274.
23. J. v. Tol, L.-C. Brunel and R. J. Wylde, *Rev. Sci. Instrum.*, 2005, **76**, 074101.
24. H. Blok, J. A. J. M. Disselhorst, S. B. Orlinskii and J. Schmidt, *J. Magn. Reson.*, 2004, **166**, 92-99.
25. T. A. Siaw, A. Leavesley, A. Lund, I. Kaminker and S. Han, *J. Magn. Reson.*, 2016, **264**, 131-153.
26. P. Neugebauer and A.-L. Barra, *Appl. Magn. Reson.*, 2010, **37**, 833-843.
27. P. Neugebauer, Ph.D., University of Grenoble, 2010.
28. S. S. Eaton, R. W. Quine, M. Tseitlin, D. G. Mitchell, G. A. Rinard and G. R. Eaton, in *Multifrequency Electron Paramagnetic Resonance*, Wiley-VCH, 2014, pp. 3-67.
29. J. S. Hyde, R. A. Strangeway, T. G. Camenisch, J. J. Ratke and W. Froncisz, *J. Magn. Reson.*, 2010, **205**, 93-101.
30. A. Doll, S. Pribitzer, R. Tschaggelar and G. Jeschke, *J. Magn. Reson.*, 2013, **230**, 27-39.
31. P. E. Spindler, Y. Zhang, B. Endeward, N. Gershernzon, T. E. Skinner, S. J. Glaser and T. F. Prisner, *J. Magn. Reson.*, 2012, **218**, 49-58.
32. P. E. Spindler, P. Schöps, W. Kallies, S. J. Glaser and T. F. Prisner, *J. Magn. Reson.*, 2017, **280**, 30-45.
33. K. Mobius, A. Savitsky, A. Schnegg, M. Plato and M. Fuchs, *Phys. Chem. Chem. Phys.*, 2005, **7**, 19-42.

34. J. A. Weil and J. R. Bolton, *Electron Paramagnetic Resonance: Elementary Theory and Practical Applications*, Wiley, 2nd edn., 2006.
35. J. Keeler, *Understanding NMR Spectroscopy*, 2nd edn., 2010.
36. V. L. Granatstein, R. K. Parker and C. M. Armstrong, *Proceedings of the IEEE*, 1999, **87**, 702-716.
37. P. M. Champion and A. J. Sievers, *J. Chem. Phys.*, 1980, **72**, 1569-1582.
38. P. L. Richards, *J. Appl. Phys.*, 1963, **34**, 1237-1238.
39. A. A. Mukhin, V. D. Travkin, A. K. Zvezdin, S. P. Lebedev, A. Caneschi and D. Gatteschi, *EPL (Europhysics Letters)*, 1998, **44**, 778.
40. A. Mukhin, B. Gorshunov, M. Dressel, C. Sangregorio and D. Gatteschi, *Phys. Rev. B*, 2001, **63**, 214411.
41. J. van Slageren, S. Vongtragool, B. Gorshunov, A. A. Mukhin, N. Karl, J. Krzystek, J. Telsler, A. Muller, C. Sangregorio, D. Gatteschi and M. Dressel, *Phys. Chem. Chem. Phys.*, 2003, **5**, 3837-3843.
42. K. Ray, A. Begum, T. Weyhermüller, S. Piligkos, J. van Slageren, F. Neese and K. Wieghardt, *J. Am. Chem. Soc.*, 2005, **127**, 4403-4415.
43. A. Schnegg, J. Behrends, K. Lips, R. Bittl and K. Holldack, *Phys. Chem. Chem. Phys.*, 2009, **11**, 6820-6825.
44. A. Schweiger and G. Jeschke, *Principles of Pulse Electron Paramagnetic Resonance*, Oxford University Press, 2001.
45. C. Altenbach, S. L. Flitsch, H. G. Khorana and W. L. Hubbell, *Biochemistry*, 1989, **28**, 7806-7812.
46. W. L. Hubbell and C. Altenbach, *Current Opinion in Structural Biology*, 1994, **4**, 566-573.
47. T. F. Prisner, in *Biolog. Magn. Reson.*, 2004, vol. 22, pp. 249-272.
48. K. S. Novoselov, A. K. Geim, S. V. Morozov, D. Jiang, Y. Zhang, S. V. Dubonos, I. V. Grigorieva and A. A. Firsov, *Science*, 2004, **306**, 666-669.
49. P. R. Wallace, *Phys. Rev.*, 1947, **71**, 622-634.
50. M. Orlita, C. Faugeras, P. Plochocka, P. Neugebauer, G. Martinez, D. K. Maude, A. L. Barra, M. Sprinkle, C. Berger, W. A. de Heer and M. Potemski, *Phys. Rev. Lett.*, 2008, **101**, 267601.
51. A. K. Geim and K. S. Novoselov, *Nat Mater*, 2007, **6**, 183-191.
52. A. K. Geim, *Science*, 2009, **324**, 1530-1534.
53. C. Berger, Z. Song, X. Li, X. Wu, N. Brown, C. Naud, D. Mayou, T. Li, J. Hass, A. N. Marchenkov, E. H. Conrad, P. N. First and W. A. de Heer, *Science*, 2006, **312**, 1191-1196.
54. C. Berger, Z. Song, T. Li, X. Li, A. Y. Ogbazghi, R. Feng, Z. Dai, A. N. Marchenkov, E. H. Conrad, P. N. First and W. A. de Heer, *J. Phys. Chem. B*, 2004, **108**, 19912-19916.
55. J. K. Galt, W. A. Yager and H. W. Dail, *Physical Review*, 1956, **103**, 1586-1587.
56. P. Neugebauer, M. Orlita, C. Faugeras, A. L. Barra and M. Potemski, *Phys. Rev. Lett.*, 2009, **103**, 136403.
57. A. S. Mayorov, D. C. Elias, I. S. Mukhin, S. V. Morozov, L. A. Ponomarenko, K. S. Novoselov, A. K. Geim and R. V. Gorbachev, *Nano Letters*, 2012, **12**, 4629-4634.
58. M. Orlita, P. Neugebauer, C. Faugeras, A. L. Barra, M. Potemski, F. M. D. Pellegrino and D. M. Basko, *Phys. Rev. Lett.*, 2012, **108**, 017602.
59. R. E. Doezema, W. R. Datars, H. Schaber and A. Van Schyndel, *Phys. Rev. B*, 1979, **19**, 4224-4230.
60. D. Gatteschi, R. Sessoli and J. Villain, *Molecular Nanomagnets*, Oxford University Press, 2006.
61. A. Caneschi, D. Gatteschi, R. Sessoli, A. L. Barra, L. C. Brunel and M. Guillot, *J. Am. Chem. Soc.*, 1991, **113**, 5873-5874.
62. R. Sessoli, D. Gatteschi, A. Caneschi and M. A. Novak, *Nature*, 1993, **365**, 141.

63. J. R. Friedman, M. P. Sarachik, J. Tejada and R. Ziolo, *Phys. Rev. Lett.*, 1996, **76**, 3830-3833.
64. L. Thomas, F. Lioni, R. Ballou, D. Gatteschi, R. Sessoli and B. Barbara, *Nature*, 1996, **383**, 145.
65. L. Gregoli, C. Danieli, A.-L. Barra, P. Neugebauer, G. Pellegrino, G. Poneti, R. Sessoli and A. Cornia, *Chem. Eur. J.*, 2009, **15**, 6456-6467.
66. T. Lis, *Acta Cryst. B*, 1980, **36**, 2042-2046.
67. R. Inglis, L. F. Jones, C. J. Milios, S. Datta, A. Collins, S. Parsons, W. Wernsdorfer, S. Hill, S. P. Perlepes, S. Piligkos and E. K. Brechin, *Dalton Trans.*, 2009, 3403-3412.
68. C. J. Milios, R. Inglis, A. Vinslava, R. Bagai, W. Wernsdorfer, S. Parsons, S. P. Perlepes, G. Christou and E. K. Brechin, *J. Am. Chem. Soc.*, 2007, **129**, 12505-12511.
69. R. Layfield and M. Murugesu, *Lanthanides and Actinides in Molecular Magnetism*, Weinheim, Wiley-VCH edn., 2015.
70. S. T. Liddle and J. van Slageren, *Chemical Society Reviews*, 2015, **44**, 6655-6669.
71. J. Rozboril, Y. Rechkemmer, D. Bloos, F. Munz, C. N. Wang, P. Neugebauer, J. Cechal, J. Novak and J. van Slageren, *Dalton Trans.*, 2016, **45**, 7555-7558.
72. M. Mannini, F. Pineider, P. Sainctavit, C. Danieli, E. Otero, C. Sciancalepore, A. M. Talarico, M.-A. Arrio, A. Cornia, D. Gatteschi and R. Sessoli, *Nat. Mater.*, 2009, **8**, 194-197.
73. M. Mannini, F. Bertani, C. Tudisco, L. Malavolti, L. Poggini, K. Misztal, D. Menozzi, A. Motta, E. Otero, P. Ohresser, P. Sainctavit, G. G. Condorelli, E. Dalcanale and R. Sessoli, *Nat. Commun.*, 2014, **5**.
74. M. N. Leuenberger and D. Loss, *Nature*, 2001, **410**, 789-793.
75. M. N. Leuenberger and D. Loss, *Phys. Rev. B*, 2000, **61**, 12200-12203.
76. A. Ardavan, O. Rival, J. J. L. Morton, S. J. Blundell, A. M. Tyryshkin, G. A. Timco and R. E. P. Winpenny, *Phys. Rev. Lett.*, 2007, **98**, 057201.
77. L. Bogani and W. Wernsdorfer, *Nat Mater*, 2008, **7**, 179-186.
78. A. R. Rocha, V. M. García-suárez, S. W. Bailey, C. J. Lambert, J. Ferrer and S. Sanvito, *Nature Materials*, 2005, **4**, 335.
79. A. L. Barra, *Inorganica Chimica Acta*, 2008, **361**, 3564-3569.
80. L. Vergnani, A.-L. Barra, P. Neugebauer, M. J. Rodriguez-Douton, R. Sessoli, L. Sorace, W. Wernsdorfer and A. Cornia, *Chem. Eur. J.*, 2012, **18**, 3390-3398.
81. S. Petit, P. Neugebauer, G. Pilet, G. Chastanet, A.-L. Barra, A. B. Antunes, W. Wernsdorfer and D. Luneau, *Inorg. Chem.*, 2012, **51**, 6645-6654.
82. F. El Hallak, P. Neugebauer, A.-L. Barra, J. van Slageren, M. Dressel and A. Cornia, *J. Magn. Reson.*, 2012, **223**, 55-60.
83. T. K. Prasad, G. Poneti, L. Sorace, M. J. Rodriguez-Douton, A.-L. Barra, P. Neugebauer, L. Costantino, R. Sessoli and A. Cornia, *Dalton Trans.*, 2012, **41**, 8368-8378.
84. Y.-Y. Zhu, T.-T. Yin, S.-D. Jiang, A.-L. Barra, W. Wernsdorfer, P. Neugebauer, R. Marx, M. Dorfel, B.-W. Wang, Z.-Q. Wu, J. van Slageren and S. Gao, *Chem. Commun.*, 2014, **50**, 15090-15093.
85. C. Aronica, Y. Chumakov, E. Jeanneau, D. Luneau, P. Neugebauer, A.-L. Barra, B. Gillon, A. Goujon, A. Cousson, J. Tercero and E. Ruiz, *Chem. Eur. J.*, 2008, **14**, 9540-9548.
86. D. Schweinfurth, Y. Rechkemmer, S. Hohloch, N. Deibel, I. Peremykin, J. Fiedler, R. Marx, P. Neugebauer, J. van Slageren and B. Sarkar, *Chem. Eur. J.*, 2014, **20**, 3475 – 3486.
87. K. Bader, D. Dengler, S. Lenz, B. Endeward, S.-D. Jiang, P. Neugebauer and J. van Slageren, *Nat. Commun.*, 2014, **5**, 5304.
88. E. Moreno Pineda, N. F. Chilton, R. Marx, M. Dorfel, D. O. Sells, P. Neugebauer, S.-D. Jiang, D. Collison, J. van Slageren, E. J. L. McInnes and R. E. P. Winpenny, *Nat. Commun.*, 2014, **5**, 5243.

89. I. Nemeč, R. Marx, R. Herchel, P. Neugebauer, J. van Slageren and Z. Trávníček, *Dalton Trans.*, 2015, **44**, 15014-15021.
90. Y. Rechkemmer, J. E. Fischer, R. Marx, M. Dörfel, P. Neugebauer, S. Horvath, M. Gysler, T. Brock-Nannestad, W. Frey, M. F. Reid and J. van Slageren, *J. Am. Chem. Soc.*, 2015, **137**, 13114-13120.
91. A. Abhervé, M. Palacios-Corella, J. M. Clemente-Juan, R. Marx, P. Neugebauer, J. van Slageren, M. Clemente-León and E. Coronado, *J. Mater. Chem. C*, 2015, **3**, 7936-7945.
92. M. van der Meer, Y. Rechkemmer, F. D. Breitgoff, R. Marx, P. Neugebauer, U. Frank, J. van Slageren and B. Sarkar, *Inorg. Chem.*, 2016, **55**, 11944-11953.
93. M. van der Meer, Y. Rechkemmer, U. Frank, F. D. Breitgoff, S. Hohloch, C.-Y. Su, P. Neugebauer, R. Marx, M. Dörfel, J. van Slageren and B. Sarkar, *Chem. Eur. J.*, 2016, **22**, 13884-13893.
94. S. Realista, A. J. Fitzpatrick, G. Santos, L. P. Ferreira, S. Barroso, L. C. J. Pereira, N. A. G. Bandeira, P. Neugebauer, J. Hruby, G. G. Morgan, J. van Slageren, M. J. Calhorda and P. N. Martinho, *Dalton Trans.*, 2016, **45**, 12301-12307.
95. M. van der Meer, Y. Rechkemmer, F. D. Breitgoff, S. Dechert, R. Marx, M. Dorfel, P. Neugebauer, J. van Slageren and B. Sarkar, *Dalton Trans.*, 2016, **45**, 8394-8403.
96. M. Gysler, F. El Hallak, L. Ungur, R. Marx, M. Hakl, P. Neugebauer, Y. Rechkemmer, Y. Lan, I. Sheikin, M. Orlita, C. E. Anson, A. K. Powell, R. Sessoli, L. F. Chibotaru and J. van Slageren, *Chem. Sci.*, 2016, **7**, 4347-4354.
97. Y. Rechkemmer, F. D. Breitgoff, M. van der Meer, M. Atanasov, M. Hakl, M. Orlita, P. Neugebauer, F. Neese, B. Sarkar and J. van Slageren, *Nat. Commun.*, 2016, **7**, 10467.
98. J.-J. Liu, S.-D. Jiang, P. Neugebauer, J. van Slageren, Y. Lan, W. Wernsdorfer, B.-W. Wang and S. Gao, *Inorg. Chem.*, 2017, **56**, 2417-2425.
99. M. G. Sommer, R. Marx, D. Schweinfurth, Y. Rechkemmer, P. Neugebauer, M. van der Meer, S. Hohloch, S. Demeshko, F. Meyer, J. van Slageren and B. Sarkar, *Inorg. Chem.*, 2017, **56**, 402-413.
100. I. Nemeč, R. Herchel, M. Kern, P. Neugebauer, J. van Slageren and Z. Trávníček, *Materials*, 2017, **10**, 249.
101. P. Lutz, D. Aguilà, A. Mondal, D. Pinkowicz, R. Marx, P. Neugebauer, B. Fåk, J. Ollivier, R. Clérac and J. van Slageren, *Phys. Rev. B*, 2017, **96**, 094415.
102. A. Abragam and B. Bleaney, *Electron Paramagnetic Resonance of Transition Ions*, Dover Publications, Inc., New York, 1986.
103. C. Sauvée, M. Rosay, G. Casano, F. Aussenac, R. T. Weber, O. Ouari and P. Tordo, *Angew. Chem., Int. Ed.*, 2013, **52**, 10858-10861.
104. C. Sauvée, G. Casano, S. Abel, A. Rockenbauer, D. Akhmetzyanov, H. Karoui, D. Siri, F. Aussenac, W. Maas, R. T. Weber, T. Prisner, M. Rosay, P. Tordo and O. Ouari, *Chem. Eur. J.*, 2016, **22**, 5598-5606.
105. P. Neugebauer, J. G. Krummenacker, V. P. Denysenkov, G. Parigi, C. Luchinat and T. F. Prisner, *Phys. Chem. Chem. Phys.*, 2012, **15**, 6049 - 6056.
106. P. Neugebauer, J. G. Krummenacker, V. P. Denysenkov, C. Helmling, C. Luchinat, G. Parigi and T. F. Prisner, *Phys. Chem. Chem. Phys.*, 2014, **16**, 18781-18787.
107. A. S. Lilly Thankamony, J. J. Wittmann, M. Kaushik and B. Corzilius, *Progress in Nuclear Magnetic Resonance Spectroscopy*, 2017, **102-103**, 120-195.
108. A. W. Overhauser, *Phys. Rev.*, 1953, **92**, 411-415.
109. T. R. Carver and C. P. Slichter, *Phys. Rev.*, 1953, **92**, 212-213.
110. T. Maly, G. T. Debelouchina, V. S. Bajaj, K. N. Hu, C. G. Joo, M. L. Mak-Jurkauskas, J. R. Sirigiri, P. C. A. van der Wel, J. Herzfeld, R. J. Temkin and R. G. Griffin, *J. Chem. Phys.*, 2008, **128**, 052211-052219.

111. J. H. Ardenkjær-Larsen, B. Fridlund, A. Gram, G. Hansson, L. Hansson, M. H. Lerche, R. Servin, M. Thaning and K. Golman, *Proceedings of the National Academy of Sciences of the United States of America*, 2003, **100**, 10158-10163.
112. C. Griesinger, M. Bennati, H. M. Vieth, C. Luchinat, G. Parigi, P. Höfer, F. Engelke, S. J. Glaser, V. Denysenkov and T. F. Prisner, *Progress in Nuclear Magnetic Resonance Spectroscopy*, 2012, **64**, 4-28.
113. I. Solomon, *Phys. Rev.*, 1955, **99**, 559-565.
114. K. H. Hausser, Stehlik, D., *Advances in Magnetic Resonance*, 1968, **3**, 79-139.
115. J. Wolber, F. Ellner, B. Fridlund, A. Gram, H. Jóhannesson, G. Hansson, L. H. Hansson, M. H. Lerche, S. Månsson, R. Servin, M. Thaning, K. Golman and J. H. Ardenkjær-Larsen, *Nuclear Instruments and Methods in Physics Research Section A: Accelerators, Spectrometers, Detectors and Associated Equipment*, 2004, **526**, 173-181.
116. M. Reese, D. Lennartz, T. Marquardsen, P. Höfer, A. Tavernier, P. Carl, T. Schippmann, M. Bennati, T. Carlomagno, F. Engelke and C. Griesinger, *Appl Magn Reson*, 2008, **34**, 301-311.
117. A. Krahn, P. Lottmann, T. Marquardsen, A. Tavernier, M.-T. Turke, M. Reese, A. Leonov, M. Bennati, P. Hofer, F. Engelke and C. Griesinger, *Phys. Chem. Chem. Phys.*, 2010, **12**, 5830-5840.
118. V. P. Denysenkov, M. J. Prandolini, A. Krahn, M. Gafurov, B. Endeward and T. F. Prisner, *Appl Magn Reson*, 2008, **34**, 289-299.
119. R. E. Hoffman, *J. Magn. Reson.*, 2006, **178**, 237-247.
120. G. Liu, M. Levien, N. Karschin, G. Parigi, C. Luchinat and M. Bennati, *Nature Chemistry*, 2017, **9**, 676.
121. M. Tseitlin, A. Dhami, R. W. Quine, G. A. Rinard, S. S. Eaton and G. R. Eaton, *Appl. Magn. Reson.*, 2006, **30**, 651-656.
122. J. W. Stoner, D. Szymanski, S. S. Eaton, R. W. Quine, G. A. Rinard and G. R. Eaton, *J. Magn. Reson.*, 2004, **170**, 127-135.
123. N. Bloembergen, E. M. Purcell and R. V. Pound, *Phys. Rev.*, 1948, **73**, 679-712.
124. J. Dadok and R. F. Sprecher, *J. Magn. Reson.*, 1974, **13**, 243-248.
125. B. Král and A. Blatná, *Slaboproudý obzor*, 2016, **72**.
126. R. Beeler, D. Roux, G. Béné and R. Extermann, *Phys. Rev.*, 1956, **102**, 295-295.
127. [http://www.ebyte.it/library/hist/NMR\\_Tesla\\_cs.html](http://www.ebyte.it/library/hist/NMR_Tesla_cs.html).